

# **Origin of perpendicular magnetic anisotropy in Co/Ni multilayers and their use in STT-RAM**

by

**Monika Arora**

M.Sc., Guru Nanak Dev University, 2001

Thesis Submitted in Partial Fulfillment of the  
Requirements for the Degree of  
Doctor of Philosophy

in the  
Department of Physics  
Faculty of Science

© Monika Arora 2017  
**SIMON FRASER UNIVERSITY**  
**Fall 2017**

Copyright in this work rests with the author. Please ensure that any reproduction or re-use is done in accordance with the relevant national copyright legislation.

# Approval

**Name:** **Monika Arora**

**Degree:** **Doctor of Philosophy (Physics)**

**Title:** **Origin of perpendicular magnetic anisotropy in Co/Ni multilayers and their use in STT-RAM**

**Examining Committee:** **Chair:** Dr. Malcolm Kennett  
Associate Professor

**Dr. Erol Girt**  
Senior Supervisor  
Associate Professor

**Dr. Brett Heinrich**  
Co-Supervisor  
Emeritus Professor

**Dr. Karen Kavanagh**  
Supervisor  
Professor

**Dr. George Kirczenow**  
Internal Examiner  
Professor  
Department of Physics, SFU

**Dr. Andrew Kent**  
External Examiner  
Professor  
Department of Physics, New York University

**Date Defended:** **December 8th, 2017**

# Abstract

Magnetic properties of (111)-textured SAF/Cu/FL multilayer film structures were optimized by varying individual layer thickness and sputtering conditions. The SAF is a synthetic antiferromagnet consisting of Co/Ni multilayers coupled antiferromagnetically across a Ru spacer layer, and the FL is a free layer consisting of a single Co/Ni multilayer. The Co and Ni thicknesses were varied to obtain larger perpendicular magnetic anisotropy. The perpendicular magnetic anisotropy, saturation magnetization, damping and zero-frequency line broadening of the Co/Ni multilayers strongly depend on the number of bilayers. With increasing Cu seed-layer thickness, the texture of the Co/Ni multilayers improves while the grain size and film roughness increase. The increase in grain size results in the reduction of the direct exchange coupling between magnetic grains, which enhances the coercivity of the SAF and the FL. Experimentally measured coercivities of the SAF and FL are compared with calculations obtained from a coherent rotation model. The effect of the role of the Co/Cu interface in the magnetoresistance, is also discussed.

Spin-transfer-torque induced switching is investigated in 200 nm diameter circularly shaped, perpendicular magnetized nanopillars. The SAF layer is used as a reference layer to minimize the dipolar field on the free layer. The use of Pt and Pd was avoided to lower the spin-orbit scattering in magnetic layers and intrinsic damping in the free layer, and therefore, reduce the critical current required for spin-transfer-torque switching. In zero magnetic field the critical current required to switch the free layer from the parallel to antiparallel (antiparallel to parallel) alignment is 5.2 mA (4.9 mA). Given the volume of the free layer,  $V_{FL} = 1.01 \times 10^{-22} \text{ m}^3$ , the switching efficiency,  $I_c / (V_{FL} \times \mu_0 H_c)$ , is  $5.28 \times 10^{20} \text{ A/Tm}^3$ , twice as efficient as any previously reported device with a similar structure.

Variation in perpendicular magnetic anisotropy of (111) textured  $\text{Au}/N \times [\text{Co/Ni}]/\text{Au}$  films as a function of number of bilayer repeats  $N$  is studied. The experimental measurements show that the perpendicular magnetic anisotropy of Co/Ni multilayers first increases with  $N$  for  $N \leq 10$  and then moderately decreases for  $N > 10$ . The model we propose reveals that the decrease of the anisotropy for  $N < 10$  is predominantly due to the reduction in the magnetoelastic and magnetocrystalline anisotropies. A moderate decrease in the perpendicular magnetic anisotropy for  $N > 10$  is due to the reduction in the magnetocrystalline and the surface anisotropies.

**Keywords:** Magnetic anisotropy, giant magneto-resistance, spin transfer torque, magnetron sputtering



# Dedication

"dedicated to my family".

# Acknowledgements

First and foremost, I would like to express my utmost gratitude to my senior supervisor, Prof. Erol Girt. With his experience, knowledge and attitude on research, he is an ideal role model to me. He has devoted his precious time and patience to guide me in my Ph.D tenure. He guided me from project directions to presentation styles, writing scientific papers to curriculum vitae.

I would like to sincerely thank my co-supervisor Prof. Bret Heinrich for his guidance and support over the past few years. I very much enjoyed discussing the papers with him that made me always learn something new. His knowledge about the experimental and theoretical aspects of our work were crucial for completion of this thesis. I cannot think of anybody I have ever met who is more humble about their achievements and abilities.

I would like to thank the members of my thesis committee: Prof. Erol Girt and Prof. Prof. Bret Heinrich for taking time to review my thesis and for their very helpful comments and suggestions.

I would like to thank Physics department for organizing the course work. The most memorable time I had was when we had countless discussions of homework assignments, working together till four in the morning. A special thank goes to Prof. Simon Watkins, Prof. Karen Kavanagh, Prof. David Broun and Prof. Erol Girt who made the learning objectives, assessments and instructional strategies perfectly aligned. A special thanks to Prof. Zaven Altounian (McGill University) for his scientific discussions.

I wish to express my appreciation to my co-workers. A heartiest thank to Ken Myrtle for his unconditional support and physics discussions. His opinions is always highly valued. I would also like to thank Eric, Paul, Tommy, Nicholas, Zach, Farnaz, Wendell, Ricky, Bobo for helping me out with various parts of this thesis.

A part of my thesis work was conducted at Helmholtz Zentrum Dresden Rossendorf center, spintronics lab. I am particularly grateful to Dr. Alina Maria Deac and Dr. Ciaran Fowley for thier endless encouragement and mentorship. I would like to extend my gratitude to Dr. Volker Sluka, Ewa Kowalska and other members of HZDR for all their support over the course of my stay.

I would specifically like to acknowledge the other truly fantastic people with whom I interacted during this Ph.D. Special acknowledgement to Hoda Bagheri for her emotional and moral support; Kolawole Akintola, Alex Fang, Anand Pal and Avinash Kumar for lis-

tening to my endless discussions, Mpumelelo Matse and Matthew Fitzpatrick for helping me with mathematica coding, Faezeh Mohamadbeigi, Yule Wang, Dorna Niroomand, Lavisha Jindal, Cristina Cordoba, Shima Alagha for their great company and time we spent together.

Support from the structural characterization facilities at the HZDR Ion Beam Center, and financial support from the Natural Sciences and Engineering Research Council of Canada, and the Canadian Institute for Advanced Research are gratefully acknowledged.

Finally, I thank my family for their innumerable support, without whom I would not have likely finished this thesis.

# Table of Contents

<b>Approval</b>	<b>ii</b>
<b>Abstract</b>	<b>iii</b>
<b>Dedication</b>	<b>v</b>
<b>Acknowledgements</b>	<b>vi</b>
<b>Table of Contents</b>	<b>viii</b>
<b>List of Tables</b>	<b>xi</b>
<b>List of Figures</b>	<b>xii</b>
<b>1 Introduction</b>	<b>1</b>
1.1 An overview . . . . .	1
1.2 Working of STT-RAM . . . . .	2
1.3 Applications and challenges . . . . .	4
1.4 Motivation for using perpendicular STT-RAM devices . . . . .	4
1.5 A brief review . . . . .	6
1.6 Thesis Outlines . . . . .	7
<b>2 Theory</b>	<b>9</b>
2.1 Magnetic free energy . . . . .	9
2.2 Spin dependent scattering . . . . .	13
2.3 Giant Magnetoresistance (GMR) effect . . . . .	14
2.4 Spin Transfer Torque . . . . .	17
2.4.1 Mechanism of Spin Transfer Torque . . . . .	17
<b>3 Experimental Methods</b>	<b>19</b>
3.1 Sputter deposition . . . . .	20
3.1.1 Principles of sputtering (DC discharge): . . . . .	20
3.1.2 Radio Frequency (RF) sputtering: . . . . .	23
3.1.3 Magnetron sputtering . . . . .	25

3.2	Thin Film Characterization . . . . .	29
3.2.1	Structural characterization: X-ray Diffraction . . . . .	29
3.2.2	X-ray Reflectivity (XRR) . . . . .	31
3.2.3	Magnetic Technique: Magneto-Optical Kerr effect (MOKE) . . . . .	35
3.2.4	Superconducting quantum interference device (SQUID) Magnetometer: . . . . .	37
3.2.5	Ferromagnetic Resonance (FMR) . . . . .	40
3.2.6	Van der Pauw method . . . . .	48
3.2.7	TEM sample preparation . . . . .	49
3.3	Lithography . . . . .	49
3.3.1	Nano-pillar device preparation . . . . .	49
<b>4</b>	<b>Optimization of the magnetic properties of Co/Ni multilayer structures for use in STT-RAM</b>	<b>52</b>
4.1	Optimization Strategy . . . . .	52
4.1.1	Effect of Cu seed layer thickness on film microstructure . . . . .	52
4.1.2	Optimizing the magnetic properties of the single Co/Ni multilayer . . . . .	55
4.1.3	Optimizing the magnetic properties of the SAF layer . . . . .	64
4.1.4	Full structure optimization and GMR . . . . .	70
4.2	Summary . . . . .	75
<b>5</b>	<b>Spin torque switching in nanopillars with antiferromagnetic reference layer</b>	<b>77</b>
5.1	A brief introduction . . . . .	77
5.2	Logistics behind the design . . . . .	78
5.3	Sample Preparation . . . . .	78
5.4	Measurements on the continuous films . . . . .	79
5.4.1	Polar MOKE measurements and SQUID measurements: . . . . .	79
5.4.2	FMR measurements . . . . .	80
5.5	Transport measurements on nano-pillars . . . . .	81
5.5.1	Resistance measurements as a function of applied field . . . . .	81
5.5.2	Resistance change as a function of d.c. current . . . . .	84
5.6	Summary . . . . .	86
<b>6</b>	<b>The origin of perpendicular magnetic anisotropy in Co/Ni multilayers</b>	<b>88</b>
6.1	Brief background . . . . .	88
6.2	Theory . . . . .	89
6.2.1	Magnetoelastic anisotropy, $K_{ME}$ . . . . .	90
6.2.2	Magnetocrystalline anisotropy, $K_{MC}$ : . . . . .	90
6.2.3	Dipolar magnetic anisotropy including surface roughness, $K_{DIP}$ . . . . .	91
6.2.4	Surface anisotropy, $K_S$ . . . . .	94

6.2.5	Inter-diffusion induced anisotropy energy . . . . .	95
6.3	Studied structure . . . . .	95
6.4	As-deposited films . . . . .	96
6.4.1	X-ray measurements: . . . . .	96
6.4.2	Microstructure of Co/Ni MLs . . . . .	98
6.4.3	Magnetic properties of Co/Ni MLs . . . . .	101
6.5	Annealed films . . . . .	104
6.5.1	Structural and magnetic properties . . . . .	104
6.6	A Simplified Model including only surface anisotropies: . . . . .	106
6.7	Models for magnetic anisotropy . . . . .	109
6.8	Summary . . . . .	111
<b>7</b>	<b>Conclusion</b>	<b>113</b>
7.1	Future work . . . . .	115
	<b>Bibliography</b>	<b>117</b>

# List of Tables

Table 4.1	Magnetic moment and perpendicular magnetic anisotropy, $K_u$ from SQUID magnetometry, zero field line broadening, $\Delta H_0$ and damping, $\alpha$ , from FMR measurements for Ta/Cu( $d_{Cu1}$ )/8×[Co(0.21)/Ni(0.58)]/Ta with $d_{Cu1} = 1.9, 10$ and $30$ nm. . . . .	60
Table 6.1	$N$ , $d$ , $\sigma$ , and $\xi$ are the number, thicknesses, roughness and roughness period of the Co/Ni MLs, respectively. For $N = 0$ , $\sigma = \sigma^{Au/Co}$ and $\xi = \xi^{Au/Co}$ are the roughness and roughness period of the bottom Co/Ni MLs surface (Au/ML interface). For $N > 0$ , $\sigma = \sigma^{Ni/Au}$ and $\xi = \xi^{Ni/Au}$ are the roughness and roughness period of the top Co/Ni MLs surface (ML/Au interface). $K_V^{DIP} = -\mu_0 M_s^2/2$ is the dipolar volume anisotropy coefficient of a perfectly flat MLs, $K_S^{DIP} = K_{S,T}^{DIP} + K_{S,B}^{DIP}$ , where $K_{S,T}^{DIP}$ and $K_{S,B}^{DIP}$ are calculated using Eq.6.7, $K_{DIP} = K_V^{DIP} - K_S^{DIP}/d$ , and $H_{DIP} = 2K_{DIP}/\mu_0 M_s$ . $K_{DIP}(calc)$ and $H_{DIP}(calc)$ are the total dipolar anisotropy coefficient and field of rough MLs calculated using numerical methods. . . . .	101
Table 6.2	$N$ is the number of the Co/Ni MLs, and $M_s$ and $K_u(SQUID)$ are respectively the saturation magnetization and anisotropy of the as-deposited Co/Ni MLs measured by SQUID at 5 and 300 K. $K_2^\perp$ , $K_4^\perp$ , $K_u(FMR) = K_2^\perp + K_4^\perp$ are anisotropy coefficients, and $g^\perp$ and $g^\parallel$ are g-factors of the Co/Ni MLs measured by FMR at 300 K. $K_4^\perp$ and $g^\perp$ of the Co/Ni MLs with $N = 64$ are not determined since the perpendicular FMR measurements induce the spin wave oscillations in the MLs. $K_S^{DIP}/d(calc)$ and $K_{DIP}(calc)$ listed in Table 6.1 are used to calculate $K_u(SQUID)$ and $K_u(FMR)$ . For Co/Ni MLs with $N = 4$ and 6, the error bar in $M_s$ is $12 \times 10^{23} A/m$ and the error bar in $K_u(SQUID)$ is 0.06 and 0.05 $J/m^3$ , respectively. . . . .	104

# List of Figures

Figure 1.1	A schematic representation of a STT-RAM memory cell with a GMR device structure. The SL is a source line, BL is a bit line and WL is a word line. . . . .	3
Figure 2.1	Illustration of demagnetizing field using surface charges (a) in-plane and (b) perpendicular to plane. . . . .	11
Figure 2.2	(left) and (right) represents the schematic of energy band structure of non magnetic and ferromagnetic $d$ transition metals, respectively. $N(E)$ is the density of states. Thin blue and orange arrows represents the magnetization directions. The thick blue arrow in the bottom represents the direction of the spin angular momentum [71]. . . . .	13
Figure 2.3	Schematic illustration of GMR two spin channel model for (a) anti-parallel magnetic layers and (b) parallel magnetic layers. Brown arrows represents the magnetization direction of FM1 and FM2 layers, red and blue arrows represents the up and down spin of electrons. .	16
Figure 2.4	Schematic illustration of spin transfer torque in RL/NM/FL structure. Black arrows with the yellow circles represents the electrons. The tip of the arrow represents the direction of magnetic momentum. The black arrows without the circle represents the magnetization directions of RL and FL, green arrows shows the direction of electrons flow (opposite to the direction of current) and red arrows shows the direction of torque. . . . .	17
Figure 3.1	DC sputtering process: $Ar$ is ionized by a strong potential difference and energetic $Ar^+$ accelerate towards the target (cathode). After impact, $Ar^+$ ions impart their energy to the target and eject the target atoms. The ejected target atoms travel to the substrate, where they form layers of atoms in thin films. ( <a href="https://commons.wikimedia.org/wiki/File:DCplasmaSputtering.jpg">https://commons.wikimedia.org/wiki/File:DCplasmaSputtering.jpg</a> ) . . . . .	21
Figure 3.2	Plot of breakdown voltage versus pressure, $P$ , and distance, $d$ , between the electrodes. . . . .	22



Figure 3.3	An electric potential distribution in a DC sputtering discharge. The time-averaged electric potential in the RF discharge exhibits a similar profile. . . . .	23
Figure 3.4	Formation of negative DC bias on capacitively coupled cathode in RF discharge with the net current and zero self-bias voltage [90]. . .	25
Figure 3.5	Formation of negative DC bias on capacitively coupled cathode in RF discharge zero net current and negative self-bias voltage [90, 88].	26
Figure 3.6	Schematic diagram of the typical RF magnetron sputtering. E and B-field lines configuration. Magnet below the target trap electrons in the helical orbits around the magnetic field lines [90]. . . . .	27
Figure 3.7	The top view of sputter deposition system used for sample preparation. It has six guns of 2" diameter numbered as 1 to 6 in the figure, and two guns of 6" diameter named as "HERO" guns, and an etching gun at the center. HERO guns can be brought in and out from the chamber through a moving arm. . . . .	28
Figure 3.8	Sample stage for the PANalytical X'Pert PRO MRD with source (X-ray tube) and detector. The sample is placed at the centre of the sample stage. . . . .	30
Figure 3.9	X-ray scattering from the planes of atoms exhibit constructive interference if Bragg condition is satisfied. $d$ is the distance between the crystal planes, $\theta$ is the angle between the incident beam and the diffracted planes, $2\theta$ is the angle between the incident beam and the detector. $k_0$ and $k_1$ are the wave vectors of the incident and reflected beams respectively, and $Q = k_1 - k_0$ is the scattering vector, perpendicular to the plane of atoms. . . . .	31
Figure 3.10	X-ray diffraction measurements of Ta(3)/Cu(12)/8×[Co(0.2)/Ni(0.6)]/Ta(4). The dotted lines at $43.37^\circ$ and $44.54^\circ$ represent the expected $2\theta$ position of the Cu(111) and Co/Ni(111) peaks assuming unstrained films. . . . .	32
Figure 3.11	Geometry of in-plane XRD measurement. . . . .	33
Figure 3.12	X-ray reflectivity measurements of 20 nm thick Ru film. Thickness of the film is calculated by using the angular positions of the Kiessig fringes. $\theta_1$ , $\theta_2$ indicate the peak positions of the fringes that are due to constructive interference between X-rays reflected from the top (air/film) and bottom (film/substrate) film interfaces. $\theta_c$ is the critical angle. . . . .	34
Figure 3.13	Ray diagram of two optical path of X-rays through a single layer is shown: one reflects from the top surface and the other from the bottom surface (substrate). . . . .	35

Figure 3.14	Schematic of experimental polar MOKE setup. The magnetic field is in a direction perpendicular to the surface of sample. (MOKE Experimental Setup, (2017), Figure 3.14 is available at: <a href="https://www.montanainstruments.com/library/images/MOKE-experimental-setup-1.png">https://www.montanainstruments.com/library/images/MOKE-experimental-setup-1.png</a> [Accessed 21 Dec. 2017].) . . . . .	36
Figure 3.15	MOKE measurements of Ta(3)/Cu(10)/4×[Co/Ni]/Ta(3). . . . .	37
Figure 3.16	Schematic diagram of a SQUID assembly placed in a magnetic field. The dc magnetic field is axial and detection coils are also along the solenoid axis. The detection coil is further attached with the SQUID device. The right side shows the induced voltage as a function of position of the sample in the coils [100]. Figure 3.16 is adapted from [100]. . . . .	38
Figure 3.17	Schematic representation of a SQUID placed in a magnetic field. . .	39
Figure 3.18	SQUID measurements of 8×[Co/Ni] multilayers along the hard (blue) and easy (red) axes at 298K. . . . .	40
Figure 3.19	Illustration of the magnetization precession for motion (a) without damping and (b) with damping. . . . .	42
Figure 3.20	Schematic of the laboratory and magnetization coordinate systems. The laboratory system of coordinates is described by $X_{lab}$ , $Y_{lab}$ , $Z_{lab}$ while $x$ , $y$ , $z$ are the coordinates to describe the magnetization dynamics. . . . .	43
Figure 3.21	Schematic of the FMR set up for co-planar waveguide configuration	46
Figure 3.22	(left) FMR measurements of 16×[Co/Ni] multilayers along the in-plane (hard) at 52.608 GHz and (right) perpendicular (easy) directions at 46.302 GHz respectively. . . . .	47
Figure 3.23	Plots of resonance field versus frequency of 8×[Co/Ni] multilayers obtained from FMR measurements with the applied field (a) parallel and (b) perpendicular to the sample surface. . . . .	48
Figure 3.24	Schematic of the Van der Pauw set up (a) current flows along the edge, AB, and voltage is measured across the edge, BC, (b) current flows along the edge, AB, and voltage is measured across the edge, AD. . . . .	49

Figure 3.25	Schematic representation of the fabrication steps. (a) The deposited film structure with a bilayer of PRs and the photomask used in the mask aligner. (b) The optical microscope image of the multilayers stack after patterning of the bottom contact and subsequent deposition of the first SiO layer. (c) A schematic picture of the spin coated layer of the negative PR on the top of the wide contact pads of the device and the central nanopillar. (d) A schematic picture of the patterned contact pads and the nanopillar (inset) on the top of the bottom contact. (e) A top view of the bottom and top contact design after removal of the photoresist. (f) The cross section view of the patterned device with Cr/Au bottom and top contacts. . . . .	50
Figure 4.1	Schematic representation of the full film structure, Ta/Cu( $d_{Cu1}$ )/SAF/Cu/FL/Ta. The Ta and Cu seed layers are used to establish (111) texture of the Co/Ni multilayers. $d_{Cu1}$ is varied from 1.9 to 30 nm [113]. . . . .	53
Figure 4.2	X-ray measurements of Ta/Cu( $d_{Cu1}$ )/SAF/Cu/FL/Ta layer structure with $d_{Cu1}$ varying from 1.9 to 30 nm. This is a log plot of intensity as a function of $2\theta$ with offsets. . . . .	54
Figure 4.3	FWHM of Co/Ni (111) in Ta(3)/Cu( $d_{Cu1}$ )/SAF /Cu/FL/Ta as a function of $d_{Cu1} = 1.9, 3, 7, 10, 20$ and $30$ nm. Error bars are determined from measuring 4 different samples with the same film structure	55
Figure 4.4	(a, b) Cross-sectional bright-field TEM images of the complete film structure, i.e. Si/Ta(3)/Cu( $d_{Cu1}$ )/SAF/Cu(3)/FL/Ta with SAF = FM1/Ru(0.38)/FM2, FM1 = $4 \times [\text{Co}(0.21)/\text{Ni}(0.57)]/\text{Co}(0.4)$ , FM2 = $\text{Co}(0.4)/3 \times [\text{Ni}(0.57)/\text{Co}(0.21)]/\text{Ni}(0.57)/\text{Co}(0.4)$ , and FL = $\text{Co}(0.4)/3 \times [\text{Ni}(0.57)/\text{Co}(0.21)]/\text{Ni}(0.57)$ , where $d_{Cu1} = 1.9$ nm in (a) and $d_{Cu1} = 30$ nm in (b). (c) High-resolution TEM image of the rectangular area marked in (b). (d, e) Fast Fourier transforms are calculated from the corresponding two square areas marked in (c). Values in brackets are in nm. . . . .	56
Figure 4.5	Schematic representation of the structure, Ta(3)/Cu( $d_{Cu1}$ )/N $\times$ [Co( $d_{Co1}$ )/Ni( $d_{Ni}$ )]/Ta. Thicknesses, $d_{Cu1}$ , $d_{Co1}$ and $d_{Ni}$ are varied to optimize the perpendicular magnetic anisotropy. . . . .	57
Figure 4.6	The dependence of $M_s$ of Ta/Cu(10)/8 $\times$ [Co( $d_{Co1}$ )/Ni( $d_{Ni}$ )]/Ta on $d_{Co1}$ , $d_{Ni}$ , and on deposition rates (low rate, LR is 0.01 nm/s, high rate, HR, is 0.05 nm/s). SQUID measurements were performed at room temperature. Lines linking data points in this and subsequent figures are guides to the eye. . . . .	58

Figure 4.7	The dependence of $K_u$ of Ta/Cu(10)/8×[Co( $d_{Co1}$ )/Ni( $d_{Ni}$ )]/Ta on $d_{Co1}$ , $d_{Ni}$ , and on deposition rates (LR = 0.01 nm/s and HR = 0.05 nm/s). $K_u$ was measured by SQUID at room temperature. . . .	59
Figure 4.8	The dependence of $K_u$ and $M_s$ of Ta/Cu(10)/ $N_1$ ×[Co(0.21)/Ni(0.58)]/Ta on the number of bilayers, $N_1$ . $K_u$ was measured by both SQUID ( $K_u$ (SQUID)) and FMR ( $K_u$ (FMR)). All measurements were performed at room temperature. . . . .	60
Figure 4.9	Dependence of damping, $\alpha$ , and zero field offset, $\Delta H_0$ , of Ta/Cu(10)/ $N_1$ ×[Co(0.21)/Ni(0.58)]/Ta as a function of the number of bilayers, $N_1$ . FMR measurements were performed at room temperature. . . .	61
Figure 4.10	Dependence of (left) $K_u$ and (right) $M_s$ on the number of bilayers, $N_1$ , in Ta/Cu(10)/ $N_1$ ×[Co(0.21)/Ni(0.58)]/Ta. All the as-deposited films are subsequently annealed at 473 K, 498 K, 523 K and 548 K for 15 min. $N_1 = 4$ and 16 are furthermore annealed at 573 K to ensure the fabrication process will not change their magnetic properties. . .	62
Figure 4.11	Normalized Polar MOKE measurements of (left): Ta(3)/Cu/4×[Co(0.21)/Ni(0.58)]/Ta and, (right): Ta(3)/Cu/16×[Co(0.21)/Ni(0.58)]/Ta at room temperature and annealed at 473 K, 498 K, 523 K, 548 K and 573 K. . . . .	63
Figure 4.12	Polar MOKE measurements of, (left): Ta(3)/Ru/4×[Co(0.21)/Ni(0.58)]/Ta(4) measured at room temperature, annealed at 523 K and 573 K. . . .	64
Figure 4.13	Polar MOKE data for a film with structure Ta/Cu(10)/FM1/Ru(0.38)/FM2/Ta (with FM1 = 6×[Co(0.21)/Ni(0.58)]/Co(0.4) and FM2 = Co(0.4)/8×[Ni(0.58)/Co(0.21)]/Ni(0.58)], showing the reversal of individual magnetic layers with magnetic field. $H_{ex}$ is used to calculate the exchange coupling between ferromagnetic layers across the Ru spacer. The switching order of the layers is indicated by the arrows for a field ramping from positive to negative values. The orange and red arrows represent the the bottom and top magnetic layers of the SAF, respectively. . . . .	65
Figure 4.14	Calculated magnetization curves for different exchange couplings, for the FM1/Ru( $d_{Ru}$ )/FM2 layers. Calculations were performed with parameters derived from films with FM1 = 6×[Co(0.21)/Ni(0.58)]/Co(0.4), $d_{Ru} = 0.38$ to 2.1 nm, and FM2 = Co(0.4)/8×[Ni(0.58)/Co(0.21)]/Ni(0.58). . . . .	66

Figure 4.15	Oscillation of the exchange coupling between FM1 and FM2 in the SAF (red triangles). the coercive field of the SAF (blue circles), and the calculated coercive field (orange squares) as a function of Ru spacer-layer thickness. The structure is Ta/Cu(10)/FM1/Ru( $d_{\text{Ru}}$ )/FM2/Ta (with FM1 = $6 \times [\text{Co}(0.21)/\text{Ni}(0.58)]/\text{Co}(0.4)$ and FM2 = $\text{Co}(0.4)/8 \times [\text{Ni}(0.58)/\text{Co}(0.21)]/\text{Ni}(0.58)$ ). The negative value of $J_{\text{ex}}$ indicates antiferromagnetic coupling of the FM1 and FM2 layers. . . . .	67
Figure 4.16	Dependence of coercivity on the seed layer thickness in Ta/Cu( $d_{\text{Cu1}}$ )/SAF/Ta (with FM1 = $4 \times [\text{Co}(0.21)/\text{Ni}(0.58)]/\text{Co}(0.4)$ , $d_{\text{Ru}}$ = 0.38 and 0.77 nm, and FM2 = $\text{Co}(0.4)/3 \times [\text{Ni}(0.58)/\text{Co}(0.21)]/\text{Ni}(0.58)/\text{Co}(0.4)$ ) (blue circles and orange squares), and Ta/Cu( $d_{\text{Cu1}}$ )/FM1/Ta (with FM1 = $8 \times [\text{Co}(0.21)/\text{Ni}(0.58)]$ ) (red triangles). . . . .	70
Figure 4.17	The exchange coupling between FM1 and FM2 in Ta/Cu(10)/FM1/Ru(0.38)/FM2/Ta (with FM1 = $6 \times [\text{Co}(0.21)/\text{Ni}(0.58)]/\text{Co}(d_{\text{Co2}})$ and FM2 = $\text{Co}(d_{\text{Co2}})/8 \times [\text{Ni}(0.58)/\text{Co}(0.21)]/\text{Ni}(0.58)$ ) as a function of the thickness of the Co layers adjacent to the Ru layer, $d_{\text{Co2}}$ . The negative value of $J_{\text{ex}}$ indicates antiferromagnetic coupling of FM1 and FM2 layers. . . . .	71
Figure 4.18	Polar MOKE data of the Ta/Cu(7)/SAF/Cu( $d_{\text{Cu2}}$ )/FL/Ta (with $d_{\text{Cu2}}$ = 1.6 and 3 nm deposited at high rate, FM1 = $4 \times [\text{Co}(0.21)/\text{Ni}(0.58)]/\text{Co}(0.4)$ , $d_{\text{Ru}}$ = 0.38 nm, FM2 = $\text{Co}(0.4)/3 \times [\text{Ni}(0.58)/\text{Co}(0.21)]/\text{Ni}(0.58)/\text{Co}(0.4)$ , and FL = $\text{Co}(0.4)/3 \times [\text{Ni}(0.58)/\text{Co}(0.21)]/\text{Ni}(0.58)$ ), showing the reversal of individual layers with magnetic field. The switching order of the layers is indicated by the arrows on the top plot for a field ramping from positive to negative values, with SAF layer represented by the orange and red arrows and free layer represented by grey arrows. . . . .	72
Figure 4.19	The exchange coupling between SAF and FL layers in Ta/Cu(7)/SAF/Cu( $d_{\text{Cu2}}$ )/FL/Ta (with FM1 = $4 \times [\text{Co}(0.21)/\text{Ni}(0.58)]/\text{Co}(0.4)$ , $d_{\text{Ru}}$ = 0.38 nm, FM2 = $\text{Co}(0.4)/3 \times [\text{Ni}(0.58)/\text{Co}(0.21)]/\text{Ni}(0.58)/\text{Co}(0.4)$ , and FL = $\text{Co}(0.4)/3 \times [\text{Ni}(0.58)/\text{Co}(0.21)]/\text{Ni}(0.58)$ ) as a function of a Cu layer thickness, $d_{\text{Cu2}}$ . Blue circles: Low Cu deposition rate – 0.01 nm/s. Orange squares: High Cu deposition rate – 0.2 nm/s. . . . .	73
Figure 4.20	GMR of Ta/Cu(1.9)/SAF/Cu(3)/FL/Ta (with FM1 = $4 \times [\text{Co}(0.21)/\text{Ni}(0.58)]/\text{Co}(0.4)$ , $d_{\text{Ru}}$ = 0.38 nm, FM2 = $\text{Co}(0.4)/3 \times [\text{Ni}(0.58)/\text{Co}(0.21)]/\text{Ni}(0.58)/\text{Co}(d_{\text{Co3}})$ , and FL = $\text{Co}(d_{\text{Co3}})/3 \times [\text{Ni}(0.58)/\text{Co}(0.21)]/\text{Ni}(0.58)$ ) as a function of Co layer thickness, $d_{\text{Co3}}$ , and deposition rate. Blue circles: Low Cu deposition rate – 0.01 nm/s. Orange squares: High Cu deposition rate – 0.2 nm/s. . . . .	74

Figure 5.1	The SEM image with a inset of the schematic structure of nano-pillar. The structural composition of the nano-pillar is Ta/Cu/SAF/Cu/FL/Ta. In the insert the numbers in the brackets represent layer thicknesses in nm. . . . .	79
Figure 5.2	Polar MOKE data of the Ta/Cu/SAF/Cu/FL/Ta structure, showing the reversal of individual layers with magnetic field. The hysteresis loop of the FL is also shown in the inset. The switching order of the layers is indicated by the arrows on the top plot for a field ramping from positive to negative values, with SAF layer represented by the blue arrows and free layer represented by red arrows. . . . .	80
Figure 5.3	FMR line width versus frequency measurements of the FL. The intrinsic damping $\alpha$ is calculated from the slope and $\Delta H_0$ from the intercept. . . . .	81
Figure 5.4	$R_{dc}$ measurement of the nanopillars as a function of the applied magnetic field. The vertical arrows represent the directions of the magnetic moments of FM1 (bottom arrow), FM2 (middle arrow) and FL (top arrow). The solid line represents the resistance measurements when the field sweeps from 0.9 T to -0.9 T and the dotted line represents the change in resistance when the field sweeps from -0.9 T to 0.9 T. . . . .	82
Figure 5.5	$R_{dc} = dV/dI$ measurements of the nanopillars as a function of applied magnetic field. The arrows represent the directions of the magnetizations of FM1 (bottom arrow), FM2 (middle arrow) and FL (top arrow). . . . .	84
Figure 5.6	Current induced switching of the FL between P and AP states at a zero applied magnetic field. The arrows represent the directions of the magnetizations of FM1 (bottom arrow), FM2 (middle arrow) and FL (top arrow). . . . .	85
Figure 5.7	Field-current phase diagram showing region where the FL is parallel and antiparallel to the SAF reference layer. . . . .	86
Figure 6.1	Cross-sectional bright-field STEM micrographs of Ta(3)/Au(12)/16 $\times$ [Co(0.21)/Ni(0.58)] /Au(12). . . . .	92
Figure 6.2	Simulated ML roughness used for the numerical calculation of the total dipolar surface anisotropy coefficient, $K_S^{DIP}(calc)$ . . . . .	93
Figure 6.3	Structure illustration of the deposited samples. . . . .	96

Figure 6.4	(a) Out-of-plane and (b) in-plane X-ray measurements of as-deposited Ta(3)/Au(12)/ $N \times [\text{Co}(0.21)/\text{Ni}(0.58)]/\text{Au}(12)$ with $N = 4, 6, 8, 10, 16$ and $32$ . The major X-ray diffraction peaks at $38.22^\circ$ , $44.54^\circ$ and $76.49^\circ$ are respectively from Au (111), $N \times [\text{Co}/\text{Ni}]$ (111) and $N \times [\text{Co}/\text{Ni}]$ (220). The dashed black lines at $38.22^\circ$ and $44.54^\circ$ represents the expected positions of Au (111) and Co/Ni (111) peaks, respectively. The arrows indicate the fitted positions of the $N \times [\text{Co}/\text{Ni}]$ (111) and (220) peaks. We assumed that the Co/Ni ML have fcc structure in agreement with STEM results by Gottwald et al. [156].	97
Figure 6.5	(a) The spacing between the (111) ( $d_{111}$ ) and (220) ( $d_{220}$ ) lattice planes and (b) $d_{111}/d_{220}$ of the as-deposited Co/Ni ML as a function of $N$ . The dashed red line represents the expected $d_{111}/d_{220}$ for the ideal cubic lattice structure. The X-ray measurements are performed at room temperature. . . . .	98
Figure 6.6	(a) Cross-sectional bright-field STEM micrograph of Ta(3)/Au(12)/ $16 \times [\text{Co}(0.21)/\text{Ni}(0.58)]/\text{Au}(12)$ (b) with corresponding element maps for Au (c) for Ni and (d) for Co obtained by EDXS analysis. . . . .	99
Figure 6.7	Cross-sectional bright-field STEM micrographs of Ta(3)/Au(12)/ $16 \times [\text{Co}(0.21)/\text{Ni}(0.58)]/\text{Au}(12)$ (a) and (c), and of Ta(3)/Au(12)/ $32 \times [\text{Co}(0.21)/\text{Ni}(0.58)]/\text{Au}(12)$ (b) and (d). . . . .	99
Figure 6.8	Analytical ( $K_S^{DIP}/d = (K_{S,T}^{DIP} + K_{S,B}^{DIP})/d$ ) and numerical ( $K_S^{DIP}/d(\text{calc})$ and $K_{S,r-f}^{DIP}/d(\text{calc})$ ) calculations of the dipole surface anisotropy as a function of $N$ . $K_S^{DIP}/d$ is calculated from Eq.6.7 and assuming that the roughness of top and bottom surfaces of the ML are uncorrelated. $K_S^{DIP}/d(\text{calc})$ is calculated assuming correlated roughness of the top and bottom film surfaces, and $K_{S,r-f}^{DIP}/d(\text{calc})$ is calculated assuming rough top and flat bottom film surfaces. . . . .	102
Figure 6.9	The $M_s$ and $K_u$ of the as-deposited Co/Ni MLs as a function of number of multilayers measured at 5 and 300 K. The dotted black and red lines represents $M_s$ of Co/Ni MLs calculated assuming bulk $M_s$ values for Co and Ni at 0 K and 300 K respectively [69] . . . . .	103
Figure 6.10	The spacing between the (111) and (220) lattice planes of the Co/Ni MLs as a function of $N$ annealed at 523 K. The X-ray measurements are performed at room temperature. . . . .	105
Figure 6.11	The $M_s$ and $K_u$ of as the deposited and annealed at 523 K Co/Ni MLs as a function of number of MLs. The SQUID measurements are performed at room temperature. . . . .	106

Figure 6.12	(a) $K_u(SQUID)$ as a function of $1/d$ for as-deposited and annealed at 523 K MLs. The intercepts and slopes are obtained from a linear fit of the anisotropy coefficients for as-deposited (blue solid line) and annealed at 523 K (red dotted line) MLs. (b) $\Delta K_u = K_u(\text{annealed}) - K_u(\text{as-deposited})$ as a function of $1/d$ . The solid blue line represents a linear fit of $\Delta K_u$ values. . . . .	107
Figure 6.13	(a) The SQUID measured magnetic anisotropy coefficients $K_u(SQUID)$ (black line) and the calculated anisotropy coefficients $K_u(calc) = K_{ME} + K_{MC} + K_S^S/d + K_S^V$ (solid red circles). The values of $\alpha$ , $K_S^S$ and $K_S^V$ are obtained from fitting $K_u(SQUID)$ to the model. (b) Plots of $K_{ME}$ (solid orange triangles), $K_{MC}$ (solid red circles) and $K_S^S/d$ (solid blue squares). . . . .	108
Figure 6.14	Plot of $\Delta K_S^{Au/Co}/d$ , $\Delta K_S^{Ni/Au}/d$ and $\Delta K_S^{Co/Ni}/d$ as a function of $N$ . . . . .	111



# Chapter 1

## Introduction

### 1.1 An overview

Over the past decades, the amount of digital information is increasing tenfold every five years. According to a report prepared by International Data Corporation (IDC) in 2014, the total amount of digital data generated globally will reach 44 ZB (1 ZB =  $10^{12}$  GB) by 2020 [1].

Hard drives are the most inexpensive devices used to store digital information that is infrequently accessed and stored for a long time. Hard drives, like magnetic tapes, have large storage capacity, however they are physically larger in size and slower in speed than the solid-state drives (SSD). Moreover, they have movable parts, which makes them more prone to damage and read/write errors.

As of now, there are three main types of solid-state semiconductor storage devices: static random access memory (SRAM), dynamic RAM (DRAM) and flash memory. These are charge-based solid-state electronic random access memories (RAMs) and each one of these has some merits and demerits. DRAM is being used as the main memory in all forms of modern computing devices. It is comprised of a single MOSFET (metal-oxide semiconductor field-effect transistor) and a capacitor, which needs to be frequently refreshed as the capacitor leaks and the DRAM forgets its state. SRAM does not need to be refreshed. It is composed of 4-6 transistors, which makes SRAM much faster but requires more chip space. Flash memories are made up of solid state chips in which the transistors are connected so they function similar to the NAND or NOR logic gates. These memories have a very high density but comparatively low write speeds and endurance [2, 3]. In this context, endurance means the number of read/write cycles a memory cell can go through before degradation occurs. Recently, in 2015 Samsung introduced the solid state flash memory having 16 TB storage capacity packed in a 2.5" case [4], and almost, a year after Seagate unveiled the world's largest flash memory having 60 TB storage capacity packed in a 3.5" solid state drive [5].

The demand for improved memory has led to the emergence of new memory types. It was recently discovered that the interaction between the spin polarized current and the localized magnetic moment of a ferromagnet (FM) can induce magnetization reversal [6, 7]. This effect is known as spin transfer torque and has been used to develop novel spin transfer torque random access memory (STT-RAM) solid state devices. In these type of memory cells, the switching of the magnetic bits can be achieved by local application of current flowing through the bit, rather than by applying an external magnetic field.

In STT-RAM devices information is stored in the magnetic state of nanopillars with a diameter of the order of sub 100 *nm*. Each nanopillar is a spin valve, consisting of two ferromagnetic layers separated by a thin, nonmagnetic (NM) spacer layer, with read and write operations carried out by passing a current through the spin valve, from one magnetic layer to the other [7]. During a read-out operation, the first FM layer, the reference layer (RL) is used to create a spin-polarized current, which then passes through the nonmagnetic layer without a significant change in polarization and interacts with the second FM layer, the free layer (FL). This interaction exerts a spin torque on the magnetic moment of the FL through a transfer of angular momentum from the polarized current to the FL magnetization. If the polarized current density is large enough  $>10^6$  A/cm<sup>2</sup>, the spin torque will induce magnetization reversal in the FL [7].

The electrical resistance encountered by the current depends on the relative orientations of the magnetization of the RL and FL (low resistance for parallel, and high resistance for antiparallel), giving rise to giant magnetoresistance (GMR) if NM layer is metallic, [8, 9] and tunnelling magnetoresistance (TMR), if NM layer is insulator [10, 11, 12, 13, 14]. GMR or TMR is then used to detect the magnetization direction of the FL [15, 16].

Spin-torque transfer random access memory (STT-RAM) is a promising candidate for future magnetic memory devices. These devices have the potential to be non-volatile like flash memory, have DRAM-like densities, SRAM-like read/write speeds and low power consumption [17].

## 1.2 Working of STT-RAM

A memory cell in a STT-RAM is composed of a GMR (or TMR) structure device, a transistor, a word line (WL), a bit line (BL), and a source line (SL) as shown in the Figure 1.1. The BL and WL are orthogonal to each other and this is indicated by the "×" sign. Each GMR device in a memory cell is connected in series to a transistor that controls the magnitude of current that passes through the GMR/TMR device. The transistor is controlled by the WL voltage that is adjusted for both read and write operations so that a current can pass through the transistor. During a read operation a small voltage difference is applied between the BL and SL. This voltage difference causes a current density that is significantly lower than that required for reversal of the FL to flow through the GMR/TMR device.

The magnitude of current depends on the relative orientation of the magnetic layers in the GMR/TMR device: a parallel alignment corresponds to low resistance and large current (a "0" state), and an antiparallel alignment to high resistance and low current (a "1" state). During a write operation a large voltage difference is applied between the BL and SL to generate a current density large enough to reverse the direction of the magnetization of the FL. The torque on the magnetic moment of the FL is proportional to the current density flowing through the multilayer, and it changes sign when the current direction is reversed. Therefore, the magnetization of the FL can be reversed either parallel ( P ) or antiparallel (AP), with respect to RL, by changing the current direction from BL to SL [18, 19].

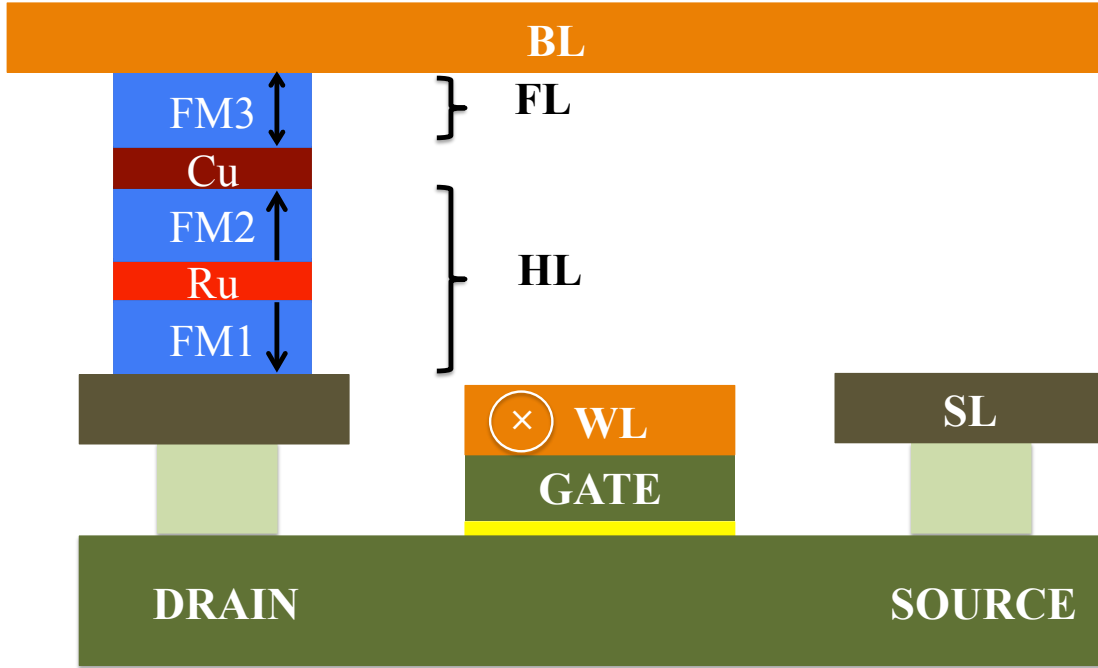


Figure 1.1: A schematic representation of a STT-RAM memory cell with a GMR device structure. The SL is a source line, BL is a bit line and WL is a word line.

In high frequency electronics, impedance matching is extremely important. Although the signal for the GMR devices is smaller than that of the TMR devices, impedance matching of the GMR devices with the circuit is much easier to achieve due to their significantly lower resistance [20]. The TMR sensors are successfully applied to the read heads for the high density hard disk drives of areal density over  $200 \text{ Gbit/in}^2$ . For the devices with a

TMR ratio of 50 %, the RA product <sup>1</sup> is of the order of  $0.4 \Omega(\mu m)^2$  [20]. To achieve higher areal density exceeding 500 Gbit/in<sup>2</sup>, much lower RA product is required. A fully metallic current perpendicular to plane (CPP) GMR devices have low RA product ( $\approx 0.05 \Omega(\mu m)^2$ ) and thus may offer an alternative to the TMR sensors.

### 1.3 Applications and challenges

STT-RAM memories eliminate the need of applying magnetic field to switch the magnetization direction of the FL. It is a non-volatile random-access magnetic memory (it retains its information when power is turned off) that suffers no degradation over time and has no moving parts [21]. It is also much faster than flash memory [17].

Recently, there has been a lot of industrial efforts to develop STT-RAM due to its high recording density, fast write/read speed (a few ns), unlimited endurance, excellent scalability and potential of low power consumption [22]. In 2012 Everspin Technologies released the first commercially available DDR3 dual in-line memory module STT-RAM, which has a capacity of 64 Mb [23]. In July 2015, Avalanche technology has announced the availability of its high-speed, non-volatile, 32/64 Mbit STT-RAM magnetic memory [24]. Other companies working on STT-RAM include Samsung, IBM, Intel, IMEC, Hitachi, FUJITSU, GRANDIS, Hynix, Crocus Technology [25], and Spin Transfer Technologies [26, 27].

One of the main difficulties in commercializing the STT-RAM is that the critical current density needed to reorient the magnetization is at present too high. For this reason, finding ways to minimize the critical current is the focus of intense research in both industrial and academic circles.

### 1.4 Motivation for using perpendicular STT-RAM devices

Initially, most research efforts were focused on in-plane spintronic devices in which the magnetization of both the fixed and free layers lie in the film plane. For a given thermal stability, perpendicular spintronic devices, in which the magnetization is perpendicular to the film surface, require smaller critical current densities for the reversal of magnetic layers relative to in-plane devices [19]. In the macrospin approximation, for in-plane magnetized STT-RAM devices, the critical current required for the spin-transfer reversal of the FL from P to AP and from AP to P state is given by [19]

$$I_c^{P-AP} \approx \left( \frac{2e}{\hbar} \right) \frac{\alpha \mu_0 M_s V_{FL}}{g(0)p} (H_{app} + H_{dip} + H_{K\parallel} + M_s/2) \quad (1.1)$$

<sup>1</sup>Since the resistance of a homogeneous pillar with cross sectional area A varies as the resistivity times the thickness of the pillar divided by A, it is common to express the current perpendicular to plane (CPP) resistance in terms of resistance  $\times$  area (RA) product. This allows for the description of the intrinsic properties of the material independently of geometrical consideration.

$$I_c^{AP-P} \approx \left( \frac{2e}{\hbar} \right) \frac{\alpha \mu_0 M_s V_{FL}}{g(\pi)p} (H_{app} + H_{dip} - H_{K\parallel} - M_s/2) \quad (1.2)$$

where  $M_s$ ,  $\alpha$ , and  $V_{FL}$  are the saturation magnetization, intrinsic Gilbert damping constant, and volume of the FL, respectively,  $p$  is the spin polarization of the current collinear with the RL magnetization, and  $g(0)$ ,  $g(\pi)$  are the pre-factors depending on the relative angle between the RL and the FL.  $H_{app}$ ,  $H_{dip}$  and  $H_{K\parallel}$  are the in-plane applied field, dipolar field acting on the FL due to the RL, and in-plane uniaxial anisotropy field, respectively. The factor  $\mu_0 M_s$  arises from the demagnetizing field of the thin-film geometry [19].

For perpendicularly magnetized devices, the critical currents required to reverse the FL from P to AP and AP to P are given by [28, 19]

$$I_c^{P-AP} \approx \left( \frac{2e}{\hbar} \right) \frac{\alpha \mu_0 M_s V_{FL}}{g(0)p} (H_{K\perp} - M_s - H_{app} - H_{dip}) \quad (1.3)$$

$$I_c^{AP-P} \approx \left( \frac{2e}{\hbar} \right) \frac{\alpha \mu_0 M_s V_{FL}}{g(\pi)p} (-H_{K\perp} + M_s - H_{app} - H_{dip}) \quad (1.4)$$

where  $H_{K\perp}$  is the perpendicular uniaxial anisotropy field of the FL. To switch the orientation of the FL, some energy input is required to overcome the energy barrier between two easy directions. The lower the energy barrier,  $E_b$ , the easier is to switch the magnetization of the FL. However, the magnetization has to be stable against thermal fluctuations, the minimum value of  $E_b$ , given by the figure of merit [29] is

$$\Delta = \frac{E_b}{k_B T} = \frac{K_{eff} V}{k_B T} \quad (1.5)$$

where  $k_B$  is the Boltzmann constant,  $T$  is absolute temperature, and  $V$  and  $K_{eff}$  are the volume and effective anisotropy of the free layer. For 10 years of retention, the thermal stability requirement is set to be  $\Delta > 60$  [30, 29]

For in-plane devices, the energy barrier,  $K_{eff} V$ , of a bit against thermal fluctuation of the magnetization is  $\mu_0 M_s V H_{K\parallel}$ , whereas for the perpendicular devices, it is  $\mu_0 M_s V (H_{K\perp} - M_s)/2$ . Therefore, the potential benefit of the perpendicular geometry is that the critical current required to switch the magnetization (for a small  $H_{app}$  and  $H_{dip}$ ) is directly proportional to anisotropy, and, hence the stability of the bit. However, for in-plane devices, the critical current must overcome an additional factor of  $\mu_0 M_s/2$  that does not contribute to the stability of the bit against thermal fluctuations [31].

The most widely successful in-plane STT-RAM system has structure composed of CoFeB/MgO/CoFeB. The thickness of the CoFeB is of the order of 2-3 nm and the damping factor in these systems is as low as 0.006 [32]. The transition from in-plane to perpendicular media is still challenging. One of the major issue is higher damping factor ( $I_c$  is proportional to the damping,  $\alpha$ , see Eq. (1.1 to 1.4) of typical perpendicularly magnetized materials relative to the material used for in-plane STT-RAM. In addition, materials with perpendicular

magnetic anisotropy have low spin polarization ( $I_c$  is inversely proportional to the spin polarization,  $p$ , see Eq. (1.1 to 1.4). The development of the novel materials with large anisotropy, small damping and high spin polarization is critical.

## 1.5 A brief review

In the physical STT-RAM structure, two ferromagnetic layers (FM1 and FM2) are separated by a thin non-magnetic spacer layer. The thickness of the spacer layer is below its spin diffusion length in order to preserve the spin polarization of electrons. The coercivity of one of the two layers (referred as fixed or hard or pinned or reference layer) is significantly larger than that of the other (referred as free or soft layer). This can be realized either by one of the following

- using the same material but different thicknesses of the layers,
- using different materials with different anisotropy for each magnetic layer,
- coupling the fixed layer to another magnetic layer,
- exchange coupling the fixed layer to an antiferromagnet. The pinning of the fixed layer with an anti-ferromagnetic material increase the magnetic stability of the fixed layer, which is crucial for the sensitivity of the devices. For instance, antiferromagnetic materials such as IrMn [33, 34, 35, 36], FeMn [37, 34], NiMn [34], PtMn [34, 36] and NiO [38] can be used to pin the FM1 layer.

Among these, the last two methods are typically used to reduce the demagnetizing field near the free layer.

Studies have shown that the perpendicular STT-RAM devices require lower critical current to switch the free layer and have higher STT efficiency [31, 39]. CoCrPt [40, 41], rare earth/transition metal compounds [42, 43] and FePt L<sub>10</sub> [44, 45] ordered alloys have perpendicular magnetic anisotropy and have shown promise in perpendicular recording media. Co-based PMA multilayers such as Co/Au, Co/Pt, Co/Pd, CoFe/Pd, CoNi/Pt, CoFe/Ni or Co/Ni [28, 46, 47, 48, 49, 50, 51, 52, 53] have received a lot of attention for their potential application in STT-RAM, spin-torque oscillators and bit patterned media.

In this thesis, the thin film structures and STT-RAM devices were fabricated consisting solely of Co/Ni multilayers. Co/Ni multilayers (MLs) are particularly interesting due to the lower cost of Ni compared to Pt, Pd, and Au. Co/Ni MLs also have tunable magnetization, high spin polarization [19], low damping [54, 31, 55], and large perpendicular magnetic anisotropy ( $K_u \approx 7 \times 10^5$  J/m<sup>3</sup>) [56], making them ideal for the fabrication of thermally-stable sub-30 nm-diameter magnetic nanopillars for spintronic memory devices.

CoPtCr alloys, rare earth/transition metal compounds, L<sub>10</sub> compounds, and multilayers with Pd, Pt have magnetic anisotropies larger than  $1 \times 10^6$  J/m<sup>3</sup>. Thus, to increase stability

a reference layer consisting of two Co/Ni layers coupled antiferromagnetically through Ru as a spacer layer was designed.

The optimization of the perpendicular magnetic anisotropy of the RL and the FL plays a crucial role in designing of STT-RAM devices. Since Co/Ni multilayers were used in both the RL and the FL of our STT-RAM devices, it is of utmost importance to understand the origin of perpendicular magnetic anisotropy in Co/Ni MLs. Deposition of multilayers with optimal magnetic and structural properties, fabrication of magnetic nanopillars along with their study of transport properties are also emphasized in the thesis.

## 1.6 Thesis Outlines

The entire work of this thesis is divided into seven chapters. Some of the results and discussion part in the thesis is paraphrased from the submitted and published work by the Ph.D candidate.

**Chapter 2** describes an overview of magnetic interactions with the emphases on the origin of magnetic anisotropy in ferromagnets, spin based scattering of the conduction electrons in non magnetic and ferromagnetic materials that sets the basis for the understanding of giant magnetoresistance effect (GMR). The chapter is continued by an introduction and theory of spin transfer torque (STT).

**Chapter 3** presents the experimental magnetron sputtering method used for deposition of films, characterization tools such as X-ray diffraction (XRD), X-ray reflectivity (XRR), Magneto-optical Kerr effect (MOKE), Superconducting quantum interference device (SQUID), Ferromagnetic resonance spectrometer (FMR) and Van der Pauw method. Fabrication process used to fabricate 200 nm circular nano-pillars is also discussed.

**Chapter 4** presents a detailed study of Co/Ni multilayers to design a SAF/Cu/FL structure, where SAF is a synthetic antiferromagnet and FL is a free-layer. We investigated how the structural and magnetic properties of these thin film structures are affected by layer thickness and structure design. We have also characterized how deposition rate and spacer layer structure affect the giant magneto-resistance (GMR) and the coupling between the free and hard magnetic layers.

**Chapter 5** discusses the optimized structure of Co/Ni multilayers that were used to design the 200 nm diameter circularly shaped nano-pillars with e-beam lithography. This chapter presents the transport measurements performed on perpendicularly magnetized nano-pillars: a) Major and minor magnetoresistance loops measurement, and b) spin-transfer torque induced switching of magnetization in FL.

**Chapter 6** discusses the origin of magnetic anisotropy in Co/Ni multilayers as a function of number of bilayer repeats. The influence of Au seed and cap interface layers on the magnetic anisotropy of a single CoNi multilayer is also discussed. The variation in magnetic anisotropy is modelled by taking into account the contributions from 1) the magnetoelas-

tic anisotropy due to the strain, 2) the magnetocrystalline anisotropy due to the orbital asymmetry between easy and hard axis, 3) the roughness induced anisotropies, and 4) the inter-diffusion of Au in the Co/Ni MLs.

*Chapter 7* concludes the thesis, beside providing scope for future work.



# Chapter 2

## Theory

In this chapter, some basics about magnetic interactions leading to magnetic anisotropy energy in the ferromagnetic materials are discussed. The fundamentals of spin dependent scattering of electrons in ferromagnetic materials, giant magnetoresistance (GMR) effect and spin transfer torque (STT) effect have also been described. The results presented in this thesis have been obtained by studying the magnetic properties of Co/Ni multilayers to optimize their use in STT-RAM devices explicitly based on GMR structures and to explore the origin of perpendicular magnetic anisotropy in Co/Ni multilayers. Therefore, understanding of these phenomena will serve as a background information for the rest of the thesis.

### 2.1 Magnetic free energy

According to micromagnetic theory, the total free-energy density  $E_{tot}$ , of a typical ferromagnetic system in an external magnetic field can be expressed as the sum

$$E_{tot} = E_{Zee} + E_{ex} + E_{demag} + E_{anis} \quad (2.1)$$

where  $E_{Zee}$  is the Zeeman energy density,  $E_{ex}$  is the energy density associated with exchange interaction,  $E_{demag}$  is the demagnetizing energy density and  $E_{anis}$  is the magnetic anisotropy energy density [57, 58, 59, 60].

**(i) Zeeman Energy:** The energy of interaction between the magnetization,  $M$ , and an external field,  $H_{dc}$ , is called as the Zeeman energy. The Zeeman energy density is given by [61]

$$E_{zee} = -\mu_0 M \cdot H_{dc} \quad (2.2)$$

where  $\mu_0$  is the permeability of free space. Zeeman energy is minimized when the magnetic moments align with the external magnetic field.

**(ii) Exchange Energy:** The exchange energy in a magnetic material arises due to the Coulomb interactions combined with the Pauli exclusion principle. According to Pauli's exclusion principle, two fermions (e.g. electrons) cannot occupy the same quantum state. Therefore, for a two electron system with parallel spins, Coulomb energy is lower due to the necessary spatial separation between the electrons [62]. For a system of  $N$  atoms with spins  $S_i, S_j, \dots, S_N$ , the exchange energy can be expressed as

$$E_{ex} = - \sum_{i < j}^N J_{ij} (S_i \cdot S_j) \quad (2.3)$$

where  $J_{ij}$  is the exchange integral or exchange constant between the  $i^{th}$  and  $j^{th}$  spin. Positive value of  $J_{ij}$  favour parallel alignment of the spins leading to the ferromagnetic ordering (ferromagnetic materials) while negative value of  $J_{ij}$  favour anti-parallel alignment of the spins leading to anti-ferromagnetic ordering (anti-ferromagnetic material) [63]. The exchange integral does not account for the number of nearest pairs of spin. Therefore, for cross material comparison, a better term exchange stiffness,  $A_{ex}$ , is used. The exchange stiffness,  $A_{ex}$ , is a material specific magnetic energy parameter that include  $J_{ij}$  as

$$A_{ex} = \frac{n J_{ij} S_{ij}^2}{a} \quad (2.4)$$

where  $n$  is the number of nearest spin pairs and  $a$  is the lattice constant (proportional to the distance between the spins). The value of  $A_{ex}$  for a bulk film of Co and Ni is of the order of  $1.5 \times 10^{-11} J/m$  and  $0.6 \times 10^{-11} J/m$ , respectively [64, 65, 66, 67]. In ferromagnetic materials, there is a competition between exchange energy and magnetostatic energy. The exchange interaction is a short range force and favours uniform magnetization. However, the magnetostatic energy is a long range force and favours non uniform magnetization. The competition between both the forces results in a characteristic length scale, the exchange length,  $l_{ex}$ , over which a uniform magnetization reversal can be assumed. The length scale is of the order of 2 to 5 nm. On the other hand, for larger length scales, the magnetization reversal is generally non uniform [68].

In this thesis the magnetic anisotropy of Co/Ni multilayers is measured with ferromagnetic resonance (FMR) and SQUID. FMR measurements are performed in large magnetic fields such that magnetic moments of Co/Ni multilayers is fully saturated during the measurements. In SQUID measurements the magnetic moment of Co/Ni multilayers is initially fully saturated in an external magnetic field. Subsequently, the magnetic field is first removed and then reversed causing the reversal of the magnetic moment in the multilayers. Since both measurements yield the same magnetic anisotropy values, we assume that the magnetization reversal in SQUID measurements is uniform. In this case, the exchange energy is constant during the magnetization reversal and does not play an important role in minimizing the magnetic free energy.

**(iii) Demagnetizing Energy:** In the finite size uniform magnetic thin films, the magnetic moments at the boundaries gives rise to uncompensated magnetic charges. These surface charges generate a magnetic field in a direction opposite to the direction of magnetization in the film, called the demagnetization field,  $H_{demag}$ . The surface charges resulting in a dipole-dipole interaction gives a demagnetizing energy density of the form

$$E_{demag} = \frac{\mu_0}{2} M \cdot H_{demag} \quad (2.5)$$

The interaction is determined by the shape of the sample and is therefore not an intrinsic property. The calculation of the demagnetizing field of an arbitrarily shaped magnetic body is generally complicated. However, for a uniformly magnetized ellipsoid, it is simplified to

$$H_{demag} = -\bar{\bar{N}}M \quad (2.6)$$

where  $\bar{\bar{N}}$  is the dimensionless demagnetizing tensor. If the coordinate system lies along the principle axis of the ellipsoid,  $\bar{\bar{N}}$  can be written as

$$\bar{\bar{N}} = \begin{pmatrix} N_x & 0 & 0 \\ 0 & N_y & 0 \\ 0 & 0 & N_z \end{pmatrix} \quad (2.7)$$

$N_x + N_y + N_z = 1$ . The samples used in this thesis can be treated as infinitely extended films. This geometry is a limiting case of an oblate ellipsoid and therefore Eq. (2.6) can be used.

For an in-plane magnetized film, the surface charge density of a magnetic film with the magnetic moment parallel to the film surface is negligible compared to the magnetic moment perpendicular to the film surface. For this reason, in films with in-plane magnetization demagnetizing factors vanish ( $N_x = N_y = 0$ ) (see Figure 2.1 (a)) and is  $N_z = 1$  (see Figure 2.1 (b)) for films with perpendicular magnetization.

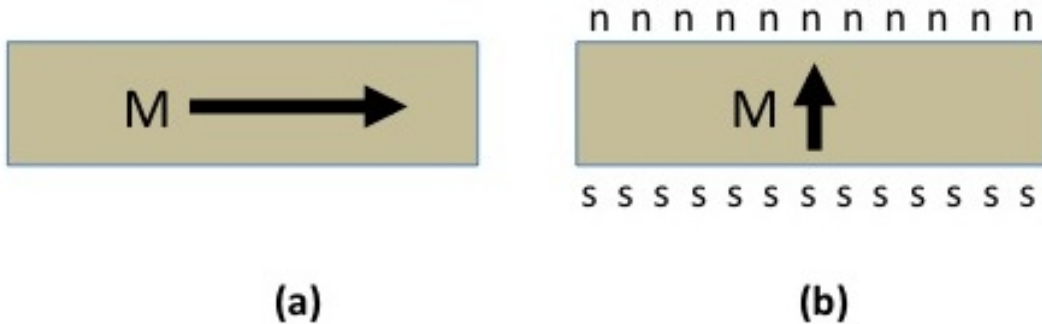


Figure 2.1: Illustration of demagnetizing field using surface charges (a) in-plane and (b) perpendicular to plane.

To minimize the energy in the thin film geometry, the magnetization would prefer to lie in the plane of the film. The demagnetizing energy in the simplified form is expressed as

$$E_{demag} = \frac{\mu_0}{2} M \cdot H_{demag} = \frac{\mu_0}{2} M \bar{N} \cdot M = \frac{\mu_0}{2} (\hat{z} \cdot M)^2 \quad (2.8)$$

where  $\hat{z}$  is the unit vector normal to the film plane. For uniform magnetization, the magnitude of  $M = M_s$  ( $M_s$  is the saturation magnetization). Eq.(2.8) in that case, becomes:

$$E_{demag} = \frac{\mu_0}{2} M_s^2 \cos^2 \theta \quad (2.9)$$

where  $\theta$  is the angle between the magnetization and the normal to the sample surface. Since different shapes may lead to different preferred directions of  $M$ , the anisotropy caused by the demagnetizing field is often referred to as shape anisotropy.

**(iv) Magnetic anisotropy energy:** Magnetic anisotropy describes the dependence of internal energy of a magnetic material on its direction of magnetization. The magnetic anisotropy can originate from the magnetocrystalline, magnetoelastic and interface anisotropies [69].

**Magnetocrystalline anisotropy:** Magneto-crystalline anisotropy arises due to the symmetry of the crystal lattice which dictates the symmetry of an electric charge distribution in the crystals. The electron orbits are linked to the crystallographic structure due to Coulomb interaction between of electron orbits of magnetic atoms and the surrounding charge distribution in the crystal. Then the interaction of the orbits with the spins (spin orbit interaction) make latter to align along the well defined crystallographic axes [62, 57], thus giving a preferred magnetic easy axis. It is therefore, easier to magnetize the crystal along certain directions than others. For example, hcp cobalt has preferential direction of magnetization, parallel to the c-axis ([0001] crystal direction). This is the simplest case of magnetocrystalline anisotropy known as uniaxial magnetocrystalline anisotropy [69]. Magnetic crystals with uniaxial anisotropy exhibit the largest magnetocrystalline anisotropies, such as  $\text{SmCo}_5$  which has an anisotropy of the order of  $10^7 \text{ J/m}^3$ .

**Magnetoelastic anisotropy:** Magneto-elastic anisotropy is a form of magneto-crystalline anisotropy originating from a direct deformation of the unit cell. In magnetic films, it can arise due to the lattice mismatch between the adjacent layers, which causes the strain in the films. Since the strain alters the distance between the atoms in any magnetic crystals, the interaction energies are changed which induce anisotropy in the films [69, 62].

**Interface/surface anisotropy:** In 1954, Néel suggested the existence of surface anisotropy in ultrathin films [50]. According to Néel, the magnetic anisotropy is induced due to the symmetry breaking at the surfaces of the film [70].

A detailed theory and calculations of magnetic anisotropies contributing to the origin of perpendicular magnetic anisotropy in Co/Ni multilayers will be discussed later in chapter 6.

## 2.2 Spin dependent scattering

The conductivity in metals is primarily determined by the electrons near the Fermi level and the available density of electronic states close to the Fermi level. The electronic band structure of a material determines its spin dependent conduction.

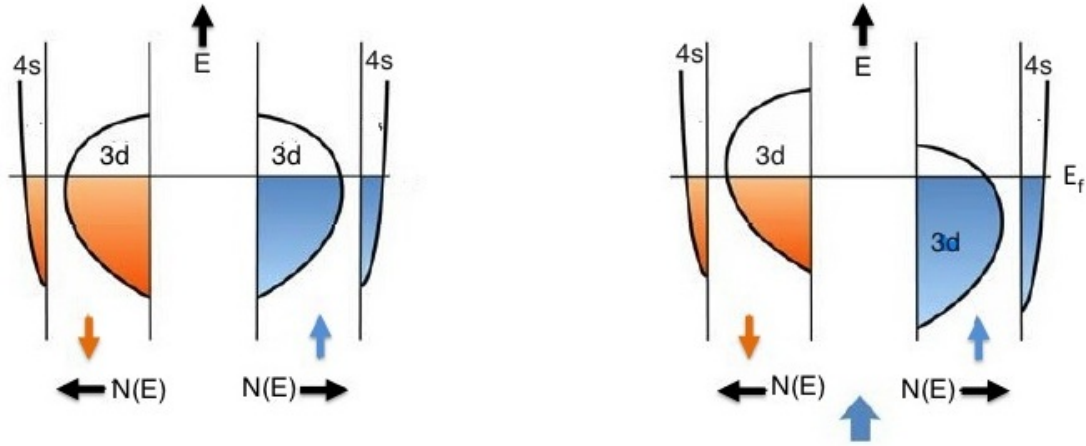


Figure 2.2: (left) and (right) represents the schematic of energy band structure of non magnetic and ferromagnetic  $d$  transition metals, respectively.  $N(E)$  is the density of states. Thin blue and orange arrows represents the magnetization directions. The thick blue arrow in the bottom represents the direction of the spin angular momentum [71].

The  $3d$  transition metals are characterized by the presence of  $4s$ ,  $4p$  and  $3d$  valence states. The  $4s$  and  $4p$  electrons are hybridized and create dispersive  $sp$  band similar to a free electron band. The  $sp$  electrons have a low density of states and high velocity of electrons at the Fermi level. On the other hand,  $3d$  orbitals are much less extended and have relatively narrow energy range.  $3d$  bands have high density of states and low velocity of electrons at the Fermi level. In practice, the  $sp - d$  bands can not be considered as independent bands since they are strongly hybridized with each other.

In non magnetic metals such as Cu,  $d$  bands are fully occupied and the Fermi level lies within the  $sp$  band. The number of spin up and spin down electrons at Fermi level are equal, as shown in Figure 2.2 (left), giving a net zero magnetization. When the conduction

electrons pass through a non magnetic metal, they are likely to be scattered into the empty energy states of the same spin at the Fermi level. Since the density of states for spin up and spin down electrons at the Fermi level is the same, the scattering probability of electrons does not depend on its spin state [72].

On the other hand, in ferromagnetic metals such as Co, Ni, Fe and their alloys, the two  $3d$  subbands are split due to the exchange interaction giving rise to non-zero magnetic moment (see Figure 2.2 (right)). It is due to this reason that localized  $d$  electrons experience a strong Coulomb repulsion. Pauli's exclusion principle does not allow the electrons with the same spin orientation to occupy the same state. Thus, the parallel spin alignment increases average distance between electrons that decreases the Coulomb interaction. Therefore, to reduce energy, it is advantageous for the  $d$  electrons to have parallel oriented spins. On the other hand, aligning spins of electrons by transferring some of spin down electrons from the spin down band into the spin up band leads to increase in the kinetic energy. Therefore, to create a balance between the two competing tendencies, the  $3d$  bands (only  $3d$  elements with large density of states at the Fermi level) split into two subbands of opposite spins with different densities of states at the Fermi level. This can be formulated with Stoner criterion,  $JN(E_F) > 1$ , where  $J$  is called the Stoner exchange parameter and  $N(E_F)$  is the density of states for a given spin at the Fermi energy [73].

In order to distinguish the high and low occupied spin states, the conduction electrons are termed as spin up (majority) and spin down (minority) carriers. Due to the difference in the number of available states at Fermi level, the conduction electrons experience different scattering rates. For example, in a typical Co, the empty states for the majority spin electrons are lower than the empty states available for minority spin electrons. Therefore, the spin up electrons will experience less scattering than spin down electrons (scattering of charge carriers is proportional to the available density of empty states at Fermi level).

In this case, electrons with up spin will carry most of the electrical current. This implies that an electric current which passes through a ferromagnet can gain spin polarization, with majority of the spins pointing parallel to the local magnetization direction of the ferromagnet. The spin polarized currents are utilized in spintronic devices and play an important role in giant magneto-resistance (GMR) effect [74, 72].

## 2.3 Giant Magnetoresistance (GMR) effect

Giant magnetoresistance (GMR) is a quantum mechanical magnetoresistance effect that was first observed independently by Albert Fert [13] and Peter Grunberg [75, 14] in 1988 on Fe(001)/Cr(001) magnetic multilayers and Fe/Cr/Fe trilayer structure respectively.

The effect manifests as a change in electrical resistance in the presence of an applied magnetic field. In Fe/Cr/Fe multilayers the coupling between magnetic moments of Fe layers across Cr spacer layer oscillates from ferromagnetic to antiferromagnetic depending on the

thickness of the Cr layer. In the experiments by Fert [13] and Grunberg [75, 14] the Cr thickness was adjusted so that the coupling between Fe layers is antiferromagnetic. In this case the relative orientation between Fe magnetic moments can be controlled by an external magnetic field; antiferromagnetic if the field is removed and ferromagnetic if the field is large enough to saturate the magnetic moments.

In the absence of an external magnetic field, the adjacent Fe layers (magnetization) are antiparallel to each other due to the antiferromagnetic coupling between them. The antiparallel configuration of Fe layers results in high resistance. However, when an external field is applied, the magnetization of the adjacent Fe layers align themselves with the direction of the field and becomes parallel to the applied field, which results in a low electrical resistance. Both Fert and Grunberg were awarded with the Nobel Prize in Physics for the discovery of GMR in 2007. The significant change in the electrical resistance led to the name as "giant magnetoresistance".

GMR effect is also observed in multilayers composed of ferromagnetic (FM) materials such as Fe, Co, Ni and their alloys such as CoNi, NiFe and CoFe separated by non-magnetic layers such as Cu, Cr, or Au [76, 77, 78, 79].

The mechanism of the GMR effect can be easily understood using the two spin channel conduction model proposed by Mott in 1936 [80]. According to Mott; 1) the electrical conductivity in metals can be described in terms of two largely independent conducting channels, corresponding to spin up and spin down electrons. This assumes that spin flip scattering is negligible below Curie temperature, and, 2) the density of states is not the same for spin up and spin down electrons at the Fermi energy. Scattering rates are proportional to the density of states, so the scattering rates and therefore resistivities are different for electrons of different spin. Therefore, the total current is considered as the current carried by spin up and spin down electrons in parallel [81].

It becomes straight forward to explain the GMR effect by using Mott's arguments based on the two spin channel model. We consider the simplest structure - Ferromagnetic (FM1)/ Nonmagnetic (NM)/ Ferromagnetic (FM2) as shown in Figure 2.3. Figure 2.3 represents the schematic diagram to describe the overall resistance when two adjacent magnetic layers FM1 and FM2 are (a) anti-parallel to each other, and (b) parallel to each other. In the anti-parallel configuration (top panel in Figure 2.3 (a)), both spin up and spin down electrons are scattered strongly within one of the magnetic layers. More explicitly, the spin up electrons experience high resistance ( $R_{HI}$ ) in the FM1 layer being anti-parallel to the local magnetization, and low resistance ( $R_{LOW}$ ) in the FM2 layer being parallel to the magnetization of FM2. Similarly the spin down electron feel low resistance,  $R_{LOW}$ , in FM1 while high resistance,  $R_{HI}$ , in FM2. Since conduction occurs in parallel for the two spin channels, the equivalent resistance,  $R_{AP}$ , for an anti-parallel configuration of the FM1/NM/FM2 metal multilayer structure is higher and given as

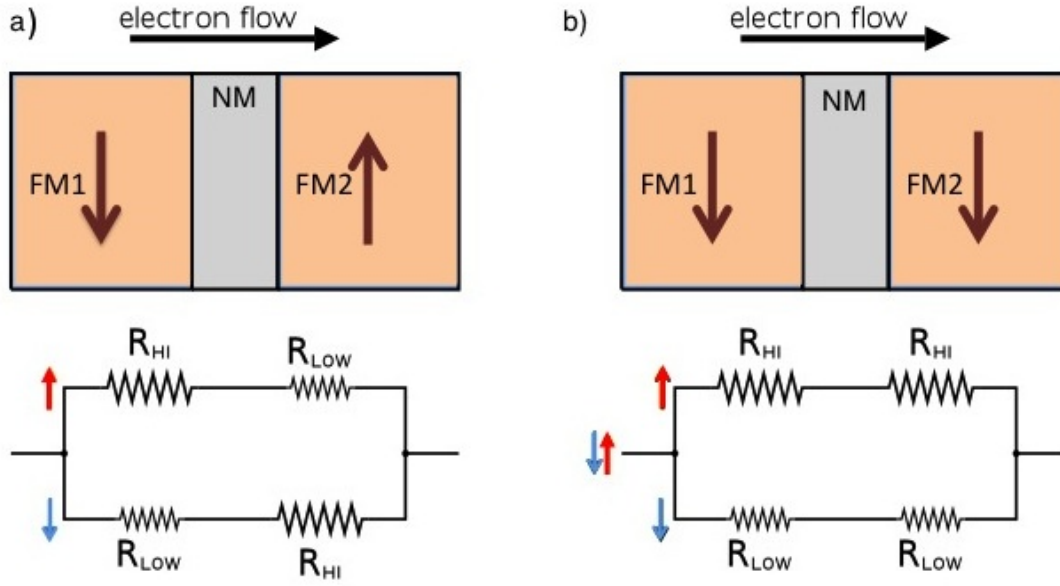


Figure 2.3: Schematic illustration of GMR two spin channel model for (a) anti-parallel magnetic layers and (b) parallel magnetic layers. Brown arrows represents the magnetization direction of FM1 and FM2 layers, red and blue arrows represents the up and down spin of electrons.

$$R_{AP} = \frac{R_{LOW} + R_{HI}}{2} \quad (2.10)$$

On the other hand, when magnetic layers FM1 and FM2 are aligned in the parallel direction (top panel Figure 2.3 (b)), the spin up electrons are strongly scattered in both FM1 and FM2, resulting  $R_{HI}$ . However, the spin down electrons are weakly scattered in both FM1 and FM2 resulting in  $R_{LOW}$ . Therefore, the overall resistance,  $R_P$ , is low and can be given as [82].

$$R_P = \frac{1}{\frac{1}{2R_{LOW}} + \frac{1}{2R_{HI}}} \quad (2.11)$$

The amplitude of GMR is defined as the variation of the resistance between the two configurations, normalized by the resistance of one of the states, such as P:

$$GMR = \frac{R_{AP} - R_P}{R_P} \times 100 \quad (2.12)$$

Since the parallel magnetization of the magnetic layers yield low resistance ("0" state) while the anti-parallel alignment of magnetic layers results in high resistance ("1" state), this effect is used in magnetic sensor applications.



The GMR effect is observed in two geometries, current in plane (CIP) and current perpendicular to plane (CPP). In the CIP geometry, the current flows mainly in the NM layer due to its lower resistivity than that of the magnetic layers, which gives a non uniform current density. However, in the CPP geometry, the current flows through the whole layered structure and therefore the spin dependent scattering can be utilized more efficiently [20].

## 2.4 Spin Transfer Torque

Spin transfer torque (STT) effect was first predicted by Slonckewski [7] and Berger [83] in 1996. According to them, the magnetization orientation in magnetic nanostructures can be affected by flowing a spin-polarized current. The STT effect is sometimes regarded as inverse to the GMR effect. In GMR effect, the relative orientations of the magnetic layers affects the electrical current, so that different configurations correspond to different values for the measured resistances. However, in the reciprocal phenomenon, a spin polarized current can alter the magnetic states of the GMR structure.

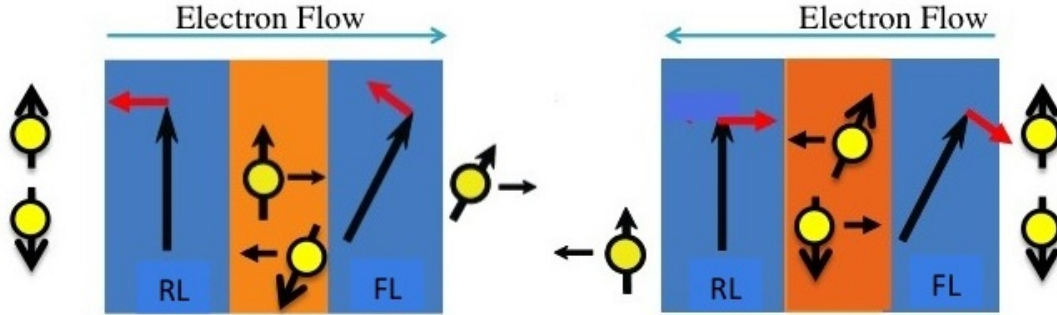


Figure 2.4: Schematic illustration of spin transfer torque in RL/NM/FL structure. Black arrows with the yellow circles represents the electrons. The tip of the arrow represents the direction of magnetic momentum. The black arrows without the circle represents the magnetization directions of RL and FL, green arrows shows the direction of electrons flow (opposite to the direction of current) and red arrows shows the direction of torque.

### 2.4.1 Mechanism of Spin Transfer Torque

The principle of STT can be illustrated using Figure 2.4. Let us consider two non-collinear ferromagnetic layers, the reference layer (RL) and the free layer (FL) separated by a non-magnetic layer, NM. The thickness of the NM layer is less than its spin diffusion length to preserve the electron spin polarization and the magnetization direction of the RL is assumed to be fixed.

When the electrons move from the RL to FL (see Figure 2.4 (a)), majority spin electrons are able to pass through the RL due to the spin dependent conductivity in ferromagnets. However, the minority spin electrons accumulate in the RL layer. The majority electrons pass through the NM layer without any spin reversal and reach to the FL.

When these electrons enter the FL, they lose their transverse angular momentum as shown in Figure 2.4 (a) by the blue arrow. Since the angular momentum has to be conserved, it is absorbed by the FL and acts as a torque on the magnetization. This torque excites the magnetization of the FL to precess at microwave frequencies around the anisotropy axis (in this case, perpendicular to the plane of the sample). If the current density is higher than the critical current, the spin torque switches the FL to a parallel alignment to the magnetization of the RL. The minority electrons are polarized with the magnetic moment anti-parallel to the magnetization of FL and travel back to the RL, where they experience an absorption of the transversal component that acts as a torque on the RL. However, the RL has a larger magnetic moment or anisotropy energy than FL and it does not rotate due to spin transfer torque.

When the electrons flow in the opposite direction, from FL to the RL (see Figure 2.4 (b)), the electrons with the spins parallel to magnetization of the FL pass through it and hence are absorbed by the RL. However, the electrons that are anti-parallel to the RL, reflect back from the RL. It is then the reflected electrons that tend to exert a torque on the magnetization of FL, leading to a rotation of the magnetization of FL towards the anti-parallel alignment. Therefore, by controlling the direction of current, the direction of the spin torque can be controlled, which favours either parallel or anti-parallel alignment of the FL with respect to the RL [72]. This is an efficient way of manipulating the magnetic moment of the FM layers. In storage industry, by changing the polarity of writing current, the magnetization of the FL is changed between parallel and anti-parallel alignment with respect to the RL, which corresponds to low resistance "0" state and high resistance "1" state in devices.

## Chapter 3

# Experimental Methods

This chapter outlines the various experimental techniques used for conducting the work presented in this thesis. The first section briefly describes the physics of the sputter deposition and the principles of DC, RF and magnetron sputtering. The next section discusses X-ray diffraction (XRD), X-ray reflectivity (XRR), superconducting quantum interference device (SQUID) magnetometry, magneto-optical Kerr effect (MOKE), ferromagnetic resonance (FMR) and giant magnetoresistance (GMR) measurements used to characterize the structural, magnetic and electrical properties of thin films. The final section is a short description of the nano-fabrication process used to fabricate 200 nm diameter circularly shaped, perpendicularly magnetized nano-pillars.

## 3.1 Sputter deposition

### 3.1.1 Principles of sputtering (DC discharge):

Sputtering is the process whereby atoms or molecules of a material are ejected from a target by the bombardment of high-energy particles [84]. These high energy particles are generally the ions of a sputter gas like argon. Since *Ar* is a noble gas, it does not react with the target material. A high electrical potential difference is established between the target (cathode) and the substrate (anode). The stray electrons in this electric potential accelerate and collide with the neutral gas atoms, *Ar* in this case, and convert them to positively charged particles.



The ionization potential of *Ar* is 15.76 eV. The positively charged  $Ar^+$  ions accelerate towards the negatively charged target surface and impart their energy to the target. If the energy of the sputtering ion ( $Ar^+$ ) is larger than the surface binding energy of the target material, a neutral atom is ejected from the target surface and deposited on the anode substrate as shown in Figure 3.1 [85].

The  $Ar^+$  impingement on the target also causes the ejection of secondary electrons from the target surface. The secondary electrons re-gain energy in the electric potential and collide with more *Ar* atoms to ionize them, which creates a cascading process that results in a gas break down and formation of a plasma <sup>1</sup>. A continuous production of electrons is mandatory to sustain the plasma. It is important to mention that, the electrons with energy less than the ionization potential of the *Ar* atom cannot ionize the *Ar* atom but only excites them to higher energy levels. The excited *Ar* atoms go back to the ground states by emitting energy in the form of light creating the glow of the plasma.

Before deposition, the sputtering chamber is evacuated to a low base pressure of approximately  $\approx 10^{-8}$  Torr to minimize the impurity concentration in the films. Once this base pressure is attained, sputtering gas (*Ar* in our case) is introduced into the chamber. The initial pressure of the *Ar* gas is adjusted to ensure that there are enough gas molecules in the chamber to be ionized. A negative potential is applied to the target (cathode) while the substrate and the walls of the chamber are grounded. At the breakdown voltage,  $V_B$ , an avalanche of ionizations starts that sets the plasma. The  $V_B$  depends on the pressure,  $P$ , in the chamber and the distance,  $d$ , between the cathode (target) and anode (substrate) [86]. At very low pressures, if the distance between the cathode and anode is small, there will not be sufficient collisions between the atoms and electrons to sustain the plasma. On the

<sup>1</sup>A plasma is a partially ionized gas consisting of ions, electrons and neutrals that is electrically quasi-neutral ( $n_i = n_e$ ).

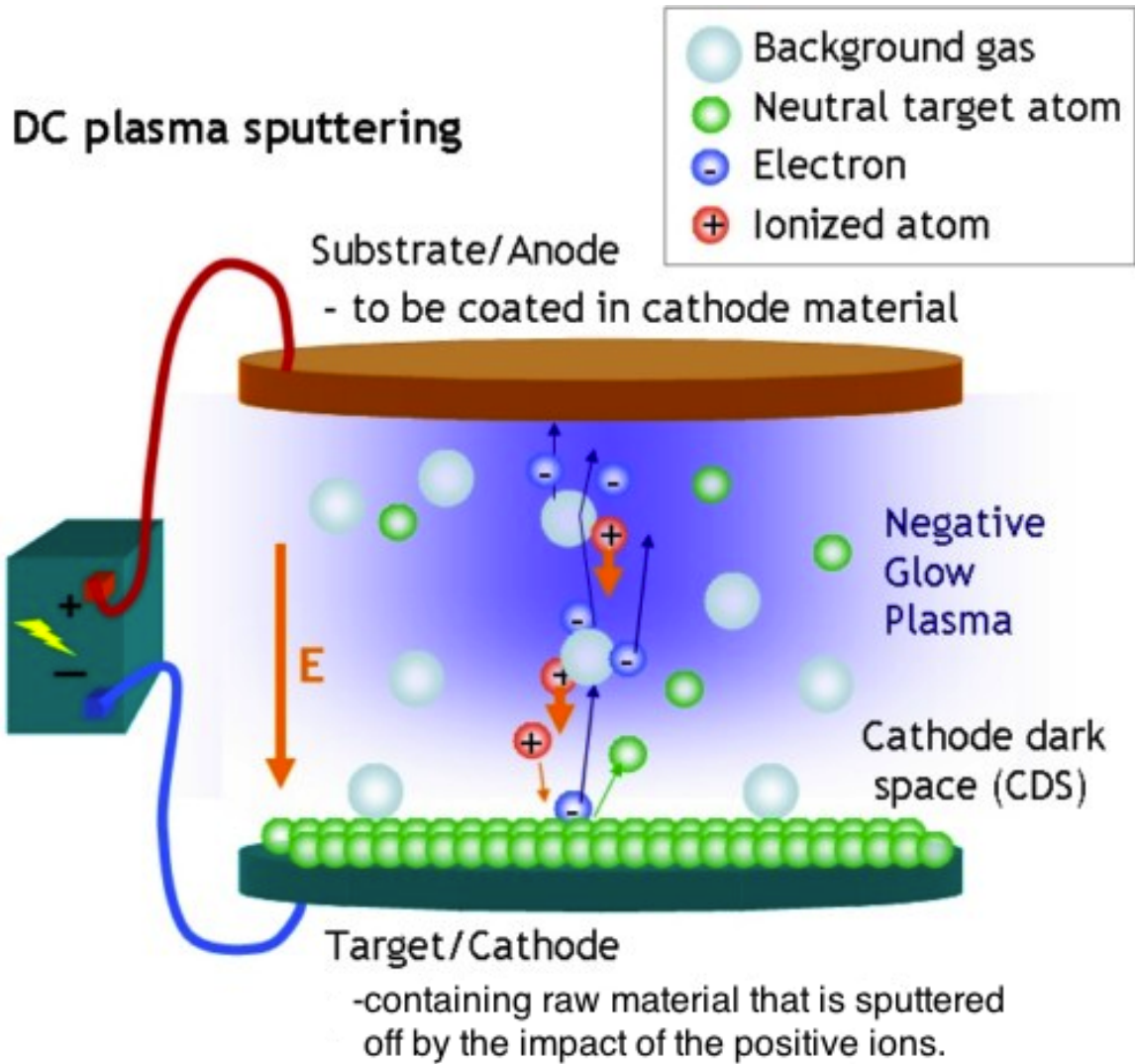


Figure 3.1: DC sputtering process:  $Ar$  is ionized by a strong potential difference and energetic  $Ar^+$  accelerate towards the target (cathode). After impact,  $Ar^+$  ions impart their energy to the target and eject the target atoms. The ejected target atoms travel to the substrate, where they form layers of atoms in thin films. (<https://commons.wikimedia.org/wiki/File:DCplasmaSputtering.jpg>)

other hand, at high pressures, there would be too many collisions such that the electrons will not have enough time to gather energy between the collisions to ionize the atoms. For a particular gas and target material,  $V_B$  is described by Paschen's law. The plot of  $V_B$  as a function  $Pd$  also known as Paschen curve is shown in Figure 3.2 [84]. It should be noted that at two extreme conditions of pressure (too low or too high), a higher  $V_B$  is needed. The minimum can be reached at certain intermediate value of  $Pd$ . The value of  $V_B$  varies for different gases and target materials, however the shape of the Paschen curve remains

the same. Once the plasma is ignited, the pressure of the *Ar* gas is reduced to a minimum level such that it can still sustain the plasma.

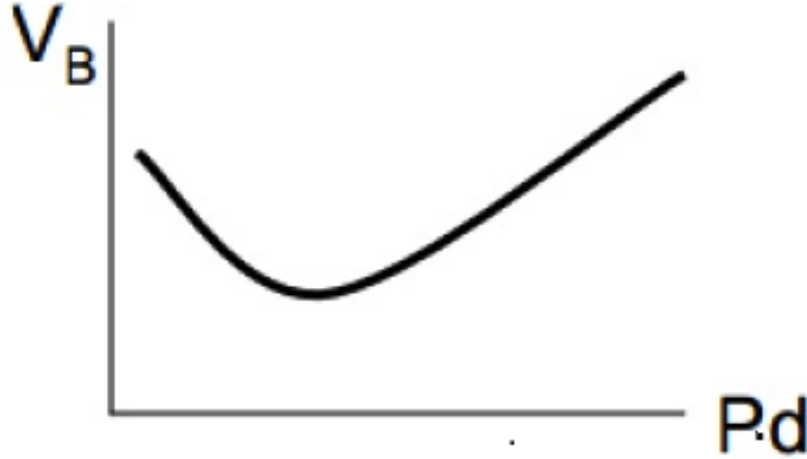


Figure 3.2: Plot of breakdown voltage versus pressure,  $P$ , and distance,  $d$ , between the electrodes.

The quality of the deposited films is highly influenced by the energy of the sputtered atoms reaching the substrate. A higher pressure in the chamber increases the number of collisions between the sputtered atoms and the *Ar* gas atoms that reduces their energy. When these atoms reach the substrate, they do not have enough energy to diffuse along the substrate surface to set themselves to the lowest energy position, which increases film roughness. The increase of collisions also causes the sputtered atoms to change their direction, which results in deposition of atoms on the walls of the chamber rather than on the substrate, which decreases the deposition rate. Therefore, it is important to have low *Ar* pressure to obtain smooth films [87].

Figure 3.3 shows a typical steady-state electric potential distribution in a DC sputtering discharge. Three major regions that can be distinguished in the discharge are: the cathode sheath (target), the glow region, and the anode sheath (substrate) [88, 89].

The formation of plasma sheaths can be understood by considering the situation where the plasma is confined between two isolated grounded electrodes. Immediately after the plasma comes into contact with the electrodes, the fast-moving electrons will drain to the walls leaving more ions in the glow region. Therefore, an electric field will be established over the positive space charge region that prevents the net flux of electrons to the walls. The electric field leads to a potential profile with a positive value within the plasma and rapidly drop to zero over the space charge regions adjacent to each electrode. The typical values of the plasma potential ( $V_p$ ) are approximately 5-10 V [88]. If the cathode (target) is connected to a large negative voltage (usually 100 - 1000 V) the electric potential profile is similar to

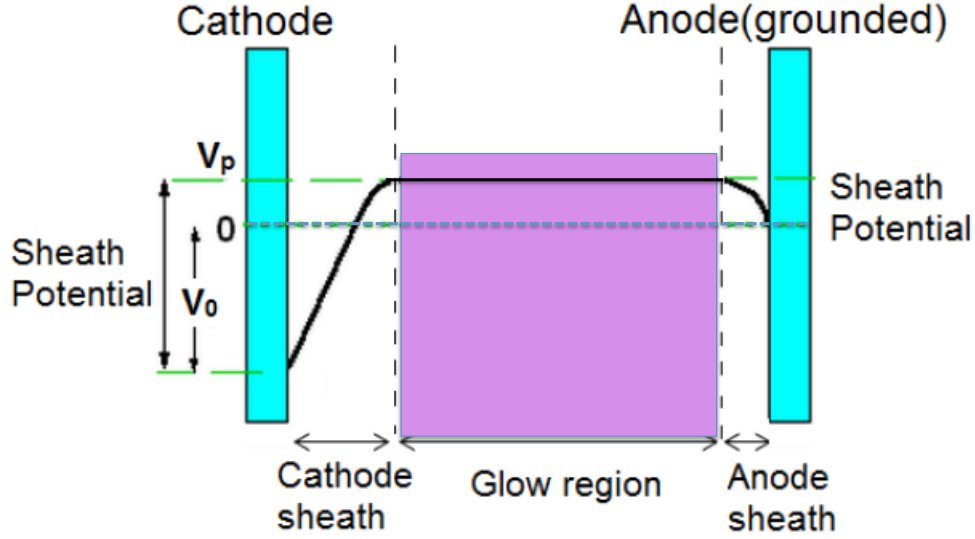


Figure 3.3: An electric potential distribution in a DC sputtering discharge. The time-averaged electric potential in the RF discharge exhibits a similar profile.

what is shown in Figure 3.3. Positive ions that enter the target and substrate sheath areas from the bulk plasma are accelerated toward the target and substrate, respectively. Only ions in the target sheath gain enough energy to ablate material.

Since most of the ejected atoms are neutral, the substrate is not required to be an anode. However, the target must be a cathode.

### 3.1.2 Radio Frequency (RF) sputtering:

The primary limitations of DC sputtering is that the target needs to be electrically conductive. The reason being that the target acts as a cathode to attract the  $Ar^+$  ions during the sputtering process.  $Ar^+$  ions that strike the target receive an electron and rebound as neutrals. Furthermore, during the collision process additional electrons leave the target. For the electrically conductive targets, the loss of negative charges is restored due to the flow of DC current through the target. However, the use of an insulating target in DC sputtering creates a charge buildup on the target surface during ion bombardment and no stable gas

discharge is produced. Sputtering from an electrically insulating or dielectric target can be carried out using an alternating (AC) or RF power supply.

In a typical RF sputtering system, the target is powered by an RF generator while the substrate is grounded. The voltage applied to the target oscillates between a negative cycle to attract  $Ar^+$  positive ions and a positive cycle to attract electrons that neutralize the positive charge buildup. It should be noted that, RF sputtering works with insulators, dielectric and metal targets while DC sputtering works only with metal targets.

The dielectric target acts as a capacitor in series with the plasma and self-biases itself to a negative potential. In this situation, the positive ions respond to the negative DC bias and accelerate toward the target. The negative bias is a result of the disparity in the mobilities of the electrons and ions in the applied RF electric field. Without the negative bias, the target electrode has a tendency to draw more electrons during the positive cycle than it draws ions during its negative cycle. This means the net average current over the one full cycle is not zero as shown in Figure 3.4. However, an insulating target does not allow the flow of a net electric current through. The establishment of negative bias over the target results in net zero current. With the negative self bias, the target can carry a negative voltage for longer time of the RF cycle. Therefore, the ion flux during the longer negative cycle balances with the electron flux of shorter positive cycle, resulting in a net zero current over the full RF cycle as shown in Figure 3.5.

For the reason that the target acts as a capacitor, its impedance is inversely proportional to the frequency. In that case, at frequencies above  $1MHz$ , the RF voltages can be coupled to almost any impedance and any material can be sputtered regardless of its resistivity. Furthermore, the electrons oscillating in the RF field couple energy more efficiently to the plasma, which leads to the higher ionization rates without requiring the secondary electrons from the target to sustain the plasma. The plasma in the RF discharge can therefore, be sustained at lower pressures as compared to a DC discharge [88]. The RF power supply used for deposition of films studied in this thesis also operates at  $13.56 MHz$ .

RF sputtering can be used to sputter conductive materials as well. In the case of a metal target, a blocking capacitor should be placed in series with the target to establish the negative DC self-bias, which is necessary in RF sputtering. Generally the blocking capacitor is built into the impedance-matching network which is placed between the RF power supply and discharge chamber. The matching network is necessary since the plasma impedance is normally different from that of the RF power supply.

**Arcing and Pulsed-DC:** Arcing during the sputter process can seriously reduce the quality of deposited films. Arcs occur primary when charge accumulates at the point of breakdown on or near the target surface. Material sputtered from the target can redeposit in non-active areas around the sputter track. This re-deposited material is often loose and is a source of arcing. Arcing is one of the main sources of particulates in deposited films.



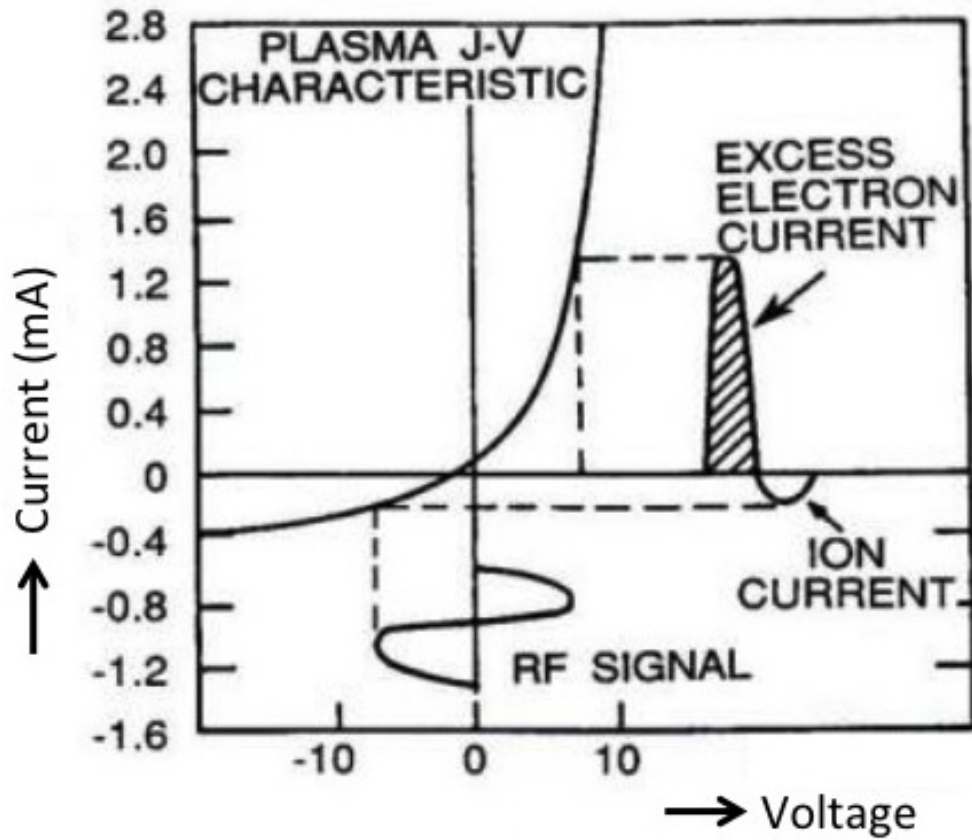


Figure 3.4: Formation of negative DC bias on capacitively coupled cathode in RF discharge with the net current and zero self-bias voltage [90].

In the 1990s it was shown that the probability of forming an arc could be greatly reduced by using mid-frequency pulsed DC sputtering [5,6]. Modern pulsed DC power supplies are equipped with arc detection and suppression (a short interruption of the process when an arc is detected). Furthermore, the arc count and rate data are recorded during the process using the data login feature within a pulsing unit. Arcs can also be suppressed by designing sputter guns with a broad plasma discharge that minimizes non-active target areas.

### 3.1.3 Magnetron sputtering

In magnetron sputtering, magnets are incorporated into the sputtering source (below the target guns) to increase the confinement of the electrons near the target and hence ionization efficiency. The Lorentz force confines electrons that are emitted from the target to helical orbits that end on the target surface. The configuration of the magnets and the field lines in a typical magnetron sputtering system is shown in Figure 3.6. In our sputtering system,

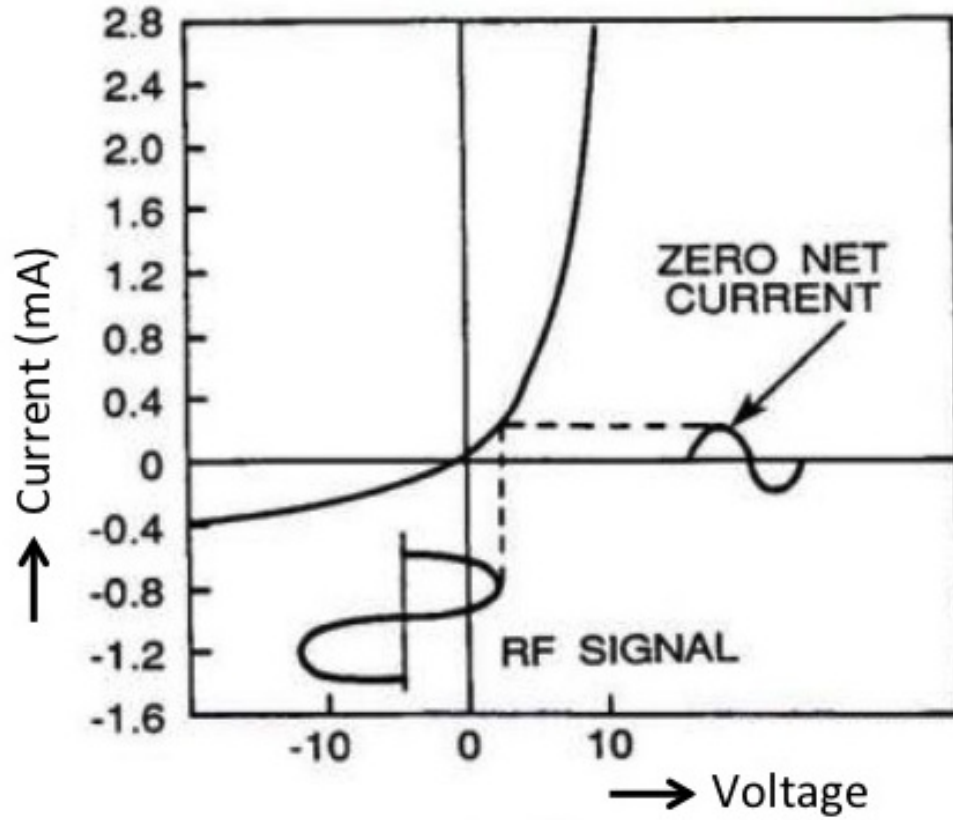


Figure 3.5: Formation of negative DC bias on capacitively coupled cathode in RF discharge zero net current and negative self-bias voltage [90, 88].

NdFeB (Neodymium Iron Boron) alloy is used as a permanent magnet to generate the magnetic fields.

The presence of the magnetic field localizes ionization regions above the target creating non-uniform erosion of the target surface. A schematic of sputter track is shown in Figure 3.6. The erosion groove is called the sputter track and its shape depends on the magnetic field profile and strength.

The electrons trapping above the target in a cyclic pattern significantly improves the ionization process by increasing the electron path length and probability of electron collision with an *Ar* atom. Due to the increase in ionization efficiency, magnetron sputtering can be carried out at lower pressures than sputtering without magnetic field assistance. Higher deposition rates also can be achieved with magnetron sputtering.

The strength of the magnetic field is adjusted in such a way that the Larmor radii ( $R_L \approx 10^{-3}$  m) of electrons are smaller in comparison to the plasma size. The magnetic field strength is of the order of 200 to 500 Gauss at the surface of the gun where the B field is

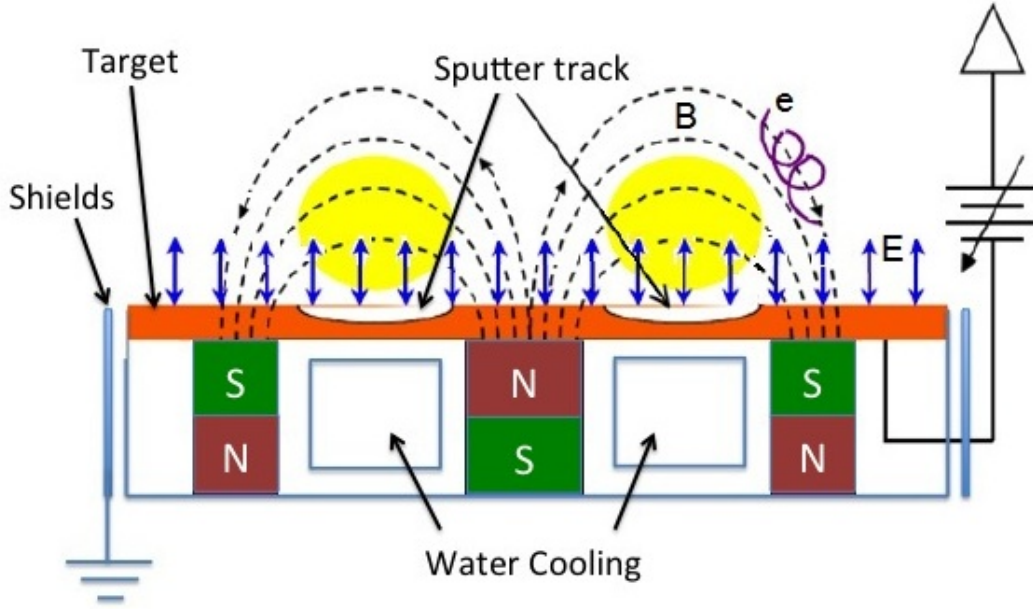


Figure 3.6: Schematic diagram of the typical RF magnetron sputtering. E and B-field lines configuration. Magnet below the target trap electrons in the helical orbits around the magnetic field lines [90].

tangential to the surface. The ions are not affected by the magnetic field since their Larmor radii ( $R_L \approx 10^{-1}$  m) become very large compared to the size of the plasma. The exact range of the magnetic field strength depends on the system geometry.

Magnetron sputtering works with DC, pulsed DC and RF power supplies and has been widely used for low pressure sputtering. However, there are few disadvantages of using the traditional magnetron sputtering system. The first drawback of the magnetron sputtering is that the uniformity of the deposited films is inferior as compared to the films obtained from the cathodes without magnetic confinement. This is due to the non uniform profile of the magnetic field leads to a non uniform erosion of the target. Another drawback is that non uniform target erosion results in poor, only 10 to 25 %, target utilization. It should be noted that, It is possible to increase the utilization rate of the targets by changing the configuration of the magnets.

All the magnetic films studied in this thesis were deposited using the "KJLC" sputter deposition system. The system comprises two high vacuum process chambers connected by a loadlock. The loadlock can hold up to 6 substrates (wafers) with up to 6" diameter. The top view of the process chamber used for growth of multilayers studied in this thesis is shown in Figure 3.7. This process chamber has six 2" diameter and two 4" diameter guns. The transfer of the substrates from the loadlock to the process chambers as well as entire

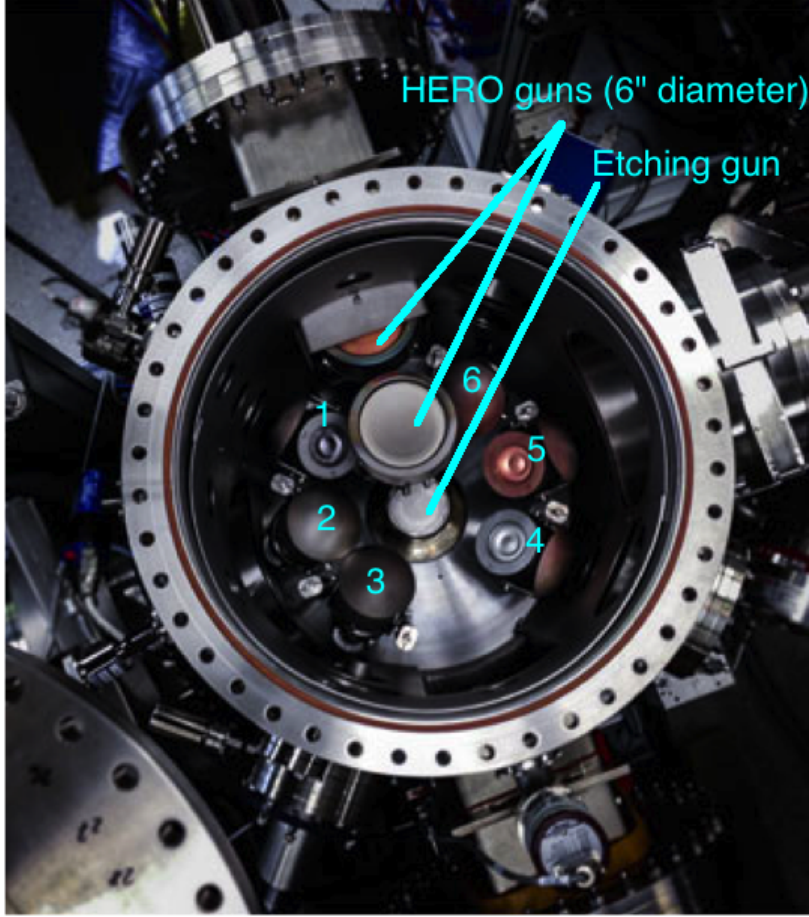


Figure 3.7: The top view of sputter deposition system used for sample preparation. It has six guns of 2" diameter numbered as 1 to 6 in the figure, and two guns of 6" diameter named as "HERO" guns, and an etching gun at the center. HERO guns can be brought in and out from the chamber through a moving arm.

deposition process in the process chambers is computer controlled. I was responsible for the sputter system for over 3 years and have written most of the subroutines used by graduate students for controlling the deposition process.

All the samples grown in this study were deposited on Si (001) wafers by magnetron sputtering in a high vacuum deposition system using both Direct Current (DC) and Radio Frequency (RF) sputtering techniques. The base pressure of the deposition system was below  $5 \times 10^{-8}$  Torr and the sputter process was performed at an Ar pressure of  $2 \times 10^{-3}$  Torr. Before deposition, the substrates were cleaned with hexane and methanol under ultrasonic conditions at 333 K. The substrates were also heated to 523 K in vacuum in the sputter system for 10 minutes to remove any adsorbed layers.

Ta/Cu or Ta/Au layers were sputtered on top of Si(001) to set (111) growth orientation for subsequently deposited Co/Ni magnetic multilayers. All the structures are mainly based on Co/Ni multilayer stack. The growth parameters such as power dissipated in the target,

pressure of the sputter gas, rotation speed of the substrate, and flow of the gas were varied to optimize the properties of the film structures. To obtain smooth films, *Ar* pressure in the chamber was kept as low as possible. Deposition of Ta, Ru, Cu and Au was carried out at 1.7 mTorr while magnetic layers were deposited at 2.2 mTorr.

The base pressure of the KJLC system was below  $10^{-7}$  Torr, generally hovering around  $5 \times 10^{-8}$  Torr. Lower base pressure indicates lower concentrations of  $N_2$ ,  $O_2$ , water vapour, and organic gasses present in the chamber. The contaminants in the chamber reduce the quality of the films.

## 3.2 Thin Film Characterization

### 3.2.1 Structural characterization: X-ray Diffraction

The X-ray diffraction (XRD) measurements were used to determine the film thicknesses, crystal structure, lattice constants, texture/orientation of the crystal planes and strains in the polycrystalline thin films. Strain in the films is measured by evaluating the spacing between the lattice planes of a crystal structure and comparing them with the lattice spacing of unstrained ((111) and (220)) crystal planes. We used PANalytical X'Pert PRO MRD X-ray diffraction system to conduct the XRD measurements with Cu-K $\alpha$  radiation of monochromatic wavelength  $\lambda = 1.5418$  Å. The sample stage of PANalytical X'Pert set up is shown in Figure 3.8.

The conditions necessary for the reflection of a X-ray in a single crystal or polycrystalline material are described by Bragg's Law. It states that the X-rays diffracted from the planes of a crystallographic sample (as shown in Figure 3.9) exhibit constructive interference when the following condition is met [91]

$$2 d \sin\theta = n \lambda \quad (3.2)$$

where  $d$  is the lattice spacing between the crystal planes,  $\theta$  is the angle between the incident X-ray and the diffraction planes,  $n$  is an integer, and  $\lambda$  is the wavelength of X-ray radiation. Figure 3.9 shows the geometry of diffraction from a series of (001) lattice planes. The incident X-ray beam penetrates the lattice and scatter from each of the atoms. When the incident and diffracted angles are equal, and Equation 3.2 is satisfied, the X-rays interfere constructively resulting in a plane wavefront, that carries the information of average lattice spacing between two (001) planes (see Eq.3.2). The wave vectors of incident and reflected beams are denoted by  $k_0$  and  $k_1$  respectively [92].

In the  $\theta$ - $2\theta$  scan,  $\theta$  is scanned by rotating the sample about the y-axis and the detector is moved through  $2\theta$ . A peak appears at the values of  $2\theta$ , for which the atomic periodicity satisfies the Bragg condition.



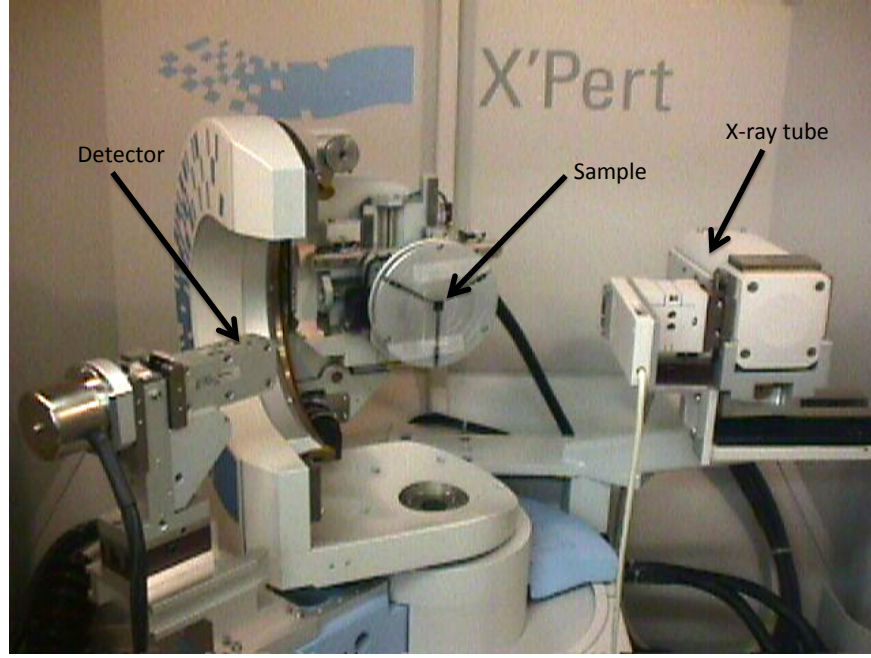


Figure 3.8: Sample stage for the PANalytical X'Pert PRO MRD with source (X-ray tube) and detector. The sample is placed at the centre of the sample stage.

Figure 3.10 shows the  $\theta$ - $2\theta$  scan of Ta(3)/Cu(12)/8×[Co(0.2)/Ni(0.6)]/Ta(4) grown on Si(001). The deposited films were textured along the direction perpendicular to the surface, which means they had a crystal grain alignment in this direction. Cu, Co and Ni grow along [111] directions. The  $\theta$ - $2\theta$  scans show the constructive interference for Cu(111) planes at  $2\theta = 43.37^\circ$ , Co (111) planes at  $2\theta = 44.54^\circ$  and Ni (111) planes at  $2\theta = 44.55^\circ$ .

To determine the preferential growth direction in the films, rocking curve measurements or  $\omega$  scans were performed [91]. After determining the Bragg reflection from a  $\theta$ - $2\theta$  scan, the detector is fixed at that Bragg reflection ( $2\theta$  is fixed) and sample is rotated around an angle  $\omega$ , where  $\omega$  is an angle between the incident beam and the film surface. Rocking curve measurement is a measure of the orientation distribution of the planes in the film with respect to the film surface, which is quantified by measuring the full-width-half-maximum (FWHM) value of these measurements. For example for Co (111), the planes are at  $2\theta = 44.54^\circ$ . In the rocking curve measurements  $2\theta$  is set to  $44.54^\circ$  and  $\omega$  is varied between  $\frac{44.54^\circ}{2} \pm 15^\circ$  (for Cu  $K_\alpha$  radiation). In all samples, the FWHM of rocking curves of Cu(111), Co(111) and Ni(111) was below  $4^\circ$ .

In-plane and out of plane XRD measurements are performed, respectively, to measure the average spacing between the planes perpendicular and parallel to the sample surface. For the in-plane XRD measurements, the incident and scattered wave vector are nearly parallel to sample surface. This allows the measurements of spacing between lattice planes

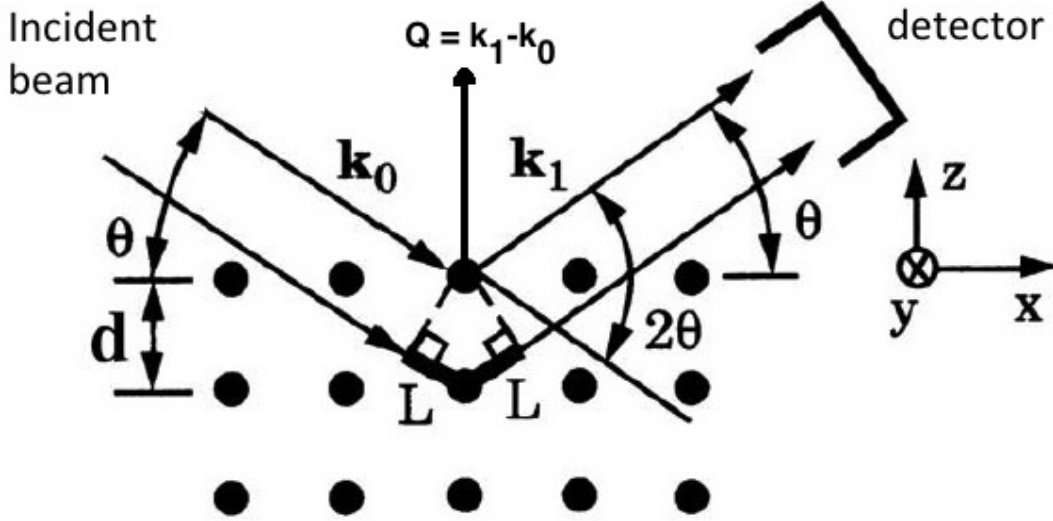


Figure 3.9: X-ray scattering from the planes of atoms exhibit constructive interference if Bragg condition is satisfied.  $d$  is the distance between the crystal planes,  $\theta$  is the angle between the incident beam and the diffracted planes,  $2\theta$  is the angle between the incident beam and the detector.  $k_0$  and  $k_1$  are the wave vectors of the incident and reflected beams respectively, and  $Q = k_1 - k_0$  is the scattering vector, perpendicular to the plane of atoms.

nearly perpendicular to the sample surface. In-plane XRD measurements were performed at a grazing angle of  $0.65^\circ$ . A geometrical layout of the in-plane XRD measurements is shown in Figure 3.11. For the out of plane XRD measurements, the scattering wave vector is normal to the film surface. This allows to measure the distance between the lattice planes parallel to the sample surface as already discussed and shown in Figure 3.9.

### 3.2.2 X-ray Reflectivity (XRR)

Low angle X-ray reflectivity  $\theta - 2\theta$  measurements were used to extract the film thicknesses. In XRR measurements, the thicknesses of a thin film is calculated from the diffraction pattern, known as Kiessig interference fringes as shown in Figure 3.12 [91]. Kiessig fringes originate from the constructive interference between the reflected X-rays from top (air/film interface) and bottom surface (film/substrate interface) of a film. Constructive interference occurs when the optical path length difference between the two X-rays is an integer multiple of the wavelength. Due to the change of refractive index at the top and bottom interfaces, we will have a change in reflection/transmission at these interfaces, which forms coherent sources for the reflected beams. The coherent sources interfere constructively and create

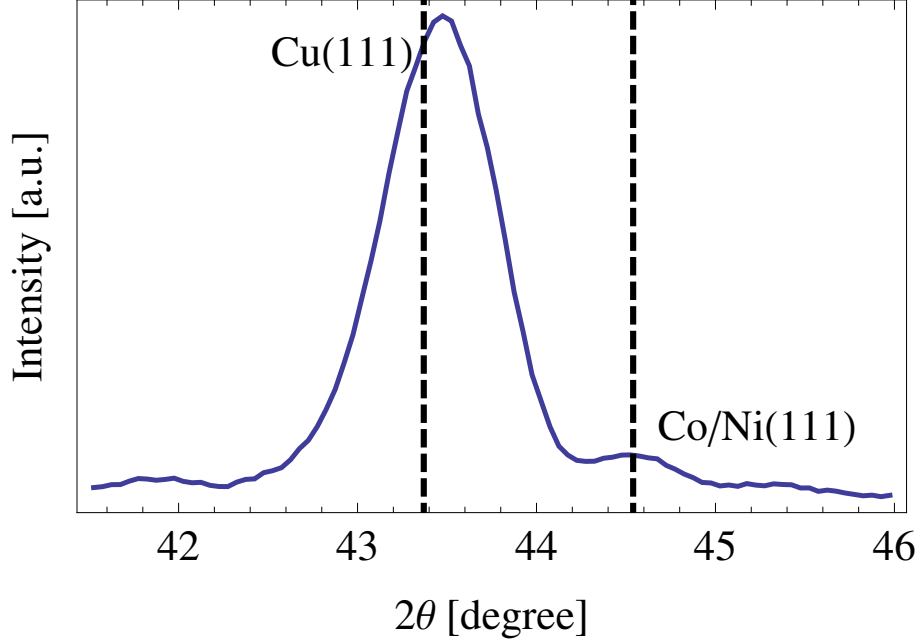


Figure 3.10: X-ray diffraction measurements of Ta(3)/Cu(12)/8×[Co(0.2)/Ni(0.6)] /Ta(4). The dotted lines at 43.37° and 44.54° represent the expected  $2\theta$  position of the Cu(111) and Co/Ni(111) peaks assuming unstrained films.

an oscillatory pattern. The interference fringes in the reflected signal (XRR measurements) can be used to determine 1) material density from the critical angle <sup>2</sup>, 2) the layer thickness from the oscillation frequency of the Kiessig interference fringes, 3) roughness of the films from the decrease in the intensity of interference fringes.

The thickness of the film can be calculated by determining the peak or valley positions shown in Figure 3.12. The single element films were used to determine the thicknesses of the films. Figure 3.13 shows a ray diagram of the optical paths in a  $\theta$ - $2\theta$  scan that produce Kiessig fringes.  $\theta$  and  $\theta_1$  represent the incident angle of X-ray in the air with respect to the top surface of the sample and the reflected angle in the film, respectively,  $n$  and  $n_1$  are the refractive indices of the air and the film, respectively and  $d$  is the thickness of the film.

Assuming that the refractive index of the film is  $n_1$ , the difference in the optical paths  $\delta L$  is given by:

$$\delta L = n_1(AB + BC) - AD \quad (3.3)$$

where  $AB$ ,  $BC$ , and  $AD$  are the line segments between the points (see Figure 3.13).

From the Figure 3.13, the optical path lengths  $AB$  and  $BC$  are identical and equal to:

$$AB = BC = \frac{d}{\sin\theta_1} \quad (3.4)$$

<sup>2</sup>the incident angle below which total internal reflection occurs



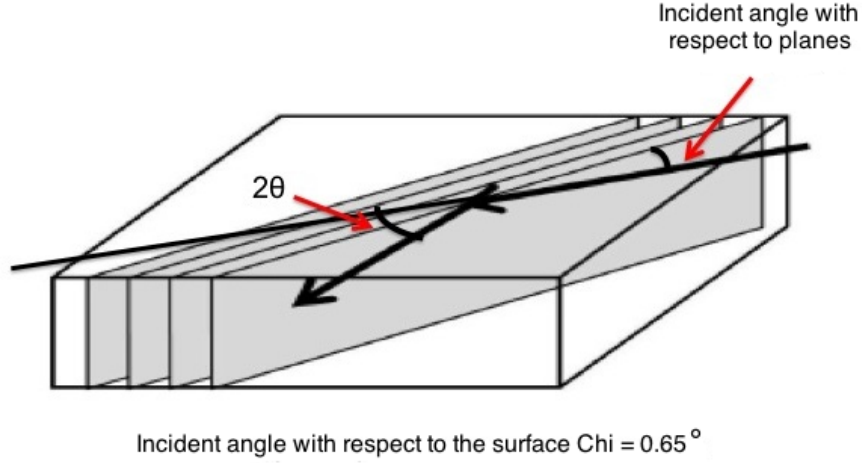


Figure 3.11: Geometry of in-plane XRD measurement.

Also, the optical path length  $AD$  can be written as:

$$AD = AC \cos\theta = 2AB \cos\theta_1 \cos\theta = 2 \frac{d}{\sin\theta_1} \cos\theta_1 \cos\theta \quad (3.5)$$

Using Snell's Law, the refracted angle,  $\theta_1$ , can be determined as:

$$\cos\theta_1 = \frac{n \cos\theta}{n_1} = \frac{\cos\theta}{n_1} \quad (3.6)$$

In the materials, the refractive index of a Cu  $k_\alpha$  X-ray is less than 1. It should be noted, this does not mean that the speed of the X-ray, given by the group velocity, is faster than the speed of light, but the phase velocity of the X-ray is greater than  $c$  [93]. For this reason,  $n_1$  can be rewritten in terms of the critical angle,  $\theta_c$ , as:

$$n_1 = \frac{n \cos\theta_c}{\cos\theta} = \cos\theta_c \quad (3.7)$$

The condition for the constructive interference is  $\delta L = m\lambda$ , where  $m$  is the peak order of the interference fringe. Therefore, by using Eq. (3.4), (3.5) and (3.7), Eq. (3.3) can be written as:

$$\delta L = 2 \cos\theta_c \frac{d}{\sin\theta_1} - 2 \frac{d}{\sin\theta_1} \cos\theta_1 \cos\theta_m = m\lambda \quad (3.8)$$

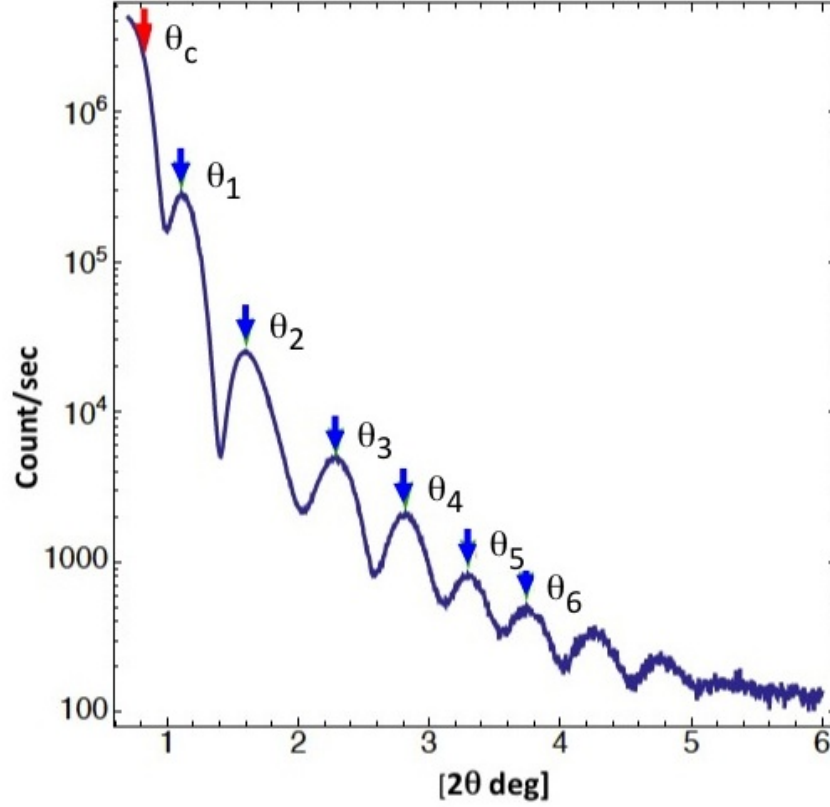


Figure 3.12: X-ray reflectivity measurements of 20 nm thick Ru film. Thickness of the film is calculated by using the angular positions of the Kiessig fringes.  $\theta_1$ ,  $\theta_2$  indicate the peak positions of the fringes that are due to constructive interference between X-rays reflected from the top (air/film) and bottom (film/substrate) film interfaces.  $\theta_c$  is the critical angle.

By replacing  $\theta_1$  with  $\theta_m$  and using trigonometric identities in Eq. (3.6), the equation for the constructive interference can be written as:

$$m\lambda = 2d\sqrt{\cos^2(\theta_c) - \cos^2(\theta_m)} \quad (3.9)$$

$\Rightarrow$

$$m\lambda = 2d\sqrt{\sin^2(\theta_m) - \sin^2(\theta_c)} \quad (3.10)$$

The thickness of the film,  $d$ , is calculated by determining the peak or valley positions of the Kiessig fringes ( $\theta_m$ ) and ( $\theta_c$ ). The value of the critical angle, ( $\theta_c$ ), is estimated from the interference pattern (see Figure 3.12). It is the angle at which the intensity is half of the maximum value. The thickness of the film is then calculated from the slope of  $\frac{m\lambda}{2}$  versus  $\sqrt{\sin^2(\theta_m) - \sin^2(\theta_c)}$  [94].

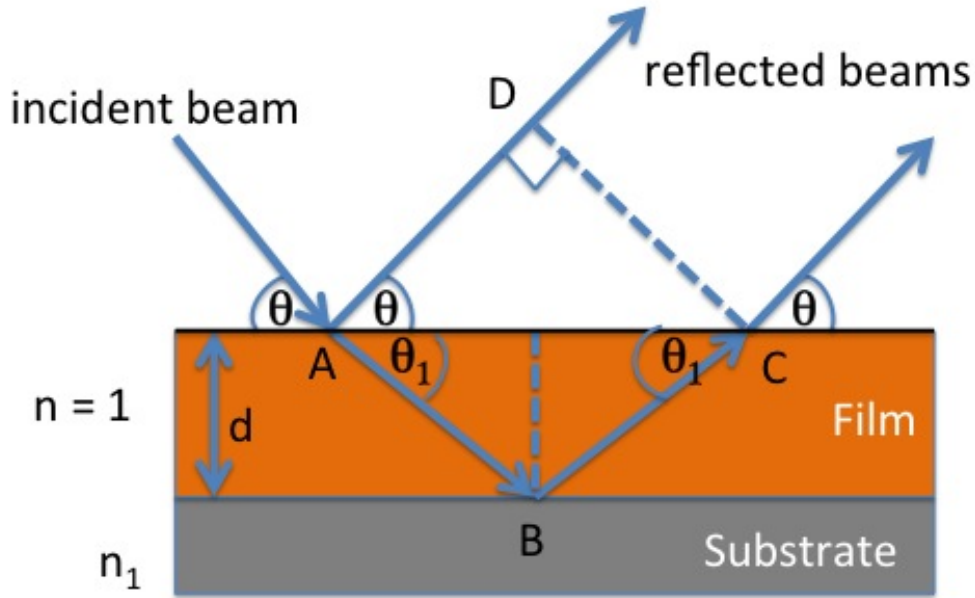


Figure 3.13: Ray diagram of two optical path of X-rays through a single layer is shown: one reflects from the top surface and the other from the bottom surface (substrate).

### 3.2.3 Magnetic Technique: Magneto-Optical Kerr effect (MOKE)

The polar magneto-optical Kerr effect (MOKE) was used to investigate the  $M(H)$  curves in order to study the magnetic properties of the samples with perpendicular magnetic anisotropy. It is an optical measurement technique that causes an incident linearly polarized light to rotate its polarization plane and become elliptically polarized upon reflection on a surface of a magnetic sample [95, 96].

It is important to mention here that, it is preferable to discuss the polarization of light in terms of electric field,  $E$ , instead of magnetic field,  $H$ . The electric field,  $E$  of the incident light forces the electron inside the material to oscillate along its plane of polarization [97]. Since the magnetization vector is oriented in a direction perpendicular to the sample surface and hence perpendicular to the oscillations of the electric field,  $E$ , a Lorentz force will induce a small component of the vibrational motion of magnetic moment perpendicular to the primary motion of electrons and direction of magnetization,  $v_{Lor} = m \times E$ . This component is responsible for generating a rotation of the polarization of the incident light that depends on magnetization.

A schematic of the experimental MOKE set up is shown in Figure 3.14 [98]. In the polar MOKE geometry, the magnetic field is applied perpendicular to the surface of the sample, so

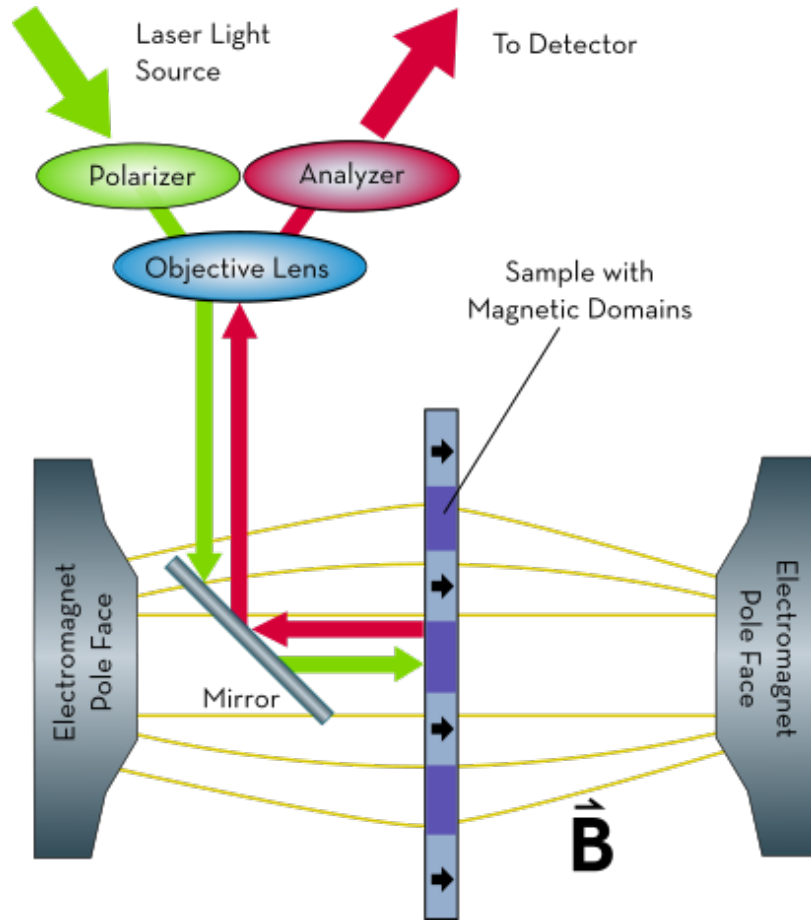


Figure 3.14: Schematic of experimental polar MOKE setup. The magnetic field is in a direction perpendicular to the surface of sample. (MOKE Experimental Setup, (2017), Figure 3.14 is available at: <https://www.montanainstruments.com/library/images/MOKE-experimental-setup-1.png> [Accessed 21 Dec. 2017].)

that the magnetization is fully aligned along the transverse direction to the sample surface (easy axis). The incident laser light is passed through a polarizer in such a way so that laser excitation is aligned perpendicular to the sample plane. The reflected light pass through the analyzer to a detector. The detector signal goes to lock-in-amplifier and a digital voltmeter and then to a computer.

The Kerr effect is particularly useful in the study of surface magnetism. It is highly sensitive to the magnetization within the skin depth region, typically 10-20 nm in most metals. This effect is utilized to obtain the hysteresis loops or domain images of magnetic samples [99]. A typical hysteresis loop of the sample Ta(3)/Cu(10)/[Co/Ni]×8/Ta(3) with perpendicular magnetic anisotropy is shown in Figure 3.15.

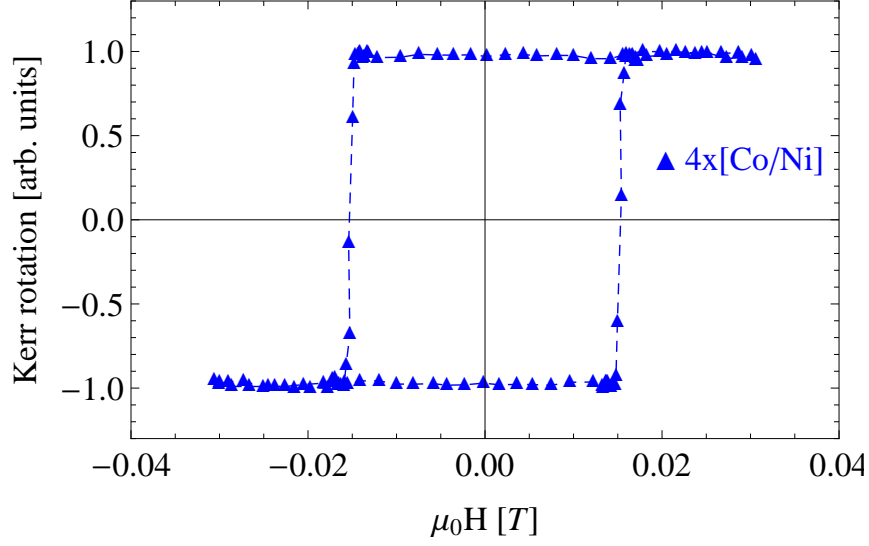


Figure 3.15: MOKE measurements of Ta(3)/Cu(10)/4x[Co/Ni]/Ta(3).

### 3.2.4 Superconducting quantum interference device (SQUID) Magnetometer:

A magnetic property measurement system (MPMS) with the superconducting quantum interference device (SQUID) is the most sensitive method for measuring the magnetic moments ( $\approx 10^{-8}$  emu).

The measurement assembly in the MPMS is mainly comprised of a superconducting magnet to generate large magnetic fields, a superconducting detection coil and a SQUID connected to the detection coil. A schematic diagram of the SQUID measurement assembly is shown in Figure 3.16 [100].

The measurements are performed in the MPMS by moving a magnetic sample through the detection coils, which are positioned at the centre of the superconducting magnets. The sample moves through the detection coils by a stepper motor. The detection coil is a single piece of a superconducting wire wound in a set of three coils. The upper coil is a single turn wound in a clockwise direction, the center coil consist of two turns wound in the anti-clockwise direction, and the bottom coil is again a single coil wound in the clockwise direction. The flux change in the two central coils is exactly cancelled by the flux change in the top and bottom coils. Therefore, the particular configuration of the detection coil reduces the noise in the detection circuit caused by the fluctuations in the large magnetic field of the superconductor magnet and minimizes the background drifts in the SQUID detection system caused by the relaxation in the magnetic field of the superconducting magnet.

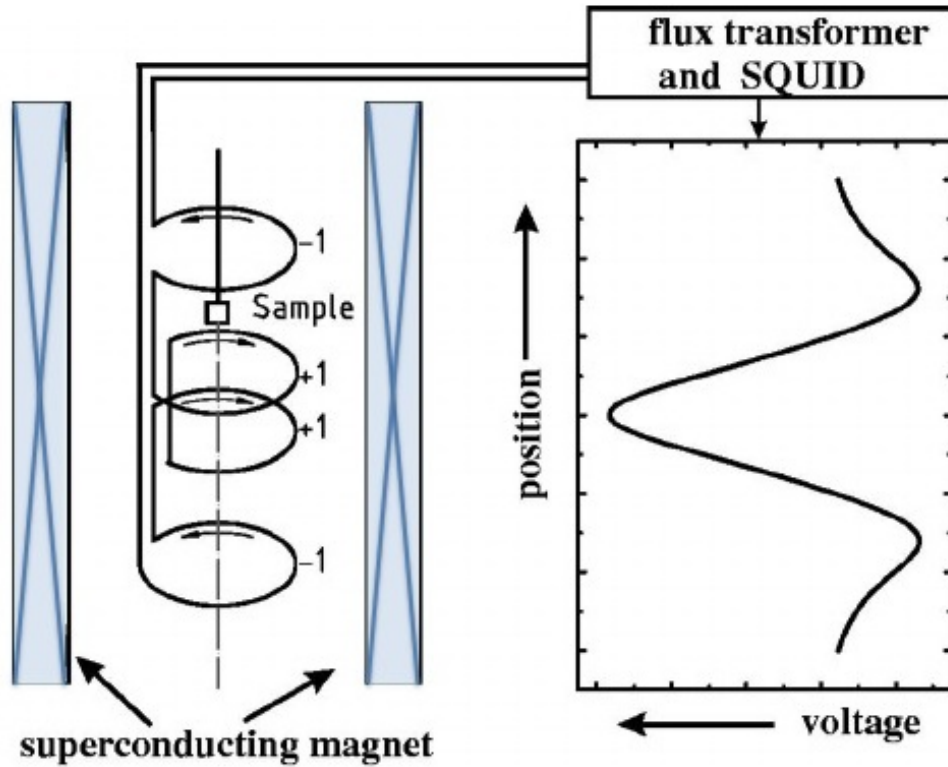


Figure 3.16: Schematic diagram of a SQUID assembly placed in a magnetic field. The dc magnetic field is axial and detection coils are also along the solenoid axis. The detection coil is further attached with the SQUID device. The right side shows the induced voltage as a function of position of the sample in the coils [100]. Figure 3.16 is adapted from [100].

Before starting the measurements, the sample is aligned exactly at the center of the detection coils (maximum voltage). The output voltage vs. position is shown in the Figure 3.16. As the sample moves through the detection coils, the magnetic moment of the sample induces a change of the magnetic flux in the coils. Any change of the magnetic flux in the detection coils will induce an electric current (Faraday's law of induction) that appears to oppose the change in the magnetic flux. The induced current is proportional to the change in magnetic flux.

Since the detection coils are connected to the SQUID through the superconducting wires, the current from the detection coils is inductively coupled to it. The DC SQUID consists of a superconducting loop with two Josephson junctions in it. When a symmetric DC SQUID is biased with an external dc current  $I$ , a current,  $I/2$ , flows through each of the two junctions. The schematic representation of a SQUID is shown in Figure 3.17. A superconducting current will flow through the SQUID, as long as the total current flowing through it does not exceeds the critical current,  $I_c$ . The  $I_c$  is the maximum current a SQUID

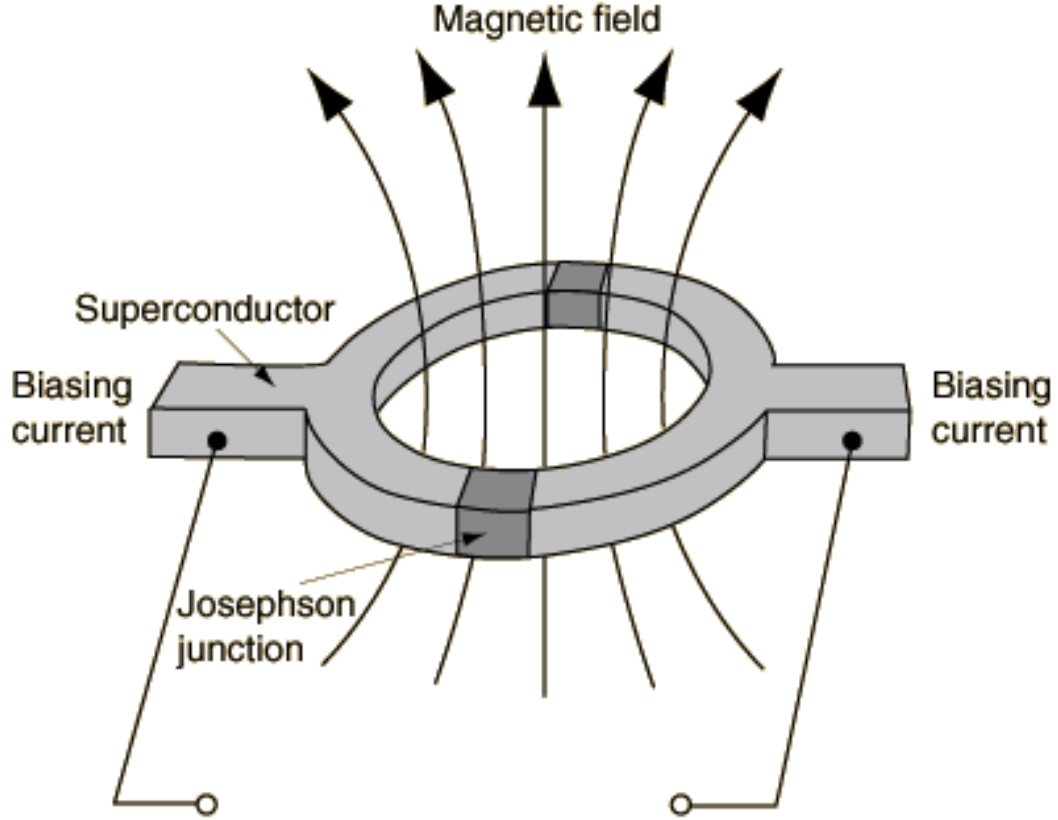


Figure 3.17: Schematic representation of a SQUID placed in a magnetic field.

can carry and remain superconducting. It is also the current at which the voltage across the SQUID develops.

The induced current in the detection coils causes the change in the magnetic flux of the SQUID, which changes the critical current of the SQUID. The SQUID electronics produces an output voltage which is strictly proportional to the current flowing in the SQUID detection coils [101, 102, 103].

A MPMS XL from Quantum Design was employed to measure the field dependence of the magnetization and determine the saturation magnetization and anisotropy of the samples with perpendicular magnetic anisotropy. The measurements are performed in magnetic fields up to  $5.5 \times 10^6$  A/m (70 kOe) and with the field direction parallel and perpendicular to the sample surface.  $K_u(SQUID)$  is calculated from the  $M(H)$  curve by finding the area enclosed between the hard and easy axes  $M(H)$ . A typical SQUID measurement along easy and hard axes of Ta(3)/Cu(10)/[Co/Ni] $\times$ 8/Ta(3) at 298K is shown in Figure 3.18.

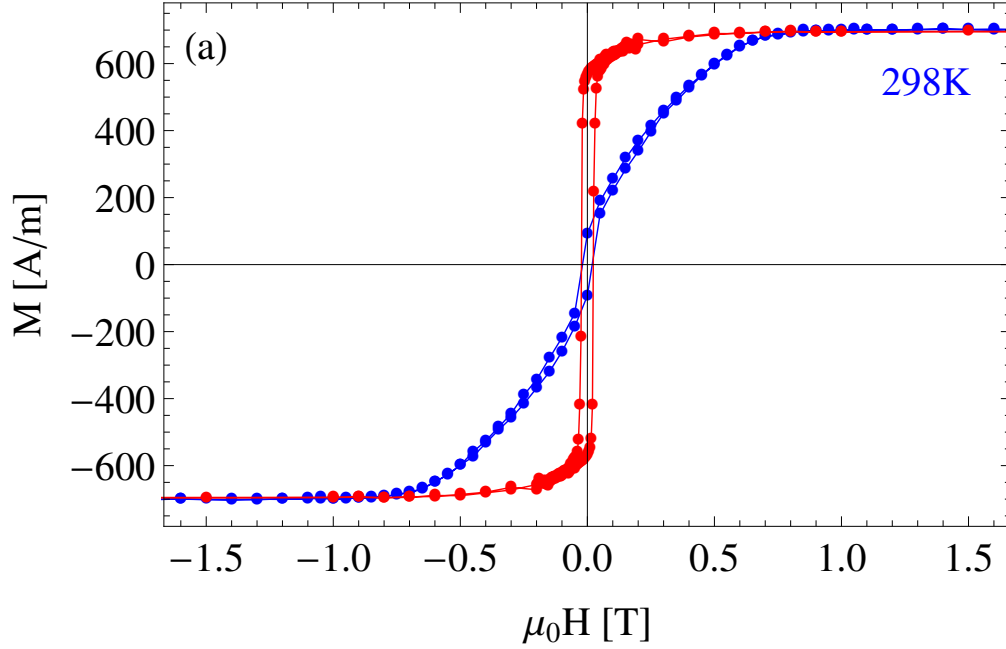


Figure 3.18: SQUID measurements of 8×[Co/Ni] multilayers along the hard (blue) and easy (red) axes at 298K.

### 3.2.5 Ferromagnetic Resonance (FMR)

#### Theory:

(i) **Magnetization Dynamics:** In classical mechanics, the equation of motion of a rigid body rotating around an axis can be written as:

$$T = \frac{dL}{dt} = r \times F \quad (3.11)$$

where  $T$  is the torque exerted on the body,  $L$  is the angular momentum,  $r$  is the position vector of the centre of mass, and  $F$  is the force applied to the body. It is clear from the Eq. (3.11) that the torque is perpendicular to the force applied to the rigid body, which causes the center of mass to spin and precess around an axis.

An electron orbiting an atom exhibits spin angular momentum (revolving around its own axis) and orbital angular momentum (revolving around the nucleus). Therefore, in a classical picture, an electron is considered as a spinning negative charge that has an angular momentum associated with it and will precess when a force is applied to it. The rotating electron ( $-e$  charge) creates a magnetic moment,  $M$ , which is anti-parallel to the angular momentum. The relation between the magnetic moment and the angular momentum is given as



$$M = -\gamma L \quad (3.12)$$

where  $\gamma = \frac{g|e|\hbar}{2m_e} = \frac{g\mu_B}{\hbar}$  is the gyromagnetic ratio and is positive by convention,  $\mu_B$  is the Bohr magneton and  $\hbar$  is the reduced Planck's constant. Since the magnetic moment and angular momentum of the electron are directly coupled, a force affecting on the magnetic moment would also affect the angular momentum. The torque exerted on the magnetic moment in an external applied field  $H$  is given by

$$T = M \times \mu_0 H \quad (3.13)$$

Eqs. (3.11), (3.14) and (3.13) can be combined to write the magnetization dynamics of a magnetic moment in an undamped condition as

$$\frac{dM}{dt} = -\gamma\mu_0 M \times H_{eff} \quad (3.14)$$

where  $H_{eff}$  is the total effective magnetic field. Following this equation, the magnetization will precess around the effective field at a constant angle without reaching to its equilibrium position. However, as experimentally observed, the magnetization aligns with the direction of minimal energy after a finite time. Therefore, in 1935, L. Landau and E. Lifshitz [104] described magnetization dynamics including a damping term leading to Landau-Lifshitz (LL) equation:

$$\frac{dM}{dt} = -\gamma\mu_0 \left[ M \times H_{eff} \right] - \frac{\lambda}{M_s^2} \left[ M \times (M \times H_{eff}) \right] \quad (3.15)$$

where  $\lambda > 0$  is the phenomenological damping parameter that corresponds to the inverse of the relaxation time. The first term in Eq. (3.15) represents the precessional torque as seen in Eq. (3.14) and the second term represents the LL damping term. Figure 3.19 (a) and (b) respectively, represents the first and second terms of Eq. (3.15). The effect of damping is to move the magnetization  $M$  so that it lines up parallel to  $H_{eff}$ . It causes  $M$  to trace a spiral pattern.

The FMR linewidth can depend on the geometry of the field and whether the sample is saturated or not. In order to avoid this dependance, the external applied magnetic field should be strong enough to satisfy  $\frac{\partial M}{\partial H_{dc}} = 0$ , where  $H_{dc}$  is the external magnetic field. An applied field less than that will result in a damping parameter, which is not intrinsic to the ferromagnetic material.

In Eq. (3.15), if we consider that  $\lambda \rightarrow \infty$  then the damping term will eventually dominate over the precessional torque, which means there will be an increasingly fast relaxation to the lattice. Therefore, the system will always be in quasi-equilibrium state. This seems to be an unrealistic behaviour. In 1955 Gilbert introduced a different relaxation torque [105].

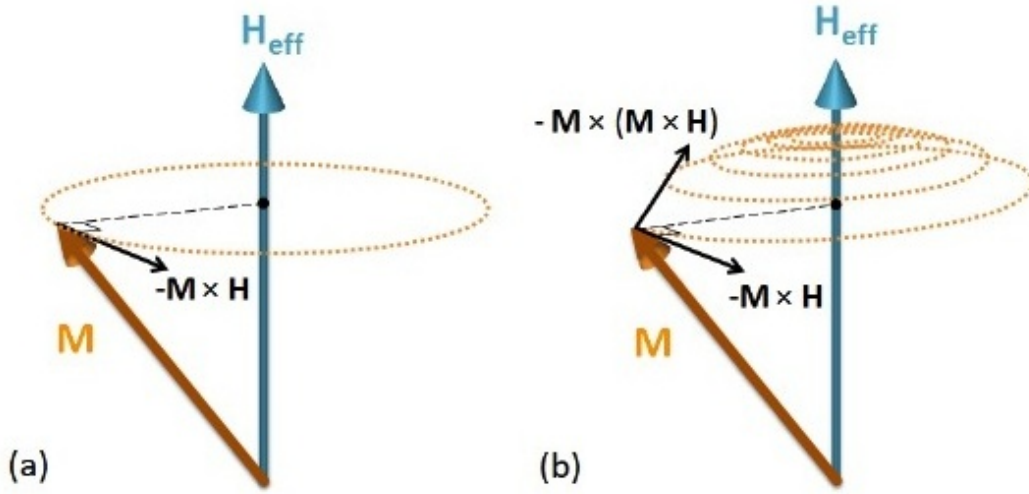


Figure 3.19: Illustration of the magnetization precession for motion (a) without damping and (b) with damping.

He reformulated the damping term using the Lagrangian and Rayleighs dissipation function [105] to give the Landau Lifshitz Gilbert (LLG) equation:

$$\frac{dM}{dt} = -\gamma\mu_0 M \times H_{eff} + \frac{\alpha}{M_s} \left( M \times \frac{dM}{dt} \right) \quad (3.16)$$

where  $\alpha$  is a phenomenological dimensionless damping parameter. Both the LL and LLG Eqs. (3.15) and (3.16) can be shown to be identical when  $\alpha \ll 1$ . In rest of the this thesis, the LLG Eq. (3.16) is used.

**(ii) Ferromagnetic Resonance Equations:** In FMR experiments, a large static magnetic field  $H_{dc}$  is applied on a ferromagnetic sample. In order to minimize the Zeeman energy of the system, the magnetization  $M$  in the material tends to align with  $H_{dc}$ . When a weak microwave field  $h_{rf} = h e^{i\omega t}$  is applied perpendicular to the static magnetic field at a fixed frequency  $\omega = 2\pi f$ , it exerts a torque on the magnetization which induce a precessional motion. Changing the external field  $H_{dc}$  changes the precessional frequency of the magnetization  $M$ ; when the frequency of the RF field matches the natural frequency of the ferromagnetic system, the absorption is maximum and the sample undergoes ferromagnetic resonance (FMR). This is detected as an additional loss in the microwave signal. The absorption is observed as a Lorentzian line shape in the absorption spectrum. In all the FMR measurements, the frequency was fixed and the DC field was swept. The FMR measurements were carried out for both, in-plane and out of plane configurations.

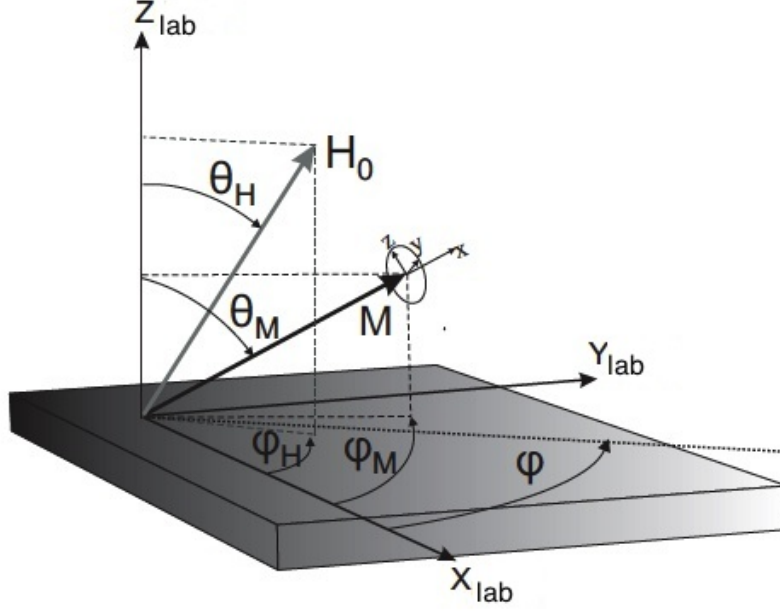


Figure 3.20: Schematic of the laboratory and magnetization coordinate systems. The laboratory system of coordinates is described by  $X_{lab}$ ,  $Y_{lab}$ ,  $Z_{lab}$  while  $x$ ,  $y$ ,  $z$  are the coordinates to describe the magnetization dynamics.

**(a) Perpendicular configuration:** In the perpendicular configuration,  $H_{dc}$  is applied perpendicular to the plane of the sample. In this case,  $\theta_H = 0$ . Since all the measured samples have perpendicular magnetic anisotropy, we have  $\theta_M = 0$  (see Figure 3.20).

For a perpendicularly magnetized sample excited by a small in-plane perturbation field, the magnetization will not strictly align along the  $z$ -axis (see Figure 3.20). However, due to small perturbation, the perpendicular component of  $M$  ( $M_z$ ) can assumed to be constant, and one can write

$$M = m_x x + m_y y + M_z z \quad (3.17)$$

$m_x$  and  $m_y$  are the oscillating high frequency components of the magnetization with units of A/m.

For perpendicularly magnetized films,  $E_{tot}$ , as described earlier in chapter 1 section (2.1) can be written as

$$E_{tot} = -\mu_0(M \cdot H_{dc}z) + \frac{\mu_0}{2}(z \cdot M)^2 - K_u(z \cdot m)^2 - K_4^1(z \cdot m)^4 \quad (3.18)$$

The internal effective field can be calculated from the free energies by using the relation [106].

$$H_{eff} = -\frac{1}{\mu_0} \frac{\partial E_{tot}}{\partial M} \quad (3.19)$$

By using Eqs. (3.18) and (3.19), the resulting simplified form of  $H_{eff}$  is

$$H_{eff} = (H_{dc} - M_{eff}^\perp)z \quad (3.20)$$

where  $M_{eff}^\perp = M_s^\perp - H_K^\perp$  and  $H_K^\perp = 2K_u^\perp/(\mu_0 M_s)$ .  $K_u^\perp = K_2^\perp + K_4^\perp$  is the uniaxial perpendicular magnetic anisotropy, and  $K_2^\perp$  and  $K_4^\perp$  are the second and forth order uniaxial magnetic anisotropy constants. Since an additional field  $h_{rf}$  is also applied perpendicular to the  $H_{dc}$  in case of FMR measurements,  $H_{eff}$  can be written as

$$H_{eff}^\perp = (H_{dc} - M_{eff}^\perp)z + h_{rf}y \quad (3.21)$$

$h_{rf}$  is assumed to be uniform, so the precession of the magnetization can be considered to be uniform throughout the sample. Substituting Eqs. (3.21) and (3.17) into (3.16), we obtain

$$\frac{dm_x}{dt} = -\gamma_\perp \mu_0 (m_y (H_{dc} - M_{eff}^\perp) - M_s h_{rf}) - \alpha \frac{dm_y}{dt} \quad (3.22)$$

$$\frac{dm_y}{dt} = \gamma_\perp \mu_0 m_x (H_{dc} - M_{eff}^\perp) + \alpha \frac{dm_x}{dt} \quad (3.23)$$

$$0 = -\gamma_\perp \mu_0 m_x h_{rf} - \frac{\alpha}{M_s} \left( m_x \frac{dm_y}{dt} - m_y \frac{dm_x}{dt} \right). \quad (3.24)$$

Eqs. (3.22), Eq. (3.23) and Eq. (3.24) can be linearized in  $h_{rf}$  and  $m_i$  by neglecting the product terms of these quantities. Considering  $m_i \propto e^{i\omega t}$  for an rf field of the same form, we get

$$i\omega m_x + (\omega_H + i\alpha\omega)m_y = \omega_M h_{rf} \quad (3.25)$$

$$(\omega_H + i\alpha\omega)m_x - i\omega m_y = 0 \quad (3.26)$$

where

$$\omega_H = \gamma_\perp \mu_0 (H_{dc} - M_{eff}^\perp) \quad (3.27)$$

$$\omega_M = \gamma_\perp \mu_0 M_s \quad (3.28)$$

are used for convenience. Rewriting Eq. (3.25) and Eq. (3.26) in the matrix form, in terms of components  $h = (0, h_{rf})$  and  $m = (m_x, m_y)$ , we get

$$\begin{pmatrix} 0 \\ h_{rf} \end{pmatrix} = \begin{bmatrix} i\omega & \omega_H + i\alpha\omega \\ \omega_H + i\alpha\omega & -i\omega \end{bmatrix} \begin{pmatrix} m_x \\ m_y \end{pmatrix} \quad (3.29)$$

The susceptibility tensor  $\bar{\bar{\chi}}$  can be obtained by considering [107].

$$\begin{pmatrix} m_x \\ m_y \end{pmatrix} = m = \bar{\bar{\chi}} h = \begin{bmatrix} \chi_{xx} & \chi_{xy} \\ \chi_{yx} & \chi_{yy} \end{bmatrix} \begin{pmatrix} 0 \\ h_{rf} \end{pmatrix} \quad (3.30)$$

The  $h_{rf}$  field is applied along the y-direction, therefore the component of susceptibility tensor  $\chi_{yy}$  is given by

$$\chi_{yy} = \frac{m_y}{h_{rf}} = \frac{\omega_M(\omega_H + i\alpha\omega)}{(\omega_H + i\alpha\omega)^2 - \omega^2} \quad (3.31)$$

For  $\alpha \ll 1$ ,  $\chi_{yy}$  can be further reduced to

$$\chi_{yy} = \frac{\omega_M(\omega_H + i\alpha\omega)}{\omega_H^2 - \omega^2 + 2i\alpha\omega\omega_H} \quad (3.32)$$

with the real and imaginary components  $\chi'_{yy} - i\chi''_{yy}$  given as

$$\chi'_{yy} = \frac{\omega_M\omega_H(\omega_H^2 - \omega^2)}{(\omega_H^2 - \omega^2)^2 + (2\alpha\omega\omega_H)^2} \quad (3.33)$$

$$\chi''_{yy} = \frac{\alpha\omega\omega_M(\omega_H^2 + \omega^2)}{(\omega_H^2 - \omega^2)^2 + (2\alpha\omega\omega_H)^2} \quad (3.34)$$

$\chi'_{yy}$  and  $\chi''_{yy}$  corresponds to the components of  $m_y$  in phase with  $h_{rf}$  and delayed by a phase angle of  $90^\circ$  from  $h_{rf}$ , respectively. The resonance condition is obtained when  $m_y$  becomes maximum for a given  $h_{rf}$ , i.e. when the denominator of Eq.(3.34) becomes minimum, therefore

$$\omega = \gamma_\perp \mu_0 (H_{dc} - M_{eff}^\perp) \quad (3.35)$$

where

$$M_{eff}^\perp = M_s^\perp - \frac{2K_2^\perp}{\mu_0 M_s^\perp} - \frac{2K_4^\perp}{\mu_0 M_s^\perp} \quad (3.36)$$

This Eq. is known as Kittel resonance formula for the perpendicular configuration. The dependance of  $\chi''_{yy}$  on the applied field can mathematically be represented by a Lorentzian with full width at a half maximum as

$$\mu_0 \Delta H(f_0) = 2\alpha \frac{\omega}{\gamma_\perp} = \frac{4\pi\alpha}{\gamma_\perp} f_0 \quad (3.37)$$

where  $f_0$  is the microwave frequency.

For inhomogeneous samples, the FMR linewidth is well described by Gilbert-like damping.

$$\mu_0 \Delta H(f_0) = \mu_0 \Delta H_0 + \frac{4\pi\alpha}{\gamma_\perp} f_0 \quad (3.38)$$

where  $\Delta H_0$  is the zero frequency line broadening due to the long range homogeneity [63, 108].

**(ii) In-plane configuration:** In the in-plane configuration of FMR measurements, both the applied magnetic dc field,  $H_{dc}$ , and the magnetization  $M$  lie in the plane of the film

with  $\theta_H = \pi/2$ ,  $\theta_M = \pi/2$  ((see Figure 3.20). Following the same treatment, the resonance equations for in-plane FMR measurements are given by

$$\left(\frac{\omega}{\gamma_{\parallel}}\right)^2 = \mu_0^2 H_{FMR} (H_{FMR} + M_{eff}^{\parallel}) \quad (3.39)$$

where

$$M_{eff}^{\parallel} = M_s^{\parallel} - \frac{2K_2^{\perp}}{\mu_0 M_s^{\perp}} \quad (3.40)$$

$\gamma_{\parallel} = \gamma_{\parallel} \mu_B / \hbar$ ,  $M_s^{\parallel}$  and  $M_{eff}^{\parallel}$  are the in-plane  $g$ -factor, saturation magnetization, and the effective magnetization respectively, and  $H_{FMR} = H_{eff}|_{H_{FMR}}$  is the resonance field.

### Experimental technique and setup

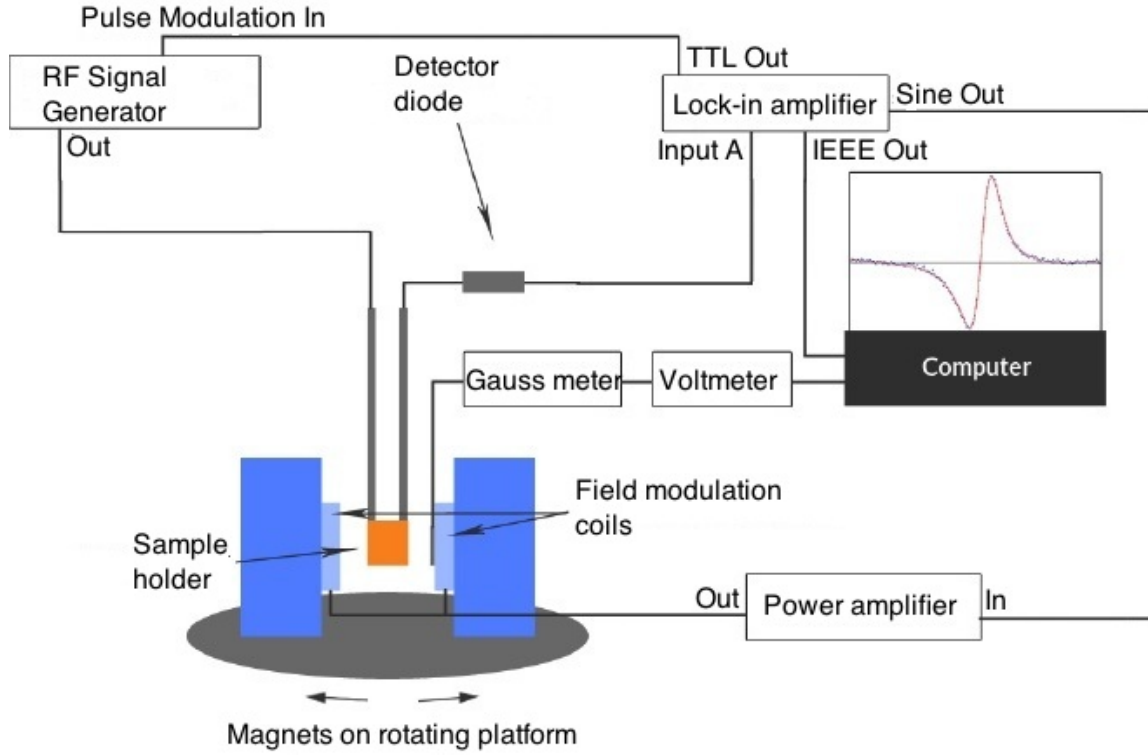


Figure 3.21: Schematic of the FMR set up for co-planar waveguide configuration

Ferromagnetic resonance (FMR) measurements were performed with a co-planar waveguide in a field-swept, field modulated configuration. Figure 3.21 shows the block diagram of the FMR setup design. A co-planar transmission line on which the sample is placed is held in the centre of the magnets. A microwave signal is generated by a microwave source and is directed by a waveguide to the sample. In our case, the RF signal is created by using an Anritsu MG369XB signal generator. This signal generator uses the internal feedback to keep the output power constant in the frequency range 0 to 70 GHz.

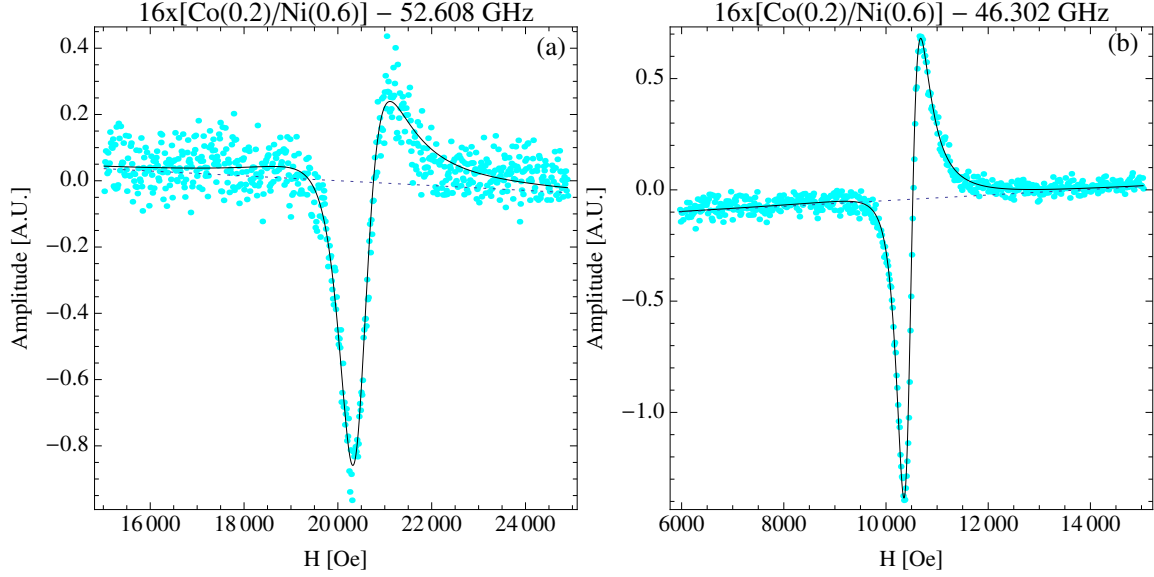


Figure 3.22: (left) FMR measurements of  $16 \times [\text{Co}/\text{Ni}]$  multilayers along the in-plane (hard) at 52.608 GHz and (right) perpendicular (easy) directions at 46.302 GHz respectively.

The magnet coils are used inside the large magnets to provide modulation to external DC field. These coils are powered by the sine wave outputs on the lock-in amplifier which is amplified by a standard power amplifier. This allows the frequency and amplitude of the field modulation to be controlled with the lock in amplifier. The oscillating field of the smaller coils is much weaker than the DC magnetic field generated by the larger magnets. Therefore, the external magnetic field oscillates slightly around the DC average. The field reading from the gauss meter is assumed to be equal to  $H_{DC}$  without modulation.

The RF signal from the microwave source (at a fixed frequency and power) passes through the co-planar transmission line, on which the sample is held. The RF current creates a  $h_{rf}$ , magnetic field perpendicular to the externally applied  $H_{DC}$  field. When the resonance condition is met, the power in the reflected wave will be less because maximum absorption occurs at resonance. Therefore, the FMR signal is detected as an additional loss in the microwave signal. As the external DC field sweeps through the resonance condition, the transmitted RF power or its derivative is plotted as a function of the external magnetic field in order to obtain an absorption line.

Since the external magnetic field is modulated, the resulting signal at the lock-in amplifier is the derivative of the real absorption peak. The actual absorption peak is Lorentzian in shape, and therefore, the modulated absorption peak has the shape of the derivative of the Lorentzian.

The absorption/transmitted RF power, or its derivative can be plotted as a function of  $H_{dc}$  to obtain the FMR signal as shown in Figure 3.22. The centre of the absorption line gives the resonance field,  $H_{FMR}$ , which is obtained by fitting the data as discussed by [109].

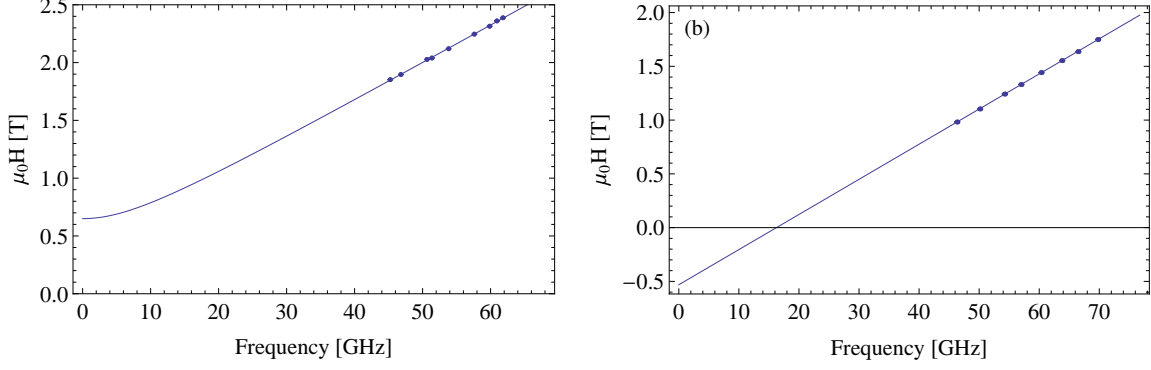


Figure 3.23: Plots of resonance field versus frequency of 8×[Co/Ni] multilayers obtained from FMR measurements with the applied field (a) parallel and (b) perpendicular to the sample surface.

By measuring absorption lines at different frequencies, one can plot  $H_{FMR}$  as a function of RF frequency  $\omega$ . Eq. (3.39) and Eq. (3.35) are used to determine  $M_{eff}$ . Figure 3.23 shows typical plots of  $H_{FMR}$  as a function of  $\omega$  for in plane and perpendicular to the plane configurations. The linewidth obtained from the signal is calculated by using Eq. (3.38), which allows the determination of the Lande's g-factor and damping in the samples.

In real systems, a frequency shift and linewidth broadening is observed due to the fact that the precession is not ideally uniform and coherent, which in turn can be used to measure the damping in the sample using Eq. 3.38.

### 3.2.6 Van der Pauw method

GMR was measured by the Van der Pauw method in fields up to 0.8 T. The van der Pauw method is a technique [110] used to measure the resistivity of arbitrary shape thin film samples that have uniform thickness. The contacts are made on the perimeter of the sample and are much smaller than the area of the sample. To measure the resistance, a current is caused to flow along one edge of the sample (for instance,  $I_{AB}$ ) and the voltage across the opposite edge (say  $V_{CD}$ ) is measured as shown in the Figure 3.24 (a). Using Ohm's law, a resistance  $R_{AB,CD} = V_{CD}/I_{AB}$  can be found. Similarly, when the current flows between B and C contacts and voltage is measured across A and D as shown in Figure 3.24 (b), the resistance is given by  $R_{BC,AD} = V_{AD}/I_{BC}$ . Then the sheet resistance of a sample can be calculated using the Van der Pauw formula as

$$R_s = \frac{\pi R_{av}}{\ln 2} f \quad (3.41)$$

where  $R_s$  is the sheet resistance of the sample and  $R_{av}$  is the average resistance of  $R_{AB,CD}$  and  $R_{BC,AD}$ .  $f$  is a correction factor which is a function of the ratio  $R_r = R_{AB,CD}/R_{BC,AD}$ . For a symmetrical sample  $R_r = 1$  and the correction factor  $f = 1$  [110]. The improvement



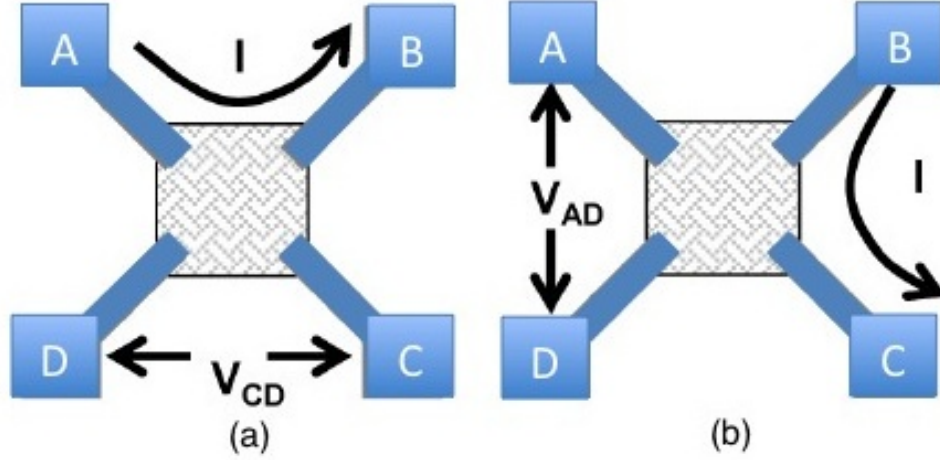


Figure 3.24: Schematic of the Van der Pauw set up (a) current flows along the edge, AB, and voltage is measured across the edge, BC, (b) current flows along the edge, AB, and voltage is measured across the edge, AD.

in the accuracy of the resistance measurement can be procured by repeating the resistance measurements by switching the polarities of both the current source and the voltage meter.

### 3.2.7 TEM sample preparation

Classical TEM cross-sections of the samples were glued together in face-to-face geometry using G2 epoxy glue (Gatan). Samples were prepared by sawing (Wire Saw WS 22, IBS GmbH), grinding (MetaServ 250, Böhler), polishing (Minimet 1000, Böhler), dimpling (Dimple Grinder 656, Gatan), and final Ar ion milling (Precision Ion Polishing System PIPS 691, Gatan)

## 3.3 Lithography

### 3.3.1 Nano-pillar device preparation

I patterned the deposited continuous films into devices (nano-pillars) by using the facilities at Institute of Ion Beam Physics and Materials Research, Helmholtz-Zentrum Dresden-Rossendorf (HZDR), Dresden, Germany. A standard fabrication technique [111] is used to pattern the films into spin valve devices as shown in Figure 3.25. The recipe has already been published in [39]. The steps used to pattern the films are discussed below:

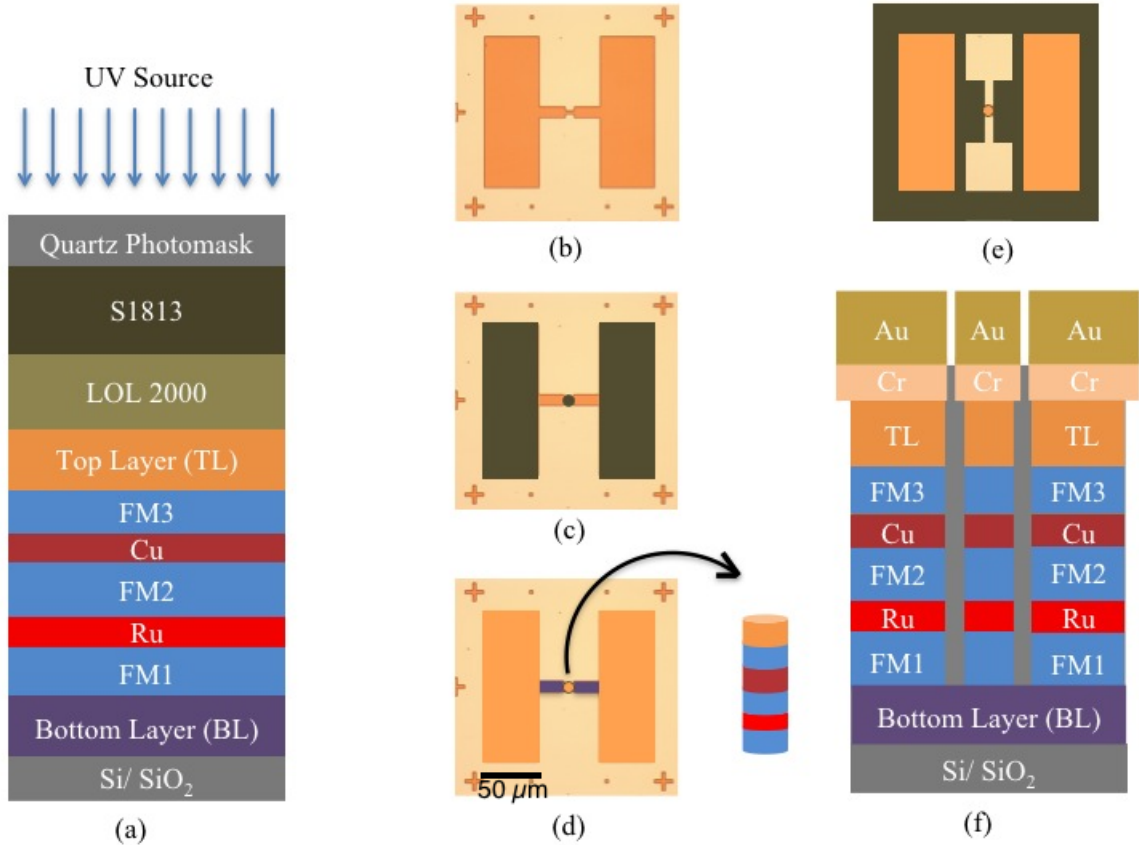


Figure 3.25: Schematic representation of the fabrication steps. (a) The deposited film structure with a bilayer of PRs and the photomask used in the mask aligner. (b) The optical microscope image of the multilayers stack after patterning of the bottom contact and subsequent deposition of the first SiO layer. (c) A schematic picture of the spin coated layer of the negative PR on the top of the wide contact pads of the device and the central nanopillar. (d) A schematic picture of the patterned contact pads and the nanopillar (inset) on the top of the bottom contact. (e) A top view of the bottom and top contact design after removal of the photoresist. (f) The cross section view of the patterned device with Cr/Au bottom and top contacts.

- The sputtered films are cleaned in an ultrasonic acetone wash for two minutes followed by isopropanol rinse for one minute and then blown dry in  $N_2$ .
- The films are coated with a bilayer of photoresist (PR) LOL 2000 (200 nm) and S1813 (1.3  $\mu m$ ) using a vacuum spin coater. The substrate is baked at 140°C for five minutes, after coating LOL 2000 and 2 minutes at 110°C for S1813, to drive out the excess solvent from the PR. LOL 2000 is not UV sensitive and its role is to help complete the liftoff of S1813. The sample with a photomask, Figure 3.25a is then loaded into the UV exposure tool. The films are developed in the MF-319 for 45 s followed by a de-ionised water rinse to remove the exposed PR and developer, respectively. The areas not protected by the PR are etched until the first Ta layer, adjacent to a Si

substrate, in an ion-milling tool using the  $\text{Ar}^+$  ions with a beam energy of 200 eV.  $\text{SiO}$  (70 nm) is deposited by thermal evaporation.  $\text{SiO}$  helps to electrically isolate the individual device. Samples were soaked in acetone and placed in an ultrasonic bath to lift off the unwanted photoresist. A single patterned device image taken by an optical microscope is shown in Figure 3.25b.

- After cleaning the samples, a negative photoresist maN-2403 (300 nm) is used to coat the patterned films. E-beam lithography (EBL) is used to expose the wide side contact pads ( $200 \times 50 \mu\text{m}$ ) of H-shaped devices and the central circular area of diameter 200 nm. Unexposed resist is removed with maD-525 developer, Figure 3.25b. The sample is then etched using  $\text{Ar}^+$  ions until the Cu seed layer that serves as bottom contact connecting the contact pads and the 200 nm in diameter nano-pillar. A 40 nm layer of  $\text{SiO}$  is deposited by thermal evaporation method. This is shown in Figure 3.25d, where the insert figure is a 3D drawing of the structure of the nanopillar. Acetone and 1165 (NMP (1-Methyl-2-pyrrolidone) based PR-remover) are used for PR lift off.
- We again spin coat the bilayer of PRs on the top of the sample surface. UV light is used to expose the wide contact pads of the H device and the top contact area for the 200 nm nanopillar between the contact pads. The developed pattern is shown in Figure 3.25e, where the green area represent the PRs. The device structure obtained after thermal evaporation of  $\text{Cr}(5 \text{ nm})/\text{Au}(125 \text{ nm})$  layers on the top of the sample surface and photoresist lift off is presented in Figure 3.25f (cross section).

## Chapter 4

# Optimization of the magnetic properties of Co/Ni multilayer structures for use in STT-RAM

Structural and magnetic properties of Co/Ni multilayers were studied for their use in STT-RAM. (111) textured SAF/Cu/FL multilayer film structures were optimized by varying the individual layer thickness and sputter conditions. The SAF is a synthetic antiferromagnet consisting of Co/Ni multilayers coupled antiferromagnetically across a Ru spacer layer, and the FL is a free layer consisting of a single Co/Ni multilayer. The dependence of magnetic properties such as perpendicular magnetic anisotropy, saturation magnetization, damping and zero-frequency line broadening of the Co/Ni multilayers on the number of bilayer was thoroughly discussed. This study provides an important step towards the realization of STT-RAM devices consisting of only Co/Ni multilayers.

### 4.1 Optimization Strategy

#### 4.1.1 Effect of Cu seed layer thickness on film microstructure

To minimize the bottom contact resistance, the metallic seed layer in STT-RAM devices can be as thick as 35 nm [19]. Thus, the effect of the Cu seedlayer thickness,  $d_{Cu1}$ , on the film microstructure of Ta/Cu( $d_{Cu1}$ )/SAF/Cu/FL/Ta was first studied.

Figure 4.1 shows the full SAF/Cu/FL structure used in this study. Films were deposited at room temperature on Si (001) wafers using rf (Co, Ni, Ta, and Ru) and dc (Cu) magnetron sputtering at an argon pressure of  $2.2 \times 10^{-3}$  torr and  $1.5 \times 10^{-3}$  torr, respectively. In all the deposited structures the deposition rates were 0.04 nm/s for Ta and 0.2 nm/s for the Cu seed layer. Six samples with different thicknesses of  $d_{Cu1} = 1.9, 3, 7, 10, 20$  and 30 nm are deposited to cover a wide range of seed layer thicknesses. For corrosion protection, the films are covered by 4 nm of Ta. Montoya et al. have shown that 3 nm Ta layer grown by sputter deposition at ambient temperature on top of Si substrate is amorphous [112].

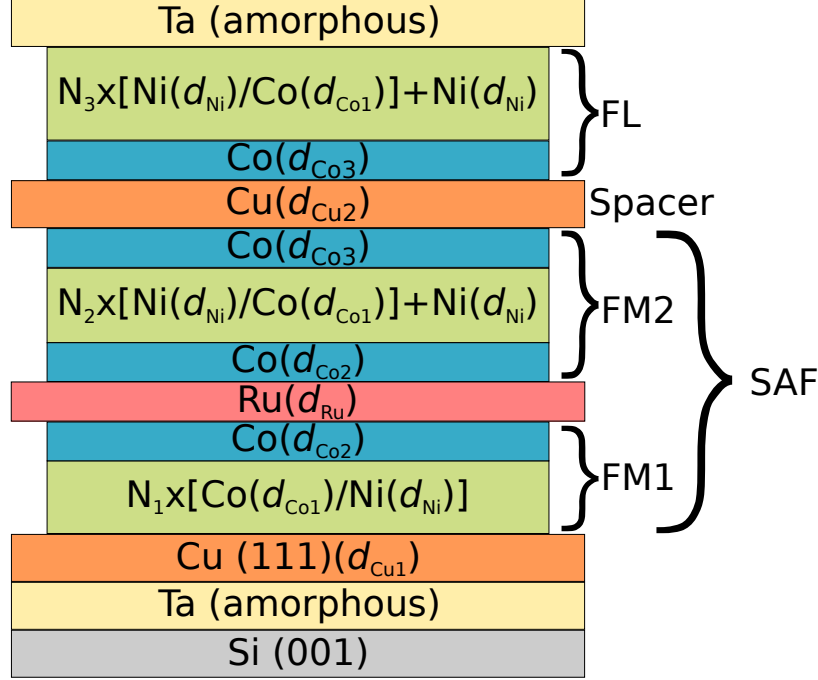


Figure 4.1: Schematic representation of the full film structure, Ta/Cu( $d_{Cu1}$ )/SAF/Cu/FL/Ta. The Ta and Cu seed layers are used to establish (111) texture of the Co/Ni multilayers.  $d_{Cu1}$  is varied from 1.9 to 30 nm [113].

**1. Film texture:** Johnson *et al.* [50] have investigated the dependence of perpendicular magnetic anisotropy (PMA) on the crystallographic orientation of Co/Ni MLs. They showed that the largest PMA is achieved for Co/Ni MLs grown along the  $\langle 111 \rangle$  crystallographic directions. To promote this growth direction, different seed layers have been investigated by other research groups [114, 115, 116, 117].

Figure 4.2 shows the  $\theta-2\theta$  scan of Ta(30)/Cu( $d_{Cu1}$ )/SAF/Cu/FL/Ta structure with the Cu thickness  $d_{Cu1}$  ranging from 1.9 to 30 nm. The presence of the X-ray diffraction peak at  $43.2^\circ$  indicates that Cu predominantly grows along the  $\langle 111 \rangle$  directions when deposited on Ta. The peak at  $44.4^\circ$  is from the constructive interference of X-rays with Co/Ni multilayers that grow epitaxially on top of Cu grains also along  $\langle 111 \rangle$  directions. The lattice mismatch between Co and Ni is only 0.02%. Therefore, it is difficult to distinguish the diffraction peaks of Co and Ni layers. As expected, the intensities of both Cu (111) and Co/Ni (111) peaks increase with the increase of Cu seedlayer and Co/Ni multilayer thicknesses, respectively. The presence of thickness fringes are seen on both sides of the two primary Cu(111) and Co/Ni(111) peaks (see Figure 4.2).

The texture of Co/Ni MLs in Ta(30)/Cu( $d_{Cu1}$ )/SAF/Cu/FL/Ta structure is determined from X-ray rocking curve measurements. In all the film structures, Co/Ni MLs grew along the  $\langle 111 \rangle$  crystallographic directions with a full width at half maximum (FWHM) of the rocking curve of Co/Ni (111) less than  $4^\circ$ . The dependence of FWHM of rocking curve of

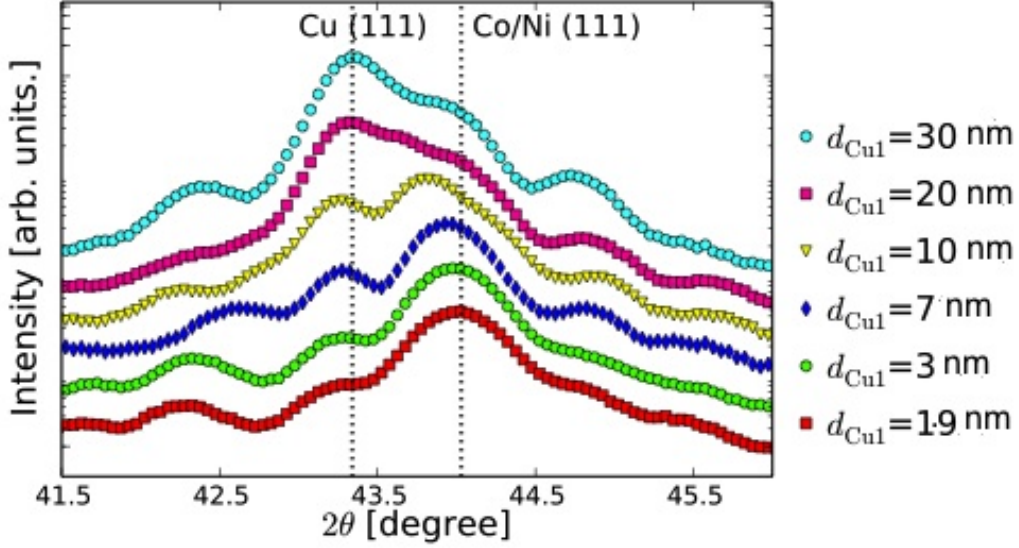


Figure 4.2: X-ray measurements of Ta/Cu( $d_{Cu1}$ )/SAF/Cu/FL/Ta layer structure with  $d_{Cu1}$  varying from 1.9 to 30 nm. This is a log plot of intensity as a function of  $2\theta$  with offsets.

Co/Ni(111) on  $d_{Cu1}$  is shown in Figure 4.3. Increasing Cu seedlayer thickness improves the (111) texture of the Co/Ni MLs. Figure 4.3 shows that FWHM is reduced from  $3.63^\circ \pm 0.03$  to  $2.59^\circ \pm 0.03$  if the thickness of the Cu seedlayer is increased from 1.9 nm to 30 nm. These results are in agreement with the studies conducted by Zhang and DenBroeder et al. [114, 115]. They showed that the (111) texture of Co/Ni MLs improves with increasing thickness of Au seedlayer.

**2. Grain size and film roughness:** The thickness of the seed layer has a strong effect on the grain size and film roughness and, as a result, on the magnetic properties of the Co/Ni MLs [118]. For this reason, we have carried out a detailed investigation of the effect of Cu seed layer thickness,  $d_{Cu1}$ , on the microstructure of the films.

Figure 4.4 (a) and Figure 4.4 (b) show cross-sectional bright-field TEM images of the full structure Si/Ta/Cu( $d_{Cu1}$ )/SAF/Cu/FL/Ta (see scheme in Figure 4.1) with  $d_{Cu1} = 1.9$  nm and 30 nm, respectively. As indicated by the Ru layer, which appears as a thin dark line due to its high mass contrast, the Co/Ni films follow the morphology of the Cu seed layer. For thin Cu films ( $d_{Cu1} = 1.9$  nm, Figure 4.4 (a)), the STT-RAM stack is almost smooth with a mean grain size on the order of 20 nm and a mean grain height (trough to peak) of 1.6 nm. The SAF/Cu/FL films grown on thick Cu seed layers ( $d_{Cu1} = 30$  nm, Figure 4.4 (b)) are rough and have a mean grain size of  $\sim 40$  nm with a mean variation in grain height of 4 nm. The modulation of the multilayer height is then comparable to the thickness of the individual FM layers [118]. To further characterize the grain orientation in the STT-RAM stack as a function of the microstructure of the Cu seed layer, high-resolution TEM (HRTEM)

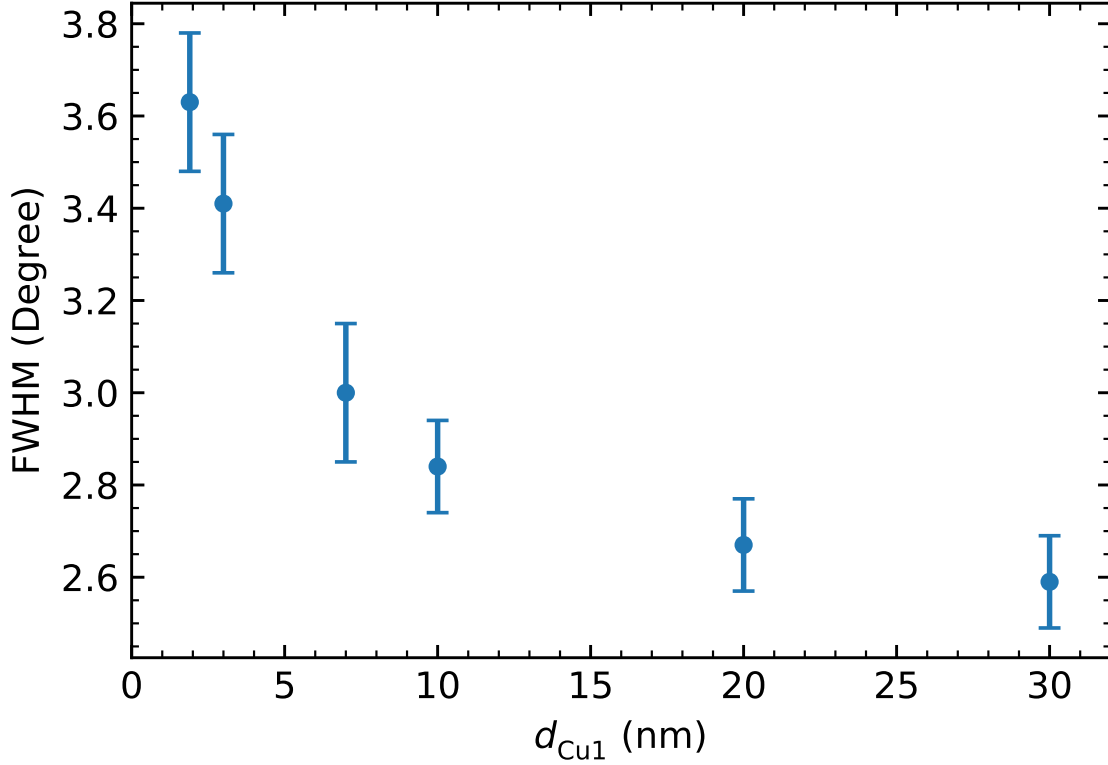


Figure 4.3: FWHM of Co/Ni (111) in Ta(3)/Cu( $d_{Cu}$ )/SAF /Cu/FL/Ta as a function of  $d_{Cu1} = 1.9, 3, 7, 10, 20$  and  $30$  nm. Error bars are determined from measuring 4 different samples with the same film structure

analysis is performed. In particular, Figure 4.4 (c) shows a HRTEM image obtained from the area marked with the black rectangle in Figure 3 (b). As indicated by the Fast Fourier Transforms (FFTs) in Figure 4.4 (d) and Figure 4.4 (e), which were calculated from the corresponding square areas marked in Figure 4.4 (c), the SAF/Cu/FL film stack grows with the same orientation as the subjacent Cu seed grain. In particular, both FFTs in Figure 4.4 (d) and Figure 4.4 (e) can be indexed with a zone axis pattern of a face-centered cubic structure having the (111) lattice planes parallel to the substrate surface, i.e. with the  $\langle 111 \rangle$  direction parallel to the substrate. This finding is in line with the XRD results showing that a preferred  $\langle 111 \rangle$  orientation of the Cu grains in the seed layer promotes a (111) texture in the overlying Co/Ni MLs.

#### 4.1.2 Optimizing the magnetic properties of the single Co/Ni multilayer

##### 1. Magnetic properties of as deposited Co/Ni multilayers:

To increase the storage density of magnetic memory while maintaining its thermal stability, the FL should have large anisotropy (see Equation 1.5). Therefore, it is foremost impor-



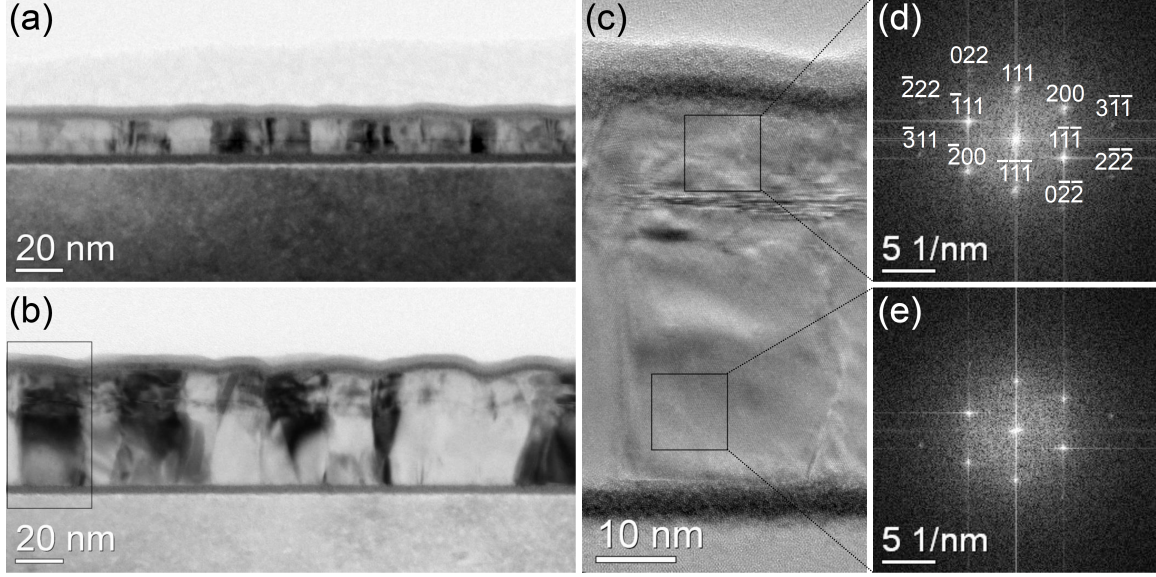


Figure 4.4: (a, b) Cross-sectional bright-field TEM images of the complete film structure, i.e. Si/Ta(3)/Cu( $d_{\text{Cu1}}$ )/SAF/Cu(3)/FL/Ta with SAF = FM1/Ru(0.38)/FM2, FM1 =  $4 \times [\text{Co}(0.21)/\text{Ni}(0.57)]/\text{Co}(0.4)$ , FM2 =  $\text{Co}(0.4)/3 \times [\text{Ni}(0.57)/\text{Co}(0.21)]/\text{Ni}(0.57)/\text{Co}(0.4)$ , and FL =  $\text{Co}(0.4)/3 \times [\text{Ni}(0.57)/\text{Co}(0.21)]/\text{Ni}(0.57)$ , where  $d_{\text{Cu1}} = 1.9$  nm in (a) and  $d_{\text{Cu1}} = 30$  nm in (b). (c) High-resolution TEM image of the rectangular area marked in (b). (d, e) Fast Fourier transforms are calculated from the corresponding two square areas marked in (c). Values in brackets are in nm.

tant to optimize the anisotropy of the magnetic layers. A schematic of the studied sample structure is shown in Figure 4.5.

**(i) Variation of  $d_{\text{Co1}}$  and  $d_{\text{Ni}}$  in the Co/Ni multilayers:** Girod *et al.* [56] have shown that the perpendicular magnetic anisotropy of Co/Ni MLs is maximized for  $d_{\text{Co1}} \sim 0.2$  nm and  $d_{\text{Ni}} \sim 0.6$  nm. To verify that their results apply to our multilayers, we have studied the anisotropy and saturation magnetization in a similar parameter regime ( $0.16 \text{ nm} \leq d_{\text{Co1}} \leq 0.26 \text{ nm}$ ,  $d_{\text{Ni}} = 0.48$  and  $0.58 \text{ nm}$ ).

Magnetic layers consisting of  $N_1 \times [\text{Co}(d_{\text{Co1}})/\text{Ni}(d_{\text{Ni}})]$  with  $N_1 = 8$ ,  $d_{\text{Co1}} = 0.16, 0.21$  and  $0.26 \text{ nm}$  and  $d_{\text{Ni}} = 0.48$  and  $0.58 \text{ nm}$  were grown on a seed layer of Ta/Cu(10 nm) using two different sputter deposition rates for both Co and Ni,  $0.01 \text{ nm/s}$  and  $0.05 \text{ nm/s}$ .

Figure 4.6 shows the saturation magnetization,  $M_s$ , as a function of the Co and Ni thickness at the two different rates. As expected  $M_s$  increases with increasing Co layer thickness as well as decreasing with Ni layer thickness. This is because, at room temperature, bulk Co has about three times larger  $M_s$  than bulk Ni:  $M_s(\text{Co}) = 1.44 \times 10^6 \text{ A/m}$ , and  $M_s(\text{Ni}) = 0.486 \times 10^6 \text{ A/m}$  [69]. To determine  $M_s(\text{Co})$  in our layers, we varied  $d_{\text{Ni}}$  and extrapolated the  $M_s$  value to  $d_{\text{Ni}} = 0$ .  $M_s(\text{Ni})$  was determined by varying  $d_{\text{Co1}}$  and extrapolating to  $d_{\text{Co1}} = 0$ . For the low deposition rate samples, the inferred saturation mag-



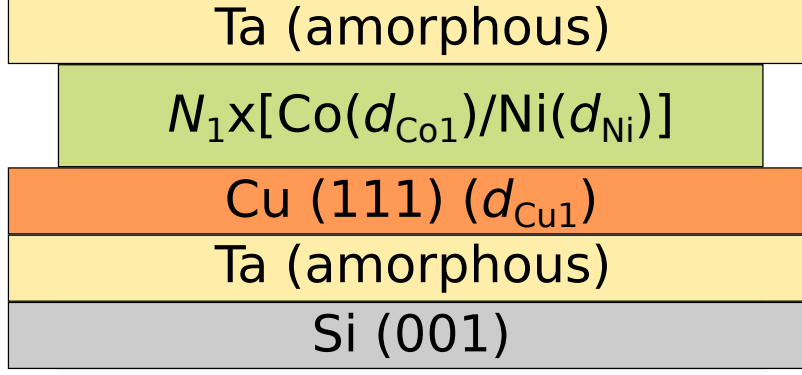


Figure 4.5: Schematic representation of the structure, Ta(3)/Cu( $d_{\text{Cu}1}$ )/ $N \times [\text{Co}(d_{\text{Co}1})/\text{Ni}(d_{\text{Ni}})]/\text{Ta}$ . Thicknesses,  $d_{\text{Cu}1}$ ,  $d_{\text{Co}1}$  and  $d_{\text{Ni}}$  are varied to optimize the perpendicular magnetic anisotropy.

netization of Ni is  $0.46 (\pm 0.04) \times 10^6$  A/m and of Co is  $1.02 (\pm 0.09) \times 10^6$  A/m. For the high deposition rate samples the inferred values are  $0.50 (\pm 0.04) \times 10^6$  A/m for Ni and  $1.07 (\pm 0.09) \times 10^6$  A/m for Co. Samples deposited at both high and low rates have a significantly reduced Co saturation magnetization compared to the bulk value of  $1.44 \times 10^6$  A/m. The results are in agreement with those of You *et al.* [119] who reported a reduction of the saturation magnetization of Co, with  $M_s(\text{Co}) = 1.06 (\pm 0.05) \times 10^6$  A/m. However, these results indicate that the presence of Co at the Ni interface does not alter the  $M_s$  of Ni, in contrast to the results of You *et al.* who found  $M_s(\text{Ni}) = 0.28 (\pm 0.03) \times 10^6$  A/m.

In addition, Figure 4.6 shows that  $M_s$  is larger for samples deposited at the higher sputtering rate. For high deposition rates, the duration of deposition of a 0.2 nm Co layer is about 4 seconds. To ensure the repeatability of the results, we made multiple samples with  $d_{\text{Co}1} = 0.21$  nm and  $d_{\text{Ni}} = 0.58$  nm at high deposition rates. The vertical error bars in Figure 4.6 indicate the standard deviation of  $M_s$ . The horizontal error bars denote the thickness variation as obtained *in-situ* from the thickness monitor.

Figure 4.7 shows the variation of perpendicular magnetic anisotropy,  $K_u$ , for samples of the form  $8 \times [\text{Co}(d_{\text{Co}1})/\text{Ni}(d_{\text{Ni}})]$ , with  $0.16 \text{ nm} \leq d_{\text{Co}1} \leq 0.26 \text{ nm}$ , and  $d_{\text{Ni}} = 0.48$  and  $0.58 \text{ nm}$ .  $K_u$  is obtained using SQUID magnetometry. The  $K_u$  of all investigated multilayers varies from  $4 \times 10^5 \text{ J/m}^3$  to  $4.6 \times 10^5 \text{ J/m}^3$ , and is maximized for  $d_{\text{Ni}} = 0.48 \text{ nm}$  (except for  $d_{\text{Co}1} = 0.16 \text{ nm}$ ). These  $K_u$  values are lower than those observed for a single crystal [56] and for polycrystalline [120] Co/Ni MLs deposited on a Au seed layer.  $K_u$  is similar to polycrystalline Co/Ni deposited on a Pt seed layer, [119] and comparable [117] or larger [121] than Co/Ni on Cu.

For designing the SAF and FL,  $d_{\text{Co}1} = 0.21 \text{ nm}$  and  $d_{\text{Ni}} = 0.58 \text{ nm}$ , which are nearly close to 1 and 3 monolayers of Co and Ni, respectively are chosen. In the rest of the thesis, Co and Ni will have the fixed thicknesses as Co =  $0.21 \text{ nm} = 1 \text{ AL}$  and Ni =  $0.58 = 3 \text{ AL}$  (AL = atomic layer) unless specified. (The distance between (111) planes in Co and Ni is

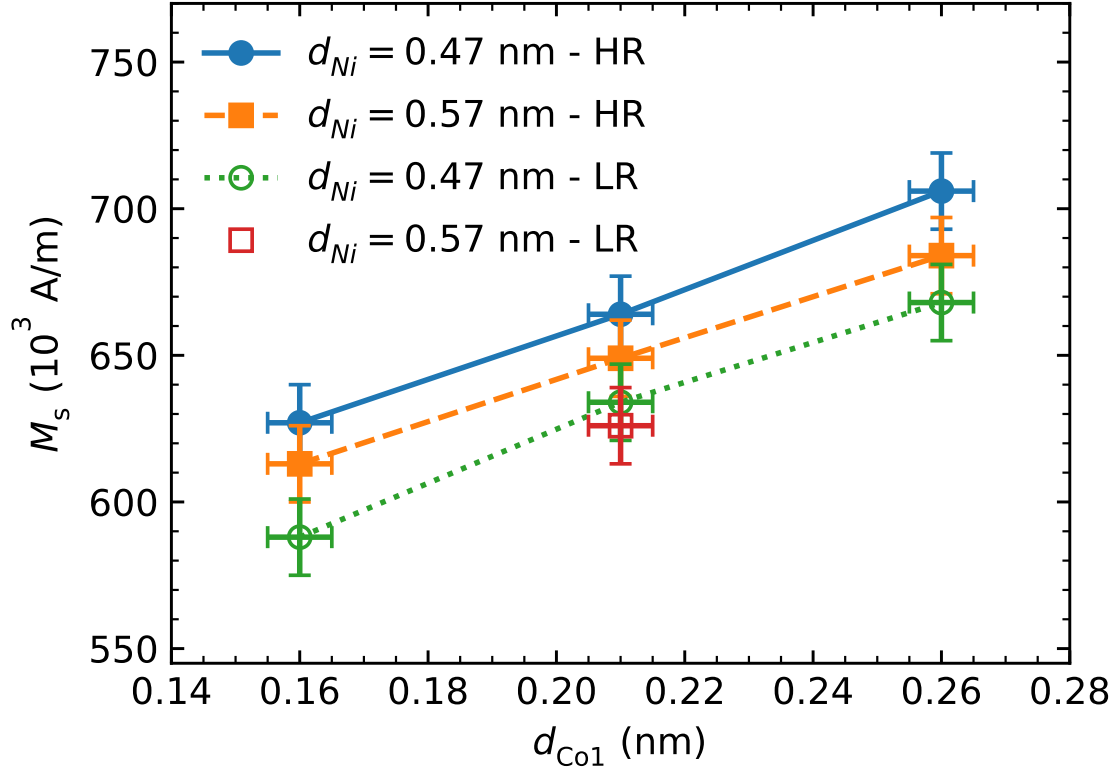


Figure 4.6: The dependence of  $M_s$  of Ta/Cu(10)/8×[Co( $d_{Co1}$ )/Ni( $d_{Ni}$ )]/Ta on  $d_{Co1}$ ,  $d_{Ni}$ , and on deposition rates (low rate, LR is 0.01 nm/s, high rate, HR, is 0.05 nm/s). SQUID measurements were performed at room temperature. Lines linking data points in this and subsequent figures are guides to the eye.

0.203 nm). Co and Ni were deposited at higher rates (0.05 nm/s) for the rest of the study to reduce the chance of incorporating foreign gas atoms. Furthermore, if these structures are to be used for the fabrication of magnetic devices, high deposition rates would be required for high volume production.

**(ii) Variation of  $N_1$ , number of bilayer repeats of Co/Ni multilayers with  $d_{Co1} = 0.21$  nm and  $d_{Ni} = 0.57$  nm:** The spin-polarized current required to switch the magnetization of the FL in nanopillars is proportional to the thickness of the FL [122, 123]. It is therefore important to minimize the number of Co/Ni layers, while at the same time maintaining enough thickness to keep the FL stable. For this reason, the dependence of  $K_u$  on the number of bilayers in Ta/Cu(10 nm)/ $N_1$ ×[Co(0.21)/Ni(0.58)]/Ta is investigated, by varying  $N_1$  from 4 to 32.  $K_u$  and  $M_s$  from SQUID magnetometry and  $K_u$  from FMR measurements are summarized in Figure 4.8.  $K_u$  and  $M_s$  sharply increase for  $4 \leq N_1 \leq 10$  and then gradually decrease for  $N_1 > 10$ . A similar trend in  $K_u$  has been reported by Qiu et al [124] in Co<sub>90</sub>Fe<sub>10</sub>/Pt superlattice structures and in Co/Ni MLs by Sabino et al [29].

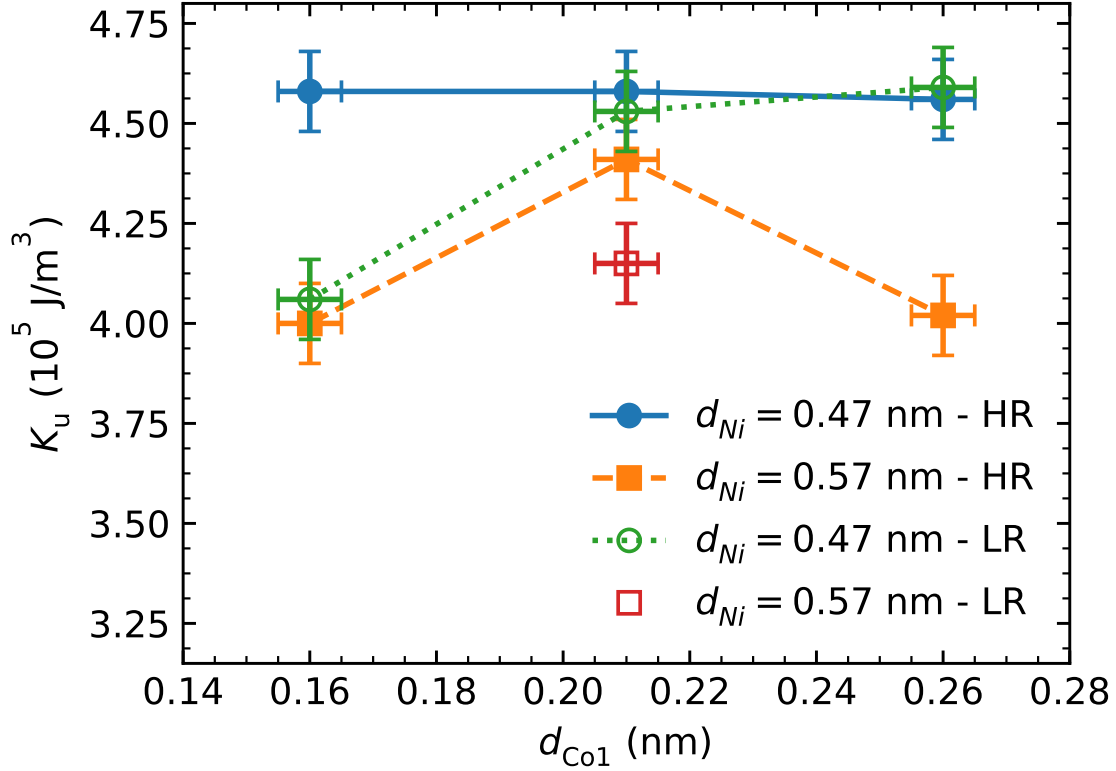


Figure 4.7: The dependence of  $K_u$  of Ta/Cu(10)/8×[Co( $d_{Co1}$ )/Ni( $d_{Ni}$ )]/Ta on  $d_{Co1}$ ,  $d_{Ni}$ , and on deposition rates (LR = 0.01 nm/s and HR = 0.05 nm/s).  $K_u$  was measured by SQUID at room temperature.

Figure 4.8 shows that the values of  $K_u$  inferred by FMR and SQUID techniques are, within error, the same.

The effective anisotropy of the FL was calculated using  $K_{eff}V = (K_u - \mu_0 M_s^2/2)V$ , where  $V$  is the volume of the FL. From the data presented in Figure 4.8 and the stability formula  $K_{eff}V/k_B T \geq 60$ , we find that 4 (or 6) multilayer Co/Ni films are adequate to fabricate thermally stable 26 (or 19) nm diameter nanopillars for use in STT-RAM.

The damping,  $\alpha$ , and zero-frequency line broadening,  $\Delta H_0$ , are also determined for films of the form Ta/Cu(10)/ $N_1$ ×[Co(0.21)/Ni(0.58)]/Ta, as a function of the number of bilayers,  $N_1$ .  $\alpha$  and  $\Delta H_0$  are obtained from the slope and intercept of the absorption line broadening as a function of frequency [109]. Figure 4.9 shows that  $\alpha$  decreases from 0.022 to 0.012 as the number of layers,  $N_1$ , is increased. To minimize the required switching currents in STT-RAM devices, it is important to reduce damping in the free magnetic layer [28, 39, ?].  $\mu_0 \Delta H_0$  sharply increases for  $N_1 \leq 8$  and gradually decreases for  $N_1 > 8$ .

**(iii) Variation of Cu seed layer thickness keeping  $N_1 = 8$ ,  $d_{Co1} = 0.21$  nm and  $d_{Ni} = 0.58$  nm:** Magnetic properties of films of the form Ta/Cu( $d_{Cu1}$ )/8×[Co(0.21)/Ni(0.58)]/Ta,

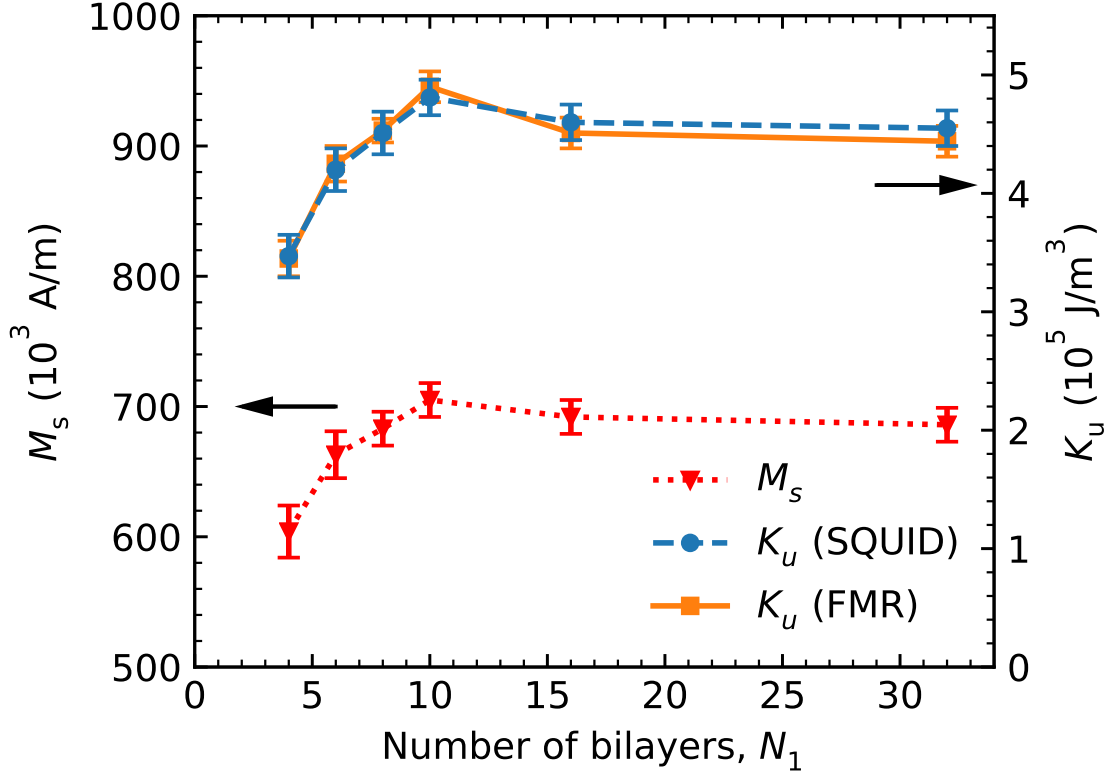


Figure 4.8: The dependence of  $K_u$  and  $M_s$  of Ta/Cu(10)/ $N_1 \times [\text{Co}(0.21)/\text{Ni}(0.58)]/\text{Ta}$  on the number of bilayers,  $N_1$ .  $K_u$  was measured by both SQUID ( $K_u(\text{SQUID})$ ) and FMR ( $K_u(\text{FMR})$ ). All measurements were performed at room temperature.

where  $d_{\text{Cu1}} = 1.9, 10$  and  $30$  nm, are summarized in Table 4.1.  $M_s$  and  $K_u$  are inferred from SQUID magnetometry. FMR with the applied field perpendicular to the plane of the sample was used to measure the anisotropy,  $K_u$ , zero field line broadening,  $\Delta H_0$ , and damping,  $\alpha$ , of the Co/Ni MLs with  $d_{\text{Cu1}} = 1.9$  and  $10$  nm. The magnetic properties of the Co/Ni multilayers with  $d_{\text{Cu1}} = 30$  nm cannot be accurately measured with FMR due to a large increase in the broadening of the absorption line.  $K_u$  obtained from SQUID and FMR are practically identical thus, in Table 4.1, we have included only  $K_u$  obtained from the SQUID measurements.

$d_{\text{Cu1}}$ [nm]	$M_s$ [kA/m]	$K_u$ [ $10^5$ J/m $^3$ ]	$\Delta H_0$ [kA/m]	$\alpha$
1.9(1)	677(13)	4.30(0.1)	6.4(3)	0.0156
10.0(3)	683(13)	4.51(0.1)	19.6(4)	0.0164
30.0(9)	703(13)	4.40(0.1)	-	-

Table 4.1: Magnetic moment and perpendicular magnetic anisotropy,  $K_u$  from SQUID magnetometry, zero field line broadening,  $\Delta H_0$  and damping,  $\alpha$ , from FMR measurements for Ta/Cu( $d_{\text{Cu1}}$ )/8 $\times$ [Co(0.21)/Ni(0.58)]/Ta with  $d_{\text{Cu1}} = 1.9, 10$  and  $30$  nm.

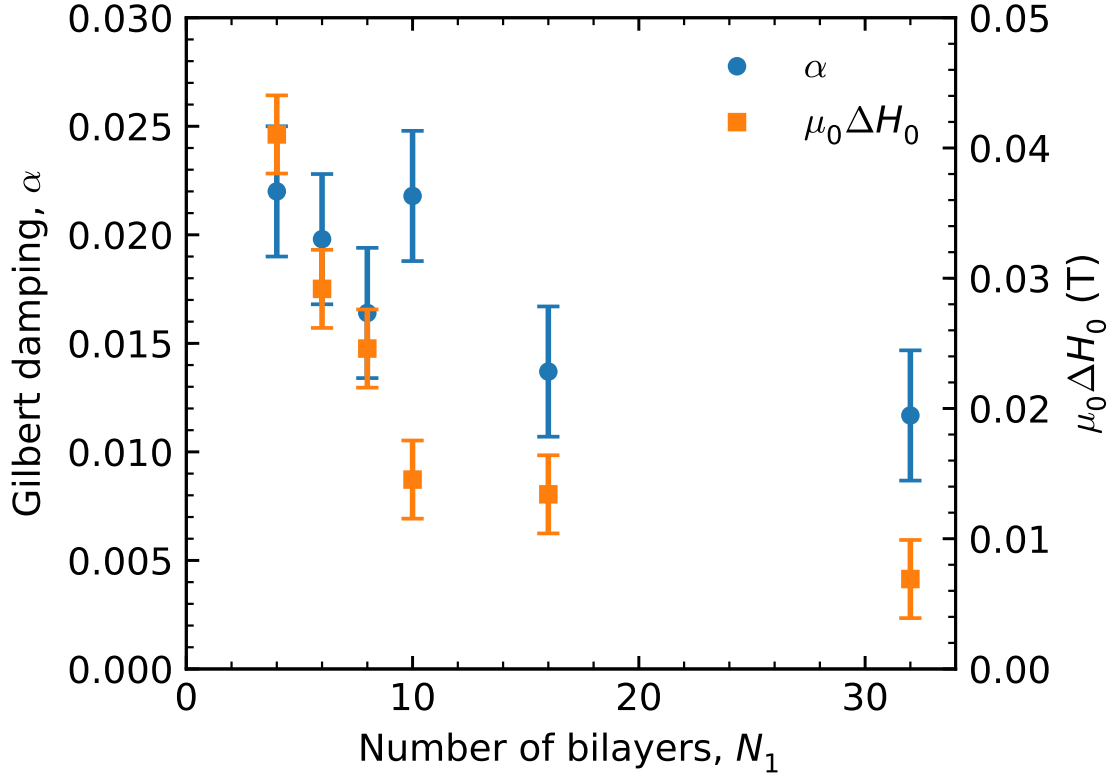


Figure 4.9: Dependence of damping,  $\alpha$ , and zero field offset,  $\Delta H_0$ , of Ta/Cu(10)/ $N_1 \times [\text{Co}(0.21)/\text{Ni}(0.58)]/\text{Ta}$  as a function of the number of bilayers,  $N_1$ . FMR measurements were performed at room temperature.

Table 4.1 shows that  $M_s$  and  $K_u$  of the Co(0.21)/Ni(0.58) MLs are not significantly affected by the changes in the Cu seed layer thickness, whereas  $\alpha$  gradually increases with Cu seed-layer thickness. Increasing Cu seed-layer thickness causes a strong increase of  $\Delta H_0$ .

When  $d_{\text{Cu1}}$  is increased from 1.9 to 30 nm, the (111) texture of the Co/Ni MLs improves, with the FWHM of the XRD rocking curve decreasing from  $3.6^\circ$  to  $2.6^\circ$ , as shown in Figure 4.3. At the same time, the grain size and film roughness increase by a factor of two as already discussed in section 4.1.1. Due to the increase in the grain size the direct exchange field between magnetic grains in Co/Ni MLs decreases. Direct exchange is expected to scale as  $1/d^2$ , where  $d$  is the distance between the grain centres, on average equal to the grain diameter. The exchange field can be written as [125]  $\mu_0 H_{\text{ex}} = (2A/M_s)k_{\text{eff}}^2 = (2A/M_s)(2\pi/d)^2$ . In continuous films, as in the case of our Co/Ni MLs, a fluctuation in the perpendicular anisotropy field is suppressed by the exchange field, resulting in the narrowing of the absorption lines in FMR. In Co/Ni MLs with a thick Cu seed layer, the exchange coupling is reduced leading to broadening of the absorption lines and an increase of the zero-frequency line broadening  $\Delta H_0$  due to the long-range inhomogeneity. Shaw et al. have

also observed that  $\Delta H_0$  of Co/Ni multilayers increases with an increase of the seed layer thickness [126].

## 2. Effect of annealing on magnetic properties of Co/Ni multilayers:

During the fabrication of nanopillars for STT-RAM, the film structures are heated to temperatures up to 473 K. For this reason, Ta(3)/Cu(10)/ $N_1 \times [\text{Co}(0.21)/\text{Ni}(0.58)]/\text{Ta}$  ( $N_1 = 4, 6, 8, 10, 16$  and 32) are annealed at 473 K for 15 minutes, to simulate the effects of fabrication. Figure 4.10 shows that both  $M_s$  and  $K_u$  of the Co/Ni multilayers remain unchanged after annealing at 473 K, suggesting that nanopillar fabrication will not alter the intrinsic properties of the magnetic multilayers when heated up to 473 K.

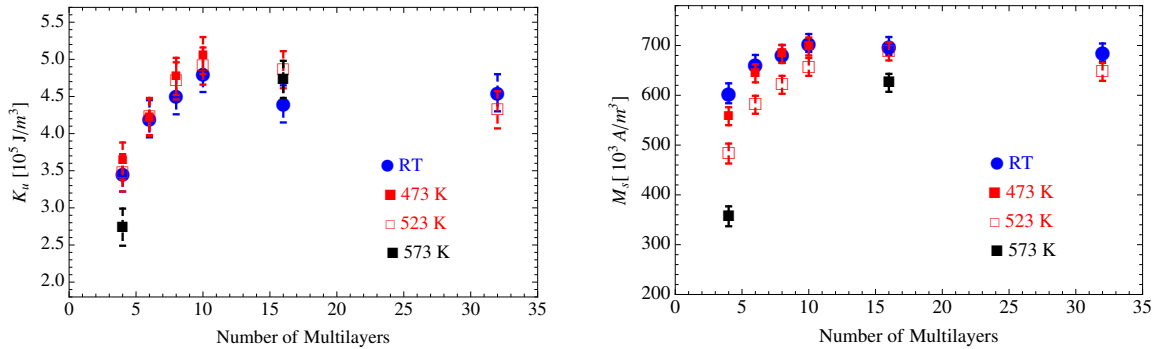


Figure 4.10: Dependence of (left)  $K_u$  and (right)  $M_s$  on the number of bilayers,  $N_1$ , in Ta/Cu(10)/ $N_1 \times [\text{Co}(0.21)/\text{Ni}(0.58)]/\text{Ta}$ . All the as-deposited films are subsequently annealed at 473 K, 498 K, 523 K and 548 K for 15 min.  $N_1 = 4$  and 16 are furthermore annealed at 573 K to ensure the fabrication process will not change their magnetic properties.

Figure 4.8 shows (left) the dependance of magnetic anisotropy,  $K_u$ , and (right) the saturation magnetization,  $M_s$  on the number of bilayer repeats,  $N_1$ , of as-deposited and annealed Ta/Cu/ $N_1 \times [\text{Co}(0.21)/\text{Ni}(0.58)]/\text{Ta}$ . Both  $M_s$  and  $K_u$  of as-deposited samples increases for  $N \leq 10$  and stays constant for higher  $N_1$ .  $K_u$  does not significantly change for the annealing temperatures up to 523 K, except it decreases for  $N = 4$ . For  $N = 16$ , it is practically not affected by the annealing temperatures up to 573 K. Figure 4.8 (right) shows that  $M_s$  remains unchanged for an annealing temperature of 473 K or below and decreases for higher annealing temperatures. This shows that annealing has much stronger effect on  $M_s$  than on  $K_u$ .

Figure 4.11 represents the normalized Polar MOKE measurements of Ta/Cu/ $N_1 \times [\text{Co}(0.21)/\text{Ni}(0.58)]/\text{Ta}$  ( $N_1 = 4$  and 16). The coercivity,  $\mu_0 H_c$ , of  $4 \times [\text{Co}/\text{Ni}]$  MLs increases and the slope of M(H) curve at  $\mu_0 H_c$  decreases with the increase of annealing temperatures (Figure 4.12 (left)). For  $N_1 = 16$ , the coercivity increases while the slope of M(H) curve at  $\mu_0 H_c$

does not change significantly with the increase in annealing temperatures (Figure 4.11 (right)).

For both  $N_1 = 4$  and 16, the increase in coercivity with annealing is about 0.22 T. The coercivity depends on the ratio of  $K_u/M_s$  and the exchange coupling between magnetic grains,  $\mu_0 H_{ex}$ . Since  $K_u$  does not significantly change with annealing and  $M_s$  decreases with annealing. The increase in coercivity is in part due to the increase of  $K_u/M_s$  with annealing temperatures. Although, this cannot explain the total increase in coercivity.

The cross-section TEM quantitative analyses [127] show that Cu diffuses into Co/Ni MLs along the grain boundaries decreasing the exchange coupling between grains and increasing probability of uniform reversal of the individual grains. As individual magnetic grains reverse the demagnetizing field,  $H_{demag}$ , acting on the magnetic grains that are not reversed is changing.  $H_{demag}$  first decreases as the external field approaches  $H_c$ , at  $H_c$  the  $H_{demag}$  is 0, and then changes direction and increases until all magnetic grains are reversed. Thus, if the magnetic grains are completely decoupled the magnetic field required to reverse the first few magnetic grains in the film is  $H_c - H_{demag}$  ( $H_{demag}$  helps external magnetic field to reverse magnetic grains) while the field required to reverse the last few magnetic grains in the film is  $H_c + H_{demag}$  ( $H_{demag}$  opposes the external field). This causes increase in the slope of M(H) curve at  $H_c$ . In addition  $H_c$  increases if the mechanism of the magnetization reversal changes from nonuniform (grains in the film strongly coupled) to uniform (grains fully decoupled) [128].

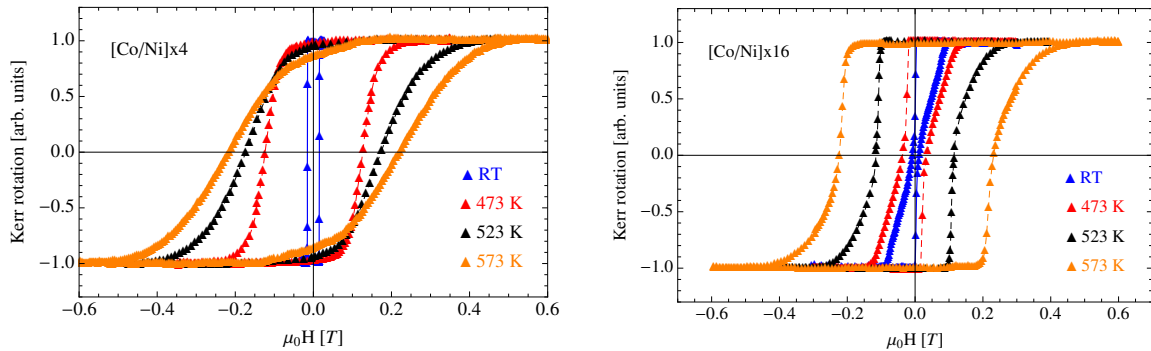


Figure 4.11: Normalized Polar MOKE measurements of (left): Ta(3)/Cu/4×[Co(0.21)/Ni(0.58)]/Ta and, (right): Ta(3)/Cu/16×[Co(0.21)/Ni(0.58)]/Ta at room temperature and annealed at 473 K, 498 K, 523 K, 548 K and 573 K.

To further confirm that Cu diffusion causes the increase in coercivity of Co/Ni MLs, 4×[Co(0.21)/Ni(0.58)] MLs are grown on Ta/Ru as a seed layer. Ru stimulates the necessary fcc(111) orientation in Co/Ni MLs [129] but is not expected to diffuse in Co/Ni grain boundary [130]. Figure 4.12 shows the Polar MOKE data of Ta/Ru/4×[Co(0.21)/Ni(0.58)]/Ta measured at room temperature, 523 K and 573 K. After annealing at 573 K, the coercivity of Co/Ni MLs increases from 0.01 to 0.045 T, which is almost five times smaller than the

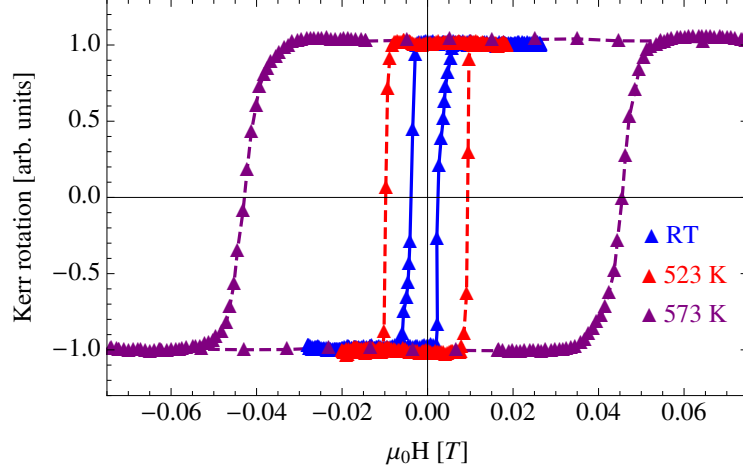


Figure 4.12: Polar MOKE measurements of, (left): Ta(3)/Ru/4×[Co(0.21)/Ni(0.58)]/ Ta(4) measured at room temperature, annealed at 523 K and 573 K.

coercivity of Co/Ni MLs with Cu seed layer. The slope of the Kerr loop does not change significantly. An insignificant change in slope indicates that Ru does not diffuse much into the Co/Ni MLs. Nevertheless, a small increase in coercivity could be due to the improvement of Ru/[Co/Ni] interface or due to the removal of defects in Co/Ni MLs. These results are consistent with the findings of Liu et al. [131]. A supporting STEM data showing the increase of coercivity in Co/Ni MLs is due to Cu diffusion is presented elsewhere by Coutts et al. [127].

#### 4.1.3 Optimizing the magnetic properties of the SAF layer

The full structure is composed of a synthetic antiferromagnet (SAF) that is decoupled from the free layer (FL) with a Cu spacer layer: SAF/Cu/FL. In this structure, (see Figure 4.1) the SAF consists of two Co/Ni ML antiferromagnetically coupled across a Ru spacer layer, and the FL consists of a single Co/Ni ML. The coupling strength between the two Co/Ni MLs in the SAF is optimized by varying the thickness of the Ru spacer layer,  $d_{Ru}$ , and the  $d_{Co2}$  thickness (see Figure 4.1). The SAF has the following structure: FM1/Ru( $d_{Ru}$ )/FM2, where FM1 =  $N_1 \times [\text{Co}(d_{Co1})/\text{Ni}(d_{Ni})]/\text{Co}(d_{Co2})$  and FM2 =  $\text{Co}(d_{Co2})/N_2 \times [\text{Ni}(d_{Ni})/\text{Co}(d_{Co1})]/\text{Ni}(d_{Ni})/\text{Co}(d_{Co3})$ .

High thermal stability as well as resistance to external magnetic fields and spin-polarized currents are important characteristics of the hard magnetic layer that is used as a reference layer in STT-RAM devices. He *et al.* [132] have shown that the synthetic antiferromagnets in which two ferromagnetic layers are antiferromagnetically coupled through a nonmagnetic layer such as Ru have much better stability as a reference layer than a single magnetic layer of comparable thickness. The increase in stability of SAF as a function of exchange



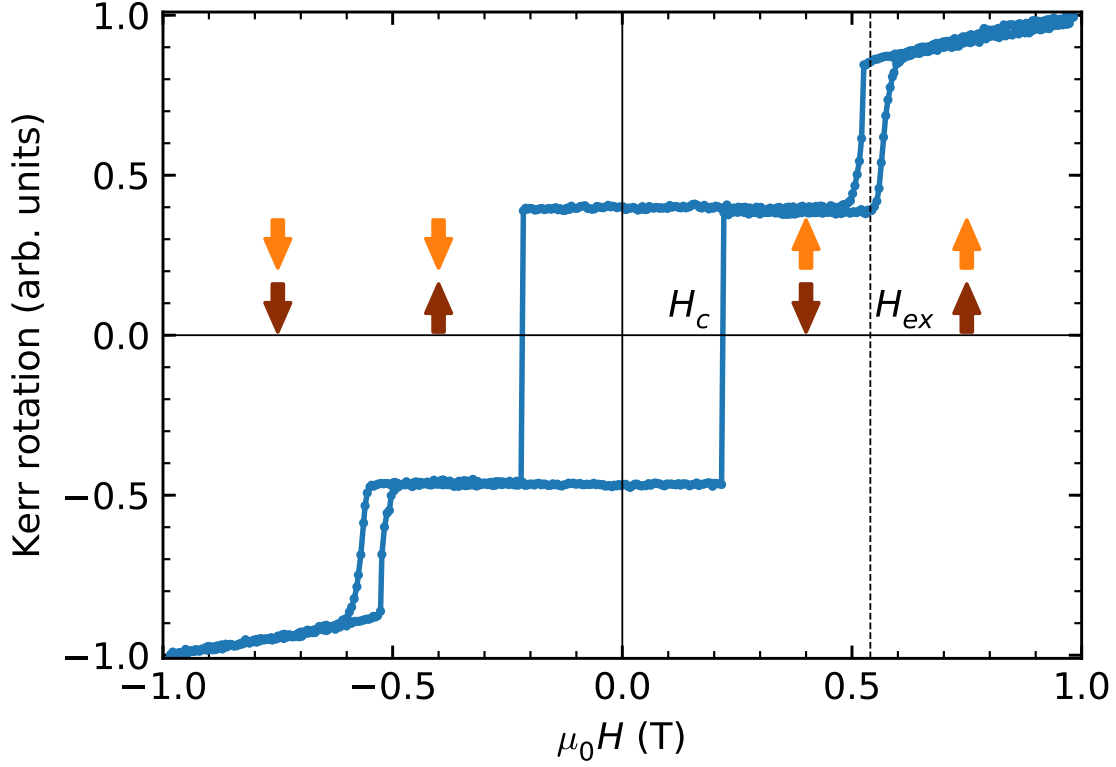


Figure 4.13: Polar MOKE data for a film with structure Ta/Cu(10)/FM1/Ru(0.38)/FM2/Ta (with FM1 =  $6 \times [\text{Co}(0.21)/\text{Ni}(0.58)]/\text{Co}(0.4)$  and FM2 =  $\text{Co}(0.4)/8 \times [\text{Ni}(0.58)/\text{Co}(0.21)]/\text{Ni}(0.58)$ ), showing the reversal of individual magnetic layers with magnetic field.  $H_{\text{ex}}$  is used to calculate the exchange coupling between ferromagnetic layers across the Ru spacer. The switching order of the layers is indicated by the arrows for a field ramping from positive to negative values. The orange and red arrows represent the the bottom and top magnetic layers of the SAF, respectively.

coupling has been calculated by Richter *et al.* [133, 134]. Furthermore, the antiferromagnetic arrangement significantly reduces the dipolar interaction between the hard and free layers [28]. This can lead to a smaller difference between critical current densities for switching the free layer between parallel and antiparallel alignment with the hard layer. A SAF layer is also less sensitive to spin-torque excitation [28, 135].

Building on the results obtained in the previous section, we deposited a SAF structure of the form Ta/Cu(10)/FM1/Ru( $d_{\text{Ru}}$ )/FM2/Ta, where FM1 =  $N_1 \times [\text{Co}(0.21)/\text{Ni}(0.58)]/\text{Co}(d_{\text{Co}2})$  and FM2 =  $\text{Co}(d_{\text{Co}2})/N_2 \times [\text{Ni}(0.58)/\text{Co}(0.21)]/\text{Ni}(0.58)/\text{Co}(d_{\text{Co}3})$ , with  $N_1$  and  $N_2$  the respective number of bilayers. The films were deposited at high rates as discussed above. The thickness of the Ru spacer layer,  $d_{\text{Ru}}$ , was varied between 0.38 nm and 2.1 nm to determine the optimal thickness for antiferromagnetic coupling and high coercivity.

The exchange coupling,  $J_{\text{ex}}$ , is given by  $J_{\text{ex}} = M_s H_{\text{ex}} d$ , where  $M_s$  is the saturation magnetization,  $d$  is the thickness of the Co/Ni layer that is switched by the external field (in this

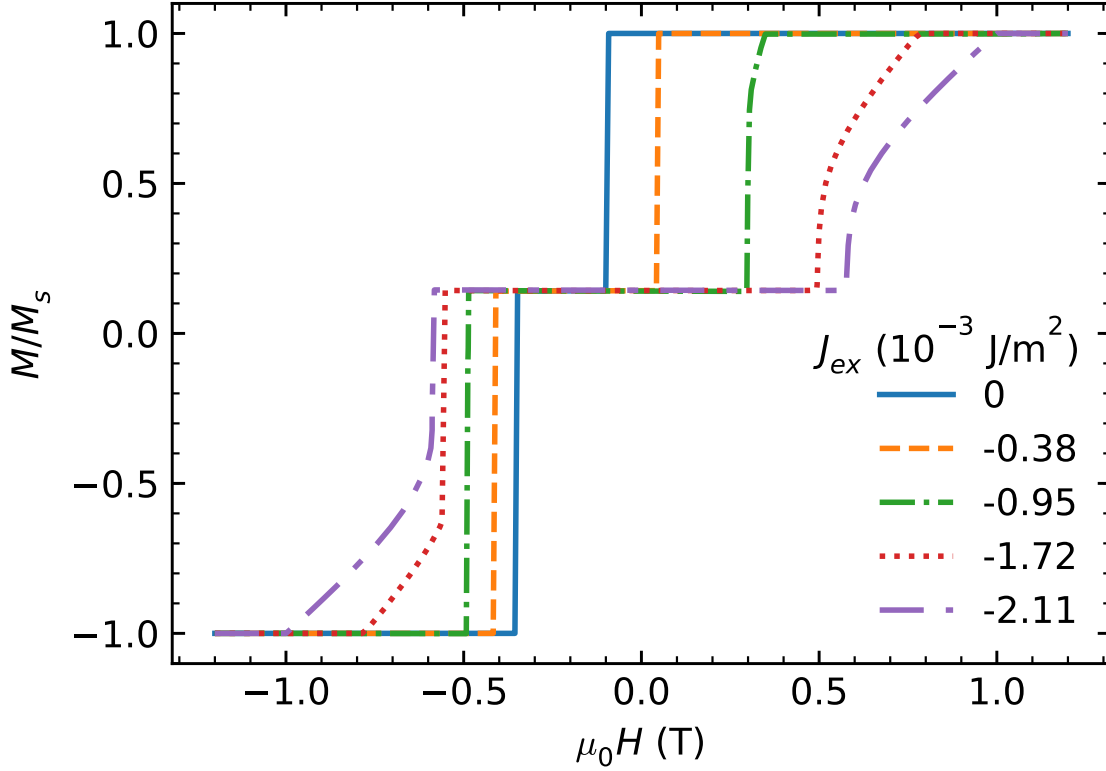


Figure 4.14: Calculated magnetization curves for different exchange couplings, for the FM1/Ru( $d_{\text{Ru}}$ )/FM2 layers. Calculations were performed with parameters derived from films with FM1 =  $6 \times [\text{Co}(0.21)/\text{Ni}(0.58)]/\text{Co}(0.4)$ ,  $d_{\text{Ru}} = 0.38$  to  $2.1$  nm, and FM2 =  $\text{Co}(0.4)/8 \times [\text{Ni}(0.58)/\text{Co}(0.21)]/\text{Ni}(0.58)$ .

case the thinner layer), and  $H_{\text{ex}}$  is the field at which the SAF switches from antiferromagnetic to ferromagnetic alignment. This field was determined by polar MOKE measurements, an example of which is shown in Figure 4.13. The coercive field,  $H_c$ , is the field at which the magnetization of the SAF is equal to zero, as shown in Figure 4.13. In order to measure the ferromagnetic coupling between FM1 and FM2, one of the ferromagnetic layers should have significantly larger anisotropy field and total magnetic energy [136]. Since anisotropies and  $M_s$  of both FM1 and FM2 are nearly equal, we could not measure the ferromagnetic coupling in AFC structure. Therefore, for these structures we kept  $j_{\text{ex}} = 0$ .

To interpret the measurements of the SAF and to determine its ideal behaviour, PhD student Nicholas Lee Hone has modelled the SAF using a coherent rotation model. The magnetizations of the two layers are given, respectively, by  $\mathbf{M}_i = M_{s,i} \mathbf{m}_i$ , where  $\mathbf{m}_i$  is a unit vector representing the direction of the magnetization,  $M_{s,i}$  is the saturation magnetization, and  $i = 1, 2$ . The reversal of the SAF layer is simulated by solving the Landau–Lifshitz–

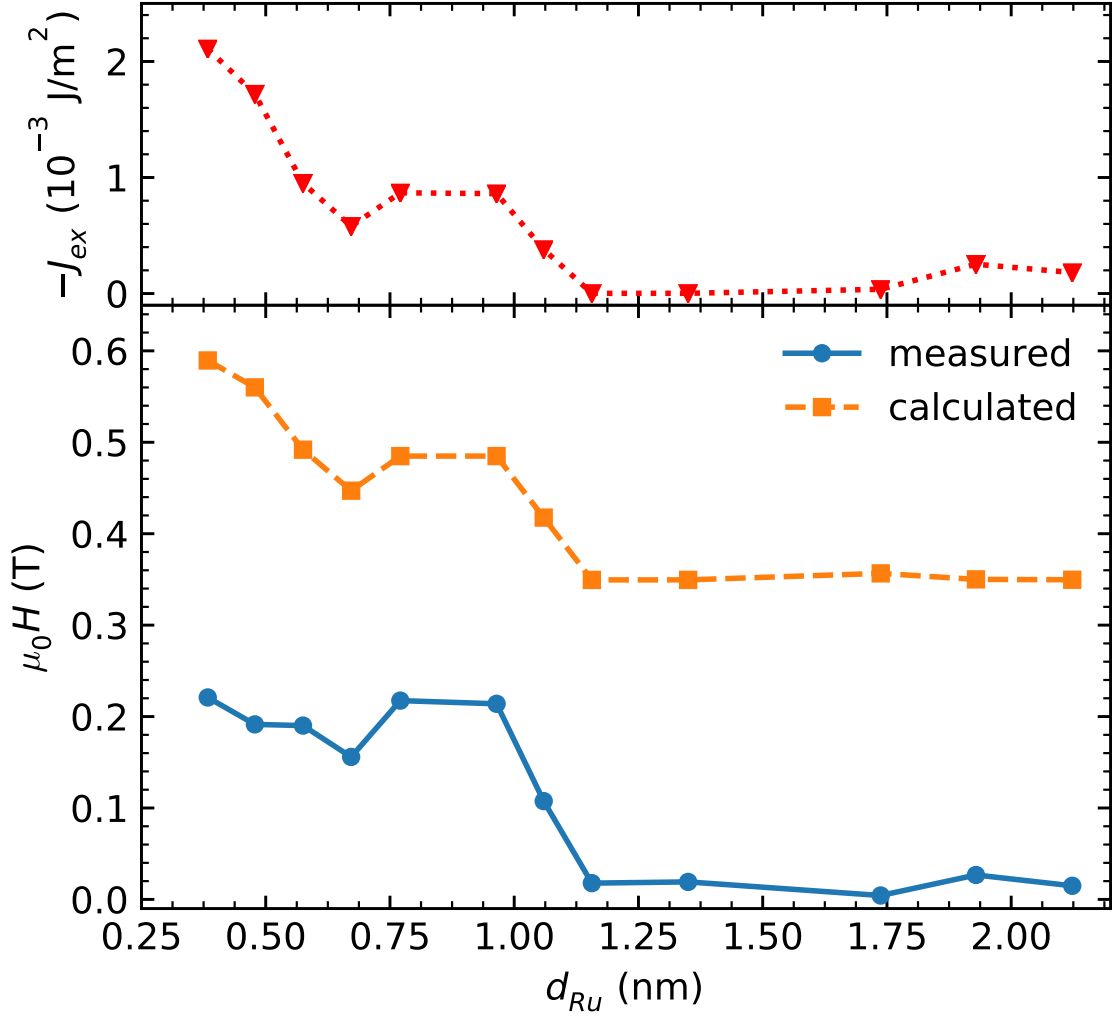


Figure 4.15: Oscillation of the exchange coupling between FM1 and FM2 in the SAF (red triangles), the coercive field of the SAF (blue circles), and the calculated coercive field (orange squares) as a function of Ru spacer-layer thickness. The structure is Ta/Cu(10)/FM1/Ru( $d_{Ru}$ )/FM2/Ta (with FM1 = 6×[Co(0.21)/Ni(0.58)]/Co(0.4) and FM2 = Co(0.4)/8×[Ni(0.58)/Co(0.21)]/Ni(0.58)). The negative value of  $J_{ex}$  indicates antiferromagnetic coupling of the FM1 and FM2 layers.

Gilbert (LLG) equation:

$$\frac{d\mathbf{M}_i}{dt} = -\frac{|\gamma|}{1+\alpha^2}\mathbf{M}_i \times \mu_0\mathbf{H}_{\text{eff},i} - \frac{\alpha|\gamma|}{1+\alpha^2}\frac{\mathbf{M}_i}{M_{s,i}} \times (\mathbf{M}_i \times \mu_0\mathbf{H}_{\text{eff},i}) \quad (4.1)$$

where  $\alpha$  is the Gilbert damping,  $\gamma$  is the gyromagnetic ratio, and the effective field is given by

$$\mu_0\mathbf{H}_{\text{eff},i} = -\frac{1}{M_{s,i}}\frac{\partial e_{\text{tot}}}{\partial \mathbf{m}_i}. \quad (4.2)$$

Here, the total magnetic Gibbs free energy is

$$e_{\text{tot}} = \sum_{i=1}^2 (e_{Z,i} + e_{K,i} + e_{\text{sh},i} + e_{\text{dd},i}) + e_{\text{ex}} . \quad (4.3)$$

The dipole–dipole energy ( $e_{\text{dd},i}$ ) vanishes, since the films are modelled as infinite planes. The shape anisotropy energy ( $e_{\text{sh},i}$ ), perpendicular anisotropy energy ( $e_{K,i}$ ), Zeeman energy ( $e_{Z,i}$ ) and exchange interaction energy ( $e_{\text{ex}}$ ) are given, respectively, by

$$e_{\text{sh},i} = -\frac{\mu_0 M_{s,i}^2}{2} (N_{\perp} - N_{\parallel}) (\mathbf{m}_i \cdot \mathbf{n})^2 d_i / d_1 \quad (4.4)$$

$$e_{K,i} = -K_{u,i} (\mathbf{m}_i \cdot \mathbf{u})^2 d_i / d_1 \quad (4.5)$$

$$e_{Z,i} = -\mathbf{M}_{s,i} \cdot \mu_0 \mathbf{H} d_i / d_1 \quad (4.6)$$

$$e_{\text{ex}} = -J_{\text{ex}} \mathbf{m}_1 \cdot \mathbf{m}_2 / d_1 , \quad (4.7)$$

where  $K_{u,i}$  is the perpendicular magnetic anisotropy energy,  $\mathbf{u}$  is the perpendicular anisotropy easy axis,  $J_{\text{ex}}$  is the exchange coupling between the two magnetic layers,  $N_{\perp}$  and  $N_{\parallel}$  are the demagnetizing factors in the plane and along the axis perpendicular to the plane ( $N_{\perp} = 1$  and  $N_{\parallel} = 0$  for films), and  $\mathbf{n}$  is the direction normal to the sample plane. The thickness of the top layer is  $d_1$ , and the thickness of the bottom layer is  $d_2$ . Note that the energies are normalized to the thickness of the top layer.

To simulate magnetization loops, at each field step the applied field,  $\mathbf{H}$ , is set and then the magnetization evolved with the LLG equation until subsequent changes in magnetization are smaller than a predetermined threshold. Simulation of the magnetization reversal of two coupled single domain magnetic grains were discussed by Richter et al. [133, 134, 137].

$M(H)$  curves for an idealized SAF have been calculated with the coherent rotation model presented in the simulation section, using the values of  $J_{\text{ex}}$  determined experimentally for  $d_{\text{Ru}}$  ranging from 0.38 to 2.10 nm. The results of the simulations are shown in Figure 4.14 and the coercivity determined from the model is shown by the diamond symbols in Figure 4.15. Figure 4.15 also shows the exchange coupling  $J_{\text{ex}}$  and coercivity  $H_c$  as a function of Ru thickness, for  $N_1 = 6$  and  $N_2 = 8$ ,  $d_{\text{Co}2} = 0.4$  nm, and  $d_{\text{Co}3} = 0$ . The maximum antiferromagnetic coupling field between FM1 and FM2 was around 0.221 T for  $d_{\text{Ru}} = 0.38$  nm.

It is readily observed that the coercivity is much lower in the experimental films than in the simulation. In particular, when the exchange coupling goes to zero, there is a large non-zero coercivity in the simulations ( $\geq 0.35$  T) in contrast with the small coercivity ( $\leq 0.02$  T) observed in the experiments. This is an indication that the measured films have nucleation centers that allow the SAF reversal to occur at lower fields.

Figure 4.15 shows that the simulated coercivity follows the shape of the exchange coupling  $J_{\text{ex}}$  quite closely. Our experimental data show a similar behaviour for  $d_{\text{Ru}} \geq 0.6$  nm, but for  $d_{\text{Ru}} \leq 0.6$  nm the coupling increases from  $\sim 0.08$  to  $0.21$  J/m<sup>2</sup> without a significant increase in the coercivity. In order to understand why  $H_c$  does not scale with  $J_{\text{ex}}$  for  $d_{\text{Ru}} \leq 0.6$  nm, SAF structures with  $d_{\text{Ru}} = 0.38$  nm and  $0.77$  nm were deposited on seed layers with thicknesses,  $d_{\text{Cu1}}$ , varying from  $1.9$  to  $30$  nm. The selected SAF has a structure of the form Ta/Cu( $d_{\text{Cu1}}$ )/FM1/Ru( $d_{\text{Ru}}$ )/FM2/Ta (with FM1 =  $4 \times [\text{Co}(0.21)/\text{Ni}(0.58)]/\text{Co}(0.4)$  and FM2 =  $\text{Co}(0.4)/3 \times [\text{Ni}(0.58)/\text{Co}(0.21)]/\text{Ni}(0.58)/\text{Co}(0.4)$ ). Due to the small difference in the total magnetization of the two ferromagnetic layers in the SAF, the coercivity is maximized. For this reason this is the ideal structure for STT-RAM and is used as our final design of the SAF layer.

Figure 4.16 shows that for both  $d_{\text{Ru}} = 0.38$  and  $0.77$  nm, the coercivity increases with increasing Cu seed-layer thickness. However, the increase is less pronounced for the thicker Ru, which results in a smaller coupling. It follows that the coercivity,  $H_c$ , of the SAF scales with  $J_{\text{ex}}$  for thicker Cu seed layers. As the thickness of the Cu seed layer increases, the grain size of the Co/Ni multilayers increases causing a reduction in the direct exchange interaction between magnetic grains [125]. Crew *et al.* [128] and Girt *et al.* [138] have shown that the coercivity can increase by almost a factor of three with decreasing coupling between magnetic grains. In samples with strong direct exchange coupling, domain wall motion involves several grains. However, when the intergrain exchange coupling is weak or absent then uniform reversal of individual grains dominates, resulting in an increased coercivity. The reversal occurs grain by grain and resembles the behaviour of isolated Stoner–Wohlfarth particles [139]. This explains the increased coercivity observed in our films for thick Cu seed layers.

Girt *et al.* [136] have studied a SAF consisting of FM1/Ru/FM2, where FM1 =  $12 \times [\text{Co}/\text{Pt}]/\text{Co}$ , FM2 =  $4 \times [\text{Pt}/\text{Co}]$  and FM1 was deposited at a higher deposition pressure. This higher pressure ensures a reduced coupling between the magnetic grains in FM1. The results of that study show that the coercivity of the SAF scales with  $J_{\text{ex}}$ , as predicted by the coherent rotation model, if the interaction between magnetic grains within each magnetic film is reduced. The intrinsic magnetic properties of Co/Ni multilayers,  $K_u$  and  $M_s$ , do not depend on  $d_{\text{Cu1}}$  for  $d_{\text{Cu1}} \leq 10$  nm, see Table 4.1, and thus do not contribute to the observed change of  $H_c$ .

Figure 4.16 also shows that the coercive field of a single magnetic layer structure, Ta/Cu( $d_{\text{Cu1}}$ )/FM1/Ta (FM1 =  $8 \times [\text{Co}(0.21)/\text{Ni}(0.58)]$ ), increases with increasing Cu seed layer thickness. For  $d_{\text{Cu1}} = 30$  nm,  $H_c$  of the single magnetic layer, FM1, is  $0.039$  T, which is 5% of the value calculated from the coherent rotation model. On the other hand, in SAF films the largest measured coercivity,  $H_c = 0.485$  T, is more than 50% of that obtained from the coherent model. For both the single magnetic layer and the SAF,  $H_c$  increases about four times with increasing  $d_{\text{Cu1}}$  from  $1.9$  to  $30$  nm.

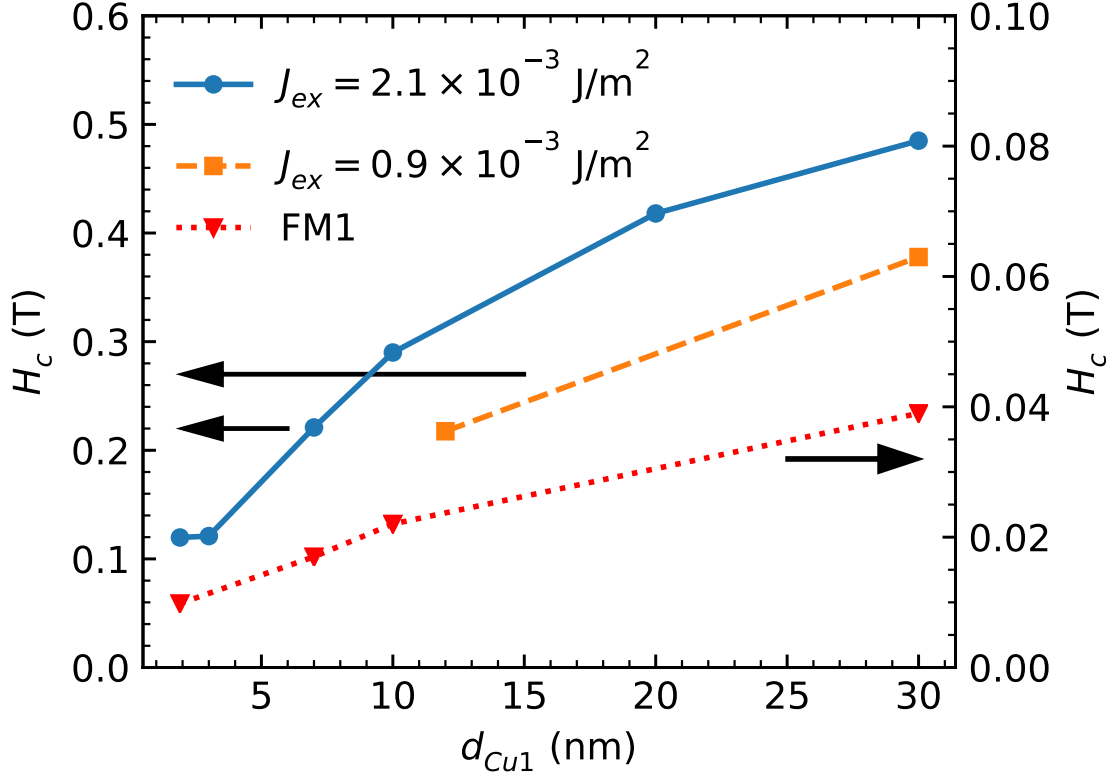


Figure 4.16: Dependence of coercivity on the seed layer thickness in Ta/Cu( $d_{Cu1}$ )/SAF/Ta (with FM1 =  $4 \times [\text{Co}(0.21)/\text{Ni}(0.58)]/\text{Co}(0.4)$ ,  $d_{Ru} = 0.38$  and  $0.77$  nm, and FM2 =  $\text{Co}(0.4)/3 \times [\text{Ni}(0.58)/\text{Co}(0.21)]/\text{Ni}(0.58)/\text{Co}(0.4)$ ) (blue circles and orange squares), and Ta/Cu( $d_{Cu1}$ )/FM1/Ta (with FM1 =  $8 \times [\text{Co}(0.21)/\text{Ni}(0.58)]$ ) (red triangles).

To further optimize the antiferromagnetic coupling strength, we varied the thickness,  $d_{Co2}$ , of the Co layer that surrounds the Ru spacer layer. Six more samples of the series Ta/Cu(10)/FM1/Ru(0.38)/FM2/Ta, where FM1 =  $6 \times [\text{Co}(0.21)/\text{Ni}(0.58)]/\text{Co}(d_{Co2})$  and FM2 =  $\text{Co}(d_{Co2})/8 \times [\text{Ni}(0.58)/\text{Co}(0.21)]/\text{Ni}(0.58)$  were deposited with  $d_{Co2}$  varying from  $0.1$  nm to  $0.8$  nm. The antiferromagnetic exchange coupling,  $-J_{ex}$ , increased with increasing Co thickness, and saturated for  $d_{Co2} \sim 0.6$  nm, as seen in Figure 4.17. Having a thick Co layer reduces the anisotropy of the Co/Ni multilayers, so we decided to keep  $d_{Co2} = 0.4$  nm, which only reduces the coupling by  $\sim 10\%$  compared to the maximum coupling strength.

#### 4.1.4 Full structure optimization and GMR

For use in STT-RAM, the SAF and FL have to be magnetically decoupled in the absence of current, which is achieved with a Cu spacer layer since the GMR effect is large in Co/Cu multilayers. The minimum thickness of Cu required to decouple the SAF and FL was therefore determined. It is also important to maximize the percentage GMR, defined as  $(R_H - R_0)/R_0 \times 100$ , where  $R_H$  is the resistance in a magnetic field  $H$  and  $R_0$  is the

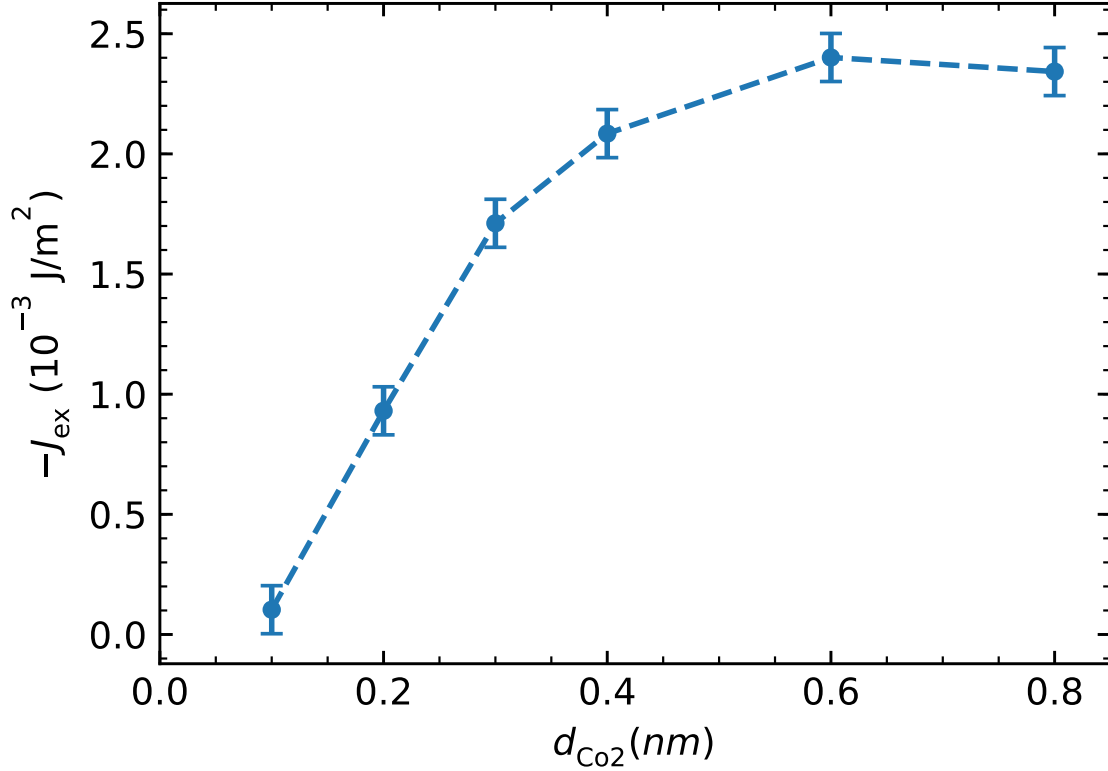


Figure 4.17: The exchange coupling between FM1 and FM2 in Ta/Cu(10)/FM1/Ru(0.38)/FM2/Ta (with FM1 =  $6 \times [\text{Co}(0.21)/\text{Ni}(0.58)]/\text{Co}(d_{\text{Co}2})$  and FM2 =  $\text{Co}(d_{\text{Co}2})/8 \times [\text{Ni}(0.58)/\text{Co}(0.21)]/\text{Ni}(0.58)$ ) as a function of the thickness of the Co layers adjacent to the Ru layer,  $d_{\text{Co}2}$ . The negative value of  $J_{\text{ex}}$  indicates antiferromagnetic coupling of FM1 and FM2 layers.

resistance at  $H = 0$ . For this part of the optimization, the effect of  $d_{\text{Cu}2}$  and  $d_{\text{Co}3}$  on GMR was also studied.

The optimal form of the film structure shown in Figure 4.1 consists of Ta/Cu( $d_{\text{Cu}1}$ )/SAF/Cu( $d_{\text{Cu}2}$ )/FL/Ta, with SAF = FM1/Ru( $d_{\text{Ru}}$ (0.38))/FM2, FM1 =  $4 \times [\text{Co}(0.21)/\text{Ni}(0.58)]/\text{Co}(0.4)$ , FM2 =  $\text{Co}(0.4)/3 \times [\text{Ni}(0.58)/\text{Co}(0.21)]/\text{Ni}(0.58)/\text{Co}(d_{\text{Co}3})$ , and FL =  $\text{Co}(d_{\text{Co}3})/3 \times [\text{Ni}(0.58)/\text{Co}(0.21)]/\text{Ni}(0.58)$ . In STT-RAM devices it is the free layer, FL, that serves to record information. For this to work, the free layer must be decoupled from the hard layer, which is achieved using a Cu spacer layer.

Increasing the thickness of the Cu seed layer,  $d_{\text{Cu}1}$ , increases the roughness [126] and the coercivity of the SAF (see Figure 4.16). The increase in roughness of the seed layer also affects the interaction between the SAF and FL across the Cu spacer layer, and therefore the seed layer thickness should be minimized. However, the SAF's coercivity should be sufficiently large to measure the ferromagnetic coupling strength between the SAF and FL.

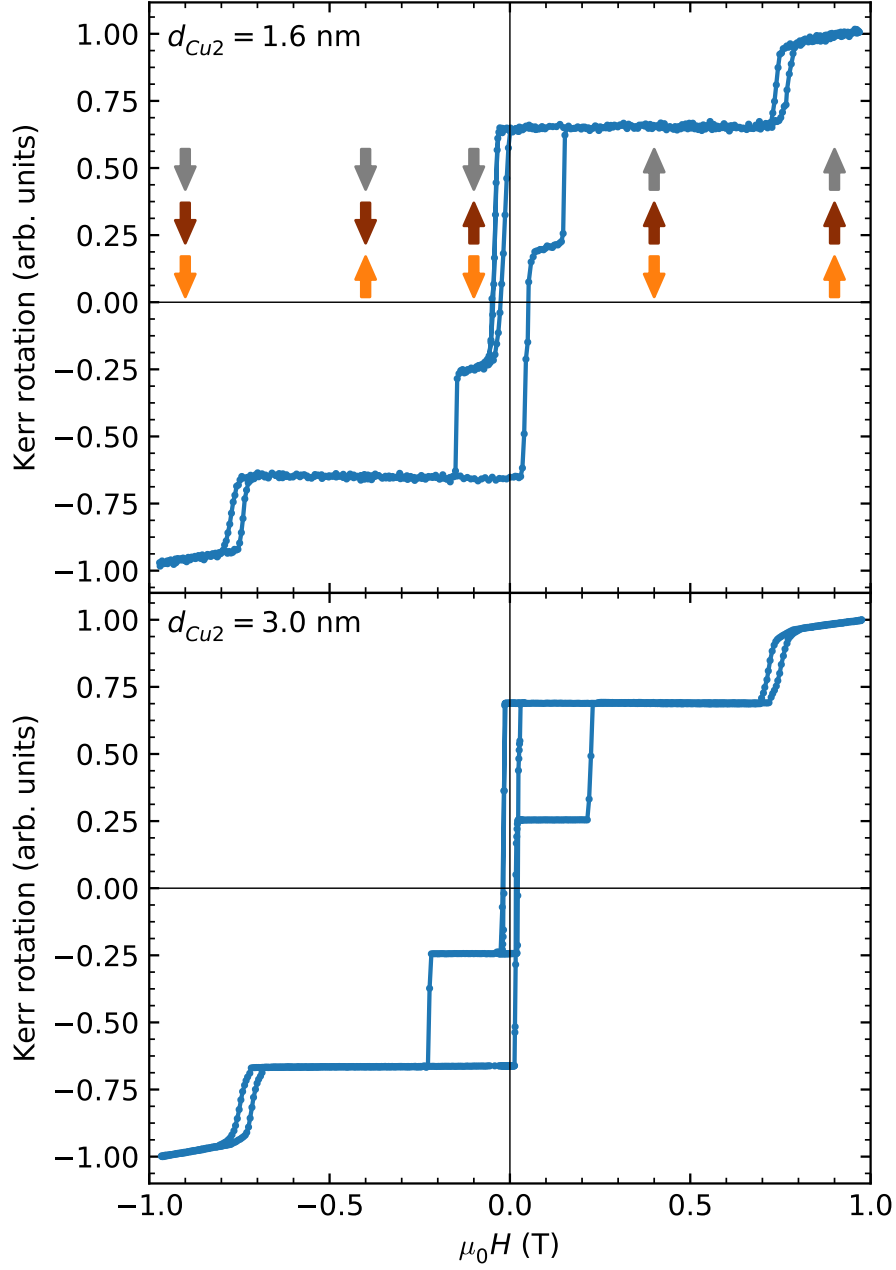


Figure 4.18: Polar MOKE data of the Ta/Cu(7)/SAF/Cu( $d_{\text{Cu}2}$ )/FL/Ta (with  $d_{\text{Cu}2} = 1.6$  and 3 nm deposited at high rate, FM1 =  $4 \times [\text{Co}(0.21)/\text{Ni}(0.58)]/\text{Co}(0.4)$ ,  $d_{\text{Ru}} = 0.38$  nm, FM2 =  $\text{Co}(0.4)/3 \times [\text{N}(0.58)/\text{Co}(0.21)]/\text{Ni}(0.58)/\text{Co}(0.4)$ , and FL =  $\text{Co}(0.4)/3 \times [\text{N}(0.58)/\text{Co}(0.21)]/\text{Ni}(0.58)$ ), showing the reversal of individual layers with magnetic field. The switching order of the layers is indicated by the arrows on the top plot for a field ramping from positive to negative values, with SAF layer represented by the orange and red arrows and free layer represented by grey arrows.



For these reasons, a 7 nm Cu seed layer ( $d_{\text{Cu1}}$ ) deposited at 0.2 nm/s was selected for the measurements of the coupling between the SAF and FL.

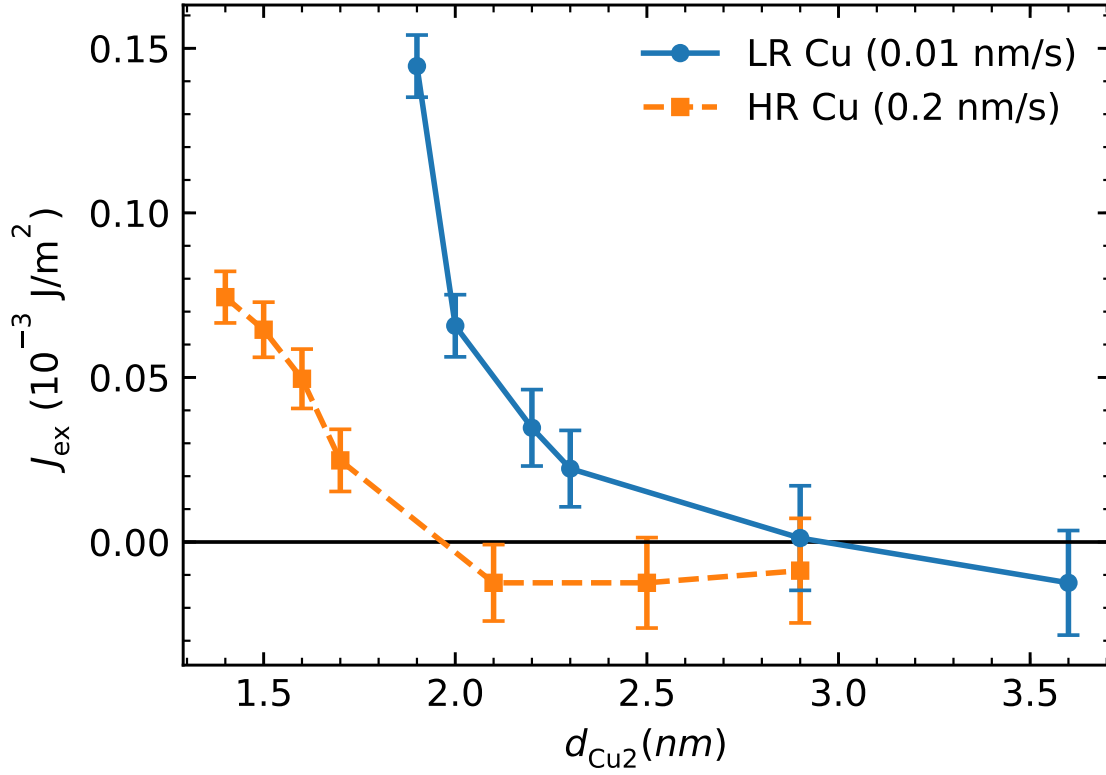


Figure 4.19: The exchange coupling between SAF and FL layers in Ta/Cu(7)/SAF/ Cu( $d_{\text{Cu2}}$ )/FL/Ta (with FM1 =  $4 \times [\text{Co}(0.21)/\text{Ni}(0.58)]/\text{Co}(0.4)$ ,  $d_{\text{Ru}} = 0.38$  nm, FM2 =  $\text{Co}(0.4)/3 \times [\text{N}(0.58)/\text{Co}(0.21)]\text{Ni}(0.58)/\text{Co}(0.4)$ , and FL =  $\text{Co}(0.4)/3 \times [\text{N}(0.58)/\text{Co}(0.21)]/\text{Ni}(0.58)$ ) as a function of a Cu layer thickness,  $d_{\text{Cu2}}$ . Blue circles: Low Cu deposition rate – 0.01 nm/s. Orange squares: High Cu deposition rate – 0.2 nm/s.

The Cu spacer layer thickness,  $d_{\text{Cu2}}$ , was varied between 1.4 nm and 3.6 nm to determine the minimum required separation. The effect of deposition rate was also investigated, by depositing Cu at rates of 0.01 nm/s and 0.2 nm/s. Figure 4.18 shows polar MOKE measurements of the full structure, for different Cu spacer-layer thicknesses ( $d_{\text{Cu2}}$ ). In these structures, the Cu spacer layer was deposited at 0.2 nm/s. If  $d_{\text{Cu2}}$  is 3 nm, the exchange interaction between SAF and FL is negligible. This is evident since the minor loop is centered at zero field. If the Cu thickness decreases to 1.6 nm, the interaction between the SAF and FL becomes strongly ferromagnetic. This coupling can be inferred from the shift of the minor loop in Figure 4.18. Due to this interaction, the coercivity of the SAF also decreases.

Figure 4.19 shows the exchange coupling between SAF and FL as a function of Cu interlayer thickness. Negative  $J_{\text{ex}}$  indicates antiferromagnetic coupling between the SAF

and FL, and positive  $J_{\text{ex}}$  indicates ferromagnetic coupling. For low deposition rates of 0.01 nm/s, we observed small antiferromagnetic coupling at  $d_{\text{Cu}2} = 3.6$  nm. The coupling is zero for  $d_{\text{Cu}2} \approx 2.9$  nm and the strength of ferromagnetic coupling sharply increases below 2.9 nm. For Cu sputtered at a rate 20 times higher, 0.2 nm/s, we observed weak antiferromagnetic coupling for  $d_{\text{Cu}2}$  between 2.1 nm and 2.9 nm. For Cu thinner than 1.9 nm the ferromagnetic coupling strength increases sharply.

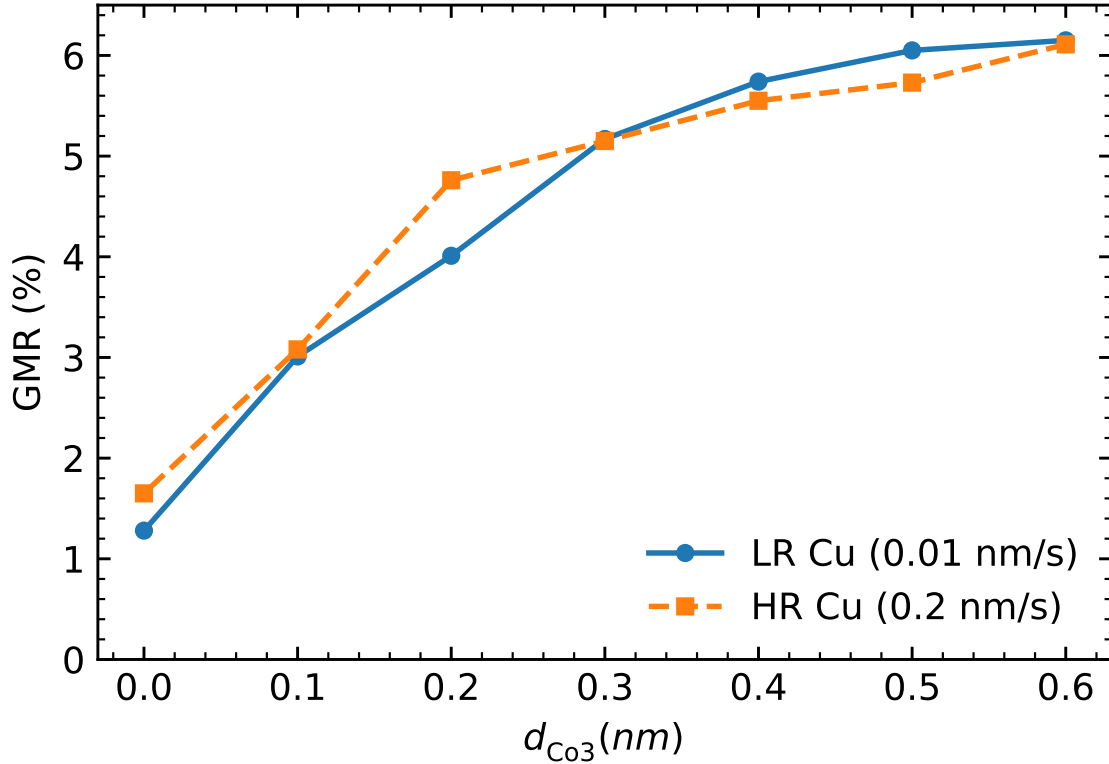


Figure 4.20: GMR of Ta/Cu(1.9)/SAF/Cu(3)/FL/Ta (with FM1 =  $4 \times [\text{Co}(0.21)/\text{Ni}(0.58)]/\text{Co}(0.4)$ ,  $d_{\text{Ru}} = 0.38$  nm, FM2 =  $\text{Co}(0.4)/3 \times [\text{Ni}(0.58)/\text{Co}(0.21)]/\text{Ni}(0.58)/\text{Co}(d_{\text{Co}3})$ , and FL =  $\text{Co}(d_{\text{Co}3})/3 \times [\text{Ni}(0.58)/\text{Co}(0.21)]/\text{Ni}(0.58)$ ) as a function of Co layer thickness,  $d_{\text{Co}3}$ , and deposition rate. Blue circles: Low Cu deposition rate – 0.01 nm/s. Orange squares: High Cu deposition rate – 0.2 nm/s.

Zheng *et al.* [140] have shown that both the Cu film roughness and the grain size of Co/Cu(111) multilayers decrease with increasing deposition rate. This was attributed to an increase in the nucleation density with increasing deposition rate. They also found that the interdiffusion between Co and Cu in Co/Cu multilayers is reduced for films deposited at high rates. If the roughness of the Cu spacer layer and interdiffusion between Co and Cu layers increases, the chance of pinholes also increases, which can induce ferromagnetic coupling between SAF and FL. On the other hand, the roughness of Cu films is lower when deposited at high rates. This could explain why, in the case of low deposition rate, Cu

thickness has to be  $\sim 50\%$  higher to decouple the SAF and FL than in the case of high deposition rate. The results presented in Figure 4.19 suggest that the Cu spacer thickness has to be at least 3 nm to ensure that the coupling between the SAF and FL is small for both high and low deposition rates.

Finally, the thickness of the Co layers ( $d_{\text{Co}3}$ ) was varied on either side of the Cu spacer layer. The effect of the Co thickness on the GMR is shown in Figure 4.20. The Cu seed layer thickness in structures used to investigate the effect of  $d_{\text{Co}3}$  on GMR was reduced to 1.9 nm. Reducing the Cu seed layer thickness minimizes the fraction of the total current passing through the seed layer, and maximizes the GMR of the structure. The GMR increases with increasing Co thickness up to a maximum of  $\sim 6\%$  for 0.6 nm of Co. This is due to a larger spin-dependent magnetic scattering at the Co–Cu interface [82]. GMR depends on the Co interlayer thickness in a similar way to that found by Parkin *et al.* [82] in multilayer structures with in-plane magnetic moments. Figure 4.20 clearly shows that the GMR does not depend on the Cu deposition rate.

## 4.2 Summary

Our experimental results show how the magnetic and transport properties of Ta/Cu/SAF/Cu/FL/Ta films with SAF = FM1/Ru( $d_{\text{Ru}}$ )/FM2, FM1 =  $N_1 \times [\text{Co}(d_{\text{Co}1})/\text{Ni}(d_{\text{Ni}})] / \text{Co}(d_{\text{Co}2})$ , FM2 =  $\text{Co}(d_{\text{Co}2})/N_2 \times [\text{Ni}(d_{\text{Ni}})/\text{Co}(d_{\text{Co}1})]/\text{Ni}(d_{\text{Ni}})/\text{Co}(d_{\text{Co}3})$ , and FL =  $\text{Co}(d_{\text{Co}3}) / N_3 \times [\text{Ni}(d_{\text{Ni}})/\text{Co}(d_{\text{Co}1})]/\text{Ni}(d_{\text{Ni}})$  are affected by  $N_1$ ,  $N_2$ ,  $N_3$ ,  $d_{\text{Co}1}$ ,  $d_{\text{Co}2}$ ,  $d_{\text{Co}3}$ ,  $d_{\text{Ni}}$ ,  $d_{\text{Ru}}$ ,  $d_{\text{Cu}1}$  and  $d_{\text{Cu}2}$ , as well as deposition rate. In addition, we have shown that the SAF hard layer can be designed with only Co/Ni multilayers coupled across a Ru spacer layer, thus avoiding the use of precious metals such as Pt and Pd. The perpendicular (uniaxial) anisotropy of  $8 \times [\text{Co}/\text{Ni}]$  multilayers exceeds  $4 \times 10^5 \text{ J/m}^3$  for  $d_{\text{Co}1}$  ranging from 0.16 to 0.26 nm and  $d_{\text{Ni}}$  ranging from 0.48 to 0.58 nm. The perpendicular magnetic anisotropy and saturation magnetization of the Co/Ni multilayers sharply increase with the number of bilayers for  $N_1 \leq 10$  and then gradually decrease for greater number of bilayers. On the other hand, the damping and zero-frequency line broadening of the Co/Ni multilayers decrease with the number of bilayers.

Increasing the thickness of the Cu seed layer improves the texture of the Co/Ni multilayers, while increasing grain size and film roughness. The increase in grain size, in particular, results in the reduction of direct exchange coupling between the magnetic grains. This increases the probability of uniform reversal of individual magnetic grains and enhances the coercivity of the Co/Ni multilayers.

To maximize the coupling between FM1 and FM2 in the SAF,  $d_{\text{Co}2}$  should be between 0.4 and 0.6 nm and  $d_{\text{Ru}}$  between 0.38 nm and 0.42 nm. To resist thermal agitation, the diameter of Ta/Cu/SAF/Cu/FL/Ta nanopillars with  $N_1 = 4$ ,  $N_2 = 3$  and  $N_3 = 6$  must be above 20 nm. The GMR effect is maximized for  $d_{\text{Co}3} = 0.6 \text{ nm}$ , and the SAF and FL

are decoupled for  $d_{\text{Cu2}}$  larger than 3 nm. Cu films deposited at higher rates require less thickness to decouple the SAF and FL than Cu films deposited at lower rates.

This study lays the foundations for future investigations of STT-RAM devices consisting of only Co/Ni multilayers.

## Chapter 5

# Spin torque switching in nanopillars with antiferromagnetic reference layer

This chapter describes the transport measurements performed on patterned nanopillars. The optimized structure of SAF/Cu/FL discussed in the previous chapter section 4.3 is used to pattern the perpendicularly magnetized, circular shaped nanopillars of diameter 200 nm. Kerr and FMR measurements performed on the optimized continuous films are also explicitly discussed to relate them with the results obtained from the nano-pillars. DC resistance vs. field (R-H) and resistance vs. current (R-I) loops of nano-pillars followed by the measurement of the phase diagram are also described.

### 5.1 A brief introduction

Spin transfer torque random access memory (STT-RAM) is one of the most promising emerging non-volatile memory technologies. It has a potential to be used as universal memory due to its high recording density, fast write/read speed (a few ns), unlimited endurance, excellent scalability and low power consumption [22].

The main challenges for implementing STT writing mode in high density and high speed memory is the reduction of the critical current,  $I_c$ , required to switch the magnetization of the free layer (FL) while maintaining its thermal stability. In the macrospin (single domain) approximation, the critical current required for spin-transfer reversal of the FL from the parallel (P) to anti-parallel (AP) and from the AP to P state is given by [28]

$$I_c \approx \left( \frac{2e}{\hbar} \right) \frac{\alpha \mu_0 M_s V_{FL}}{g(\theta)p} H_{eff} \quad (5.1)$$

where  $M_s$ ,  $\alpha$ , and  $V_{FL}$  are the saturation magnetization, intrinsic Gilbert damping constant, and volume of the FL, respectively,  $p$  is the spin polarization of the current collinear with the reference layer (RL) magnetization, and  $g(\theta)$  is a pre-factor depending on the relative angle

between the RL and the FL. The effective field acting on the perpendicularly magnetized FL [19],  $H_{eff}^{P \rightarrow AP} = -H_{k\perp} + M_s + H_{app} + H_{dip}$  and  $H_{eff}^{AP \rightarrow P} = H_{k\perp} - M_s + H_{app} + H_{dip}$ , has contributions from the perpendicular uniaxial anisotropy field  $H_{k\perp}$ , demagnetizing field  $\mu_0 M_s$ , applied field  $H_{app}$ , and the dipolar field from the reference layer  $H_{dip}$ .

## 5.2 Logistics behind the design

We propose a design of nanopillars for STT RAM devices intended to reduce the critical current required for the reversal of the FL.

- Following Equation 5.1 the optimum STT-RAM design would have magnetic layers with a high spin polarization and low damping. We chose Co/Ni multilayers because they have lower damping,  $\alpha$ , than Co/Pt and Co/Pd multilayers [151, 124] and have high spin polarization [19].
- $I_c^{P \rightarrow AP}$  (current from parallel to anti-parallel) has to be similar to  $I_c^{AP \rightarrow P}$  (current from anti-parallel to parallel). This can be achieved by controlling the dipolar interaction between the RL and FL in order to compensate the asymmetry intrinsic to  $g(\theta)$ . We have designed a RL having a synthetic antiferromagnet (SAF) structure to minimize the dipolar interaction,  $H_{dip}$ , between the RL and the FL.
- The dipole field on FL (from reference layer and the surrounding nanopillars) has to be minimized to ensure that P and AP states have similar thermal energies. Thus it is desired that the reference layer is SAF to minimize the dipole fields from reference layers.
- In most of the STT-RAM devices, the reference layer is composed of a combination of Co/Pd, Co/Pt, Co/Ni and CoFe/Ni multilayers to obtain the large PMA [28, 46, 47, 48]. Since Pt and Pd (high Z elements) have strong spin orbit coupling, the multilayers containing Pt and Pd tend to have high damping,  $\alpha$ , and low spin polarization,  $p$ . Therefore, the STT-RAM devices that contain Pt or Pd have lower spin torque efficiencies [18, 19, 54, 55, 126, 141].
- We tuned the  $M_s$  and  $K_u$  of the FL to minimize the  $I_c$  while maintaining its thermal stability.

## 5.3 Sample Preparation

We deposited two film structures: 1) Ta(3)/Cu(30)/SAF/Cu/FL/Ta(3)/Ru(7) for fabrication of nanopillar devices (Figure 4.1), and 2) Ta(3)/Cu(10)/FL/Ta(3) for ferromagnetic resonance (FMR) measurements. The details related to design and fabrication of these structures are discussed in chapter 4. The Ta/Cu bilayer structure helps set up the (111)

growth orientation for Co/Ni multilayers. For corrosion protection, the films are covered by Ta/Ru and Ta. The SEM image with a schematic structure of nano-pillar is shown in Figure 5.1.

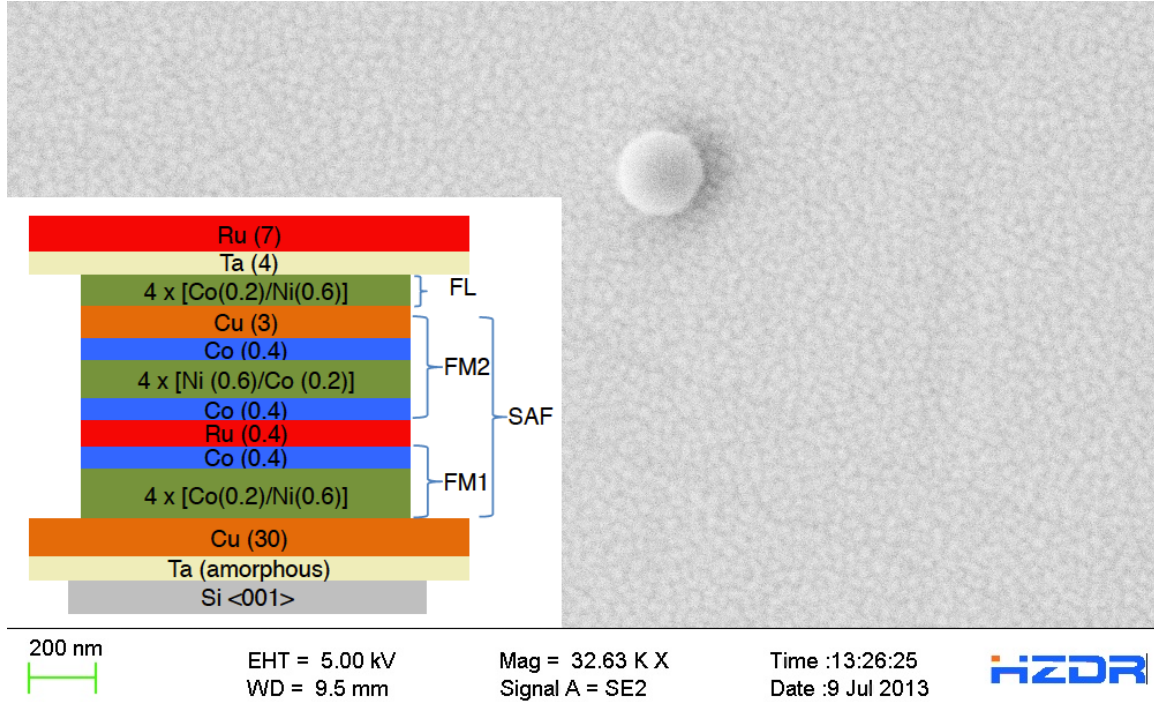


Figure 5.1: The SEM image with a inset of the schematic structure of nano-pillar. The structural composition of the nano-pillar is Ta/Cu/SAF/Cu/FL/ Ta. In the insert the numbers in the brackets represent layer thicknesses in nm.

We choose Co/Ni multilayers with  $d_{Co} = 0.2$  nm and  $d_{Ni} = 0.6$  nm in order to maximize the perpendicular magnetic anisotropy, required for thermal stability of the FL and minimize damping of the FL [56, 142, 143]. The circular shaped nanopillars with SAF/Cu/FL film structure of diameter 200 nm were patterned by electron beam lithography and  $Ar^+$  ion milling as described in chapter 2 Section 3.3.

## 5.4 Measurements on the continuous films

### 5.4.1 Polar MOKE measurements and SQUID measurements:

Magnetic measurements are performed on the continuous films before patterning as discussed in the previous chapter. Magneto-optical Kerr measurements of SAF/Cu/FL show that the magnetic coercivity,  $\mu_0 H_c$ , of the SAF and the FL in the continuous films is 0.23 T and 0.018 T, respectively as shown in the Figure 5.2. The hysteresis loop of the FL (inset in Figure 5.2) is shifted by less than 3 mT in the positive field direction indicating weak

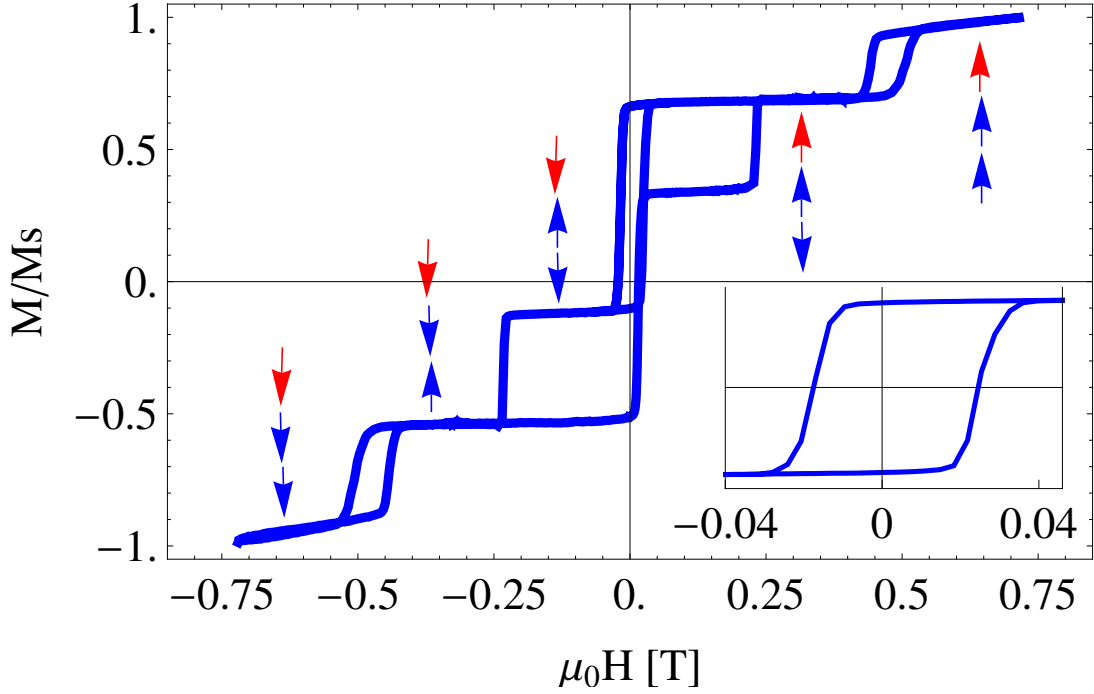


Figure 5.2: Polar MOKE data of the Ta/Cu/SAF/Cu/FL/Ta structure, showing the reversal of individual layers with magnetic field. The hysteresis loop of the FL is also shown in the inset. The switching order of the layers is indicated by the arrows on the top plot for a field ramping from positive to negative values, with SAF layer represented by the blue arrows and free layer represented by red arrows.

interaction between SAF and the FL. This interaction can be due to the oscillatory RKKY and roughness induced magnetostatic couplings.

The field dependence of the magnetization of the FL was measured using a superconducting quantum interference device (SQUID) magnetometer in magnetic fields up to 7 T. The measurements revealed a magnetization polarization of  $\mu_0 M_s = 0.79$  T.

#### 5.4.2 FMR measurements

The magnetic properties of the FL were also measured with FMR with a co-planar waveguide in a field-swept, field-modulated configuration, as detailed by Montoya et al. [109]. The FMR measurements were performed in a frequency range between 15-32 GHz and with the DC field applied perpendicular to the film surface. From the FMR measurements we found that the magnetic anisotropy constant of FL is  $K_u = 3.7 \times 10^5$  J/m<sup>3</sup> and g-factor is  $g = 2.193$ . The intrinsic Gilbert damping using Equation 3.38 is calculated to be  $\alpha = 0.0221$  and  $\Delta H_0 = 0.0416$  T as shown in Figure 5.3.



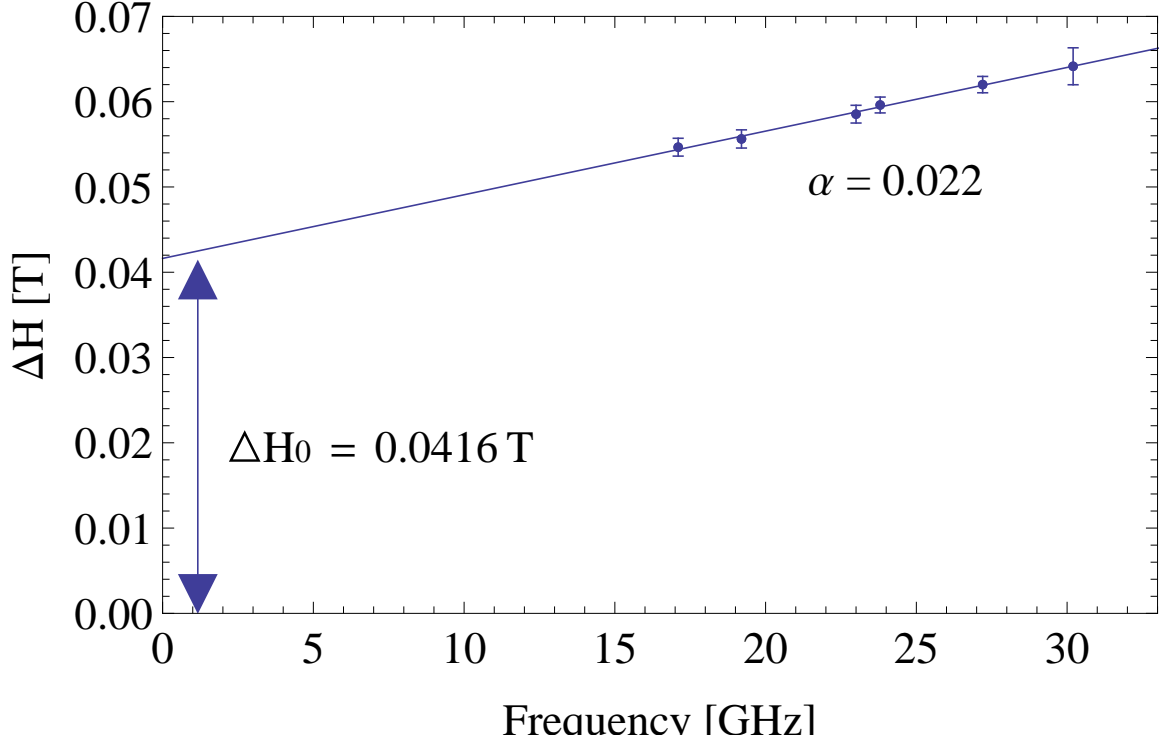


Figure 5.3: FMR line width versus frequency measurements of the FL. The intrinsic damping  $\alpha$  is calculated from the slope and  $\Delta H_0$  from the intercept.

## 5.5 Transport measurements on nano-pillars

### 5.5.1 Resistance measurements as a function of applied field

Resistance of the nanopillar is measured in a 2-point geometry using standard microwave probes. The current direction was set so that for positive current, electrons flow from SAF to FL. The probe station was capable of applying over 1 T field both in-plane and normal to the film surface.

The dc-resistance of a circular SAF/Cu/FL nanopillar of diameter 200 nm as a function of the applied field perpendicular to the surface of substrate is shown in Figure 5.4. In the measurements, the applied d.c. current is kept constant and equal to 0.5 mA.

At positive saturation field, the direction of magnetic moments of all the FM layers in the structure are parallel to the direction of the applied field, corresponding to a state of lowest resistance. As the field is reduced, the magnetic moment of FM1 reverses first at 0.62 T due to the antiferromagnetic exchange coupling between FM1 and FM2. Since FM1 and FM2 have the similar film structure their magnetic anisotropy is similar. However, the Zeeman energy of FM1 is smaller than that of FM2 because the magnetization of FM1 is smaller than that of FM2. For this reason, the magnetic moment of FM1 in the SAF reverses first. The change from the P to AP alignment at 0.62 T between the magnetic

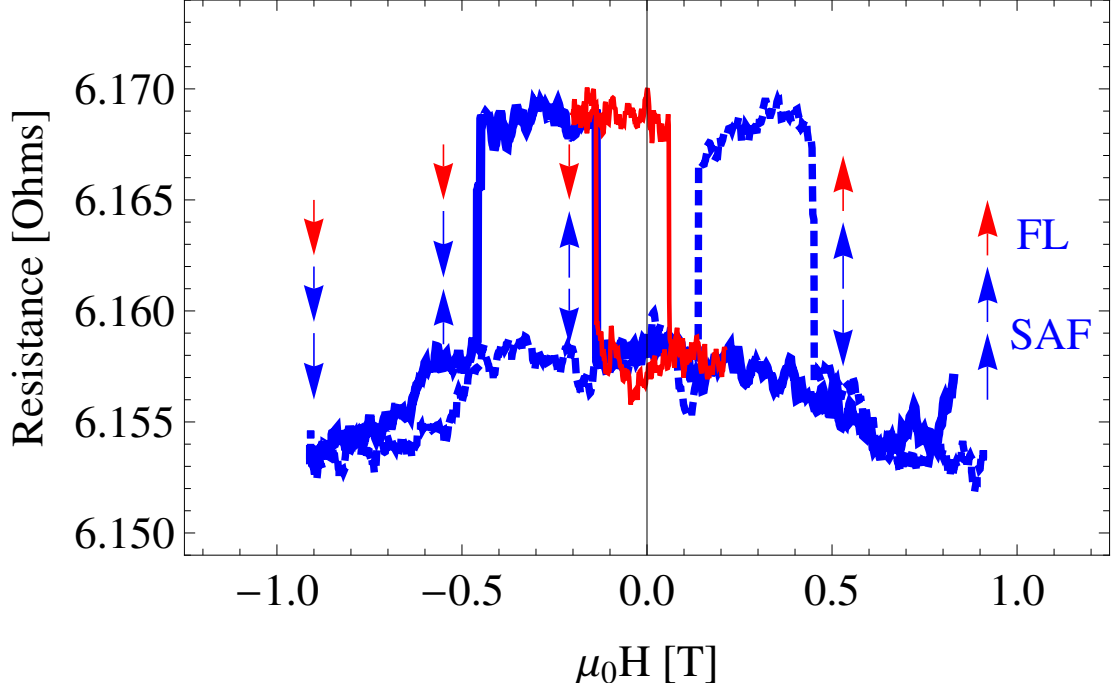


Figure 5.4:  $R_{dc}$  measurement of the nanopillars as a function of the applied magnetic field. The vertical arrows represent the directions of the magnetic moments of FM1 (bottom arrow), FM2 (middle arrow) and FL (top arrow). The solid line represents the resistance measurements when the field sweeps from 0.9 T to -0.9 T and the dotted line represents the change in resistance when the field sweeps from -0.9 T to 0.9 T.

moments of FM1 and FM2 in the SAF results in a slight increase in resistance. The CPP GMR is generally larger than the CIP GMR [144]. However, the resistance of nano-pillars is larger than the resistance of continuous films. Therefore, the change in resistance due to the switching of the free layer (see Figure 5.4) is lower in nanopillars than in continuous films.

Further reduction of the applied magnetic field causes the reversal of the magnetic moment in FL at  $\mu_0 H = -0.13$  T. At this field, alignment between the magnetic moments of the adjacent magnetic layers are AP (FM1 and FM2 are AP, and FM2 and FL are AP) and hence resistance of the nanopillar increases to its highest value. The orientation of magnetic moments in the FM layers is unchanged from  $-0.13$  T  $< \mu_0 H < -0.49$  T. At  $\mu_0 H = -0.49$  T both magnetic layers in SAF (FM1 and FM2) simultaneously rotate. This sets the magnetic moment of the FL parallel to that of FM2 resulting in a decrease of the nanopillar resistance. Even at this field the antiferromagnetic coupling across Ru is strong enough to ensure that mutual alignment between magnetic moments of FM1 and FM2 stays AP. At negative saturation field, the magnetic moments of all the FM layers are aligned with the applied field, corresponding again to a state with the lowest resistance. The same

trend is observed when the applied field sweeps from the negative saturation ( $\mu_0 H = -0.8$  T) to the positive ( $\mu_0 H = 0.8$  T).

The change in resistance due to the transition from the P to AP alignment between the magnetic moments of FM1 and FM2 (Co/Ru/Co interface at  $\pm 0.62$  T) is about two and a half times smaller than the change in resistance due to the transition from the P to AP alignment between the magnetic moments of FM2 and FL (Co/Cu/Co interface at  $\pm 0.13$  T and  $\pm 0.49$  T). The reduced GMR at the Co/Ru interface is due to the small difference between the spin-polarized density of states at the Fermi level [145] and also due to the possible inter-diffusion at Co/Ru interfaces [146]. The larger GMR from the Co/Cu/Co system is expected due to electronic structure at the Fermi level [147].

The resistance measurements are repeated for different values of applied current and it is observed that the coercive field of both the SAF and FL in the patterned nanopillars increases as compared to the continuous films, with the coercivity field of the SAF reaching  $\mu_0 H_c = 0.49$  T ( $\mu_0 H$  of SAF in the continuous films is 0.23 T) and that of the FL  $\mu_0 H_c = 0.098$  T ( $\mu_0 H$  of FL in the continuous films is 0.018 T). The increase of the coercivity field in both SAF and FL in nanopillars is due to size effects. In large magnetic structures, a defect or non-uniformity can act as a centre for a magnetic domain nucleation that causes the magnetization reversal at magnetic fields several orders of magnitude smaller than  $2K_u/M_s$  (where  $K_u$  is the magnetic anisotropy energy and  $M_s$  is the saturation magnetization of the magnetic structure). In  $nm$ -size magnetic structures much larger magnetic fields are required to nucleate a magnetic domain and cause the magnetization reversal [148, 128, 138] since the energy term due to the direct exchange interaction is dominant in  $nm$ -size structures.

Figure 5.5 shows a minor hysteresis loop of the resistance of a nanopillar as a function of the applied magnetic field in the range from 0.2 to -0.2 T. In this field range SAF does not reverse and the resistance change is only due to the reversal of the magnetic moment of the FL. A discrete drop in resistance occur at  $\mu_0 H = 0.06$  T corresponding to the magnetic moment reversal of FL from the antiparallel to parallel orientation. The resistance increases back to its original value at  $\mu_0 H = -0.136$  T due to the reversal of magnetization from the parallel to antiparallel orientation. A comparatively higher field is required to reverse the magnetic moment of the FL from the parallel to antiparallel orientation than from the antiparallel to parallel orientation with the magnetic moment of FM2. The dipolar interaction favours the parallel alignment between FM2 and the FL and results in the reversal offset field of 0.038 T. We note that the dipolar interaction is significantly less than if a single reference layer was used [19]. A further optimization of the SAF design is required to fully eliminate the dipolar interaction between SAF and FL.

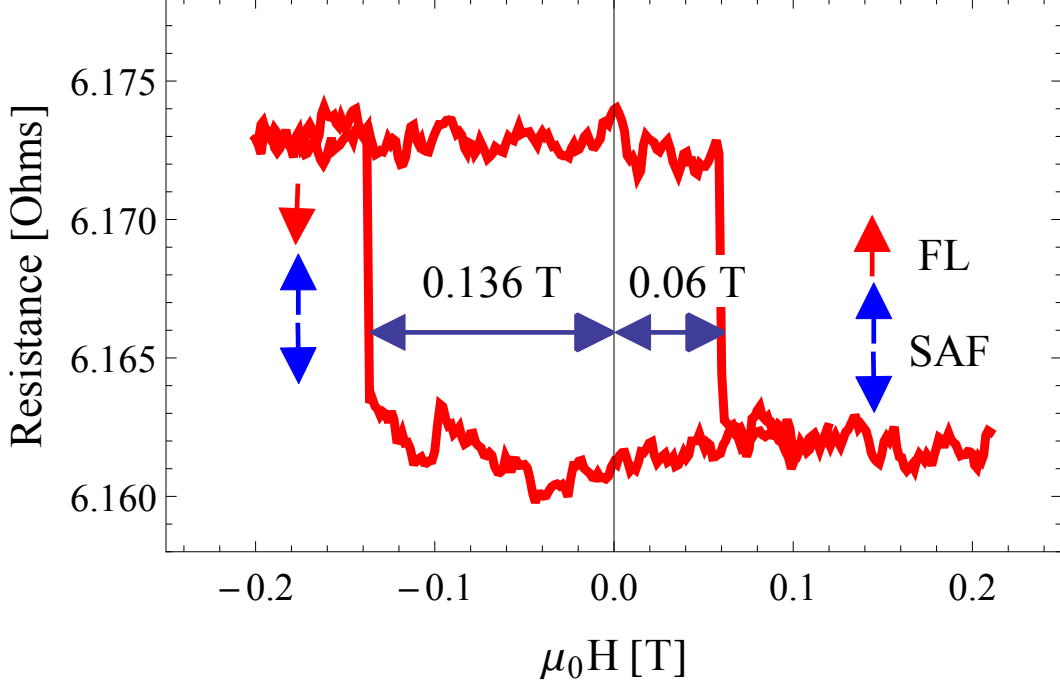


Figure 5.5:  $R_{dc} = dV/dI$  measurements of the nanopillars as a function of applied magnetic field. The arrows represent the directions of the magnetizations of FM1 (bottom arrow), FM2 (middle arrow) and FL (top arrow).

### 5.5.2 Resistance change as a function of d.c. current

The resistance as a function of d.c. current, measured at zero applied field, is shown in Figure 5.6. The critical current,  $I_c$ , required to reverse the magnetization of FL from P to AP alignment is  $I_c = 6.7$  mA and from AP to P is  $I_c = 3.3$  mA.

Starting from either P or AP alignment of SAF and FL a series of the  $R_{d.c.}$  versus  $H$  measurements are repeated for different values of applied current to construct a field-current phase diagram as shown in Figure 5.7. For each value of the applied current, the field sweeps from 0.2 T to -0.2 T. It is clear from the phase diagram that, at  $H_{app} + H_{dip} = 0$  ( $H_{dip} = 22.5$  mT), the current required to switch the FL from P to AP is around 5.2 mA ( $1.66 \times 10^7$  A cm $^{-2}$ ) while to reverse the FL from AP to P is 4.9 mA ( $1.56 \times 10^7$  A cm $^{-2}$ ). This is due to the spin-transfer-torque asymmetry in metallic spin-valve systems [7].

Figure 5.7 shows the linear dependance of  $I_c$  (P-AP) (with slope =  $-7.02 \times 10^{-2}$  mA/mT) and  $I_c$  (AP-P) (with slope =  $-6.47 \times 10^{-2}$  mA/mT) on the  $H_{app}$  for  $-70$  mT  $< H_{app} < 20$  mT. This is in agreement with the Equation 5.1 and allows us to estimate the  $\alpha/p$  ratio of the FL. This is done by substituting the slopes of  $I_c$  versus field to the pre-factor of Equation 5.1. The values of  $\alpha/p$  calculated from our measurements are  $0.33 g(\pi)$  and  $0.36 g(0)$ . These  $\alpha/p$  values are similar to those obtained by Mangin et al. [19]. For  $H_{app} < -90$  mT and  $H_{app} > 50$  mT,  $I_c$  deviates from the linear behaviour of Equation 5.1, due in-part to the finite temperature effects [149].

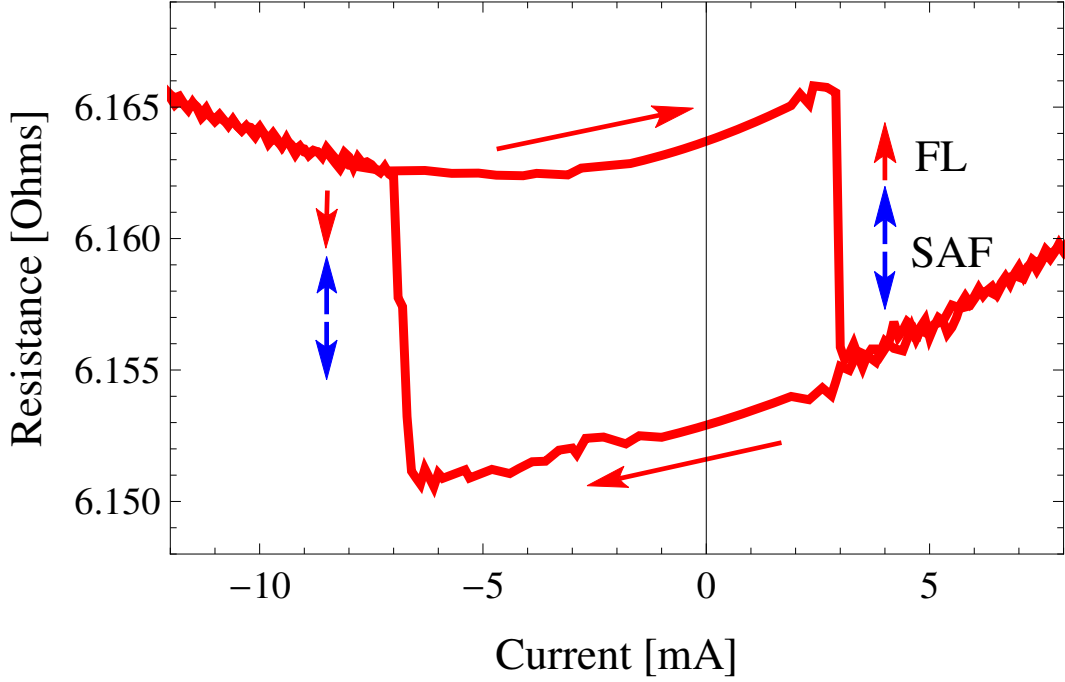


Figure 5.6: Current induced switching of the FL between P and AP states at a zero applied magnetic field. The arrows represent the directions of the magnetizations of FM1 (bottom arrow), FM2 (middle arrow) and FL (top arrow).

The efficiency of current induced magnetization reversal of the FL can be determined from the expression  $I_c/(\mu_0 V_{FL} H_c)$ , [28] where  $I_c$  is critical current,  $V_{FL}$  and  $\mu_0 H_c$  are the volume and coercivity of the FL, respectively. The smaller the ratio,  $I_c/(V_{FL} \mu_0 H_c)$ , the higher the efficiency of magnetization reversal of FL using the spin torque transfer effect. In our nanopillars  $V_{FL} = 1.01 \times 10^{-22} \text{ m}^3$  and  $\mu_0 H_c = 0.098 \text{ T}$  resulting in  $I_c/(V_{FL} \mu_0 H_c)$  is  $5.28 \times 10^{20} \text{ A/T m}^3$ . This is twice as efficient as what was reported previously for devices with SAF reference layer [28].

In the study reported by Tudosa et al. [28], the FL comprised Co/Ni and Co/Pd multilayers. Co/Pd multilayers have higher damping than Co/Ni multilayers [150, 151]. We further reduced damping in our Co/Ni multilayers by increasing the Co to Ni thickness ratio ( $4 \times [\text{Co}(0.2)/\text{Ni}(0.6)]$ ) as suggested by Shaw et al. [55] and Mizukami et al. [152]. We therefore attribute the lower damping to decrease the  $I_c$  (Eq. 5.1) and to increase in the efficiency (compared to Ref. [28]) of spin-torque driven switching in our nanopillars. It is also important to mention that the thermal fluctuations affect both  $I_c$  and  $\mu_0 H_c$  in a similar manner, therefore the coefficient describing the efficiency at temperature  $T$  is  $I_c(T)/\mu_0 H_c(T) \approx I_{c0}/\mu_0 H_{c0}$ , where  $I_{c0}$  and  $\mu_0 H_{c0}$  are the critical current and coercivity at zero temperature. Therefore, in a reasonable approximation, the ratio of  $I_c/\mu_0 H_c$  removes the temperature effects and remains close enough to its zero temperature value [19, 153].

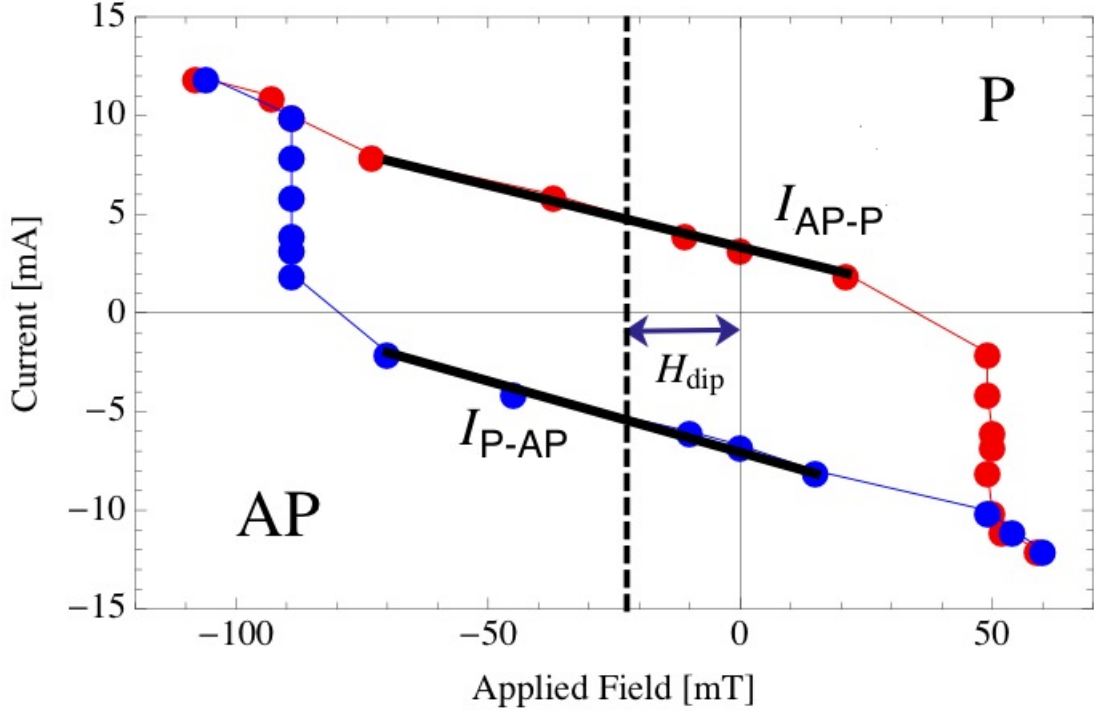


Figure 5.7: Field-current phase diagram showing region where the FL is parallel and antiparallel to the SAF reference layer.

## 5.6 Summary

We investigated current and field induced magnetization reversal in perpendicularly magnetized 200 nm diameter circular nanopillars with a unique magnetic layer design: a Co/Ni multilayer free layer (FL), and a synthetic antiferromagnet (SAF) reference layer. A synthetic antiferromagnet, consisting of two Co/Ni multilayers coupled anti-ferromagnetically across a Ru layer, is used as a reference layer to minimize the dipolar field on the free layer. In our nanopillars, the dipolar field acting on FL is only 22.5 mT, more than two times smaller than reported in devices with a single ferromagnetic reference layer [19].

The free layer is a single 4×[Co/Ni] multilayer. The use of Pt and Pd was avoided to lower the spin-orbit scattering in magnetic layers and intrinsic damping in the free layer, and therefore, reduce the critical current required for spin-transfer-torque switching. The intrinsic Gilbert damping of a continuous 4×[Co/Ni] multilayer film was measured by ferromagnetic resonance to be  $\alpha = 0.022$ , which is significantly lower than in Pt or Pd based magnetic multilayers.

In zero magnetic field the critical current required to switch the free layer from the parallel to antiparallel (antiparallel to parallel) alignment is 5.2 mA (4.9 mA). Given the volume of the free layer,  $V_{FL} = 1.01 \times 10^{-22} \text{ m}^3$ , the switching efficiency,  $I_c/(V_{FL} \times \mu_0 H_c)$ , is  $5.28 \times 10^{20} \text{ A/Tm}^3$ , twice as efficient as any previously reported device with a similar structure. This Improved reversal efficiency is attributed to the low Gilbert damping of our FL corroborated by extended films ferromagnetic resonance studies.

## Chapter 6

# The origin of perpendicular magnetic anisotropy in Co/Ni multilayers

This chapter presents a comprehensive study of the variation in perpendicular magnetic anisotropy of the as-deposited and annealed (111) textured  $N \times [\text{Co/Ni}]$  films as a function of the number of bilayer repeats  $N$ . The Co/Ni multilayers are grown on top of Au seed layer and covered with Au capping layer. The influence of Au interface layers on the magnetic anisotropy of Co/Ni multilayers has been investigated. To explain the variation of the perpendicular anisotropy of the Co/Ni multilayers on  $N$ , the following contributions are taken into account; 1) the magnetoelastic anisotropy due to the strain, 2) the magnetocrystalline anisotropy due to the orbital asymmetry between easy and hard axis, 3) the roughness induced anisotropies, and 4) the inter-diffusion of Au in the Co/Ni multilayers. The magneto-crystalline bulk anisotropy is estimated from the difference in the perpendicular and parallel g-factors of Co/Ni multilayers that are measured using the in-plane and out-of-plane ferromagnetic resonance measurements. To calculate the contribution of magnetoelastic anisotropy in the Co/Ni multilayers, in-plane and out-of-plane X-ray diffraction measurements are performed to determine the spacing between Co/Ni (111) and (220) planes. Transmission electron microscopy has been used to estimate the multilayer film roughness. These values are used to calculate the roughness-induced surface and magnetocrystalline anisotropy coefficients as a function of  $N$ .

### 6.1 Brief background

Co/Ni multilayers (MLs) exhibits high spin polarization [154], large perpendicular magnetic anisotropy (PMA) [56, 155, 156, 157, 54], and low intrinsic damping [31, 18, 126, 141] that make them a promising candidate for the spintronic devices such as spin transfer-torque



random access memory (STT-RAM) [158], spin-torque oscillators [159] and bit patterned media [160, 161, 162, 163, 164, 165].

Daalderop et al. [155] predicted and experimentally demonstrated the PMA in (111) oriented Co(1 AL)/Ni(2 AL) MLs (AL - atomic layer) in 1992. The calculations by Daalderop et al. [155] suggested that the PMA arises from the reduced symmetry and electronic structure at Co and Ni interfaces. They emphasized that in Co(1 AL)/Ni(2 AL) MLs the Fermi energy is close to the bands with  $d_{xy}$  and  $d_{x^2-y^2}$  characters (z-axis is chosen to be normal to the interface) whose spin-orbit interaction favours the PMA. Calculations by Kyuno et al. [166] also attributed the origin of PMA in (111) Co/Ni MLs to large local density of states of  $d_{x^2-y^2}$  and  $d_{xy}$  orbitals of Co and Ni minority spin just below the Fermi energy. PMA is also observed in (100) and (110) oriented Co/Ni MLs [167]. Some groups also pointed out that the magnetoelastic anisotropy due to strain in Co/Ni MLs is a source of PMA [168, 169, 170, 171]. Since these initial studies, many authors [167, 172, 56, 157, 54, 168, 169, 170, 171, 173] have studied the anisotropy in Co/Ni MLs, however, the origin of the PMA in these MLs is still a matter of debate.

Several authors have studied PMA in Co/Ni MLs as a function of the Co and Ni layer thicknesses [167, 172, 114, 54, 56, 157, 143]. They found that the maximum PMA can be achieved for the Co layer thickness between 1 and 2 AL and for the Ni layer thickness around 3 AL. Growth conditions, choice of a substrate and seed layers play an important role to improve the (111) texture and hence the PMA of Co/Ni MLs [143, 114, 174, 53]. Postdeposition techniques like annealing [175, 53, 176] and ion irradiation [177] were also studied to tune the PMA in Co/Ni MLs.

Co/Ni MLs became a model system for spin transfer torque studies in the perpendicularly magnetized magnetic materials due to their large and tunable PMA and a relatively low damping constant  $\alpha$ . One way to tune the magnetic characteristics of these MLs is by varying the number of bilayer repeats  $N$ . However, reports on the behaviour of the magnetic anisotropy as a function of  $N$  have varied in the literature [29, 124, 178, 179, 180, 119, 181, 182, 183, 184, 152, 18, 185] and they exhibit strong dependence on the layers adjacent to the Co/Ni MLs.

## 6.2 Theory

To understand the dependance of magnetic anisotropy of the Co/Ni ML on the number of multilayers, the total energy density of the ML will be expressed as

$$e_{tot} = -(K_u + K_{DIP}) \cos^2\theta \quad (6.1)$$

where  $K_u$  is the total intrinsic magnetic anisotropy given as

$$K_u = K_{ME} + K_{MC} + K_S/d \quad (6.2)$$

$K_{ME}$ ,  $K_{MC}$ ,  $K_{DIP}$  and  $K_S$  are the magnetoelastic, magnetocrystalline, dipolar and surface anisotropy coefficients, respectively.  $\theta$  is the angle between the normal to the film and the magnetization, and  $d$  is the thickness of the Co/Ni ML. The contribution to the magnetic anisotropy energy due diffusion of Au in the Co/Ni ML will be discussed only qualitatively.

### 6.2.1 Magnetoelastic anisotropy, $K_{ME}$

Co ( $a_{Co, fcc} = 0.354 \text{ nm}$ ) [186] and Ni ( $a_{Ni, fcc} = 0.352 \text{ nm}$ ) [187] are closely lattice matched. The Au inter-planer distance ( $a_{Au, fcc} = 0.408 \text{ nm}$ ) is about 14 % larger than that of Co and Ni that causes strain in the Co/Ni ML. To understand the effect of strain on the magnetic anisotropy (MA) of the Co/Ni ML, we estimated the strain induced bulk magnetoelastic energy per volume for all the multilayer samples. The magnetoelastic anisotropy coefficient for the cubic (111) structures is estimated as [168, 188]

$$K_{ME} = \frac{B_2^{Ni}(\epsilon_{//} - \epsilon_{\perp})_{Ni} V_{Ni}}{V_{Ni} + V_{Co}} + \frac{B_2^{Co}(\epsilon_{//} - \epsilon_{\perp})_{Co} V_{Co}}{V_{Ni} + V_{Co}} \quad (6.3)$$

where  $B_2^{Ni}(fcc) = 10 \text{ MJ/m}^3$ ,  $B_2^{Co}(fcc) = 7.7 \text{ MJ/m}^3$ , and  $\epsilon_{//}$  and  $\epsilon_{\perp}$  are the in-plane and out-of-plane strains, respectively.  $\epsilon_{//, \perp}$  are calculated as  $\epsilon_{//} = [d(220)_{st} - d(220)_{ust}]/d(220)_{ust}$  and  $\epsilon_{\perp} = [d(111)_{st} - d(111)_{ust}]/d(111)_{ust}$ , where  $d(220)_{st}$  and  $d(220)_{ust}$  are the distances between (220) planes of strained and unstrained Co/Ni ML, respectively, and  $d(111)_{st}$  and  $d(111)_{ust}$  are the distances between (111) planes of the strained and unstrained Co/Ni ML, respectively. In the studied Co(0.21)/Ni(0.58) ML (the numbers in parentheses indicate the layer thicknesses in nanometers),  $V_{Co}/(V_{Ni} + V_{Co}) = 0.25$  and  $V_{Ni}/(V_{Ni} + V_{Co}) = 0.75$ . In these calculations we assumed that the Co/Ni ML have a fcc structure. This is in agreement with the STEM results of Gottwald et al. [156] that showed A-B-C stacking of the (111) planes in the (111) textured  $Co_{1ML}/Ni_{3ML}$  (Co(0.21)/Ni(0.58)) ML. In-plane and out-of-plane XRD measurements are used to measure  $d(220)_{st}$  and  $d(111)_{st}$ , respectively, in order to calculate the  $\epsilon_{//}$  and  $\epsilon_{\perp}$ .

### 6.2.2 Magnetocrystalline anisotropy, $K_{MC}$ :

According to Bruno's theory the magnetocrystalline anisotropy coefficient of the Co/Ni ML per volume,  $K_{MC}$ , originates from the asymmetry in the orbital moment between the hard and easy axes and can be written as [70, 189]

$$K_{MC} = \left( \alpha \frac{n\xi}{4V} \right) \frac{\Delta\mu_L}{\mu_B} \quad (6.4)$$

where  $\xi$  is the spin-orbit coupling parameter,  $\alpha$  is the pre-factor that varies between 0 and 0.2 and is a function of electronic structure,  $n$  is the number of atoms per unit cell,  $V$  is the volume of the unit cell,  $\mu_B$  is the Bohr magneton, and  $\Delta\mu_L$  is the difference in orbital moments between the easy and hard magnetization axes [189]. The orbital moment

is proportional to the  $g$ -factor,  $g$ , that can be determined from the FMR measurements. For films the orbital asymmetry is given by [150]

$$\Delta\mu_L = \frac{\mu_s}{2}(g^\perp - g^\parallel) \quad (6.5)$$

where  $\mu_s$  is the spin magnetic moment and can be determined from the ratio of  $\mu_L/\mu_s = (g - 2)/2$  and the total magnetic moment  $\mu = \mu_s + \mu_L$ ,  $g^\perp$  and  $g^\parallel$  are the out-of-plane and in-plane  $g$ -factors, respectively. Superconducting quantum interference device (SQUID) magnetometer measurements are used to calculate  $\mu_s$ , where  $\mu_s = 2M_s/(N \cdot g)$ ,  $M_s$  is the saturation magnetization of the Co/Ni ML and  $N$  is the number of atoms per unit volume.

### 6.2.3 Dipolar magnetic anisotropy including surface roughness, $K_{DIP}$

The dipolar anisotropy coefficient can be expressed as:

$$K_{DIP} = K_V^{DIP} + K_S^{DIP}/d \quad (6.6)$$

where  $K_V^{DIP} = -\mu_0 M_s^2/2$  is the dipolar volume anisotropy coefficient of perfectly flat films, and  $d$  is ML thickness. If the roughness of the top and bottom surfaces are uncorrelated the dipolar surface anisotropy coefficient,  $K_S^{DIP}$  can be calculated analytically as  $K_S^{DIP} = K_{S,T}^{DIP} + K_{S,B}^{DIP}$ , where [190]

$$K_{S,T,B}^{DIP} = \mu_0 M_s^2 \frac{3}{8} \sigma_{T,B} \{1 - f[2\pi(\sigma_{T,B}/\xi_{T,B})]\} \quad (6.7)$$

Here  $K_{S,T}^{DIP}$  and  $K_{S,B}^{DIP}$  are the dipole surface anisotropy coefficients of the top and bottom interfaces, respectively.  $\sigma_{T,B}$  is the mean deviation of the top and bottom MLs surfaces from an ideally flat surface,  $\xi_{T,B}$  is an average lateral size of the terraces at the top and bottom MLs surfaces (see Figure 6.1), and  $f$  is the function calculated by Bruno [190]. In our calculations of  $K_S^{DIP}$  in Ta/Au/ $N \times$ [Co/Ni]/Au films, we will assume that  $\sigma_B = \sigma^{Au/Co}$  and  $\sigma_T = \sigma^{Ni/Au}$  are the roughnesses of the bottom and top surfaces of the Co/Ni MLs, respectively, and  $\xi_B = \xi^{Au/Co}$  and  $\xi_T = \xi^{Ni/Au}$  are the roughness periods of the bottom and top surfaces of the Co/Ni MLs, respectively.

Since the roughness of the top and bottom surfaces in the ML is nearly correlated, we also calculated  $K_S^{DIP}(calc)$  numerically. The calculations were done by Prof. Dieter Suess<sup>1</sup> for films with the correlated roughness of the top and bottom surfaces as shown in Figure 6.2. The numeric calculation will be used to determine the reduction of the anisotropy in the ML due to roughness. We also performed numerical calculations assuming that the top surface is rough and the bottom surface is flat. We will show later that  $K_{S,r-f}^{DIP}(calc)$  of a film with

<sup>1</sup>Prof. Dieter Suess, Department of Physics, University of Vienna, Austria

the rough top and the flat bottom surfaces is similar to that of a film with two correlated rough surfaces.

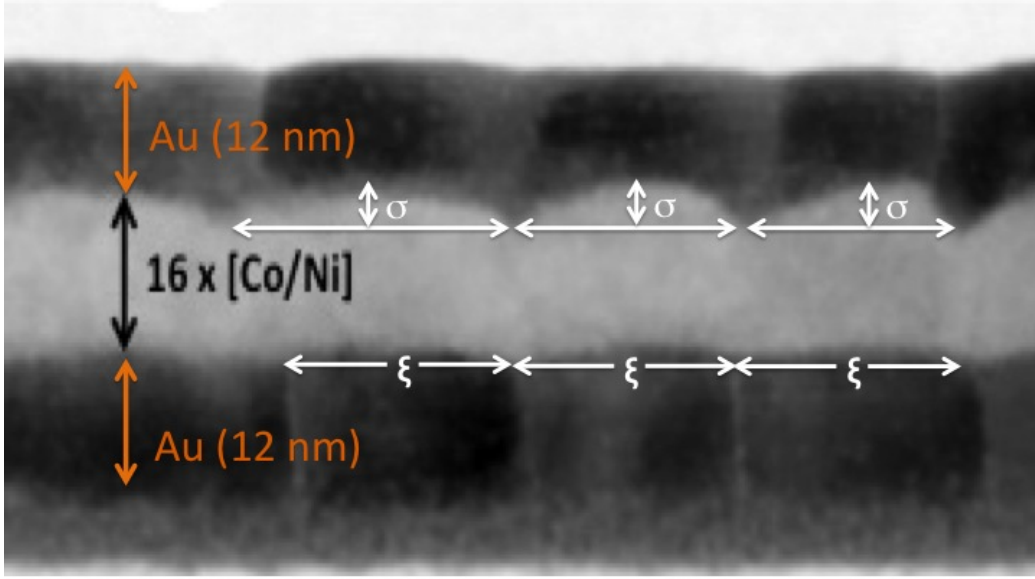


Figure 6.1: Cross-sectional bright-field STEM micrographs of Ta(3)/Au(12)/16 × [Co(0.21)/Ni(0.58)] / Au(12).

In order to calculate the effective shape anisotropy finite element simulations are performed. The topography of the top surface as function of the x and y coordinates is generated according to the following function

$$Z(x, y) = 2\sigma \cos^2\left(\frac{2\pi x}{\lambda}\right) \sin^2\left(\frac{2\pi y}{\lambda}\right) \quad (6.8)$$

where the wavelength is

$$\lambda = 2\xi \quad (6.9)$$

The parameters  $\xi$  and  $\sigma$  are given in Table 6.1. The parameters  $\xi$  and  $\sigma$  are calculated by using the STEM data of 16× [Co/Ni] and 32× [Co/Ni] MLs and extrapolating the data for the rest of the MLs samples. The STEM data of 32× [Co/Ni] MLs is shown in Figure 6.1. Two different geometries are calculated. The first geometry is calculated by extruding the top and bottom surfaces according to Eq. 6.8. Hence, the thickness  $d$ , that is along the z direction, is independent on the position x, y. For the second geometry we consider that the bottom surface is flat and the top surface has roughness of the form given by the function

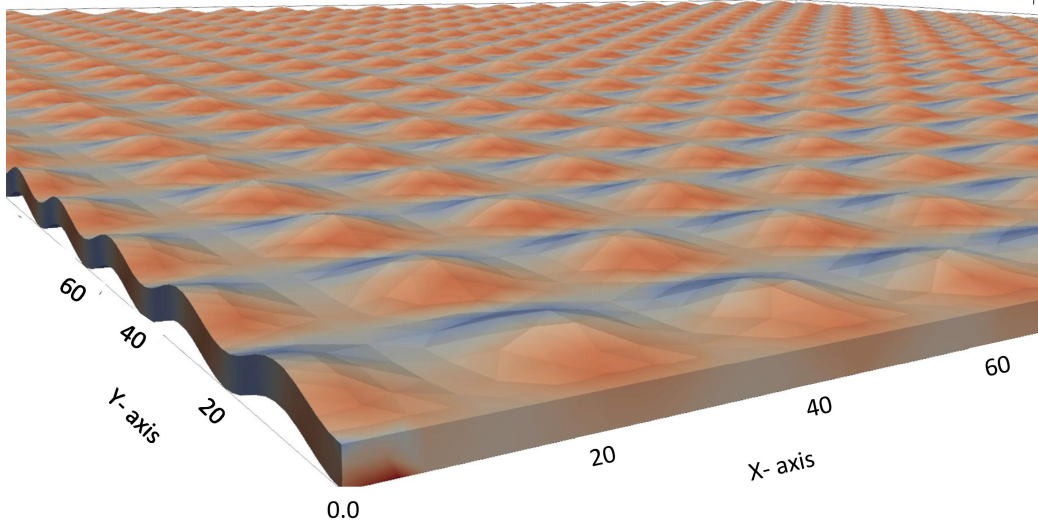


Figure 6.2: Simulated ML roughness used for the numerical calculation of the total dipolar surface anisotropy coefficient,  $K_S^{DIP}(calc)$ .

$Z(x, y)$  (see Eq.6.8). The average thickness of the film is same and equals  $d$ . The dimension in  $x$  and  $y$  direction is  $500 \text{ nm} \times 500 \text{ nm}$ . The obtained volume is discretized in tetrahedral finite elements with mesh size of  $4 \text{ nm}$ .

In order to calculate the stray field for a given magnetization which points either in the direction (001) or (010) the hybrid finite element/boundary element method is employed [191] using a magnetic scalar potential. The open boundary problem is accurately solved by the boundary element method, which effectively transforms the boundary condition of vanishing potential at infinity to the boundary of the magnet. The magnetostatic energy is calculated for the out-of-plane,  $E_{\perp}$ , and in-plane magnetization,  $E_{\parallel}$ . The effective shape anisotropy is calculated as

$$K_{DIP}(calc) = \frac{1}{V}(E_{\parallel} - E_{\perp}) \quad (6.10)$$

In order to correct for the finite size of the simulated structure, we also evaluated Eq.6.10 for the corresponding film without surface roughness but for the same lateral dimensions and thickness, denoted by  $K_V^{DIP}$ . The effective anisotropy due to surface roughness can be approximated by

$$K_S^{DIP}(calc) = K_{DIP}(calc) - K_V^{DIP} \quad (6.11)$$

which is not dependent on the lateral dimension of the simulated film in the first order.

From  $K_{DIP}$  (Eq.6.6) and  $K_{DIP}(calc)$  (Eq.6.10) one can calculate the average demagnetization fields,  $H_{DIP}$  and  $H_{DIP}(calc)$ , respectively, in the films along the direction perpendicular to the film surface using formula

$$H = -\frac{1}{\mu_0} \frac{2K_{DIP}}{M_s} \quad (6.12)$$

#### 6.2.4 Surface anisotropy, $K_S$

The surface anisotropy arises from the fact that surface atoms have an asymmetric environment as compared with bulk atoms. The total surface anisotropy coefficient of our Ta/Au/ $N \times$  [Co/Ni]/Au ML is given by

$$\frac{K_S}{d} = \frac{(K_S^{Au/Co} + K_S^{Ni/Au})}{N \cdot t_{BL}} + \frac{(2N-1)}{N \cdot t_{BL}} K_S^{Co/Ni} \quad (6.13)$$

where  $K_S^{Au/Co}$ ,  $K_S^{Ni/Au}$  and  $K_S^{Co/Ni}$  are the surface magnetocrystalline anisotropy coefficients at Au/Co (the bottom interface between Au and the Co/Ni ML), Ni/Au (the top interface between the Co/Ni ML and Au), and Co/Ni interfaces, respectively. In Eq.6.13 we assumed that the Co/Ni and Ni/Co interface anisotropies are the same. The ML thickness  $d = N \cdot t_{BL}$ , where  $N$  is number of multilayers and  $t_{BL} = t_{Co} + t_{Ni}$  is the thickness of the Co/Ni bilayer.

In rough films, some in-plane magnetic atoms are missing at the surface, which reduces the asymmetry character of the surface atoms. In our Ta/Au/ $N \times$  [Co/Ni]/Au ML this causes reduction in the magnetocrystalline surface anisotropy coefficients,  $K_S^{Au/Co}$ ,  $K_S^{Ni/Au}$  and  $K_S^{Co/Ni}$ . This effect has been calculated by Bruno [192] and for the Au/Co and Ni/Au interfaces can be calculated as

$$\Delta K_S^{Au/Co} = -2K_S^{Au/Co} \frac{\sigma^{Au/Co}}{\xi^{Au/Co}} \quad (6.14)$$

$$\Delta K_S^{Ni/Au} = -2K_S^{Ni/Au} \frac{\sigma^{Ni/Au}}{\xi^{Ni/Au}} \quad (6.15)$$

where  $\sigma^{Au/Co}$  and  $\sigma^{Ni/Au}$  are the film surface roughnesses, and  $\xi^{Au/Co}$  and  $\xi^{Ni/Au}$  are the film surface roughness periods at the bottom and top interfaces of the Co/Ni ML with Au.

In addition, roughness will also affect the magnetocrystalline surface anisotropy coefficient at Co/Ni interfaces across the ML. This can be calculated as

$$\Delta K_S^{Co/Ni} = -\frac{2K_S^{Co/Ni}}{2N-1} \sum_{i=1}^{2N-1} \frac{\sigma_i^{Co/Ni}}{\xi_i^{Co/Ni}} \quad (6.16)$$

where  $\sigma_i^{Co/Ni}$  and  $\xi_i^{Co/Ni}$  are the roughness and roughness period of the  $i$ -th Co/Ni interface of the ML, respectively.

Thus, to include the magnetocrystalline surface anisotropy that arises from the roughness of our ML,  $K_S^{Au/Co}$ ,  $K_S^{Ni/Au}$  and  $K_S^{Co/Ni}$  in Eq.6.13 have to be substituted with  $K_S^{Au/Co} + \Delta K_S^{Au/Co}$ ,  $K_S^{Ni/Au} + \Delta K_S^{Ni/Au}$  and  $K_S^{Co/Ni} + \Delta K_S^{Co/Ni}$ , respectively.

### 6.2.5 Inter-diffusion induced anisotropy energy

Another source of anisotropy could also be due to the inter-diffusion of Au into the Co/Ni ML. According to Néel's model, diffusion of Au in the Co/Ni ML will introduce randomness in the magnetic pair bonds, which will reduce the interface anisotropy [50]. This is in agreement with the calculations by Draaisma and de Jonge [193] that show that the magnetic anisotropy from the pair interaction strongly decrease with the increase of the degree of mixing. Broeder et al. [194] used ion-beam sputtering to deposit Au/Co ML. The ML had rather diffuse interfaces due to the Ar-ion bombardment during the growth. To expel Au from Co layers the ML were annealed up to 300° C resulting in strong increase of the interface anisotropy, enhanced PMA. This increase in PMA, was accompanied by a strong increase of the intensity of the multilayer reflections observed in X-ray diffraction (XRD) experiments, and was interpreted as a sharpening of the Co/Au interfaces.

Since inter-diffusion is the most pronounced at the interface we expect that the reduction of PMA will scale with the film thickness. In the Co/Ni ML the contribution to anisotropy due to inter-diffusion will decrease with the number of multilayers. In this thesis we will use element mapping based on energy-dispersive X-ray spectroscopy (EDXS) in transmission electron microscopy (TEM) to detect the inter-diffusion of Au in the Co/Ni ML. We will show that the Au concentration in the Co/Ni ML can be reduced by post-deposition annealing of the ML. Comparing magnetic properties of the Co/Ni ML before and after annealing will help us understand how the Au inter-diffusion impacts the magnetic anisotropy of the ML.

## 6.3 Studied structure

Ta(3)/Au(12)/ $N \times [\text{Co}(0.21)/\text{Ni}(0.58)]/\text{Au}(12)$  films shown in Figure 6.3 were deposited at room temperature on Si (100) wafers by means of magnetron sputtering, where the numbers in parentheses indicates the layer thicknesses in nm, and  $N = 4, 6, 8, 10, 16, 32$  and  $64$  is the number of bilayer repeats. These multilayer samples were also annealed at 523 and 553 K for 1 hour to study the post-annealing effects. Co ( $a_{Co, fcc} = 0.354 \text{ nm}$ ) [186] and

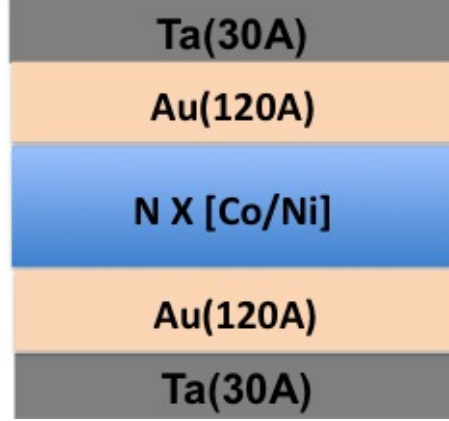


Figure 6.3: Structure illustration of the deposited samples.

$\text{Ni}(a_{\text{Ni},fcc} = 0.352 \text{ nm})$  [187] are closely matched. and  $\text{Cu}(a_{\text{Cu},fcc} = 0.361 \text{ nm})$  [195] are closely lattice matched. Therefore, it is difficult to resolve the X-ray diffraction peaks of  $\text{Cu}(111)$  and  $\text{Co/Ni}(111)$ . To resolve the seed layer and  $\text{Co/Ni}$  ML X-ray peaks and study the strain effects,  $\text{Co/Ni}$  MLs are grown on top of an Au seed layer. The Au inter-planer distances are about 14% larger than that of Co and Ni resulting in large separation of  $\text{Au}(111)$  and  $\text{Co/Ni}(111)$  X-ray peaks. This is the reason that we use Au as a seed layer to understand the effect of strain on the PMA of  $\text{Co/Ni}$  MLs.

## 6.4 As-deposited films

### 6.4.1 X-ray measurements:

Figure 6.4 (a) and (b) represent the out-of-plane and in-plane X-ray diffraction measurements, respectively, of  $\text{Ta}(3)/\text{Au}(12)/N \times [\text{Co}(0.21)/\text{Ni}(0.58)]/\text{Au}(12)$  with  $N = 4, 6, 8, 10, 16, 32$  and  $64$ . The out-of-plane X-ray measurements, Figure 6.4 (a), show two major Bragg peaks that correspond to Au (111) and Co/Ni (111) planes. The dashed black lines at  $38.22^\circ$  and  $44.54^\circ$  represents the expected positions of Au and Co/Ni (111) peaks, respectively, in the unstrained lattices. The position of the Co/Ni (111) peak shifts from  $44.42^\circ$  to  $43.40^\circ$  with the change of  $N$  from 64 to 4. This shows that the spacing between the (111) planes,  $d_{111}$ , in the Co/Ni ML increases with decreasing  $N$ . The change in spacing between Co/Ni (111) planes as a function of  $N$  is shown in Figure 6.5 (a) (left axis). The presence of thickness fringes are seen on both sides of the two primary peaks of Au(111) and Co/Ni(111) (see Fig. 1(a)). We also obtained the thickness of  $N \times [\text{Co}(0.21)/\text{Ni}(0.58)]$  from the period of oscillation of the thickness fringes. The calculated thicknesses are the same as measured by the thickness monitor.

The dashed line at  $76.49^\circ$  (see Figure 6.4(b)) represents the expected position of the unstrained Co/Ni (220) peak. For  $N = 64$ , the Co/Ni (220) peak is shifted to  $76.22^\circ$ .



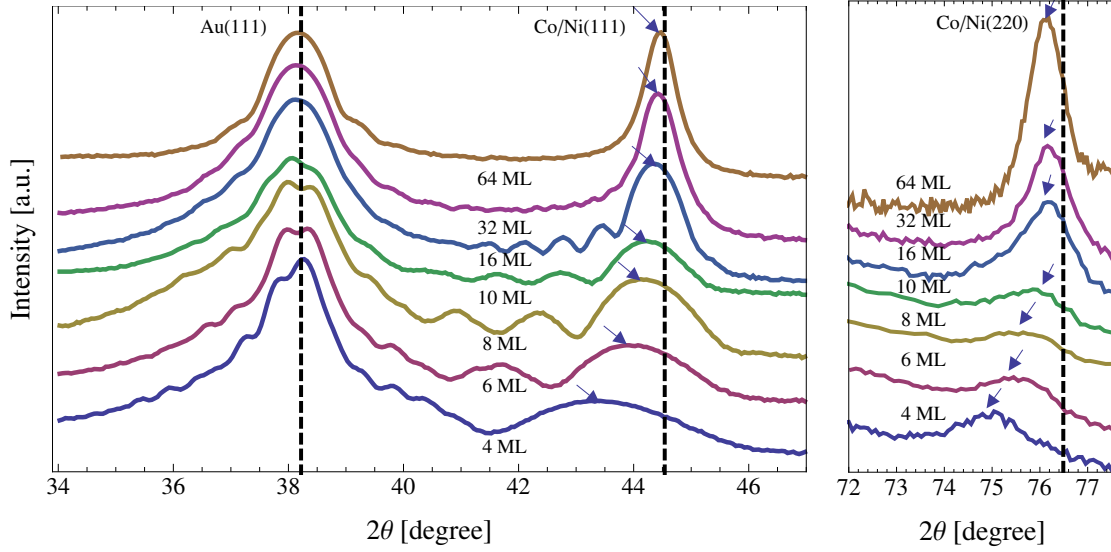


Figure 6.4: (a) Out-of-plane and (b) in-plane X-ray measurements of as-deposited Ta(3)/Au(12)/ $N \times [\text{Co}(0.21)/\text{Ni}(0.58)]/\text{Au}(12)$  with  $N = 4, 6, 8, 10, 16$  and  $32$ . The major X-ray diffraction peaks at  $38.22^\circ$ ,  $44.54^\circ$  and  $76.49^\circ$  are respectively from Au (111),  $N \times [\text{Co/Ni}]$  (111) and  $N \times [\text{Co/Ni}]$  (220). The dashed black lines at  $38.22^\circ$  and  $44.54^\circ$  represents the expected positions of Au (111) and Co/Ni (111) peaks, respectively. The arrows indicate the fitted positions of the  $N \times [\text{Co/Ni}]$  (111) and (220) peaks. We assumed that the Co/Ni ML have fcc structure in agreement with STEM results by Gottwald et al. [156].

With decreasing  $N$ , the Co/Ni (220) peak further shifts to lower angles, which indicates an increase in spacing between the (220) lattice planes,  $d_{(220)}$ . This change in the lattice spacing as a function of  $N$  is shown in Figure 6.5(a) (right axis). This behaviour is expected since the distance between the (220) planes in Au is 14 % larger than the distance between the (220) planes of the Co/Ni MLs.

In a strained film, it is assumed that the volume/atom of the film remains constant [196]. Therefore, it is expected that if there is lattice expansion along one direction, there should be lattice contraction in the perpendicular direction. However, in the present case, with the decrease in the number of MLs, the spacings between both the Co/Ni (111) planes parallel to the film surface and the Co/Ni (220) planes orthogonal to the film surface increases. Diffusion of Au atoms into the Co/Ni MLs associated with lattice expansion of the latter ones could be an explanation for the observed behaviour, as shown in the next section.

The ratio  $d_{111}/d_{220}$  of the as-deposited Co/Ni MLs is plotted as a function of  $N$  in Figure 6.5(b). From Figure 6.5(b) it is evident that  $d_{111}/d_{220}$  decreases with  $N$  for  $N \leq 10$ . For  $N \geq 16$ ,  $d_{111}/d_{220}$  gradually increases approaching to the ideal cubic crystal  $d_{111}/d_{220}$  ratio for  $N = 64$ . The observed tetragonal distortion of the Co/Ni ML lattice for  $N \leq 10$  can have profound effect on the intrinsic magnetic properties such as inducing difference in orbital moments between [111] and [220] crystal directions.

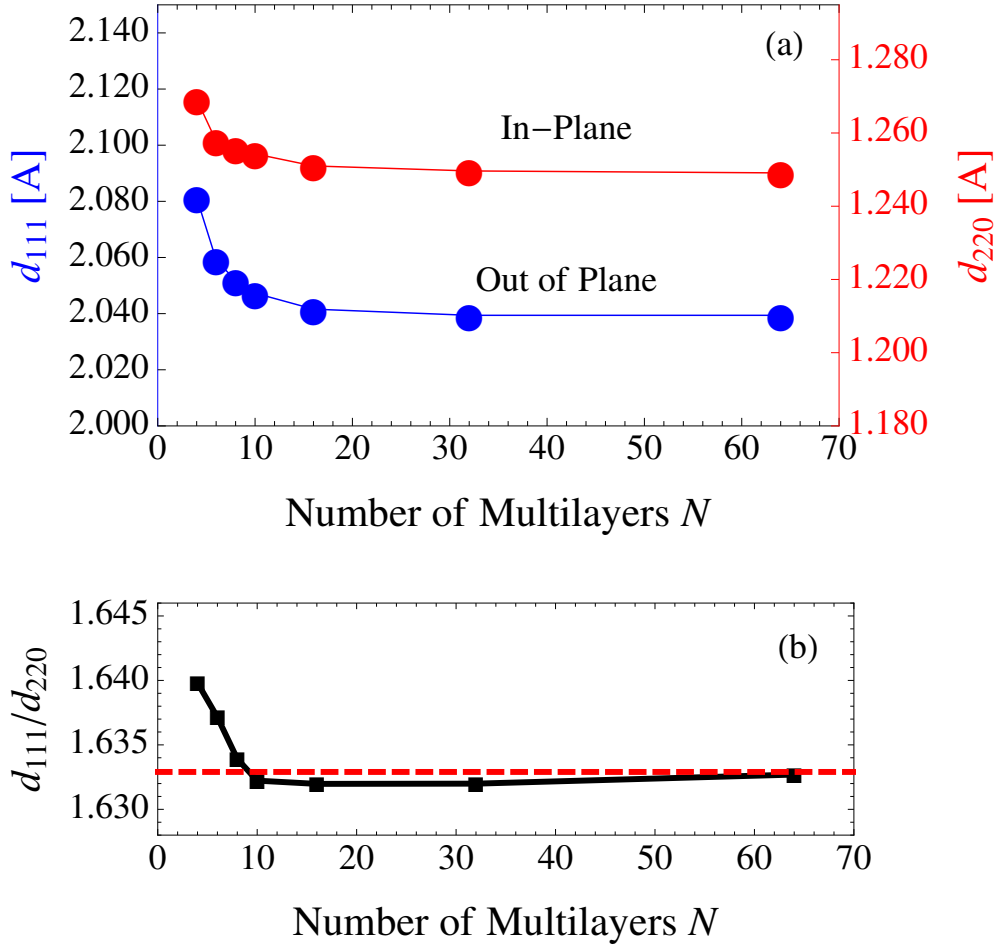


Figure 6.5: (a) The spacing between the (111) ( $d_{111}$ ) and (220) ( $d_{220}$ ) lattice planes and (b)  $d_{111}/d_{220}$  of the as-deposited Co/Ni ML as a function of  $N$ . The dashed red line represents the expected  $d_{111}/d_{220}$  for the ideal cubic lattice structure. The X-ray measurements are performed at room temperature.

#### 6.4.2 Microstructure of Co/Ni MLs

Bright-field and high-angle annular dark-field scanning transmission electron microscopy (TEM) imaging as well as element mapping based on energy-dispersive X-ray spectroscopy (EDXS) were performed at 200 kV with a Talos F200X microscope equipped with a Super-X EDXS detector system (FEI). Prior to TEM analysis, the specimen mounted in a high-visibility low-background holder was placed for 10 s into a Model 1020 Plasma Cleaner (Fischione) to remove organic contamination.

To analyze the element distribution, EDXS analyses were performed in scanning TEM (STEM) mode for the Co/Ni MLs samples with  $N = 16$  and 32. In particular, Figure 6.6 (a) shows a cross-sectional bright-field STEM image of Ta(3)/Au(12)/ $N \times [\text{Co}(0.21)/\text{Ni}(0.58)]/\text{Au}(12)$ , and Figure 6.6 (b), (c) and (d) present the corresponding Au, Ni, and Co element

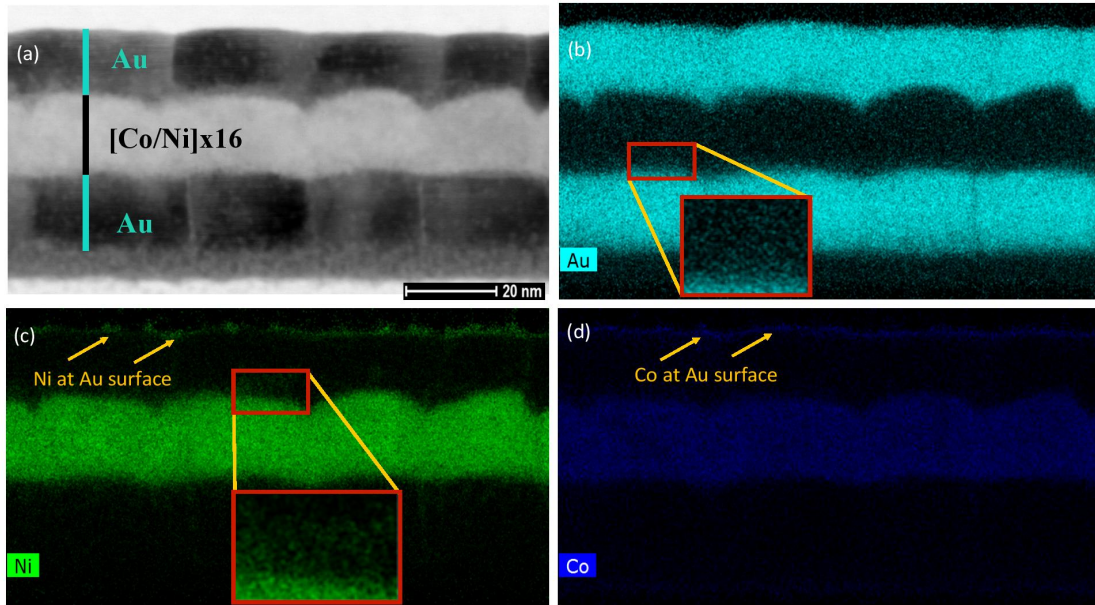


Figure 6.6: (a) Cross-sectional bright-field STEM micrograph of Ta(3)/Au(12)/16x[Co(0.21)/Ni(0.58)]/Au(12) (b) with corresponding element maps for Au (c) for Ni and (d) for Co obtained by EDXS analysis.

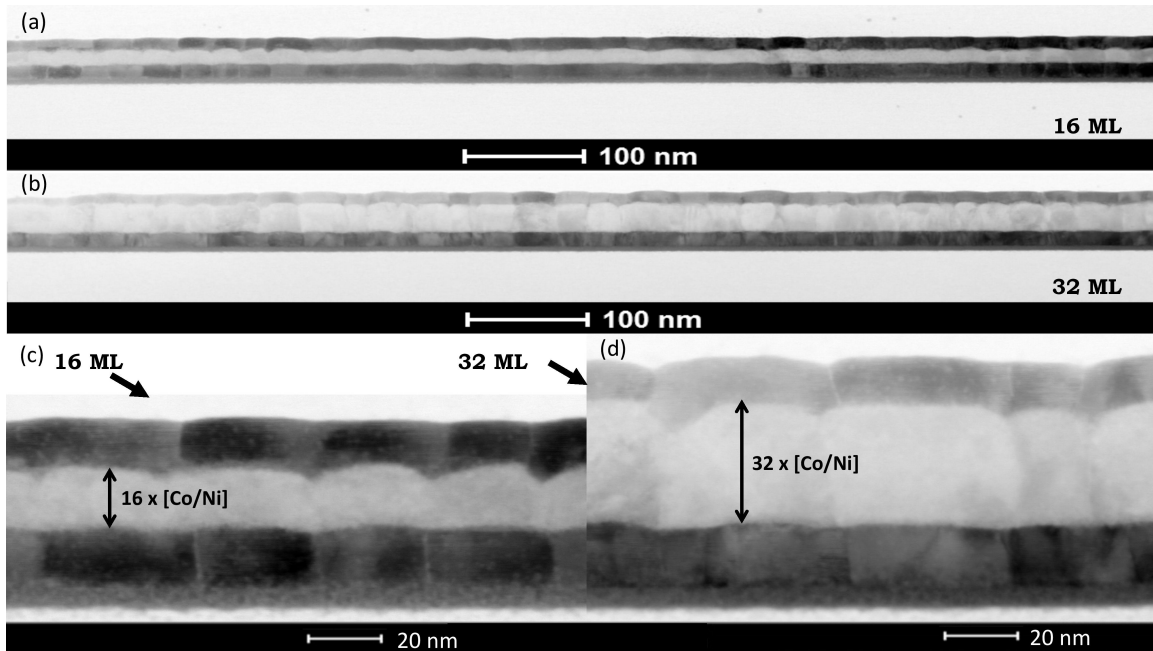


Figure 6.7: Cross-sectional bright-field STEM micrographs of Ta(3)/Au(12)/16x[Co(0.21)/Ni(0.58)]/Au(12) (a) and (c), and of Ta(3)/Au(12)/32x[Co(0.21)/Ni(0.58)]/Au(12) (b) and (d).

maps, respectively. According to Figure 6.6 (b), some gold is detected within the Co/Ni MLs with a higher Au concentration close to the bottom Au/[Co/Ni] interface. Such gold diffusion into the ML stack might explain the Co/Ni MLs lattice expansion observed in the X-ray diffraction measurements. Additionally, Figure 6.6 (c) and 4(d) show the presence of Co and Ni within both top and bottom gold layers, in particular along Au grain boundaries. It should be mentioned, however, that small Co and Ni background signals within both Au layers can be due to fluorescence excitation triggered by higher-energy Au X-rays. There is also some Co and Ni at the top of the film stack. This can be explained by a small amount of Co and Ni that effectively floats on the surface during Au deposition.

Figure 6.7(a) and (b) are cross-sectional bright-field overview STEM images of Ta(3)/Au(12)/16×[Co(0.21)/Ni(0.58)]/Au(12) (16 MLs) and Ta(3)/Au(12)/32×[Co(0.21)/Ni(0.58)]/Au(12) (32 MLs), respectively. For both samples, the Co/Ni MLs were grown on top of a Au seed layer which is characterized by an average Au grain size (average roughness period) of  $\xi = \xi^{Au/Co} = 21$  nm. Regarding the top ML/Au interface, the average roughness period,  $\xi = \xi^{Ni/Au}$ , is 23 nm for the 16 MLs and 25 nm for the 32 MLs sample, respectively. The average roughness (i.e. the mean deviation from an ideally flat surface) at the bottom Au/ML interface is  $\sigma = \sigma^{Au/Co} = 0.8$  nm, and at the top ML/Au interface  $\sigma = \sigma^{Ni/Au}$  is 1.6 nm for 16 MLs and 1.8 nm for 32 MLs. This analysis shows that both roughness and roughness period increase with the number  $N$  of ML. The increase in roughness period is clearly visible in the magnified cross-sectional STEM images of 16 and 32 MLs in Figure 6.7(c) and (d). We used the values of  $\xi$  and  $\sigma$  for  $N = 0$  (the bottom ML interface), 16 and 32 to extrapolate  $\xi$  and  $\sigma$  for the rest of our MLs.

Table 6.1 summarizes the roughness,  $\sigma$ , and roughness period,  $\xi$ , of the Co/Ni MLs as a function of  $N$ . These values are used to analytically calculate  $K_{DIP}$  (Eq.6.6) and  $H_{DIP}$  (Eq.6.12), and numerically calculate  $K_{DIP}(calc)$  and  $H_{DIP}(calc)$ .

Figure 6.8 shows the plots of  $K_S^{DIP}/d$ ,  $K_S^{DIP}/d(calc)$  and  $K_{S,r-f}^{DIP}/d(calc)$  as a function of  $N$ . We calculated  $K_S^{DIP}/d = (K_{S,T}^{DIP} + K_{S,B}^{DIP})/d$  by using equation Eq. (6.7) and assuming that the roughness of top and bottom surfaces of the MLs are uncorrelated.  $K_S^{DIP}/d(calc)$  is numerically calculated assuming correlated roughness of the top and bottom film surfaces, and  $K_{S,r-f}^{DIP}/d(calc)$  is numerically calculated assuming rough top and flat bottom film surfaces.

From Figure 6.8 it is clear that  $K_S^{DIP}(calc)$  and  $K_{S,r-f}^{DIP}/d(calc)$  are practically the same for  $N = 32$  and comparable for  $N = 6$ . This indicates that the dipole surface anisotropy is similar if films have one rough and one flat surfaces or if they have two correlated rough surfaces. The calculations of  $K_S^{DIP}/d$  by using Eq. (6.7) take into account the roughness of top and bottom surfaces.  $K_S^{DIP}/d$  for one flat and one rough surfaces is similar to the numerically calculated  $K_{S,r-f}^{DIP}/d(calc)$  for thick films. This shows why  $K_S^{DIP}/d$  of films with uncorrelated rough surfaces is about two times larger than the numerically calculated  $K_S^{DIP}(calc)$  for films with two correlated film surface.

$N$	$d$	$\xi$	$\sigma$	$K_V^{DIP}$	$K_S^{DIP}/d$	$K_{DIP}$	$H_{DIP}$	$K_S^{DIP}/d(calc)$	$K_{DIP}(calc)$	$H_{DIP}(calc)$
	(nm)	(nm)	(nm)	( $10^5$ J/m <sup>3</sup> )	( $10^4$ J/m <sup>3</sup> )	( $10^5$ J/m <sup>2</sup> )	( $10^5$ A/m)	( $10^4$ J/m <sup>3</sup> )	( $10^5$ J/m <sup>3</sup> )	( $10^5$ A/m)
0	-	22.5	0.80	-	-	-	-	-	-	-
4	3.2	23.0	1.20	-2.26	3.13	-1.95	-5.17	0.62	-2.20	-5.83
6	4.8	23.3	1.32	-2.96	3.02	-2.65	-6.16	0.86	-2.87	-6.66
8	6.4	23.6	1.40	-3.11	2.49	-2.86	-6.47	0.83	-3.02	-6.84
10	8.0	23.8	1.46	-3.62	2.45	-3.37	-7.08	0.89	-3.53	-7.40
16	12.8	24.5	1.60	-3.62	1.70	-3.45	-7.23	0.73	-3.55	-7.44
32	25.6	26.0	1.80	-3.62	0.96	-3.52	-7.39	0.44	-3.58	-7.50
64	51.2	27.5	2.00	-3.41	0.50	-3.36	-7.26	0.25	-3.39	-7.32

Table 6.1:  $N$ ,  $d$ ,  $\sigma$ , and  $\xi$  are the number, thicknesses, roughness and roughness period of the Co/Ni MLs, respectively. For  $N = 0$ ,  $\sigma = \sigma^{Au/Co}$  and  $\xi = \xi^{Au/Co}$  are the roughness and roughness period of the bottom Co/Ni MLs surface (Au/ML interface). For  $N > 0$ ,  $\sigma = \sigma^{Ni/Au}$  and  $\xi = \xi^{Ni/Au}$  are the roughness and roughness period of the top Co/Ni MLs surface (ML/Au interface).  $K_V^{DIP} = -\mu_0 M_s^2/2$  is the dipolar volume anisotropy coefficient of a perfectly flat MLs,  $K_S^{DIP} = K_{S,T}^{DIP} + K_{S,B}^{DIP}$ , where  $K_{S,T}^{DIP}$  and  $K_{S,B}^{DIP}$  are calculated using Eq.6.7,  $K_{DIP} = K_V^{DIP} - K_S^{DIP}/d$ , and  $H_{DIP} = 2K_{DIP}/\mu_0 M_s$ .  $K_{DIP}(calc)$  and  $H_{DIP}(calc)$  are the total dipolar anisotropy coefficient and field of rough MLs calculated using numerical methods.

From Figure 6.6 and Figure 6.7 it is clear that the top and bottom surfaces of the Co/Ni MLs are correlated, even though the roughness period of the top surface increases slightly with  $N$ . Since  $K_S^{DIP}/d(calc)$  is determined assuming correlated top and bottom surfaces, we will use  $K_S^{DIP}/d(calc)$  to determine anisotropy,  $K_u$ , of our Co/Ni MLs.

### 6.4.3 Magnetic properties of Co/Ni MLs

The field dependence of the magnetization is measured using a SQUID magnetometer. The measurements are performed in the magnetic fields up to  $5.5 \times 10^6$  A/m (70 kOe) and with the field direction parallel and perpendicular to the sample surface.  $K_u(SQUID)$  is calculated from the M(H) curve by finding the area enclosed between the hard and easy axes M(H) curves and by adding to this area  $K_{DIP}(calc)$  calculated using Eq. (6.10) [50]. The numerically calculated values of  $K_{DIP}(calc)$  as a function of  $N$  are listed in Table 6.1.

FMR measurements were carried out at room temperature using terminated waveguide over the frequency range from 45 to 70 GHz. To account for the reduction in the dipole anisotropy due to the MLs roughness Eq.(3.40) and Eq. (3.37) are modified as:

$$\begin{aligned}
M_{eff}^{\parallel} &= M_{s,corr}^{\parallel} - \frac{2K_2^{\perp}}{\mu_0 M_s^{\perp}} \\
M_{eff}^{\perp} &= M_{s,corr}^{\perp} - \frac{2K_2^{\perp}}{\mu_0 M_s^{\perp}} - \frac{2K_4^{\perp}}{\mu_0 M_s^{\perp}}
\end{aligned} \tag{6.17}$$

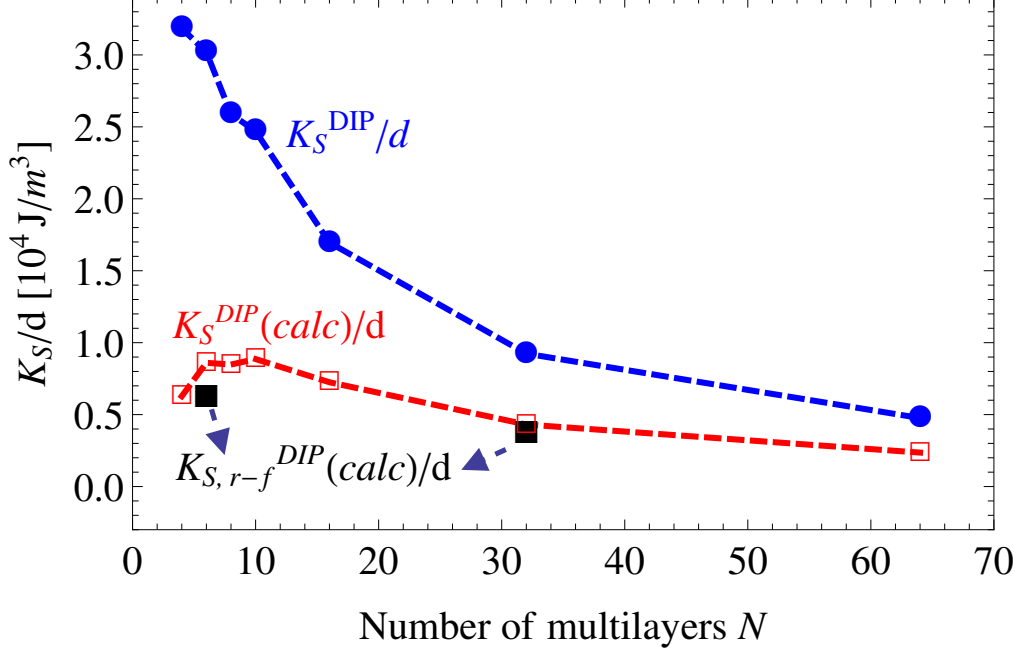


Figure 6.8: Analytical ( $K_S^{DIP}/d = (K_{S,T}^{DIP} + K_{S,B}^{DIP})/d$ ) and numerical ( $K_S^{DIP}/d(calc)$  and  $K_{S,r-f}^{DIP}/d(calc)$ ) calculations of the dipole surface anisotropy as a function of  $N$ .  $K_S^{DIP}/d$  is calculated from Eq.6.7 and assuming that the roughness of top and bottom surfaces of the ML are uncorrelated.  $K_S^{DIP}/d(calc)$  is calculated assuming correlated roughness of the top and bottom film surfaces, and  $K_{S,r-f}^{DIP}/d(calc)$  is calculated assuming rough top and flat bottom film surfaces.

where  $M_{s,corr}^{\parallel} = M_s^{\parallel} - 2K_S^{DIP}/(M_s d)$  and  $M_{s,corr}^{\perp} = M_s^{\perp} - 2K_S^{DIP}/(M_s d)$  are the in-plane and perpendicular to the plane saturation magnetizations corrected for the ML roughness, respectively. The dipolar surface anisotropy coefficients, due to the MLs roughness, are calculated numerically,  $K_S^{DIP} = K_S^{DIP}(calc)$ , and are listed in Table 6.1. We will assumed that the saturation magnetization is independent on the direction of magnetic field  $M_s^{\perp} = M_s^{\parallel}$ . This is a good approximation since  $(g^{\perp} - g^{\parallel})/g^{\parallel} < 1\%$ .

$M_s$  and  $K_u(SQUID)$  of the as-deposited Co/Ni MLs measured at 5 and 300 K by SQUID, and  $K_2^{\perp}$ ,  $K_4^{\perp}$ ,  $K_u(FMR) = K_2^{\perp} + K_4^{\perp}$ ,  $g^{\perp}$ , and  $g^{\parallel}$  of the as-deposited Co/Ni MLs measured at 300 K by FMR are summarized in Table 6.2. Due to roughness the demagnetization field in the Co/Ni MLs is lower than expected for ideally flat films. For this reason, the anisotropy coefficients in Table 6.2 are calculated using  $K_{DIP}(calc)$  listed in Table 6.1:  $K_u(SQUID)$  is calculated from the M(H) curve by finding the area enclosed between the hard axis M(H) curve and adding to this area  $K_{DIP}(calc)$ , and  $K_u(FMR)$  is calculated from Eqs.6.17.

$K_4^{\perp}$  and  $g^{\perp}$  of the Co/Ni MLs with  $N = 64$  are not determined since we observed standing spin waves with the k-vector perpendicular to the surface of the MLs. The induced spin waves are possible due to the large thickness of this 64 MLs that exceeds 50 nm.

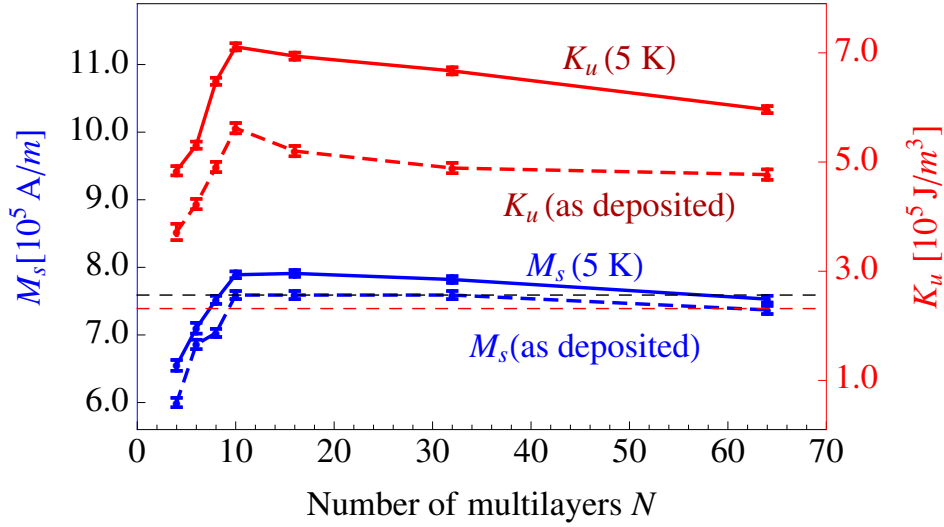


Figure 6.9: The  $M_s$  and  $K_u$  of the as-deposited Co/Ni MLs as a function of number of multilayers measured at 5 and 300 K. The dotted black and red lines represents  $M_s$  of Co/Ni MLs calculated assuming bulk  $M_s$  values for Co and Ni at 0 K and 300 K respectively [69]

Table 6.2 shows that the total anisotropy coefficients measured by FMR,  $K_u(\text{FMR})$ , are the same as those measured by SQUID,  $K_u(\text{SQUID})$ , at 300 K. For this reason in the analyses of  $K_u$  as a function of  $N$  we will only consider  $K_u(\text{SQUID})$  values.

Figure 6.9 shows the  $M_s$  and  $K_u$  of Ta(3)/Au(12)/ $N \times [\text{Co}(0.2)/\text{Ni}(0.6)]/\text{Au}(12)$  as a function of  $N$  measured at 5 and 300 K by SQUID.  $M_s$  increases with the increase in  $N$ , stays nearly constant for  $10 \leq N \leq 32$ , and then decreases for  $N = 64$ . The lower  $M_s$  for  $N \leq 8$  is at least in part due to the inter-diffusion of Au into the Co/Ni MLs that was directly observed by the EDXS analyses in the TEM (Figure 6.6).

$K_u$  also increases sharply with  $N$  for  $N \leq 10$  and then decreases with the further increase of  $N$ . The similar trend has already been observed by Qiu et al. [124] in  $\text{Co}_{90}\text{Fe}_{10}/\text{Pt}$  superlattice structures and Co/Ni MLs by Sabino et al. [29]. At 300 K,  $M_s$  and  $K_u$  are reduced by approximately 5.7 % and 29 %, respectively relative to their values at 5 K. The increase in  $K_u$  with temperature is nearly proportional to the increase in  $M_s^2$  with temperature as expected from the mean field theory. It is important to point out that the trends of both  $M_s$  and  $K_u$  do not change with increase of temperature from 5 to 300K, which indicates that they are not affected by thermal fluctuations. Thus, the drop of  $K_u$  for  $N \leq 8$  is not due to the onset of superparamagnetism in ultra thin films.

FMR measurements show that both  $g^\perp$  and  $g^\parallel$  decreases with the increase of  $N$ , and that  $g^\perp$  is larger than the  $g^\parallel$  for all  $N$ 's. Later is in agreement with the results by Shaw et al.[189] for CoFe/Ni MLs grown on a Cu seed layer.

$N$	5 K		300 K							
	$M_s$	$K_u(\text{SQUID})$	$M_s$	$K_u(\text{SQUID})$	$K_2^\perp(\text{FMR})$	$K_4^\perp(\text{FMR})$	$K_u(\text{FMR})$	$g^\perp$	$g^\parallel$	$g^\perp - g^\parallel$
	( $10^3 \text{A/m}$ )	( $10^5 \text{J/m}^3$ )	( $10^3 \text{A/m}$ )		(10 <sup>5</sup> J/m <sup>3</sup> )			$\pm 0.001$	$\pm 0.001$	$\pm 0.002$
	$\pm 8$	$\pm 0.03$	$\pm 7$	$\pm 0.04$	$\pm 0.02$	$\pm 0.02$	$\pm 0.04$			
4	655	4.84	600	3.72	3.87	-0.23	3.64	2.206	2.197	0.009
6	710	5.31	686	4.23	4.53	-0.38	4.15	2.193	2.182	0.011
8	752	6.48	703	4.91	5.30	-0.39	4.91	2.187	2.173	0.014
10	789	7.11	759	5.62	5.99	-0.39	5.60	2.182	2.163	0.019
16	791	6.94	759	5.20	5.73	-0.37	5.36	2.177	2.161	0.016
32	782	6.67	759	4.89	5.45	-0.69	4.76	2.169	2.156	0.013
64	753	5.96	737	4.77	4.89	-	-	-	-	-

Table 6.2:  $N$  is the number of the Co/Ni MLs, and  $M_s$  and  $K_u(\text{SQUID})$  are respectively the saturation magnetization and anisotropy of the as-deposited Co/Ni MLs measured by SQUID at 5 and 300 K.  $K_2^\perp$ ,  $K_4^\perp$ ,  $K_u(\text{FMR}) = K_2^\perp + K_4^\perp$  are anisotropy coefficients, and  $g^\perp$  and  $g^\parallel$  are g-factors of the Co/Ni MLs measured by FMR at 300 K.  $K_4^\perp$  and  $g^\perp$  of the Co/Ni MLs with  $N = 64$  are not determined since the perpendicular FMR measurements induce the spin wave oscillations in the MLs.  $K_S^{DIP}/d(\text{calc})$  and  $K_{DIP}(\text{calc})$  listed in Table 6.1 are used to calculate  $K_u(\text{SQUID})$  and  $K_u(\text{FMR})$ . For Co/Ni MLs with  $N = 4$  and 6, the error bar in  $M_s$  is  $12 \times 10^{23} \text{A/m}$  and the error bar in  $K_u(\text{SQUID})$  is 0.06 and 0.05  $\text{J/m}^3$ , respectively.

## 6.5 Annealed films

These multilayer samples were also annealed at 523 K and 553 K for 1 hour to study the post-annealing effects. Low angle X-ray reflectivity measurements were used to extract the film thicknesses. We also used a thickness monitor to measure the thicknesses of the sputtered films.

### 6.5.1 Structural and magnetic properties

The Au-Co and Au-Ni phase diagrams [197] depict no miscibility of Au into Co and a very small miscibility of Au into Ni below 523 K. For this reason we annealed the films at 523 and 553 K for one hour in attempt to expel the Au from the Co/Ni MLs. Broeder et al. [194] observed the increase in the perpendicular to surface magnetic anisotropy of ion beam sputtered Co/Au MLs after annealing at 523 and 553 K. They attributed the increase in PMA to the back diffusion of Au from Co layers.

In-plane and out-of-plane X-ray measurements were performed on all Co/Ni MLs after annealing at 523 K for one hour. Figure 6.10 shows the distance between the lattice planes  $d_{111}$  (left axis) and  $d_{220}$  (right axis) of the annealed Co/Ni MLs samples as a function of  $N$ . In comparison to the as-deposited samples, the spacing between both the lattice planes  $d_{111}$  and  $d_{220}$  slightly decreases after annealing (see Figure 6.5(a)). The reduction in the lattice



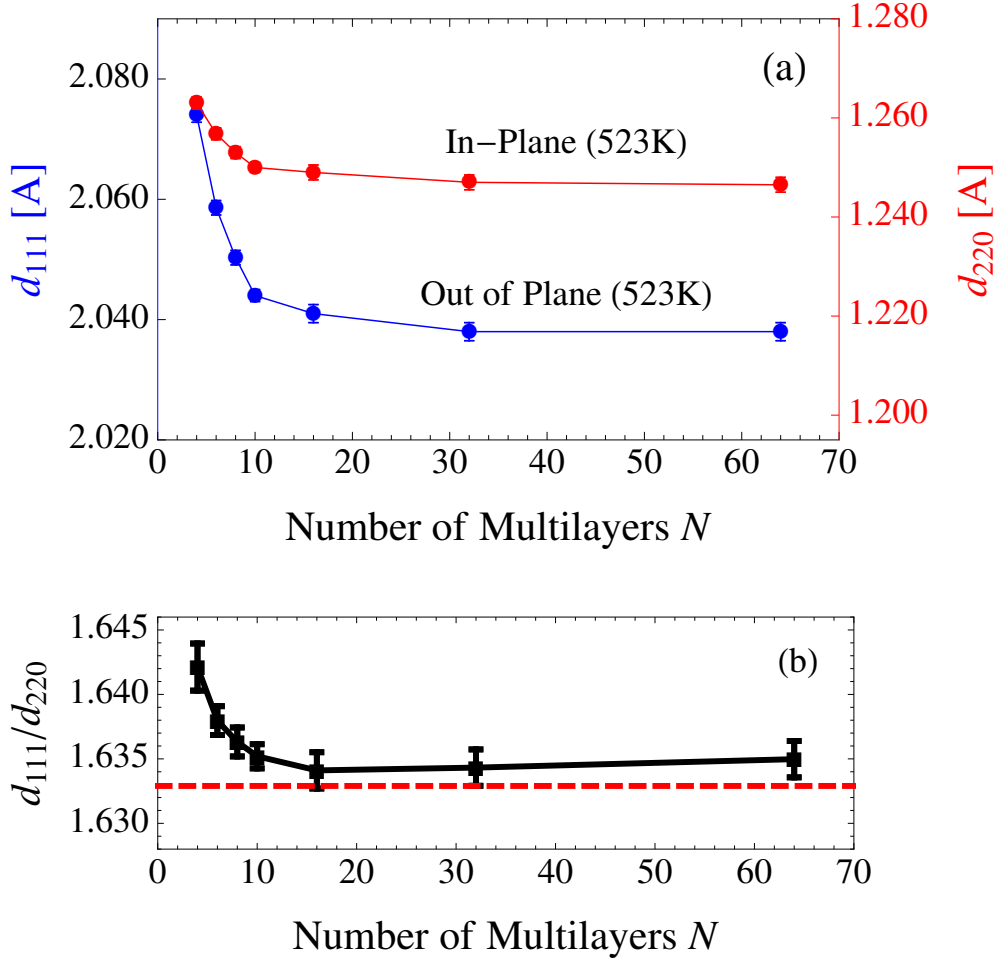


Figure 6.10: The spacing between the (111) and (220) lattice planes of the Co/Ni MLs as a function of  $N$  annealed at 523 K. The X-ray measurements are performed at room temperature.

volume due to annealing and in respect to unstrained Co/Ni lattice is 9%. This supports the hypothesis that during the annealing process a small amount of Au leaves the crystal structure of the Co/Ni MLs.

The out-of-plane X-ray measurements also show an improvement in the texture of the Co/Ni MLs, the full-width-at-half-maximum of rocking curve is reduced by  $0.2^\circ$ . This could result from grain growth and annihilation of the grains that do not grow along the (111) crystal orientations.

Figure 6.11 shows the  $M_s$  and  $K_u$  of the as-deposited and annealed (at 523 K) Co/Ni MLs as a function of number of MLs. There is an increase of both  $M_s$  and  $K_u$  after annealing the MLs samples. However, the increase in  $M_s$  and  $K_u$  is significantly larger for  $N \leq 10$ , where the concentration of Au is proportionally higher. This suggests that Au diffusion into the Co/Ni MLs causes at least in-part reduction of  $M_s$ . This may also indicate that Au

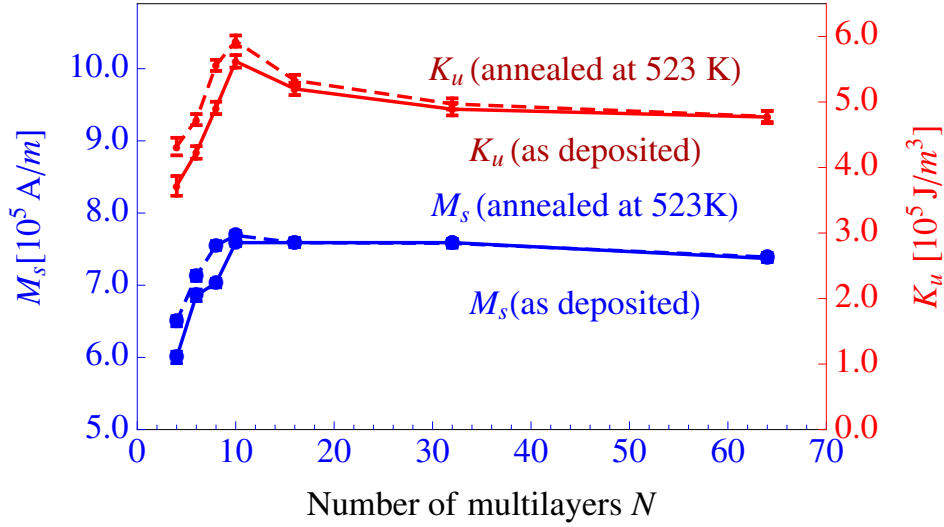


Figure 6.11: The  $M_s$  and  $K_u$  of as the deposited and annealed at 523 K Co/Ni MLs as a function of number of MLs. The SQUID measurements are performed at room temperature.

diffusion into the Co/Ni MLs cause reduction of  $K_u$ . As we will show in the next section this is due to increase of the surface anisotropy at Au/ML and ML/Au interfaces after annealing.

Increase in the annealing temperature to 553 K leads to drastic reduction in both  $M_s$  and  $K_u$ . Kurt et al. [53] also observed reduction in  $K_u$  of the Co/Ni MLs grown on top of Au seed layers after annealing above 523 K. For the Co/Ni MLs with  $N = 8$ ,  $M_s$  decreases from  $7.03 \times 10^5$  A/m to  $4.81 \times 10^5$  A/m, and  $K_u$  decreases from  $5.00 \times 10^5$  J/m<sup>3</sup> to  $2.65 \times 10^5$  J/m<sup>3</sup>. An intermixing of Co and Ni in the MLs could be responsible for the observed trend. Thus, annealing cannot be used to entirely remove Au from the Co/Ni MLs.

## 6.6 A Simplified Model including only surface anisotropies:

In many reports [29, 124, 178, 180, 181, 184, 185] the change of the magnetic anisotropy in the MLs structures as a function of MLs thickness is analyzed by taking into account only the surface anisotropies. This simplified model can be expressed by using Eq.6.2 (where  $K_{ME}$  and  $K_{MC}$  terms are ignored) and Eq.6.13 as

$$K_u(\text{calc}) = \frac{K_S}{d} = \frac{K_S^S}{d} + K_S^V = \frac{(K_S^{Au/Co} + K_S^{Ni/Au} - K_S^{Co/Ni})}{d} + \frac{2K_S^{Co/Ni}}{t_{BL}} \quad (6.18)$$

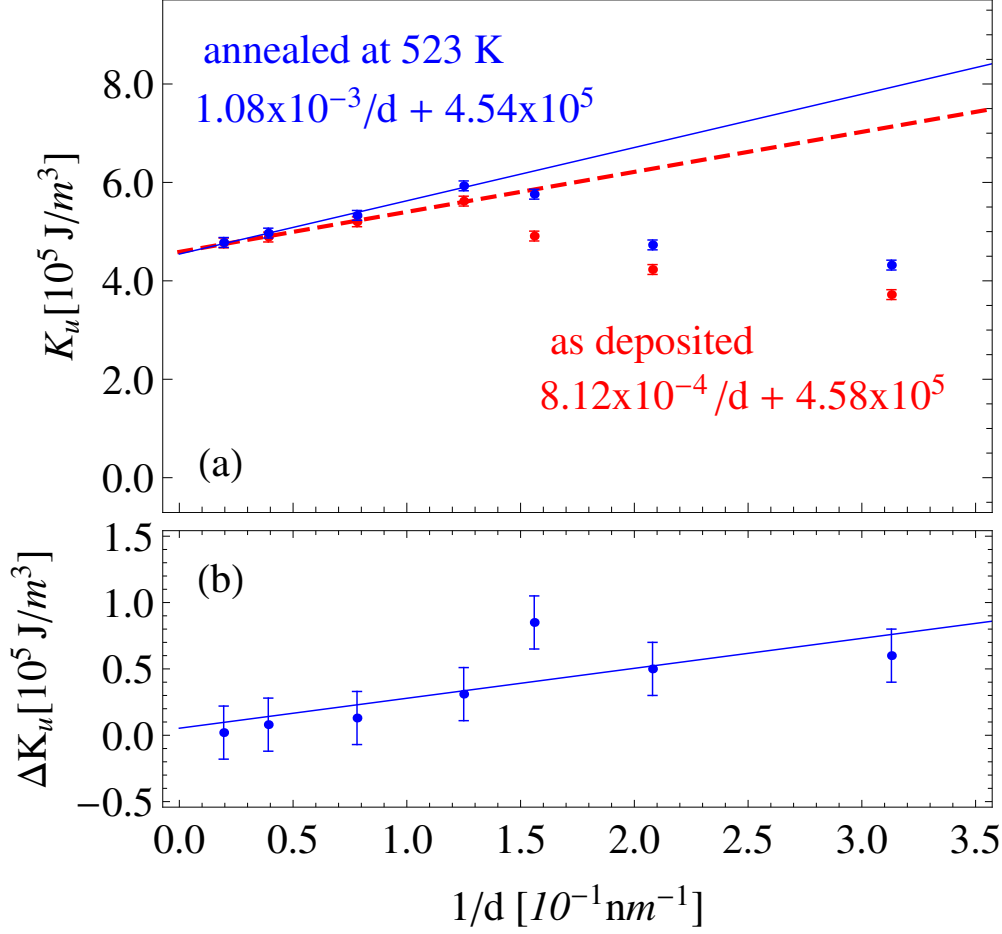


Figure 6.12: (a)  $K_u(SQUID)$  as a function of  $1/d$  for as-deposited and annealed at 523 K MLs. The intercepts and slopes are obtained from a linear fit of the anisotropy coefficients for as-deposited (blue solid line) and annealed at 523 K (red dotted line) MLs. (b)  $\Delta K_u = K_u(\text{annealed}) - K_u(\text{as-deposited})$  as a function of  $1/d$ . The solid blue line represents a linear fit of  $\Delta K_u$  values.

where  $K_u(\text{calc})$  is the calculated total intrinsic magnetic anisotropy of the MLs. The first term,  $K_S^S$ , is inversely proportional to the MLs thickness ( $\propto 1/d$ ) and the second term,  $K_S^V$ , is independent of the MLs thickness and only depends on the Co/Ni bilayer thickness,  $t_{BL}$ .

To separate  $K_S^S$  and  $K_S^V$  contributions,  $K_u(SQUID)$  of the as-deposited and annealed MLs (with  $N = 4, 6, 8, 10, 16, 32$  and  $64$ ) is plotted as a function of  $1/d$  in Figure 6.12(a).  $K_u(SQUID)$  has linear dependence on  $1/d$  for  $N \geq 10$ . From the linear fit of  $K_u(SQUID)$  with  $1/d$  we obtain: a) (from intercepts) that  $K_S^V = 2K_S^{Co/Ni}/t_{BL}$  is  $4.58 \times 10^5 \text{J/m}^3$  for as-deposited and  $4.54 \times 10^5 \text{J/m}^3$  for annealed MLs, and b) (from slopes) that  $K_S^S = K_S^{Au/Co} + K_S^{Ni/Au} - K_S^{Co/Ni}$  is  $8.19 \times 10^{-4} \text{J/m}^2$  for as-deposited and  $1.08 \times 10^{-3} \text{J/m}^2$  for annealed MLs.

From the intercepts we calculate that  $K_S^{Co/Ni} = 1.83 \times 10^{-4} \text{J/m}^2$  and  $K_S^{Co/Ni} = 1.82 \times 10^{-4} \text{J/m}^2$  for the as-deposited and annealed MLs, respectively, in agreement with the pre-

viously reported values [29, 189] for  $K_S^{Co/Ni}$ . Thus, it is evident that the bulk anisotropy,  $2K_S^{Co/Ni}/t_{BL}$ , is not affected by annealing.

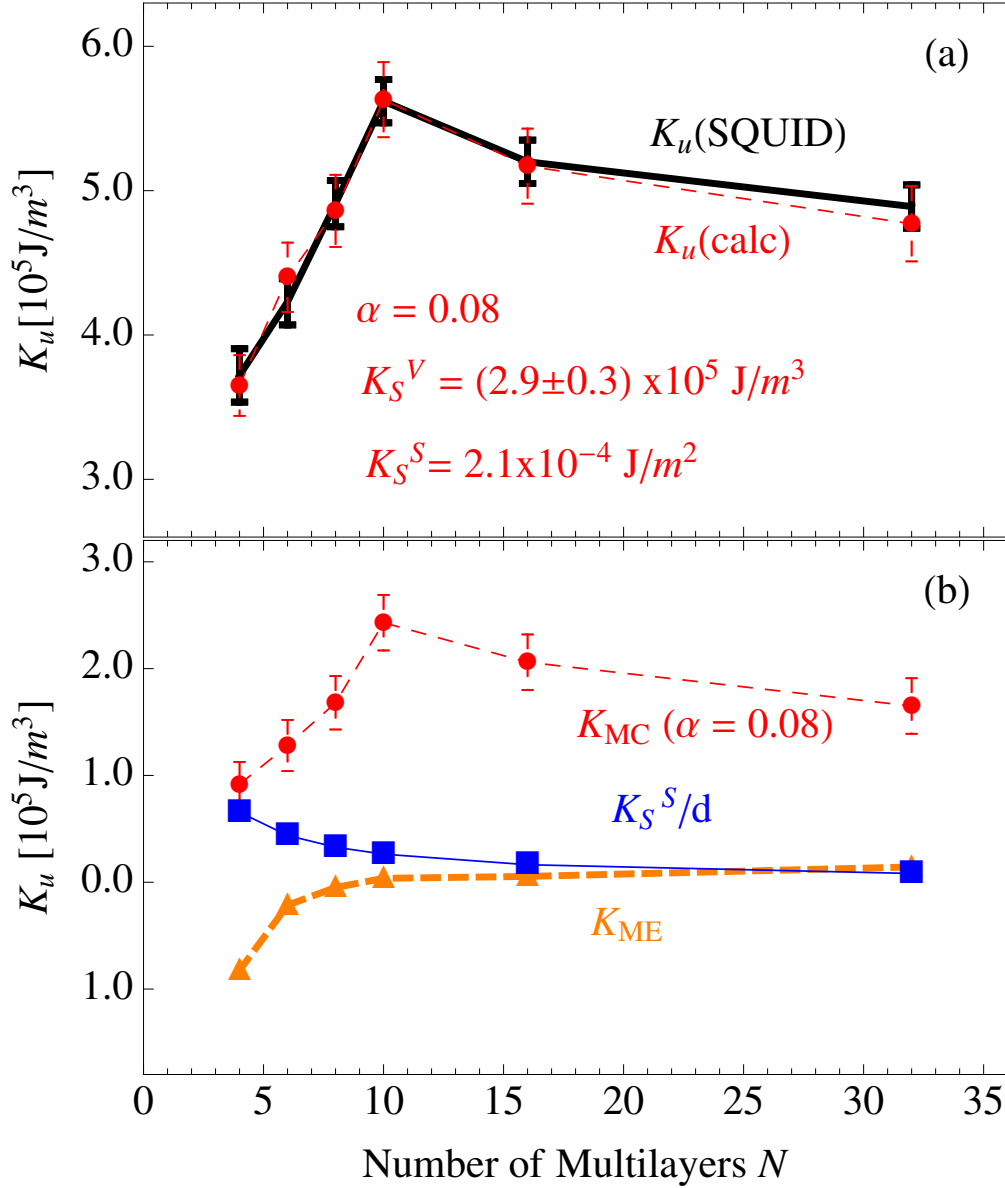


Figure 6.13: (a) The SQUID measured magnetic anisotropy coefficients  $K_u$ (SQUID) (black line) and the calculated anisotropy coefficients  $K_u(calc) = K_{ME} + K_{MC} + K_S^S/d + K_S^V$  (solid red circles). The values of  $\alpha$ ,  $K_S^S$  and  $K_S^V$  are obtained from fitting  $K_u$ (SQUID) to the model. (b) Plots of  $K_{ME}$  (solid orange triangles),  $K_{MC}$  (solid red circles) and  $K_S^S/d$  (solid blue squares).

From the slopes and the calculated value of  $K_S^{Co/Ni}$ , we determined  $K_S^{Au/Co} + K_S^{Ni/Au} = 1.0 \times 10^{-3}$  J/m<sup>2</sup> for as-deposited and  $K_S^{Au/Co} + K_S^{Ni/Au} = 1.26 \times 10^{-3}$  J/m<sup>2</sup> for annealed MLs,

respectively. These values are twice as large as reported by other groups for Co/Au [50] and Ni/Au [198] superlattices. The reported values of  $K_S^{Au/Co}$  range from  $3.7 \times 10^{-4} J/m^2$  to  $5.8 \times 10^{-4} J/m^2$  and the reported value of  $K_S^{Ni/Au}$  is  $-1.5 \times 10^{-4} J/m^2$ . For  $N \geq 10$  the linear dependence of  $K_u(SQUID)$  on  $1/N$  is not only due to the surface anisotropy coefficients  $K_S^{Au/Co} + K_S^{Ni/Au}$ , since  $g^\perp - g^\parallel$ , that is proportional to  $K_{MC}$  also scales with  $N$ . This could explain why this simplified analyses overestimate  $K_S^{Au/Co} + K_S^{Ni/Au}$  in the MLs.

Since annealing does not affect  $K_S^{Co/Ni}$ , the increase in slope ( $K_S^{Au/Co} + K_S^{Ni/Au} - K_S^{Co/Ni}$ ) after annealing is due to the increase of  $K_S^{Au/Co} + K_S^{Ni/Au}$ . It is expected that after annealing Au/Co and Ni/Au interfaces become sharper due to the back diffusion of Au at these interfaces.

The difference between  $K_u$  of annealed and as-deposited Co/Ni MLs,  $\Delta K_u = K_u(\text{annealed}) - K_u(\text{as-deposited})$ , is plotted for all Co/Ni MLs in Figure 6.12(b). The increase of  $K_u$  after annealing for all MLs scales with  $1/d$  indicating that the back diffusion of Au increases only the Au/ML and ML/Au surface anisotropies. From this we infer that the Au diffusion cannot explain the reduction of magnetic anisotropy for the Co/Ni MLs with  $N < 10$ .

The diffusion of Au in the Co/Ni MLs will introduce randomness in the magnetic pair bonding which will reduce magnetic anisotropy. On the other hand, Au is a large Z number element that may increase spin-orbit coupling in the Co/Ni MLs that could lead to increase of the magnetic anisotropy of the MLs. Since  $2K_S^{Co/Ni}/t_{BL}$ , is not affected by annealing we will assume that these two contributions cancel out and the bulk magnetic energy will not change with diffusion of Au in the Co/Ni MLs.

The simplified model that assumes only bulk and surface terms cannot explain reduction of magnetic anisotropy of the Co/Ni MLs for  $N < 10$  as evident from Figure 6.12. For this reason in the next section a more complete model, that includes all anisotropy contributions discussed in the theory section, is used to describe the dependence of  $K_u(SQUID)$  on  $N$ .

## 6.7 Models for magnetic anisotropy

In this section we will evaluate all anisotropy terms discussed in the theory section. In the proposed model the magnetic anisotropies measured by SQUID and FMR (Table 6.2) are due to the magneto-elastic and magneto-crystalline energies in addition to the surface anisotropy discussed in the simplified model. From Eq.6.2 and Eq.6.18 we can write

$$K_u(calc) = K_{ME} + K_{MC} + K_S^S/d + K_S^V \quad (6.19)$$

In the model there are three fitting parameters,  $\alpha$  in  $K_{MC}$ , surface anisotropy coefficient  $K_S^S$  and  $K_S^V$ . The magnetic anisotropies  $K_{ME}$  and  $K_{MC}$  are calculated from equations Eq.6.3 and Eq.6.4, respectively.

Figure 6.13(a) shows the experimental  $K_u$ (SQUID) (solid black line) and the fit  $K_u(calc)$  (solid red circles) obtained using the model in Eq.6.19 as a function of  $N$ . The Figure 6.13(a) shows excellent agreement between the measurements and fit for all  $N$  values.

Figure 6.13(b) shows the individual contributions of anisotropy coefficients  $K_{ME}$  and  $K_{MC}$ ,  $K_S^S$  and  $K_S^V$  as a function of  $N$ . In Figure 6.13(b)  $K_{ME}$  is practically 0 for  $N \geq 10$ . For  $N < 10$ ,  $K_{ME}$  decreases with  $N$  and reaches  $-8.25 \times 10^4 \text{ J/m}^3$  for  $N = 4$ . This is due to the expansion of d(111) and d(220) in the Co/Ni MLs observed for  $N \leq 10$  (Figure 6.5(a)). Measured  $K_{ME}$  values are significantly larger than those reported for Co/Ni MLs grown on Au seed layers [156] and for CoFe/Ni MLs grown on Cu seed layers [189].  $K_{MC}$  has the same dependance on  $N$  as  $K_u$ (SQUID); strongly increases with  $N$  for  $N \leq 10$ , and then decreases with further increase of  $N$ .

The model shows that for  $N \leq 10$ , the decrease in perpendicular magnetic anisotropy is predominantly due to  $K_{MC}$  and  $K_{ME}$ . A moderate decrease in perpendicular anisotropies for  $N > 10$  is due to the reduction of  $K_{MC}$  and  $K_S^S$ .

From the fitting of experimental  $K_u$ (SQUID) data using Eq.6.19, we find out that  $\alpha$  in  $K_{MC}$  is 0.08,  $K_S^S$  is  $2.1 \times 10^{-4} \text{ J/m}^2$  and  $K_S^V$  is  $2.9 \pm 0.3 \times 10^5 \text{ J/m}^3$ . The obtained value of  $\alpha$  is in agreement with the results shown by Shaw et al. [189] ( $\alpha = 0.097$ ) for the FeCo/Ni MLs surrounded by Cu layers. From  $K_S^V = 2K_S^{Co/Ni}/t_{BL}$  we found that  $K_S^{Co/Ni}$  is  $1.2 \times 10^{-4} \text{ J/m}^2$ . This value is almost two time smaller than the previously reported  $K_S^{Co/Ni}$  [189, 29].

The uniaxial orbital asymmetry at Co/Ni interfaces leads to an interface anisotropy  $K_S^{Co/Ni}$ , and thus, the bulk anisotropy,  $K_S^V$ , the last term in Eq.6.18. In addition this orbital asymmetry results in  $g_{\parallel} < g_{\perp}$  as shown in Table 6.2 leading to uniaxial anisotropy  $K_{MC}$  (see Eq.6.4).

Our Xray data analysis show a tetragonal distortion of the lattice (see Figure 6.5(b)). This tetragonality can also lead to a uniaxial anisotropy. However, the tetragonal distortion does not follow the dependance of  $K_{MC}$  and  $K_S^V$  on  $N$ . In fact, the tetragonal distortion changes its sign for  $N > 10$ ; is almost zero for  $N = 10$ , while  $g_{\perp} - g_{\parallel}$  reaches maximum. It can only lead to a decrease in  $g_{\perp} - g_{\parallel}$  for  $4 < N < 10$  compared to that measured by FMR.  $K_S^V$  is independent on  $N$  and therefore has nothing to do with tetragonal distortion. The tetragonal distortion therefore does not play any significant role in the measured uniaxial anisotropy.

Assuming that  $K_S^{Co/Ni} = 1.2 \times 10^{-4} \text{ J/m}^2$ ,  $K_S^{Ni/Au} = -1.5 \times 10^{-4} \text{ J/m}^2$ , [198] and  $K_S^S = K_S^{Au/Co} + K_S^{Ni/Au} - K_S^{Co/Ni} = 2.1 \times 10^{-4} \text{ J/m}^2$  we can determine that  $K_S^{Au/Co} = 4.8 \times 10^{-4} \text{ J/m}^2$ . This is in good agreement with reported values of  $K_S^{Au/Co}$  that ranges from  $3.7 \times 10^{-4}$  to  $5.8 \times 10^{-4} \text{ J/m}^2$  [198, 199, 50].

For simplicity in above discussion we neglected the surface magneto-crystalline anisotropies  $\Delta K_S^{Au/Co}$ ,  $\Delta K_S^{Ni/Au}$  and  $\Delta K_S^{Co/Ni}$  induced by the MLs roughness. Using Eq.6.14-6.16 we can calculate that  $\Delta K_S^{Au/Co} = -3.4 \times 10^{-5} \text{ J/m}^2$ ,  $\Delta K_S^{Ni/Au}$  ranges from  $1.6$  to  $2.1 \times 10^{-5} \text{ J/m}^2$  for  $N = 4$  and  $32$ , respectively, and  $\Delta K_S^{Co/Ni}$  ranges from  $-1.2$  to  $-1.4 \times 10^{-5} \text{ J/m}^2$  for  $N = 4$

and 32, respectively. The variation in  $\Delta K_S^{Ni/Au}$  and  $\Delta K_S^{Co/Ni}$  is due to the fact that,  $\sigma$  and  $\xi$  changes with thickness. In the calculations we assumed that  $K_S^{Au/Co} = 4.8 \times 10^{-4}$  J/m<sup>2</sup>,  $K_S^{Ni/Au} = -1.5 \times 10^{-4}$  J/m<sup>2</sup> and  $K_S^{Co/Ni} = 1.2 \times 10^{-4}$ . It is evident that the surface magneto-crystalline anisotropies ( $\Delta K_S$ ) are an order of magnitude lower than the surface anisotropies ( $K_S$ ). Adding  $\Delta K_S$  in the model (Eq.6.19) will not change the values of fitted parameters  $\alpha$ ,  $K_S^S$  and  $K_S^V$ . However, the surface anisotropies  $K_S^{Au/Co}$ ,  $K_S^{Ni/Au}$  and  $K_S^{Co/Ni}$  will be about 10 % larger since in this case  $K_S^S = K_S^{Au/Co} + \Delta K_S^{Au/Co} + K_S^{Ni/Au} + \Delta K_S^{Ni/Au} - K_S^{Co/Ni} - \Delta K_S^{Co/Ni}$  and  $K_S^V = 2(K_S^{Co/Ni} + \Delta K_S^{Co/Ni})/t_{BL}$  ( $\Delta K_S^{Ni/Au}$ ,  $\Delta K_S^{Au/Co}$  and  $\Delta K_S^{Co/Ni}$  have negative values).

$\Delta K_S^{Au/Co}/d$ ,  $\Delta K_S^{Ni/Au}/d$  and  $\Delta K_S^{Co/Ni}/d$  are plotted as a function of  $N$  in Figure 6.14. Figure 6.14 shows that  $\Delta K_S^{Au/Co}$  and  $\Delta K_S^{Ni/Au}$  have  $1/d$  dependance, while  $\Delta K_S^{Co/Ni}$  is practically independent on the MLs thickness. Co/Ni interfaces are uniformly distributed throughout MLs and the variation of  $\Delta K_S^{Co/Ni}$  with  $d$  is only due to the change of roughness across the MLs thickness.

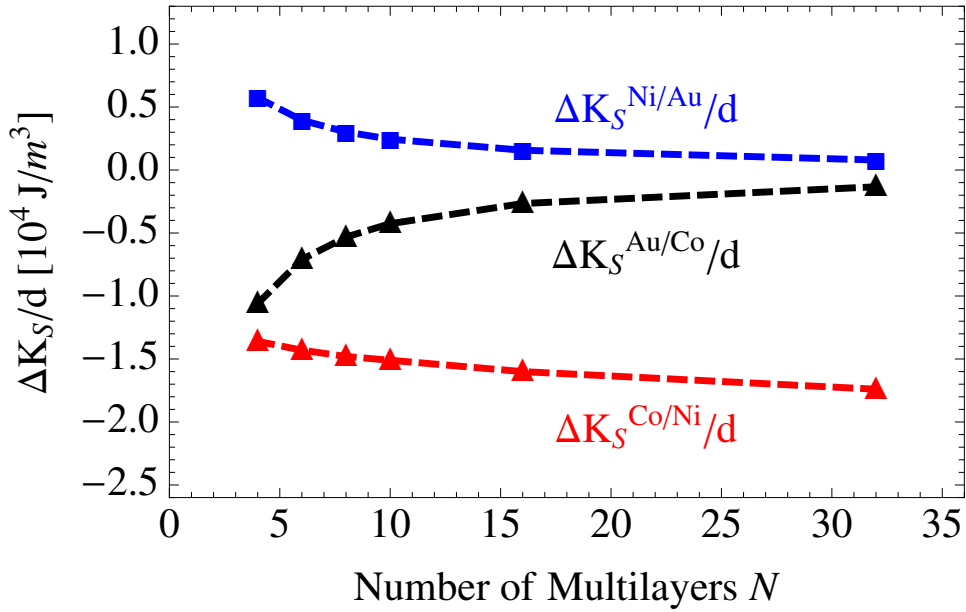


Figure 6.14: Plot of  $\Delta K_S^{Au/Co}/d$ ,  $\Delta K_S^{Ni/Au}/d$  and  $\Delta K_S^{Co/Ni}/d$  as a function of  $N$ .

## 6.8 Summary

The change in magnetic anisotropy of (111) textured Au/ $N \times$ [Co/Ni]/Au films is studied as a function of number of bilayer repeats  $N$  ( $N = 4, 6, 8, 10, 16, 32$  and  $64$ ). The ferromagnetic resonance and SQUID measurements show that the perpendicular magnetic anisotropy of as-deposited and annealed Co/Ni multilayers first increases with  $N$  ( $N \leq 10$ ) and then

moderately decreases with  $N > 10$ , reaching the maximum value  $K_u = 5.71 \times 10^5 \text{ J/m}^3$  for  $N = 10$ .

The SQUID measurements show that the trends of both  $M_s$  and  $K_u$  do not change with increase of temperature from 5 to 300 K. This indicates that the reduction in the magnetic anisotropy for  $N \leq 10$  is not due to the onset of the superparamagnetism in ultra thin films.

The in-plane and out-of-plane ferromagnetic resonance measurements show that the difference between the perpendicular and parallel g-factors of Co/Ni multilayers has the same dependence on  $N$  as the experimentally measured magnetic anisotropies.

The lattice mismatch between Co and Ni, and Au (about 14 %) induces a large strain in the films. In-plane and out-of-plane X-ray measurements show the expansion of the lattice spacing between orthogonal (220) and (111) planes of Co/Ni multilayers. EDXS analysis in TEM confirms the diffusion of Au into the Co/Ni multilayers that could be responsible for the observed expansion of the lattice volume in the multilayers. The strain calculations from X-ray measurements show that, with the change in  $N$  from 4 to 64, the magneto-elastic coefficient changes from  $-8.25 \times 10^4 \text{ J/m}^3$  to  $1.21 \times 10^4 \text{ J/m}^3$ . The diffusion of Au into the Co/Ni MLs also causes reduction of  $M_s$ .

The cross-sectional STEM reveals that roughness and roughness period increase with number of the Co/Ni MLs. The roughness causes up to 3.5 % decrease in the dipolar anisotropy of the MLs. It also causes up to 10 % reduction in the surface magneto-crystalline anisotropy of the MLs.

Annealing triggers partial back diffusion of Au from the MLs. This results in increase of only surface anisotropy while the bulk anisotropy stays unchanged.

The experimentally obtained dependence of the magnetic anisotropy of the Co/Ni MLs on  $N$  is successfully modelled assuming contributions from the surface anisotropy, the magneto-crystalline anisotropy arising from the difference between the perpendicular and parallel g-factors, and the magneto-elastic anisotropy due to the strain. The models reveal the strong decrease of the perpendicular magnetic anisotropy for  $N < 10$  is predominantly due to the reduction in the magneto-crystalline and magneto-elastic anisotropies. On the other hand, a moderate decrease in the perpendicular magnetic anisotropy for  $N > 10$  is due to the reduction in the magneto-crystalline anisotropy and the surface anisotropy between Au and MLs.



## Chapter 7

# Conclusion

The primary objective of this thesis was to create a spin transfer torque device that is intended to have a minimum critical current density for switching of the free layer. This objective has been met through the following achievements:

**Optimization of the magnetic properties of Co/Ni multilayer structures for use in STT-RAM:** Magnetic properties of (111)-textured Ta/Cu/SAF/Cu/FL multilayer film structures have been optimized by varying individual layer thickness and sputtering conditions. The SAF = FM1/Ru( $d_{\text{Ru}}$ )/FM2 is a synthetic anti-ferromagnet consisting of Co/Ni multilayers coupled antiferromagnetically across a Ru spacer layer. FM1 =  $N_1 \times [\text{Co}(d_{\text{Co1}})/\text{Ni}(d_{\text{Ni}})]/\text{Co}(d_{\text{Co2}})$ , FM2 =  $\text{Co}(d_{\text{Co2}})/N_2 \times [\text{Ni}(d_{\text{Ni}})/\text{Co}(d_{\text{Co1}})]/\text{Ni}(d_{\text{Ni}})/\text{Co}(d_{\text{Co3}})$ , and FL =  $\text{Co}(d_{\text{Co3}})/N_3 \times [\text{Ni}(d_{\text{Ni}})/\text{Co}(d_{\text{Co1}})]/\text{Ni}(d_{\text{Ni}})$  is a free layer consisting of a single Co/Ni multilayer. To maximize the perpendicular magnetic anisotropy  $d_{\text{Co1}}$  is 0.21 (1 Co monolayer) and  $d_{\text{Ni}}$  is 0.58 nm (almost 3 Ni monolayers). Our experimental results show that the magnetic and transport properties of Ta/Cu/SAF/Cu/FL/Ta films are affected by the change in thickness of individual layer, number of multilayers and also the deposition parameters. X-ray diffraction, X-ray reflectivity and TEM was used to study the microstructure of films. SQUID, MOKE and FMR was used to study the magnetic properties of the multilayer structures. The following conclusions summarizes the findings of this study:

- The increase in the thickness of the Cu seed layer improves the texture of the Co/Ni multilayers. However, it also increases the grain size and film roughness. The increase in grain size results in the reduction of direct exchange coupling between the magnetic grains, which increases the probability of uniform reversal of individual magnetic grains and enhances the coercivity of the Co/Ni multilayers.
- The reference layer, SAF, can be designed with only Co/Ni multilayers coupled across a Ru spacer layer, thus avoiding the use of precious metals such as Pt and Pd.

- To maximize the coupling between FM1 and FM2 in the SAF,  $\text{Co}(d_{\text{Co2}})$  thickness across Ru interlayer should be between 0.4 and 0.6 nm and  $\text{Ru}(d_{\text{Ru}})$  thickness between 0.38 nm and 0.42 nm.
- The GMR effect is maximized for  $\text{Co}(d_{\text{Co3}}) = 0.6$  nm across Cu spacer layer, and the SAF and FL are decoupled (the direct exchange and RKKY like interactions are negligible) for Cu spacer layer of thickness larger than 3 nm.
- Cu films deposited at higher rates require less thickness to decouple the SAF and FL than Cu films deposited at lower rates.

**Spin torque switching in nanopillars with antiferromagnetic reference layer:** A unique film structure (as discussed earlier) comprised of more than thirty layers was used for fabricating the 200 nm diameter nano-pillars of STT-RAM. Spin-transfer-torque induced switching is investigated in these circularly shaped, perpendicular magnetized nanopillars. The important results we found are listed below:

- Anti-ferromagnetic coupling between magnetic layers is used in the SAF reference layer can be used to minimize the dipolar field on the free layer. The dipolar field acting on the free layer is only 22.5 mT, more than two times smaller than reported in devices with a single ferromagnetic reference layer [19].
- The free layer is a single  $4\times[\text{Co/Ni}]$  multilayer. The use of Pt and Pd was avoided to lower the spin-orbit scattering in magnetic layers and intrinsic damping in the free layer, and therefore, reduce the critical current required for spin-transfer-torque switching. The intrinsic Gilbert damping of a continuous  $4\times[\text{Co/Ni}]$  multilayer film was measured by ferromagnetic resonance to be  $\alpha = 0.022$ , which is significantly lower than in Pt or Pd based magnetic multilayers.
- In zero magnetic field the critical current required to switch the free layer from the parallel to antiparallel (antiparallel to parallel) alignment is 5.2 mA (4.9 mA). Given the volume of the free layer,  $V_{\text{FL}} = 1.01\times 10^{-22} \text{ m}^3$ , the switching efficiency,  $I_c/(V_{\text{FL}} \times \mu_0 H_c)$ , is  $5.28\times 10^{20} \text{ A/Tm}^3$ , twice as efficient as any previously reported device with a similar structure. This is attributed to the low Gilbert damping of our FL corroborated by extended films ferromagnetic resonance studies. The study lays the foundations for future investigations of STT-RAM devices consisting of only Co/Ni multilayers.

**The origin of perpendicular magnetic anisotropy in Co/Ni multilayers:** Since anisotropy plays an important role in designing of the free layer, the origin of perpendicular magnetic anisotropy of as deposited and annealed (111) textured  $\text{Au}/N\times[\text{Co/Ni}]/\text{Au}$  films, where  $N$  is number of bilayer repeats, is studied. Both in-plane and out of plane measurements of X-ray diffraction, ferromagnetic resonance and SQUID are used to investigate the

dependence of perpendicular magnetic anisotropy on number of bilayer repeats of Co/Ni multilayers. The following conclusions are warranted from the results of this study:

- The experimental results show that the perpendicular magnetic anisotropy of as-deposited and annealed Co/Ni multilayers first increases with  $N$  ( $N \leq 10$ ) and then moderately decreases with  $N > 10$ .
- The proposed model reveals that the variation in perpendicular magnetic anisotropy can be explained by taking into account the contributions from 1) the magnetoelastic anisotropy due to the strain, 2) the magnetocrystalline anisotropy due to the orbital asymmetry between easy and hard axis, 3) the roughness induced anisotropies, and 4) the inter-diffusion of Au in the Co/Ni MLs. Therefore, in our case all the above mentioned anisotropies play an important part.
- The SQUID measurements show that the trends of both  $M_s$  and  $K_u$  do not change with increase of temperature from 5 to 300 K. This indicates that the reduction in the magnetic anisotropy for  $N \leq 10$  is not due to the onset of the superparamagnetism in ultra thin films.
- The lattice mismatch between Co and Ni, and Au (about 14 %) induces a large strain in the films. In-plane and out-of-plane X-ray measurements show the expansion of the lattice spacing between orthogonal (220) and (111) planes of Co/Ni multilayers. EDXS analysis in TEM confirms the diffusion of Au into the Co/Ni multilayers that could be responsible for the observed expansion of the lattice volume in the multilayers.
- The cross-sectional STEM reveals that roughness and roughness period increase with number of the Co/Ni MLs.
- Annealing trigger partial back diffusion of Au from the MLs. This results in increase of only surface anisotropy while the bulk anisotropy stays unchanged.

## 7.1 Future work

In terms of future work, it would be valuable to replace the Cu seed layer in (111)-textured Ta/Cu/SAF/Cu/FL multilayer film structures. At high temperatures, Cu easily diffuses along the grain boundaries of Co/Ni multilayers and reduces the exchange interaction between the magnetic grains. This alters the magnetic properties of Ta/Cu/ $N \times [\text{Co}(0.21)/\text{Ni}(0.58)]$ /Ta;  $M_s$  decreases while the coercivity increases due to the more uniform magnetization reversal of the individual grains. A metallic material with least roughness such as Ru might prove as a better substitute of Cu. It stimulates the necessary fcc(111) orientation in Co/Ni MLs and has much lower diffusion into Co due to its high melting point [127]. For the device implementation, a further improvement can be made by eliminating the roughness

in magnetic grains. Thus, a Ru seed layer may play an influential role in the designing of STT-RAM. Furthermore, it would be interesting to build Ta/Ru/SAF/MgO/FL, magnetic tunnel junction structure. The non magnetic Cu spacer layer can be replaced by an insulating barrier such as MgO or  $\text{Al}_2\text{O}_3$ , which is desired to offer much higher signal (change in resistance). In this case the SAF and FL design will have to be changed to maximize the TMR and spin torque transfer across an oxide layer.

# Bibliography

- [1] V. Turner, J. F. Gantz, D. Reinsel, and S. Minton. The digital universe of opportunities: Rich data and the increasing value of the internet of things. Technical Report April, International Data Cooperation, 2014.
- [2] J Joshua Yang, Dmitri B Strukov, and Duncan R Stewart. Memristive devices for computing. *Nature nanotechnology*, 8(1):13–24, January 2013.
- [3] E. Kultursay, M. Kandemir, A. Sivasubramaniam, and O. Mutlu. Evaluating STT-RAM as an energy-efficient main memory alternative. In *2013 IEEE International Symposium on Performance Analysis of Systems and Software (ISPASS)*, pages 256–267. IEEE, April 2013.
- [4] D. Bohn. The Verge, 2015.
- [5] S. Anthony. Seagate’s new 60TB SSD is world’s largest, 2016.
- [6] D.C. Ralph and M.D. Stiles. Spin transfer torques. *Journal of Magnetism and Magnetic Materials*, 320(7):1190–1216, April 2008.
- [7] J. C. Slonczewski. Current-driven excitation of magnetic multilayers. *Journal of Magnetism and Magnetic Materials*, 159(1-2):L1–L7, June 1996.
- [8] G. Binasch, P. Grunberg, F. Saurenbach, and W. Zinn. Enhanced magnetoresistance in layered magnetic structures with antiferromagnetic interlayer exchange. *Physical Review B*, 39(7):4828–4830, March 1989.
- [9] M. N. Baibich, J. M. Broto, A. Fert, F. Nguyen Van Dau, and F. Petroff. Giant Magnetoresistance of (001)Fe/(001)Cr Magnetic Superlattices. *Physical Review Letters*, 61(21):2472–2475, November 1988.
- [10] M. Julliere. Tunneling between ferromagnetic films. *Physics Letters A*, 54(3):225–226, September 1975.
- [11] S. Yuasa, T. Nagahama, A. Fukushima, Y. Suzuki, and K. Ando. Giant room-temperature magnetoresistance in single-crystal Fe/MgO/Fe magnetic tunnel junctions. *Nature materials*, 3(12):868–71, December 2004.
- [12] S. S. P. Parkin, C. Kaiser, A. Panchula, P. M Rice, B. Hughes, M. Samant, and S. Yang. Giant tunnelling magnetoresistance at room temperature with MgO (100) tunnel barriers. *Nature materials*, 3(12):862–7, December 2004.

- [13] M. N. Baibich, J. M. Broto, A. Fert, F. Nguyen Van Dau, and F. Petroff. Giant Magnetoresistance of (001)Fe/(001)Cr Magnetic Superlattices. *Physical Review Letters*, 61(21):2472–2475, November 1988.
- [14] G. Binasch, P. Grunberg, F. Saurenbach, and W. Zinn. Enhanced magnetoresistance in layered magnetic structures with antiferromagnetic interlayer exchange. *Physical Review B*, 39(7):4828–4830, March 1989.
- [15] M. Tsoi, A. G. M. Jansen, J. Bass, W. C. Chiang, M. Seck, V. Tsoi, and P. Wyder. Excitation of a Magnetic Multilayer by an Electric Current. *Physical Review Letters*, 80(19):4281–4284, May 1998.
- [16] J. E. Wegrowe, D. Kelly, Y. Jaccard, P. Guittienne, and J. Ansermet. Current-induced magnetization reversal in magnetic nanowires. *Europhysics Letters (EPL)*, 45(5):626–632, March 1999.
- [17] A. V. Khvalkovskiy, D. Apalkov, S. Watts, R. Chepulsii, R. S. Beach, A. Ong, X. Tang, A. Driskill-Smith, W. H. Butler, P. B. Visscher, D. Lottis, E. Chen, V. Nikitin, and M. Krounbi. Basic principles of STT-MRAM cell operation in memory arrays. *Journal of Physics D: Applied Physics*, 46(7):074001, February 2013.
- [18] H. Song, Kyeong-D. Lee, Jeong-W. Sohn, See-H. Yang, Stuart S. P. Parkin, Chun-Y. You, and Sung-C. Shin. Observation of the intrinsic Gilbert damping constant in Co/Ni multilayers independent of the stack number with perpendicular anisotropy. *Applied Physics Letters*, 102(10):102401, 2013.
- [19] S. Mangin, D. Ravelosona, J. A. Katine, M. J. Carey, B. D. Terris, and Eric E. Fullerton. Current-induced magnetization reversal in nanopillars with perpendicular anisotropy. *Nature Materials*, 5(3):210–215, February 2006.
- [20] J.A. Katine and Eric E. Fullerton. Device implications of spin-transfer torques. *Journal of Magnetism and Magnetic Materials*, 320(7):1217–1226, April 2008.
- [21] J. Akerman. APPLIED PHYSICS: Toward a Universal Memory. *Science*, 308(5721):508–510, April 2005.
- [22] Y. Huai. Spin-transfer torque MRAM (STT-MRAM): Challenges and prospects. *AAPPS Bulletin*, 18(6):33–40, 2008.
- [23] Lucas M. Everspin ships first ST-MRAM memory with 500X performance of flash, 2012.
- [24] Avalanche Samples Industry’s First STT-MRAM Chips On 300MM Wafers Utilizing Advanced Perpendicular MTJ, 2015.
- [25] L. McHale. Crocus Technology Enters STT Memory Race and Sets Industry Pace with New Prototype, 2009.
- [26] V. Chun. Interview with Vincent Chun from Spin Transfer Technologies, 2008.
- [27] MRAM Companies. MRAM-info Companies, 2012.

- [28] I. Tudosa, J. A. Katine, S. Mangin, and E. E. Fullerton. Perpendicular spin-torque switching with a synthetic antiferromagnetic reference layer. *Applied Physics Letters*, 96(21):212504, 2010.
- [29] Maria Patricia R. Sabino, M. Tran, Hin S. C., Ji F. Y., and K. Eason. Seed influence on the ferromagnetic resonance response of Co/Ni multilayers. *Journal of Applied Physics*, 115(17):17C512, May 2014.
- [30] D. D. Tang and Y. Lee. *Magnetic Memory: Fundamentals and Technology*. Cambridge University Press, 1 edition edition, 2010.
- [31] S. Mangin, D. Ravelosona, J. A. Katine, M. J. Carey, B. D. Terris, and Eric E. Fullerton. Current-induced magnetization reversal in nanopillars with perpendicular anisotropy. *Nature Materials*, 5(3):210–215, February 2006.
- [32] C. Bilzer, T. Devolder, J. Kim, G. Counil, and C. Chappert. Study of the dynamic magnetic properties of soft CoFeB films. *Journal of Applied Physics*, 100(5):053903, 2006.
- [33] G. Vermijs, A. Solignac, J. Koo, J. T. Kohlhepp, H. J. M. Swagten, B. Koopmans, and A. V. Brink. Field-free magnetization reversal by spin-Hall effect and exchange bias. *Nature Communications*, 7:1–6, 2016.
- [34] G. W. Anderson, Y. Huai, and M. Pakala. Spin-valve thermal stability : The effect of different antiferromagnets Spin-valve thermal stability : The effect of different antiferromagnets. *Journal of Applied Physics*, 5726(2000):1998–2001, 2001.
- [35] H. N. Fuke, K. Saito, Y. Kamiguchi, H. Iwasaki, M. Sahashi, H. N. Fuke, K. Saito, Y. Kamiguchi, H. Iwasaki, and M. Sahashi. Spin-valve giant magnetoresistive films with antiferromagnetic Ir-Mn layers Spin-valve giant magnetoresistive films with antiferromagnetic Ir-Mn layers. *Journal of Applied Physics*, 4004(1997):1–4, 2000.
- [36] G. W. Anderson and Y. Huai. Spin valves exchange biased by IrMn / PtMn laminated antiferromagnets Spin valves exchange biased by IrMnÖPtMn laminated antiferromagnets. *Journal of Applied Physics*, 4924(2000):1–4, 2006.
- [37] E. Gapihan, R. C. Sousa, J. H  rault, C. Papusoi, M. T. Delaye, B. Dieny, I. L. Prejbeanu, C. Ducruet, C. Portemont, K. Mackay, and J. Nozi  res. FeMn Exchange Biased Storage Layer for Thermally Assisted MRAM. *IEEE Transactions on Magnetics*, 46(6):2486–2488, 2010.
- [38] Q. Li, J. H. Liang, Y. M. Luo, Z. Ding, T. Gu, Z. Hu, C. Y. Hua, H. Lin, and T. W. Pi. Antiferromagnetic proximity effect in epitaxial CoO / NiO / MgO ( 001 ) systems. *Scientific Reports*, (October 2015):1–9, 2016.
- [39] M. Arora, C. Fowley, T. Mckinnon, E. Kowalska, V. Sluka, and A. M. Deac. STT-RAM Memory Devices. *Physics in Canada*, 72(2), 2016.
- [40] D. J. Smith. Structural and magnetic properties of CoCrPt perpendicular media grown on different buffer layers. *Journal of Magnetism and Magnetic Materials*, 247:153–158, 2002.

- [41] Y. Hiravama, I. Tamai, I. Takekuma, Y. Nishida, and Y. Hosoe. CoCrPt-alloy Perpendicular Media for High-density Magnetic Recording. *IEEE Transactions on Magnetics*, (6):45, 2003.
- [42] D. Jeannot, J. Desserre, D. Jeannot, and J. Desserre. A transition-metal-rare-earth alloy for perpendicular magnetic recording. *Journal of Applied Physics*, 2820(54):1–5, 1983.
- [43] A. Chekanov, K. Matsumoto, K. Ozaki, A. Chekanov, K. Matsumoto, and K. Ozaki. Fluctuation field and time dependence of magnetization in TbFeCo amorphous rare earth-transition metal thin films for perpendicular magnetic recording Fluctuation field and time dependence of magnetization in TbFeCo amorphous rare earth-transition metal t. *Journal of Applied Physics*, 90(9):4657, 2001.
- [44] J. F. Hu, J. S. Chen, B. C. Lim, and T. J. Zhou. L1 0 ordered FePt based double-layered perpendicular recording media with ( 002 ) oriented FeCo films as a soft magnetic underlayer. *Thin Solid Films*, 516:2067–2070, 2008.
- [45] F. Wang, X. Xu, Y. Liang, J. Zhang, and J. Zhang. Perpendicular L1 0 -FePt / Fe and L1 0 -FePt / Ru / Fe graded media obtained by. *Materials Chemistry and Physics*, 126(3):843–846, 2011.
- [46] Y. Jiang, T. Nozaki, S. Abe, T. Ochiai, A. Hirohata, N. Tezuka, and K. Inomata. Substantial reduction of critical current for magnetization switching in an exchange-biased spin valve. *Nature materials*, 3(6):361–4, June 2004.
- [47] Y. Jiang, G. H. Yu, Y. B. Wang, J. Teng, T. Ochiai, N. Tezuka, and K. Inomata. Spin transfer in antisymmetric exchange-biased spin-valves. *Applied Physics Letters*, 86(19):192515, 2005.
- [48] D. B. Gopman, D. Bedau, S. Mangin, E. E. Fullerton, J. A. Katine, and A. D. Kent. Bimodal switching field distributions in all-perpendicular spin-valve nanopillars. *Journal of Applied Physics*, 115(17):17C707, May 2014.
- [49] P. F. Carcia, A. D. Meinhaldt, and A. Suna. Perpendicular magnetic anisotropy in Pd/Co thin film layered structures. *Applied Physics Letters*, 47(2):178, 1985.
- [50] M. T. Johnson, P. J. H. Bloemen, F. J. A. Den Broeder, and J. J. De Vries. Magnetic anisotropy in metallic multilayers. *Reports on Progress in Physics*, 59(11):1409–1458, November 1996.
- [51] F. den Broeder, D. Kuiper, A. van de Mosselaer, and W. Hoving. Perpendicular Magnetic Anisotropy of Co-Au Multilayers Induced by Interface Sharpening. *Physical Review Letters*, 60(26):2769–2772, June 1988.
- [52] S. Fukami, H. Sato, M. Yamanouchi, S. Ikeda, and H. Ohno. CoNi Films with Perpendicular Magnetic Anisotropy Prepared by Alternate Monoatomic Layer Deposition. *Applied Physics Express*, 6(7):073010, July 2013.
- [53] H. Kurt, M. Venkatesan, and J. M. D. Coey. Enhanced perpendicular magnetic anisotropy in Co/Ni multilayers with a thin seed layer. *Journal of Applied Physics*, 108(7):073916, 2010.



- [54] J. M. L. Beaujour, W. Chen, K. Krycka, C. C. Kao, J. Z. Sun, and A. D. Kent. Ferromagnetic resonance study of sputtered Co|Ni multilayers. *The European Physical Journal B*, 59(4):475–483, March 2007.
- [55] J. M. Shaw, H. T. Nembach, and T. J. Silva. Damping phenomena in Co<sub>90</sub>Fe<sub>10</sub>/Ni multilayers and alloys. *Applied Physics Letters*, 99(1):012503, 2011.
- [56] S. Girod, M. Gottwald, S. Andrieu, S. Mangin, J. McCord, Eric E. Fullerton, J. M. L. Beaujour, B. J. Krishnatreya, and A. D. Kent. Strong perpendicular magnetic anisotropy in Ni/Co(111) single crystal superlattices. *Applied Physics Letters*, 94(26):262504, 2009.
- [57] J. Linder and M. Farle. In Hartmut Zabel and Samuel Bader D., editors, *Magnetic Heterostructures*, chapter 2, pages 45–96. Springer Berlin Heidelberg, Berlin/Heidelberg, 2008.
- [58] E Y Tsymbal and I. Zutic, editors. *Basics of Nano-Thin Film Magnetism*. CRC Press Book., 1 edition, 2011.
- [59] D. Sander. The magnetic anisotropy and spin reorientation of nanostructures and nanoscale films. *Journal of Physics: Condensed Matter*, 16(20):R603–R636, May 2004.
- [60] M. J. Hurlen and C. E. Patton. Theory of magnetostatic waves for in-plane magnetized isotropic films. *Journal of Magnetism and Magnetic Materials*, 139(3):263–291, January 1995.
- [61] S. Blundell. *Magnetism in Condensed Matter*. Oxford University Press, 1st edition, 2001.
- [62] S. Chikazumi. *Physics of Ferromagnetism*. OUP Oxford, 2 edition, 2009.
- [63] B. Heinrich and J. F. Cochran. Ultrathin metallic magnetic films: magnetic anisotropies and exchange interactions. *Advances in Physics*, 42(5):523–639, October 1993.
- [64] C. Eyrych. *Exchange Stiffness in Thin-Film Cobalt Alloys*. PhD thesis, Simon Fraser University, 2012.
- [65] C. Eyrych, W. Huttema, M. Arora, E. Montoya, F. Rashidi, C. Burrowes, B. Kardasz, E. Girt, B. Heinrich, O. N. Mryasov, M. From, and O. Karis. Exchange stiffness in thin film Co alloys. *Journal of Applied Physics*, 7:07C919, 2012.
- [66] E. Girt, W. Huttema, O. N. Mryasov, E. Montoya, B. Kardasz, C. Eyrych, B. Heinrich, A. Yu Dobin, and O. Karis. A method for measuring exchange stiffness in ferromagnetic films. *Journal of Applied Physics*, 109(7):07B765, 2011.
- [67] C. Eyrych, A. Zamani, W. Huttema, M. Arora, D. Harrison, F. Rashidi, D. Broun, B. Heinrich, O. Mryasov, M. Ahlberg, O. Karis, Petra E. Jönsson, M. From, X. Zhu, and E. Girt. Effects of substitution on the exchange stiffness and magnetization of Co films. *Physical Review B*, 90(23):235408, 2014.

- [68] C. Eyrich, A. Zamani, W. Huttema, M. Arora, D. Harrison, F. Rashidi, D. Broun, B. Heinrich, O. Mryasov, M. Ahlberg, O. Karis, M. From, X. Zhu, and E. Girt. Effects of substitution on the exchange stiffness and magnetization of Co films. *Phys. Rev. B*, 90:235408, 2014.
- [69] J. M. D. Coey. *Magnetism and Magnetic Materials*. Cambridge University Press, Dublin, 2009.
- [70] P. Bruno. Tight-binding approach to the orbital magnetic moment and magnetocrystalline anisotropy of transition-metal monolayers. *Physical Review B*, 39(1):865–868, January 1989.
- [71] The Discovery of Giant Magnetoresistance, 2007.
- [72] E. Y. Tsymbal and D. G. Pettifor. Perspectives of Giant Magnetoresistance. *Solid state physics*, 56:113–237, 2001.
- [73] E. C. Stoner. Collective Electron Ferromagnetism. *Proceedings of the Royal Society of London Series A*, 165(922), 1938.
- [74] H. S. Nalwa, editor. *Handbook of thin film materials*. Academic Press, 2005.
- [75] P. Grunberg, R. Schreiber, and Y. Pang. Layered Magnetic Structures: Evidence for Antiferromagnetic Coupling of Fe Layers across Cr Interlayers. *Phys. Rev. Lett.*, 57(19), 1986.
- [76] S. S. P. Parkin, R. Bhadra, and K. P. Roche. Oscillatory magnetic exchange coupling through thin copper layers. *Phys. Rev. Lett.*, 66(16):2152–2155, 1991.
- [77] S. S. P. Parkin. Oscillations in giant magnetoresistance and antiferromagnetic coupling in [ Ni<sub>81</sub>Fe<sub>19</sub> / Cu ] N multilayers Oscillations in giant magnetoresistance in [ hiis , Fe<sub>19</sub> / CuJ „ multilayers and antiferromagnetic coupling. *Phys. Rev. Lett.*, 60:512, 1992.
- [78] E. Velu, C. Dupas, D. Renard, J. P. Renard, and J. Seiden. Enhanced magnetoresistance of ultrathin (Au/Co)<sub>n</sub> multilayers with perpendicular anisotropy. *Phys. Rev. B*, 37(1):4–7, 1988.
- [79] C. Dupas, P. Beauvillain, C. Chappert, J. P. Renard, F. Trigui, P. Veillet, and E. Renard. Very large magnetoresistance effects induced by antiparallel magnetization in two ultrathin cobalt films Very large magnetoresistance effects induced by antiparallel magnetization in two ultrathin cobalt films. *Journal of Applied Physics*, 67, 1990.
- [80] N. F. Mott. The Electrical Conductivity of Transition Metals. *Proceedings of the Physical Society*, 47:571, 1935.
- [81] E. Tsymbal. Giant Magnetoresistance, 2017.
- [82] S. Parkin. Origin of enhanced magnetoresistance of magnetic multilayers: Spin-dependent scattering from magnetic interface states. *Physical Review Letters*, 71(10):1641–1644, September 1993.

- [83] L Berger. Emission of spin waves by a magnetic multilayer traversed by a current. *Physical Review B*, 54(13):9353–9358, October 1996.
- [84] S. Swann. Magnetron sputtering. *Physics in Technology*, 19(2):67–75, March 1988.
- [85] R. Behrisch, editor. *Sputtering by Particle Bombardment*. Springer Berlin Heidelberg, 1981.
- [86] M. A. Lieberman and A. J. Lichtenberg. *Principles of Plasma Discharge and Materials*. Wiley Interscience, New York, 2 edition, 1994.
- [87] E. Girt, S. Wu, B. Lu, G. Ju, T. Nolan, S. Harkness, B. Valcu, A. Dobin, J. D. Risner, M. Munteanu, C. Chang, T. Tran, X. Wu, O. Mryasov, D. Weller, and S. Hwang. Influence of oxide on the structural and magnetic properties of CoPt alloy Influence of oxide on the structural and magnetic properties of CoPt alloy. *Journal of Applied Physics*, 99:08E715, 2006.
- [88] M. Ohring. *Material Science of Thin Films*. Acedemic Press, USA, 2 edition, 1992.
- [89] John. E. Mahan. *Physical Vapor Deposition of Thin Films*. John Wiley & Sons, New York, 2000.
- [90] R. A. Surmenev. A review of plasma-assisted methods for calcium phosphate-based coatings fabrication. *Surface and Coatings Technology*, 206(8-9):2035–2056, January 2012.
- [91] B. D. Cullity. *Elements of X-ray diffraction*. Mass: Addison-Wesley Pub. Co., 6th edition, 1956.
- [92] L. J. Singh. *Co<sub>2</sub>MnSi Heusler alloy thin films*. PhD thesis, Cambridge, 2005.
- [93] E. Hecht. *Optics*. Addison-Wesley, 4 edition, 2002.
- [94] M. Yasaka. V . *The Rigaku Journal*, 26(2):1–9, 2010.
- [95] Lewis, E. P., editor. *The Effects of a Magnetic Field on Radiation: Memoirs by Faraday, Kerr, and Zeeman*. American Book Company, New York; Cincinnati; Chicago: American Book Company, [1900], 1900.
- [96] J. Kerr. XLIII. On rotation of the plane of polarization by reflection from the pole of a magnet. *Philosophical Magazine Series 5*, 3(19):321–343, May 1877.
- [97] A. Hubert and R. Schäfer. *Magnetic Domains: The analysis of Magnetic Microstructure*. Springer-Verlag Berlin Heidelberg, 1 edition, 1998.
- [98] Spintronics: Magneto-Optical Kerr Effect (MOKE), 2009.
- [99] M. Ali. *Growth and study of magnetostrictive FeSiBC thin films, for device applications*. PhD thesis, The University of Sheffield, 1999.
- [100] S. Bedanta, O. Petravic, M. Aderholz, and W. Kleemann. A sample holder design for high temperature measurements in superconducting quantum device. *Review of Scientific Instruments*, 76(8):083910, 2005.

- [101] J. Lenz and S. Edelstein. Magnetic sensors and their applications. *IEEE Sensors Journal*, 6(3):631–649, June 2006.
- [102] J.R. Waldram. *Superconductivity of Metals and Cuprates*. CRC Press Book, 1996.
- [103] Shaikh Y. S. *Electron spin resonance in low-dimensional spin chains and metals*. PhD thesis, University of Stuttgart, 2008.
- [104] L. Landau and E. Lifshits. ON THE THEORY OF THE DISPERSION OF MAGNETIC. *Phys. Z. Sowjet.*, 8(1):153, 1935.
- [105] T. L. Gilbert. A lagrangian formulation of the gyromagnetic equation of the magnetic field. *Phys. Rev.*, 100:1243, 1955.
- [106] J. R. Macdonald. Ferromagnetic Resonance and the Internal Field in Ferromagnetic Materials. *Proceedings of the Physical Society*, 64(11):968–983, 1951.
- [107] D. Podler. On the Quantum Theory of Ferromagnetic Resonance. *Phys Review*, 73(9):1116, 1948.
- [108] J. A. C. Bland and B. Heinrich, editors. *Ultrathin Magnetic Structures III*. Springer-Verlag, Berlin/Heidelberg, 2005.
- [109] E. Montoya, T. McKinnon, A. Zamani, E. Girt, and B. Heinrich. Broadband ferromagnetic resonance system and methods for ultrathin magnetic films. *Journal of Magnetism and Magnetic Materials*, 356:12–20, April 2014.
- [110] L. J van der Pauw. A Method of measuring the resistivity and Hall coefficient of Lamellae of arbitrary shape. *Philips Res. Rep*, 13(1):1–9, 1958.
- [111] CAMPBELL The Science and Engineering of Microelectronic Fabrication.pdf.
- [112] E. Montoya, P. Omelchenko, C. Coutts, N. R. Lee-Hone, R. Hübner, D. Broun, B. Heinrich, and E. Girt. Spin transport in tantalum studied using magnetic single and double layers. *Phys. Rev. B*, 94:054416, 2016.
- [113] M. Arora, R. Hübner, D. Suess, B. Heinrich, and E. Girt. Origin of perpendicular magnetic anisotropy in Co/Ni multilayers. *Phys. Rev. B*, 96:024401, 2017.
- [114] Y. B. Zhang, J. A. Woollam, Z. S. Shan, J. X. Shen, and D. J. Sellmyer. Anisotropy and magneto-optical properties of sputtered Co/Ni multilayer thin films. *IEEE Transactions on Magnetics*, 30(6):4440–4442, 1994.
- [115] F. J. A. den Broeder, E. Janssen, W. Hoving, and W. B. Zeper. Perpendicular magnetic anisotropy and coercivity of Co/Ni multilayers. *IEEE Transactions on Magnetics*, 28(5):2760–2765, 1992.
- [116] Y. B. Zhang, P. He, J. A. Woollam, J. X. Shen, R. D. Kirby, and D. J. Sellmyer. Magnetic and magneto-optic properties of sputtered Co/Ni multilayers. *Journal of Applied Physics*, 75(10):6495, 1994.
- [117] G. Wang, Z. Zhang, B. Ma, and Q. Y. Jin. Magnetic anisotropy and thermal stability study of perpendicular Co/Ni multilayers. *Journal of Applied Physics*, 113(17):17C111, 2013.

- [118] N.R. Lee-Hone, R. Thanhoffer, V. Neu, R. Schfer, M. Arora, R. Hübner, D. Suess, D.M. Broun, and E. Girt. Roughness-induced domain structure in perpendicular co/nl multilayers. *Journal of Magnetism and Magnetic Materials*, 441:283 – 289, 2017.
- [119] L. You, R. C. Sousa, S. Bandiera, B. Rodmacq, and B. Dieny. Co/Ni multilayers with perpendicular anisotropy for spintronic device applications. *Applied Physics Letters*, 100(17):172411, April 2012.
- [120] M. Arora, C. Fowley, T. Mckinnon, E. Kowalska, V. Sluka, Alina M. Deac, B. Heinrich, and E. Girt. Spin Torque Switching in Nanopillars With Antiferromagnetic Reference Layer. *IEEE Magentic Letters*, 8, 2017.
- [121] F. Macia, P. Warnicke, D. Bedau, M.Y. Im, P. Fischer, D. A. Arena, and A. D. Kent. Perpendicular magnetic anisotropy in ultrathin multilayer films studied with ferromagnetic resonance and magnetic x-ray microspectroscopy. *Journal of Magnetism and Magnetic Materials*, 324(22):3629–3632, November 2012.
- [122] T. Taniguchi and H. Imamura. Critical current of spin-transfer-torque-driven magnetization dynamics in magnetic multilayers. *Physical Review B*, 78(22):224421, December 2008.
- [123] H. B. Huang, X. Q. Ma, Z. H. Liu, F. Y. Meng, S. Q. Shi, and L. Q. Chen. Micro-magnetic simulation of critical current density of spin transfer torque switching in a full-Heusler Co<sub>2</sub>FeAl<sub>0.5</sub>Si<sub>0.5</sub> alloy spin valve nanopillar. *Journal of Magnetism and Magnetic Materials*, 330:16–20, March 2013.
- [124] J. Qiu, Z. Meng, Y. Yang, J. F. Ying, Q. J. Yap, and G. Han. Effect of roughness on perpendicular magnetic anisotropy in (Co<sub>90</sub>Fe<sub>10</sub>/Pt)<sub>n</sub> superlattices. *AIP Advances*, 6(5):056123, May 2016.
- [125] B. Heinrich, T. Monchesky, and R. Urban. Role of interfaces in higher order angular terms of magnetic anisotropies: ultrathin film structure. *Journal of magnetic materials*, 236(3):339–346, 2001.
- [126] J. M. Shaw, H. T. Nembach, and T. J. Silva. Roughness induced magnetic inhomogeneity in Co/Ni multilayers: Ferromagnetic resonance and switching properties in nanostructures. *Journal of Applied Physics*, 108(9):093922, 2010.
- [127] C. Coutts, M. Arora, R. Hubner, B. Heinrich, and E. Girt. Cu diffusion in Co/Ni grain boundaries after annealing. *AIP Advances*, Submitted, 2017.
- [128] D. Crew, Er. Girt, D. Suess, T. Schrefl, K. Krishnan, G. Thomas, and M. Guilot. Magnetic interactions and reversal behavior of Nd<sub>2</sub>Fe<sub>14</sub>B particles diluted in a Nd matrix. *Physical Review B*, 66(18):184418, November 2002.
- [129] J. Chatterjee. Seed layer effect on the magnetic properties of ultrathin Co/Pt multilayers with perpendicular magnetic anisotropy. *IEEE Transactions on Magnetics*, 50(11):1–4, 2014.
- [130] T. B. Massalski. *Binary alloy phase diagrams*. ASM International, 2 edition, 1986.

- [131] E. Liu, J. Swerts, T. Devolder, S. Couet, S. Mertens, T. Lin, V. Spampinato, A. Franquet, T. Conard, S. VanElshocht, A. Furnemont, J. De. Boeck, and G. Kar. perpendicular magnetic anisotropy Seed layer impact on structural and magnetic properties of [ Co / Ni ] multilayers with perpendicular magnetic anisotropy. *Journal of Applied Physics*, 121(043905):1–8, 2017.
- [132] H. He, Z. Zhang, B. Ma, and Q. Jin. Synthetic Antiferromagnet With Perpendicular Anisotropy and Its Application in Pseudo Spin Valves. *IEEE Transactions on Magnetics*, 46(6):1327–1330, June 2010.
- [133] H. J. Richter and Er. Girt. Simplified analysis of two-layer antiferromagnetically coupled media. *Appl. Phys. Lett.*, 80:2529, 2002.
- [134] H.J. Richter and E. Girt. How antiferromagnetic coupling can stabilize recorded information. *IEEE Transactions on Magnetics*, 38(5):1867 – 1872, 2002.
- [135] N. Smith, S. Maat, M. Carey, and J. Childress. Coresonant Enhancement of Spin-Torque Critical Currents in Spin Valves with a Synthetic-Ferrimagnet Free Layer. *Physical Review Letters*, 101(24):247205, December 2008.
- [136] E. Girt and H. J. Richter. Antiferromagnetically coupled perpendicular recording media. *IEEE Transactions on Magnetics*, 39(5):2306–2310, September 2003.
- [137] H.J. Richter and E. Girt. Recording potential of anti-ferromagnetically coupled longitudinal media. *IEEE Transactions on Magnetics*, 37(4).
- [138] Er. Girt, Kannan M. Krishnan, G. Thomas, E. Girt, and Z. Altounian. Coercivity limits and mechanism in nanocomposite Nd-Fe-B alloys. *Journal of Magnetism and Magnetic Materials*, 231:219–230, 2001.
- [139] E. C. Stoner and E. P. Wohlfarth. A Mechanism of Magnetic Hysteresis in Heterogeneous Alloys. *Philosophical Transactions of the Royal Society of London*, A249(826):599–642, 1948.
- [140] M. Zheng, J. Shen, J. Barthel, P. Ohresser, C. V. Mohan, and J. Kirschner. Growth, structure and magnetic properties of Co ultrathin films on Cu(111) by pulsed laser deposition. *Journal of Physics: Condensed Matter*, 12(6):783–794, February 2000.
- [141] T. Kato, Y. Matsumoto, S. Kashima, S. Okamoto, N. Kikuchi, S. Iwata, O. Kitakami, and S. Tsunashima. Perpendicular Anisotropy and Gilbert Damping in Sputtered Co/Pd Multilayers. *IEEE Transactions on Magnetics*, 48(11):3288–3291, November 2012.
- [142] M. Gottwald, S. Girod, S. Andrieu, and S. Mangin. Tuneable perpendicular magnetic anisotropy in single crystal [Co/Ni](111) superlattices. *IOP Conference Series: Materials Science and Engineering*, 12:012018, June 2010.
- [143] F. J. A. den Broeder, E. Janssen, W. Hoving, and W.B. Zeper. Perpendicular magnetic anisotropy and coercivity of Co/Ni multilayers. *IEEE Transactions on Magnetics*, 28(5):2760–2765, 1992.

- [144] J. Bass. CPP magnetoresistance of magnetic multilayers: A critical review. *Journal of Magnetism and Magnetic Materials*, 408:244–320, June 2016.
- [145] T. Kai, Y. Ohashi, and K. Shiiki. Study of giant magnetoresistance in Co/X superlattices (X= Cu, Ru, Rh and Pd) by first-principle band calculation. *Journal of magnetism and magnetic materials*, 183:292–298, 1998.
- [146] S. Zoll, A. Dinia, J. P. Jay, C. Meny, G. Z. Pan, A. Michel, L. El Chahal, V. Pierron-Bohnes, P. Panissod and H. A. M. Van den Berg. No Title. *Phys. Rev. B*, 57(8):4842, 1998.
- [147] J. C. Slonczewski. Currents and torques in metallic magnetic multilayers. *Journal of Magnetism and Magnetic Materials*, 247(3):324–338, June 2002.
- [148] E. Girt, K. M. Krishnan, and G. Thomas. Optimization of magnetic properties of nanostructured Nd-Fe-B: approaching ideal Stoner-Wohlfarth behaviour. *Scripta Materialia*, 44(8-9):1431–1435, May 2001.
- [149] D. Lacour, J. A. Katine, N. Smith, M. J. Carey, and J. R. Childress. Thermal effects on the magnetic-field dependence of spin-transfer-induced magnetization reversal. *Applied Physics Letters*, 85(20):4681, 2004.
- [150] J. M. Shaw, H. T. Nembach, and T. J. Silva. Determination of spin pumping as a source of linewidth in sputtered Co 90 Fe 10 /Pd multilayers by use of broadband ferromagnetic resonance spectroscopy. *Physical Review B*, 85(5):054412, February 2012.
- [151] S. Pal, B. Rana, O. Hellwig, T. Thomson, and A. Barman. Tunable magnonic frequency and damping in [Co/Pd]<sub>8</sub> multilayers with variable Co layer thickness. *Applied Physics Letters*, 98(8):082501, 2011.
- [152] S. Mizukami, X. Zhang, T. Kubota, H. Naganuma, M. Oogane, Y. Ando, and T. Miyazaki. Gilbert Damping in Ni/Co Multilayer Films Exhibiting Large Perpendicular Anisotropy. *Applied Physics Express*, 4(1):013005, January 2011.
- [153] M. P. Sharrock. Time dependence of switching fields in magnetic recording media (invited). *Journal of Applied Physics*, 76(10):6413–6418, November 1994.
- [154] F. Gimbert, L. Calmels, and S. Andrieu. Localized electron states and spin polarization in Co/Ni(111) overlayers. *Physical Review B*, 84(9):094432, September 2011.
- [155] G. H. Daalderop, P. J. Kelly, and den Broeder F. J. Prediction and confirmation of perpendicular magnetic anisotropy in Co/Ni multilayers. *Physical review letters*, 68(5):682–685, February 1992.
- [156] M. Gottwald, S. Andrieu, F. Gimbert, E. Shipton, L. Calmels, C. Magen, E. Snoeck, M. Liberati, T. Hauet, E. Arenholz, S. Mangin, and E. E. Fullerton. Co/Ni(111) superlattices studied by microscopy, x-ray absorption, and ab initio calculations. *Physical Review B*, 86(1):014425, July 2012.
- [157] M. Gottwald, S. Girod, S. Andrieu, and S. Mangin. Tuneable perpendicular magnetic anisotropy in single crystal [Co/Ni](111) superlattices. *IOP Conference Series: Materials Science and Engineering*, 12:012018, June 2010.

- [158] S. Kaka, M. R. Pufall, W. H. Rippard, T. J. Silva, S. E. Russek, J. A. Katine, and M. Carey. Spin transfer switching of spin valve nanopillars using nanosecond pulsed currents. *Journal of Magnetism and Magnetic Materials*, 286:375–380, February 2005.
- [159] Shehzaad Kaka, Matthew R Pufall, William H Rippard, Thomas J Silva, Stephen E Russek, and Jordan A Katine. Mutual phase-locking of microwave spin torque nano-oscillators. *Nature*, 437(7057):389–92, September 2005.
- [160] O. Hellwig, T. Hauet, T. Thomson, E. Dobisz, J. D. Risner-Jamtgaard, D. Yaney, B. D. Terris, and E. E. Fullerton. Coercivity tuning in Co/Pd multilayer based bit patterned media. *Applied Physics Letters*, 95(23):232505, 2009.
- [161] T. Hauet, E. Dobisz, S. Florez, J. Park, B. Lengsfeld, B. D. Terris, and O. Hellwig. Role of reversal incoherency in reducing switching field and switching field distribution of exchange coupled composite bit patterned media. *Applied Physics Letters*, 95(26):262504, 2009.
- [162] M. Ranjbar, S. N. Piramanayagam, S. K. Wong, R. Sbiaa, and T. C. Chong. Anomalous Hall effect measurements on capped bit-patterned media. *Applied Physics Letters*, 99(14):142503, 2011.
- [163] B. D. Terris and T. Thomson. Nanofabricated and self-assembled magnetic structures as data storage media. *Journal of Physics D: Applied Physics*, 38(12):R199–R222, June 2005.
- [164] Manfred E. Schabes. Micromagnetic simulations for terabit/in<sup>2</sup> head/media systems. *Journal of Magnetism and Magnetic Materials*, 320(22):2880–2884, November 2008.
- [165] H. J. Richter, A. Y. Dobin, R. T. Lynch, D. Weller, R. M. Brockie, O. Heinonen, K. Z. Gao, J. Xue, R. J. M. V. D. Veerdonk, P. Asselin, and M. F. Erden. Recording potential of bit-patterned media. *Applied Physics Letters*, 88(22):222512, 2006.
- [166] K. Kyuno, J. Ha, R. Yamamoto, and S. Asano. Perpendicular Magnetic Anisotropy of Metallic Multilayers Composed of Magnetic Layers Only: Ni/Co and Ni/Fe Multilayers. *Japanese Journal of Applied Physics*, 35(Part 1, No. 5A):2774–2778, May 1996.
- [167] M. T. Johnson, de Vries J. J., N. W. McGee, aan de Stegge J., and den Broeder F. J. Orientational dependence of the interface magnetic anisotropy in epitaxial Ni/Co/Ni sandwiches. *Physical review letters*, 69(24):3575–3578, December 1992.
- [168] D. Sander. The magnetic anisotropy and spin reorientation of nanostructures and nanoscale films. *Journal of Physics: Condensed Matter*, 16(20):R603–R636, May 2004.
- [169] O. Hjortstam, K. Baberschke, J. M. Wills, B. Johansson, and O. Eriksson. Magnetic anisotropy and magnetostriction in tetragonal and cubic Ni. *Physical Review B*, 55(22):15026–15032, June 1997.
- [170] M. Sakamaki, K. Amemiya, M. O. Liedke, J. Fassbender, P. Mazalski, I. Sveklo, and A. Maziewski. Perpendicular magnetic anisotropy in a Pt/Co/Pt ultrathin film arising from a lattice distortion induced by ion irradiation. *Physical Review B*, 86(2):024418, July 2012.



- [171] C. R. Chang. Magnetostrictive surface anisotropy of epitaxial multilayers. *Physical Review B*, 48(21):15817–15822, December 1993.
- [172] M.T. Johnson, F.J.A. den Broeder, J.J. de Vries, N.W.E. McGee, R. Jungblut, and J. aan de Stegge. Perpendicular anisotropy of epitaxial wedge-shaped Co/Ni sandwiches grown on single crystal Cu substrates. *Journal of Magnetism and Magnetic Materials*, 121(1-3):494–497, March 1993.
- [173] F. Gimbert and L. Calmels. First-principles investigation of the magnetic anisotropy and magnetic properties of Co/Ni(111) superlattices. *Physical Review B*, 86(18):184407, November 2012.
- [174] V. M. Naik, S. Hameed, R. Naik, L. Pust, L. E. Wenger, G. L. Dunifer, and G. W. Auner. Effect of [111] texture on the perpendicular magnetic anisotropy of Co/Ni multilayers. *Journal of Applied Physics*, 84(6):3273, 1998.
- [175] Y. B. Zhang and J. A. Woollam. Annealing effects of Co/Ni multilayers. *IEEE Transactions on Magnetics*, 31(6):3262–3264, 1995.
- [176] E. Yang, V. M. Sokalski, M. T. Moneck, D. M. Bromberg, and J. G. Zhu. Annealing effect and under/capping layer study on Co/Ni multilayer thin films for domain wall motion. *Journal of Applied Physics*, 113(17):17C116, 2013.
- [177] D. Stanescu, D. Ravelosona, V. Mathet, C. Chappert, Y. Samson, C. Beigneux, N. Vernier, J. Ferre, J. Gierak, E. Bouhris, and E. E. Fullerton. Tailoring magnetism in CoNi films with perpendicular anisotropy by ion irradiation. *Journal of Applied Physics*, 103(7):07B529, 2008.
- [178] P. J. H. Bloemen, W. J. M. Jonge, and F. J. A. Broeder. Magnetic anisotropies in Co / Ni ( 111 ) multilayers. *Journal of Applied Physics*, 72:4840, 1992.
- [179] A.S.H. Rozatian, B.D. Fulthorpe, T.P.A. Hase, D.E. Read, G. Ashcroft, D.E. Joyce, P.J. Grundy, J. Amighian, and B.K. Tanner. Anisotropy and interface structure in sputtered Co/Pt multilayers on Si. *Journal of Magnetism and Magnetic Materials*, 256(1-3):365–372, January 2003.
- [180] M. Suzuki, K. Kudo, K. Kojima, T. Yasue, N. Akutsu, W. A. Dino, H. Kasai, E. Bauer, and T. Koshikawa. Magnetic domain patterns on strong perpendicular magnetization of Co/Ni multilayers as spintronics materials: I. Dynamic observations. *Journal of physics. Condensed matter : an Institute of Physics journal*, 25(40):406001, October 2013.
- [181] S. T. Lim, M. Tran, J. W. Chenchen, J. F. Ying, and G. Han. Effect of different seed layers with varying Co and Pt thicknesses on the magnetic properties of Co/Pt multilayers. *Journal of Applied Physics*, 117(17):17A731, May 2015.
- [182] A. Barman, S. Wang, O. Hellwig, A. Berger, E. E. Fullerton, and H. Schmidt. Ultrafast magnetization dynamics in high perpendicular anisotropy [Co $\overline{\text{Pt}}$ ]<sub>n</sub> multilayers. *Journal of Applied Physics*, 101(9):09D102, May 2007.

- [183] E. H. M. van der Heijden, K. J. Lee, Y. H. Choi, T. W. Kim, H. J. M. Swagten, C.Y. You, and M H. Jung. Perpendicular magnetic anisotropic characteristics of amorphous [CoSiB/Pt] N multilayers. *Applied Physics Letters*, 102(10):102410, March 2013.
- [184] A S H Rozatian, C H Marrows, T P A Hase, and B K Tanner. The relationship between interface structure, conformality and perpendicular anisotropy in CoPd multilayers. *Journal of physics. Condensed matter : an Institute of Physics journal*, 17(25):3759–70, June 2005.
- [185] M. Haertinger, C. H. Back, S. H. Yang, S. S. P. Parkin, and G. Woltersdorf. Properties of Ni/Co multilayers as a function of the number of multilayer repetitions. *Journal of Physics D: Applied Physics*, 46(17):175001, May 2013.
- [186] D. R. Linde. *CRC Handbook of Chemistry and Physics*. CRC Press LLC, 84th edition, 2004.
- [187] J.C.A. Huang, T.E. Wang, C.C. Yu, Y.M. Hu, P.B. Lee, and M.S. Yang. Epitaxial growth and characterization of (100) and (110) permalloy films. *Journal of Crystal Growth*, 171(3-4):442–446, February 1997.
- [188] D. Sander. The correlation between mechanical stress and magnetic anisotropy in ultrathin films. *Reports on Progress in Physics*, 62(5):809–858, May 1999.
- [189] J. M. Shaw, H. T. Nembach, and T. J. Silva. Measurement of orbital asymmetry and strain in Co 90 Fe 10 /Ni multilayers and alloys: Origins of perpendicular anisotropy. *Physical Review B*, 87(5):054416, February 2013.
- [190] P. Bruno. Dipolar magnetic surface anisotropy in ferromagnetic thin films with interfacial roughness. *Journal of Applied Physics*, 64(6):3153, 1988.
- [191] D. Suess, T. Schrefl, J. Fidler, and J. N. Chapman. Micromagnetic simulation of the long-range interaction between NiFe nano-elements using the BE-method. *Journal of Magnetism and Magnetic Materials*, 196-197:617–619, May 1999.
- [192] P. Bruno. Magnetic surface anisotropy of cobalt and surface roughness effects within Neel’s model. *Journal of Physics F: Metal Physics*, 18(6):1291–1298, June 1988.
- [193] H. J. G. Draaisma and W. J. M. de Jonge. Surface and volume anisotropy from dipole-dipole interactions in ultrathin ferromagnetic films. *Journal of Applied Physics*, 64(7):3610, 1988.
- [194] den Broeder F. J., D. Kuiper, van de Mosselaer A. P., and W. Hoving. Perpendicular magnetic anisotropy of Co-Au multilayers induced by interface sharpening. *Physical review letters*, 60(26):2769–2772, June 1988.
- [195] M. E. Straumanis and L. S. Yu. Lattice parameters, densities, expansion coefficients and perfection of structure of Cu and of Cu $\alpha$ –In  $\alpha$  phase. *Acta Crystallographica*, 25(6):676–682, 1969.
- [196] M. Henini. *Molecular Beam Epitaxy, 1st Edition From Research to Mass Production*. Elsevier Science, 2012.

- [197] B. C. Giessen. *Developments in the structural chemistry of alloy phases*. New York, Plenum Press, 1969.
- [198] J. R. Childress, C. L. Chien, and A. F. Jankowski. Magnetization, Curie temperature, and magnetic anisotropy of strained (111) Ni/Au superlattices. *Physical Review B*, 45(6):2855–2862, February 1992.
- [199] C. Chappert, K. Le Dang, P. Beauvillain, H. Hurdequint, and D. Renard. Ferromagnetic resonance studies of very thin cobalt films on a gold substrate. *Physical Review B*, 34(5):3192–3197, September 1986.